Towards Cold State-Selected Ion-Molecule Reactions

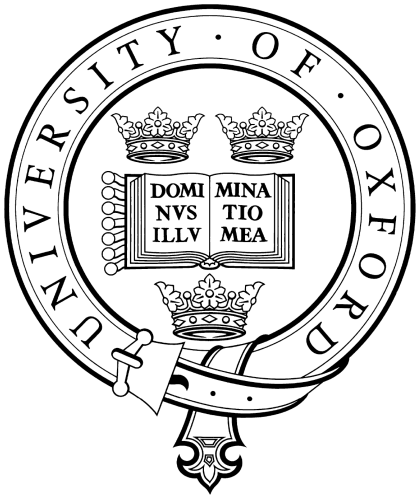

Nabanita Deb

Linacre College

University of Oxford

A thesis submitted for the degree of

Doctor of Philosophy

Trinity 2014

for my father

Towards Cold State-Selected Ion-Molecule Reactions

Nabanita Deb, Linacre College

A thesis submitted in partial fulfilment of the requirements for the degree of Doctor of Philosophy of the University of Oxford

Trinity 2014

Abstract

In recent years there has been much progress in the field of cold and ultracold molecular physics and a variety of experimental techniques for producing cold matter now exist. In particular, the generation of trapped molecular ions at mK temperatures has been achieved by sympathetic-cooling with laser-cooled atomic ions. By implementing schemes to selectively prepare and control the internal quantum state of molecular ions, and developing detection techniques, it will be increasingly possible to study cold state-selected chemical collisions in an ion-trap.

Most molecular species produced in a selected rovibrational state have a lifetime of a few seconds, before the population is redistributed across numerous rovibrational states by interaction with the ambient blackbody radiation (BBR). Consequently, the investigation of state-selected reaction dynamics at low temperatures in experiments where long time scales (minutes to hours) are required, is hindered. This thesis looks into developing strategies that maintain state selection in molecular ions, allowing one to observe state-selected reactions in cold environments, in particular the state-selected reaction between $C_2H_2^+$ and ND_3. Examining reactive ion molecule collisions under cold conditions provides insight into fundamental reaction dynamics, which are thermally averaged out at higher temperatures.

A theoretical model is used to investigate laser-driven, blackbody-mediated, rotational cooling schemes for several $^1\Sigma$ and $^2\Pi$ diatomic species. The rotational cooling is particularly effective for DCl^+ and HCl^+, for which 92% and $>$99% (respectively) of the population can be driven into the rovibrational ground state. For the other systems a broadband optical pumping source is found to enhance the population that can be accumulated in the rovibrational ground state by up to 29% more than that achieved when exciting a single transition. The influence of the rotational constant, dipole moments and electronic state of the diatomics on the achievable rotational cooling is also studied.

This approach is extended to consider the BBR interaction and rotational cooling of a linear polyatomic ion, $C_2H_2^+$, which has a $^2\Pi$ electronic ground state. The (1-0) band of the ν_5 cis-bending mode is infrared active and strongly overlaps the 300 K blackbody spectrum. Hence the lifetimes of state-selected rotational levels are found to be short compared to the typical timescale of ion trapping experiments. Laser cooling schemes are proposed that could be experimentally viable, which involves simultaneous pumping of a set of closely

spaced Q-branch transitions on the $^2\Delta_{5/2}$–$^2\Pi_{3/2}$ band together with two $^2\Sigma^+$–$^2\Pi_{1/2}$ lines. It is shown that this should lead to >70% of total population in the lowest rotational level at 300 K and over 99% at 77 K.

In order to identify states of the acetylene ion that could be trapped sufficiently long enough for state-selected reactions in the ion trap with decelerated ND_3, the theoretical work has been complemented by experimental investigations into the production of $C_2H_2^+$ in selected states, and ion trapping of the same using sinusoidal and digital trapping voltages. Appropriate (2+1) REMPI (Resonance Enhanced Multiphoton Ionization) schemes are used to produce $C_2H_2^+$ in different quantum states, with (1+1) Resonance Enhanced Multiphoton Dissociation (REMPD) employed to detect the ion thus produced.

The concept of digital ion trapping for ejection onto MCPs is introduced. A comprehensive comparison between sinusoidal and digital trapping fields has been performed with respect to trap depth and stability regions. Programs have been developed to calculate the stability regions for different ions under varying experimental conditions. The trap depth has been derived for both digital and sinusoidal trapping fields. It is observed that as τ increases, the trap depth of a digital trap increases. For τ = 0.293, the trap depth and stability diagram for both sinusoidal and digital trapping fields would be equivalent. The trap depth at which the sinusoidal trap operates experimentally in our research group is $\sim$1.36 eV. In contrast, the experimental parameters at which the digital trap operates generates a trap depth of 1.21 eV. Ca^+ Coulomb crystals have been formed, stably trapped and stored for extended periods of time in both sinusoidally and digitally time-varying trapping fields. The sympathetic cooling of a diverse range of ions into Ca^+ Coulomb crystals is demonstrated, again using both sinusoidal and digital trapping fields.

Mass spectrometric detection of ionic reaction products using a novel ejection scheme has been developed, where ejection is achieved by switching off the trapping voltage and converting the quadrupole trap into an extractor-repeller pair by providing the ion trap electrodes with appropriate ejection pulses. This technique is developed using a digital trapping voltage rather than the sinusoidal trapping voltage, as ejection with sinusoidal trapping voltages is not clean (resonance circuitry used in the electronics induces ringing after switching off the trapping voltage). Coulomb crystals, both pure Ca^+ and multi-component crystals, are ejected from the ion trap and the TOF trace obtained is recorded on an oscilloscope. When the integrated, base-line subtracted TOF peak is plotted against the number of ions in a Ca^+ crystal and sympathetically-cooled Ca^+ – CaF^+ crystal, a linear relationship is obtained. This technique is found to be well mass-resolved, with the signal arising from $CaOH^+$ (57 amu) and $CaOD^+$ (58 amu) resolvable on the TOF trace.

This technique would enable one to monitor a reaction in a Coulomb crystal where the reactant and product species are both either lighter or heavier than calcium, such as the reaction between $C_2H_2^+$ and ND_3, something which has not been previously possible. It is, also, potentially a very important technique for reactions with many product channels.

Acknowledgements

It has been an enormous pleasure and privilege for me to undertake doctoral research in the Department of Chemistry at Oxford University. I am honoured to thank here the extraordinary people and institutions that have facilitated and invigorated the research that has led to this dissertation.

First and foremost, I would like to express my sincerest gratitude to my supervisor, Professor Timothy P. Softley, Head of the Department of Chemistry and the Softley Research Group, for the brilliance of his example and guidance, for the generosity of his time and for his unwavering support of my research.

I would also like to thank all the members of the Softley Research Group, including Dr. Martin Bell, Dr. Alexander Gingell, my fellow doctoral candidate Laura Pollum, Dr. Chris Rennick, Part II student Alexander Smith and Dr. Atreju Tauschinsky. I am grateful to Dr. Brianna Heazlewood, Royal Commission for the Exhibition of 1851 Research Fellow in the Softley Research Group, for her generous readings of drafts, superlative practical suggestions and for her kind support of my work. I am also grateful to the excellent staff in the Electronics and Mechanical workshops at the Department of Chemistry.

This research would not have been possible without financial support from the Felix Scholarship, the Department of Chemistry, Linacre College and Oxford University. Linacre College has played a special role in my time at Oxford, becoming a home away from home. I thank all the wonderful staff at Linacre College for their kind help.

I feel fortunate for the happy camaraderie and cheerful encouragement of a close set of friends, and would like in particular to thank Dr. Cecelia Cauchy, Dr. Sashikesh Ganeshalingam, Dr. David Jackson, Tommy Khoo, P. J. Mohan, Dr. Xiaolin Li, Dr. Chelsea Robles, Dr. Pei Jen Tiong, Venus Tsang and Carryn Yong. I am also thankful to Dr. Manav Ratti for his unflagging support, warm friendship and astute mentorship.

Last but not least, I am grateful to my father and mother, Dr. Pradip Kumar Deb and Dr. Debjani Deb, for their infinite love, care and support. With her constant joy and love, my sister, Amrita Deb, continues to be a blessing. I also heartily acknowledge the support of all my extended family, particularly my uncle Dr. Sudip Kumar Deb, Mr. Santanu Roy and all my cousins, especially Souradeep Roy. I remain thankful for the inspiration and wisdom of my late greatgrandmother and late grandfather.

Chapter 2 of this doctoral dissertation has appeared as the following article:

N. Deb, B. R. Heazlewood, M. T. Bell and T. P. Softley, "Blackbody-mediated rotational laser cooling schemes in MgH^+, DCl^+, HCl^+, LiH and CsH", *Phys. Chem. Chem. Phys.*, 2013, 15(34), 14270.

Chapter 3 of this doctoral dissertation has appeared as the following article:

N. Deb, B. R. Heazlewood, C. J. Rennick and T. P. Softley, "Laser induced rovibrational cooling of the linear polyatomic ion $C_2H_2^+$", *J. Chem. Phys.*, 2014, 140(16), 164314.

I am grateful to the anonymous referees of these articles for the meticulousness, thoroughness, and excellence of their feedback.

Nabanita Deb
Linacre College, Oxford
July 2014

Contents

Conference Posters Presented

[1] Spectroscopy and Dynamics Group conference, Oxford, UK, January 2014.

[2] COST-IOTA workshop on "Cold Molecular Ions", Arosa, Switzerland, September 2013.

[3] European Science Foundation (ESF) conference on "Cold and Ultracold Molecules", Obergurgl, Austria, November 2012.

[4] The European Conference on the Dynamics of Molecular Systems, MOLEC, Oxford, UK, September 2012.

[5] 10th European Conference on Atoms Molecules and Photons, Salamanca, Spain, July 2010.

[6] Spectroscopy and Dynamics Group conference, Birmingham, UK, January 2010.

Publications

[1] N. Deb, B. R. Heazlewood, M. T. Bell and T. P. Softley, "Blackbody-mediated rotational laser cooling schemes in MgH^+, DCl^+, HCl^+, LiH and CsH", *Phys. Chem. Chem. Phys.*, 2013, 15(34), 14270.

[2] N. Deb, B. R. Heazlewood, C. J. Rennick and T. P. Softley, "Laser induced rovibrational cooling of the linear polyatomic ion $C_2H_2^+$", *J. Chem. Phys.*, 2014, 140(16), 164314.

[3] N. Deb*, L. L. Pollum*, A. D. Smith, M. Keller, C. J. Rennick, B. R. Heazlewood and T. P. Softley, "Coulomb crystal mass spectrometry in a linear Paul ion trap with pulsed digital rf waveforms", submitted to *Phys. Rev. Lett.*

List of Figures

List of Tables

Chapter 1

Introduction

1.1 Motivations for studying cold state-selected reactions

Understanding the kinetics of a chemical reaction and the fundamental underlying processes is a subject that has been intriguing scientists for centuries. From a classical point of view, as temperature is lowered the speed of gas phase molecules is lowered. Molecules move at different speeds at different temperatures; for instance, gas phase ND_3 molecules have an average speed of 564 m/s at 300 K, 103 m/s at 10 K, 32.5 m/s at 1 K and 1.03 m/s at 1 mK.[1] This decrease in the speed of the gas phase molecules at low temperatures is crucial as this makes the wave nature of particles no longer negligible.

The de Broglie equation is given by $p = h/\lambda$, where p is the momentum of a molecular species in the gas phase (or more generally any particle), h is Planck's constant and λ is the de Broglie wavelength. The thermal de Broglie wavelength at temperature T is given by equation 1.1,

$$\lambda = \frac{h}{\sqrt{2\pi m k_B T}}. \tag{1.1}$$

Wave effects are likely to dominate the collisional behaviour if the de Broglie wavelength is sufficiently long compared to molecular dimensions. The de Broglie wavelength for gas phase ND_3 molecules is 0.354 Å at 300 K, 1.94 Å at 10 K, 6.13 Å at 1 K and 194 Å at 1 mK.[1] Thus at 1 mK, the de Broglie wavelength is significantly longer, by an order of magnitude or more, than molecular dimensions. As the wavelength increases the quantum nature increases and dominates the chemical dynamics and quantum reactive scattering

occurs.[2]

At room temperature, a molecular species occupies a range of internal (vibrational and rotational) quantum states, as dictated by the Boltzmann distribution. The "ultracold" regime is defined as the < 1 mK temperature range, the regime where Bose-Einstein condensates are formed. "Cold" refers to temperatures < 10 K, all the way down to mK.[3] In the cold and ultracold temperature regimes, the internal population distribution is minimized.

A primary goal behind studying chemical reactions at very low temperatures is to investigate how the transition to the quantum regime leads to novel behaviour in the collision dynamics. Reaction data at low temperatures are no longer thermodynamically and statistically averaged over many states (as in room temperature studies); this is because as temperature is lowered fewer and fewer internal quantum states are occupied. The collisional angular momentum is highly restricted in this regime, allowing observation of even a single angular momentum collisional state, with pure s-wave or p-wave scattering. This is the main reason for targeting a cold state-selected reaction – to probe fundamental reaction processes when all the reactants are in their ground state or are distributed over a limited number of internal quantum states.

The quantum effects that become important at low temperatures include: tunnelling, quantum reflection and quantum scattering resonances. In the low temperature regime, the long range potential becomes important and influences the chemical reaction. The study of chemical reactions at cold and ultracold temperatures can help probe this important region of the potential energy surface. The long-range interactions are weak and thus at low temperatures it becomes possible to use, for example, electromagnetic field control over species with appropriate properties. This, in turn, can result in better control of the dynamics of chemical reactions.

1.1.1 Chemistry in the interstellar medium

Interstellar clouds of dust particles and gases constitute 10% of the Milky Way galaxy. The diffuse interstellar clouds have temperatures of 50 – 100 K and density of 10^2 – 10^3 molecules/cm^3. Dense interstellar clouds can be characterised by even lower temperatures ($\sim$ 10 K) and densities ($\sim 10^4$ molecules/cm^3). The cosmic microwave background has a temperature of 2.8 K.[3, 4]

Molecular ions are abundant in the interstellar medium (ISM) and play an important role in the chemistry of the ISM. Such ions are formed as a result of the intense short-wavelength radiation fields that prevail in such environments. The rich gas-phase chemistry occurring in the ISM is dominated by ion-molecule reactions, though neutral-free radical reactions also play an important role, as do reactions on grain surfaces. The most abundant reaction in the universe is the bimolecular collision between H_2 molecules and H_2^+ ions.[3] Barrierless ion-molecule reactions of unsaturated hydrocarbon species are essential for the formation of conjugated hydrocarbons and clusters. In these reactions, such as that of acetylene cations with N atoms or HCN, C–N bond formation is likely to be fast and of importance in building larger molecules.

Most of the reactions in the ISM are taking place in the temperature range of 3 – 20 K. To fully understand the chemistry occurring in the ISM, it is necessary to investigate reaction mechanisms under low temperature conditions. For example, the reaction of $C_2H_2^+$ with molecular hydrogen displays an unusual temperature dependence, with the opening of a new reaction channel at very low collision energies.[5] The experimentally observed rate constant for this reaction has a strong negative temperature dependence below $\sim$100 K.

The reactions occurring in the ISM are typically barrierless along the minimum energy pathway, as only then could a reaction proceed under the cold conditions which exist in the ISM. The dynamics of ion-molecule complex formation are dictated by the long-range inter-molecular potential and are fundamentally different from the transition state model, which is commonly used to describe reactions with an activation barrier. Simple extrapolation of trends from data recorded at temperatures down to 80 K cannot predict the behaviour of

barrierless reactions at low temperatures. This illustrates the importance of experimentally studying astrochemically-relevant ion-molecule reactions under cold conditions to develop our understanding of the fundamental chemistry of the ISM.

1.1.2 Reaction dynamics at low temperature

One of the classical models used for reaction kinetics is transition state theory. According to this theory, reactions proceed via the formation of a transition state. The rate of a reaction is directly proportional to $e^{-\Delta E/RT}$. Here, ΔE is the activation energy, which is the difference in energy between the reactants and the transition state at temperature T and R is the gas constant ($R = k/N_a$, k is the Boltzman's constant).[6, 7] According to this theory, as temperature increases the reaction rate increases, as described by the Arrhenius equation given by equation 1.2,

$$k_{\text{bi}} = Ae^{\left(-\frac{\Delta E}{RT}\right)}, \tag{1.2}$$

where k_{bi} is the bimolecular rate constant and A is the Arrhenius factor. The rate of the reaction is thus dependent on the height of the barrier, ΔE, and the temperature, T and the pre-exponential factor.

The difference in barrier heights associated with the zero-point vibrational energy of the reactants involved can yield isotopic differences in reaction rates: the kinetic isotope effect. The kinetic isotope effect is often used in organic chemistry to determine the mechanism of reactions and the rate determining steps. The simple kinetic picture is that reactions involving D_2 are typically slower than the ones involving H_2, as H_2 has a higher zero-point energy compared to D_2, and hence typically lower energy barriers. For instance, if any organic reaction involves the breaking or making of a C–H a bond, then labelling that particular bond with D can help deduce whether the bond was involved in the rate determining step. [7]

At very low temperatures, this simple description becomes less useful and our interpretations of low collisional energy reactions must consider more factors. When lowering the temperature, as discussed above, quantum mechanical effects can play a more important

role; reaction rates that differ by many orders of magnitude (compared to room-temperature studies) can be observed. At low temperatures, molecular collisions can be influenced by long-range intermolecular forces, which in turn control the orientation of the approaching reactants. Angular momentum must be conserved during the molecular collision; this conservation of energy and the centrifugal barrier play an important role in determining the rate of reaction.

The distance of closest approach for a two-particle reactive collision is related to the orbital angular momentum. The magnitude of the classical orbital angular momentum associated with the collision is given by:[3]

$$\mid L \mid = \mu\nu b, \tag{1.3}$$

where μ is the reduced mass of the collision pair, ν is the relative velocity and b (the impact parameter) indicates whether the impact is head-on or glancing. At low temperatures, the velocity of the gas phase molecules decreases, and that in turn leads to a decrease in the relative velocity of the reacting pair. The classical orbital angular momentum L is replaced by its quantum mechanical counterpart,

$$\mid L \mid = \hbar\sqrt{l(l+1)}\,. \tag{1.4}$$

Here, l is the orbital angular momentum quantum number of the collision pair. Different orbital angular momenta, l, correspond to different partial waves: l = 0 (s), 1 (p), 2 (d),.....

Quantum mechanically, the reaction rate is determined by summing over all partial waves, as opposed to classically where the rate is calculated by integrating over all possible impact parameters. At cold or ultracold temperatures, very few internal quantum states are occupied, thus very few orbital angular momentum states contribute to the reaction. At $T \rightarrow 0$ K, only s wave scattering is observed. Classically, this corresponds to a head-on collision. Collisions with non-zero orbital angular momenta possess centrifugal rotational energy,

$$E_{\text{centri}} = \mid L \mid^2 /(2\mu R^2), \tag{1.5}$$

where R is the distance between the two colliding reactants. This, when added to the barrierless potential energy surface for the reaction, leads to a centrifugal barrier as the reacting molecules come closer to each other.

Tunneling through the angular momentum (centrifugal) barrier is termed "orbiting resonance". Orbiting (or shape) resonances result from the formation of quasi-bound states trapped behind the barrier. An enhancement of reaction rates is displayed at collisions occurring close to these resonances, by quantum tunneling through the centrifugal barrier. Quite obviously, these effects are difficult to observe at room temperature as many l states are occupied and the contribution from individual resonances is averaged out.

1.1.3 Capture theories of barrierless chemical reactions

For many ion-molecule reactions, there is no activation barrier and the rate of reaction is dominated by long-range interactions.[3] Such barrierless reactions are typically fast and have rate constants on the order of 10^{-9} – 10^{-11} $\mathrm{cm^3 s^{-1} mol^{-1}}$ (several orders of magnitude larger than reactions with barriers).

Capture theories have been developed to calculate the reaction rate constants and explain these barrierless reactions and their initial quantum state dependencies. Classical capture theory assumes that trajectories with energy above the centrifugal barrier do not recross the transition state; in such circumstances, products are formed with unit probability. The motion along the reaction co-ordinate (radial motion), in many capture theories, can be described classically. The maximum impact parameter for successful collisions, $b_{\max}(E_c)$ can facilitate the definition of the 'Langevin' cross section, $\sigma_L(E_c)$ as,

$$\sigma_L(E_c) = \pi b_{max}^2(E_c) \tag{1.6}$$

By working out analytically the position and height of centrifugal barrier, we can determine the capture probability. For an intermolecular potential described by inverse-power law the effective potential is given by,

$$V_{\text{eff}} = \frac{b^2 E_c}{r^2} - \frac{C_s}{r^s}. \tag{1.7}$$

The first term in equation 1.7 is the centrifugal potential and the second term is the long range potential. C_s is the constant that determines the position of the barrier and s (an integer) is usally 4 for long range potentials. For the inter-nuclear potential given in equation 1.7, the Langevin cross section can be written as,

$$\sigma_L(E_c) = \pi \left(\frac{s}{s-2} \right)^{1-2/s} \left(\frac{sC_s}{2E_c} \right)^{2/s} \tag{1.8}$$

The thermal rate constant can be derived from equation 1.8 by integrating over a thermal distribution of collisional energies. The thermal rate constant (equation 1.9) has a temperature dependence different from that of Arrhenius behaviour. This is because, unlike the collision frequency, the capture probability increases at low temperature.[3]

$$k(T) \sim T^{1/2-2/s} \tag{1.9}$$

With the knowledge of the potential energy surface in the long-range region, reaction rate constants can be derived at different temperatures. Reactions between ions and molecules with zero or small dipole moments are not as affected by temperature (s = 4 in equation 1.9 in this case), and a simple Langevin capture model is able to accurately predict the rate of reaction. Reaction rates between ions and polar molecules are dependent on temperature and have been shown to increase as temperature is lowered.[8, 9]

This is a simple capture theory picture, and not all barrierless reactions obey such simple dynamics. Many details including rotation of the colliding molecules and the orientation dependence of their interaction are neglected. Rotationally adiabatic capture theory, developed by Clary and co-workers,[10, 11] and the statistical adiabatic theory, developed by Troe and co-workers,[12] takes into account radial potential curves that depend on the initial rotational quantum states of the molecules and quantization of the total angular momentum. It allows consideration of the centrifugal potential associated with the rotation of the reactant complex on the potential energy surface.

Other theories can be combined with the assumptions of capture theory to accommodate scenarios where there is more than one reaction pathway. Capture-wavepacket methods, for example, can predict product branching ratios.[13]

1.2 Cold chemistry with state selected reactants

Experiments have lagged behind theory in exploring chemical interactions at temperatures sufficiently low that translational degrees of freedom can no longer be treated classically. The difficulty has been largely in generating conditions in the laboratory that provide access to this regime.

1.2.1 Experimental studies of cold ion – molecule reactions

Cold molecule sources typically produce a very low number density ($\sim 10^8$ cm^{-3}) of neutral molecules. This makes the experimental investigation of reactive collisions between neutral species at ultra-low collision energies difficult to observe and monitor. Product detection is an ongoing experimental challenge, as the number of reactive collisions that occur per unit time is very small (typically only a few per second). In contrast to most neutral species, it is possible to observe and manipulate cold trapped ions at a single particle level. This is due to the strong localisation of the ions in an ion-trap and the high sensitivity of laser-induced-fluorescence detection, usually used to monitor a reaction. This has enabled the study of ion-molecule chemical reactions on the single-particle level, at temperatures $\leq$1 K.

Cold ion-molecule reactions have been demonstrated using an ion-trap, together with laser-cooling and the formation of Coulomb crystals (also known as Wigner crystals). Coulomb crystals (see figure 1.1) are spatially ordered low density ($\sim 10^8$ cm^{-3}) structures that form when ions (mostly alkaline earth ions, Be^+, Mg^+, Ca^+, Ba^+) are cooled (by Doppler laser cooling) below a certain critical temperature in an ion trap (typically a linear Paul trap). The temperature at which Coulomb crystals are formed is typically $\sim$10 mK.[14] More details on ion trapping in a linear Paul trap, laser-cooling and Coulomb crystals are provided in Chapter 5.

Sympathetic cooling can occur when molecular ions are simultaneously trapped with laser-cooled atomic ions, where efficient transfer of energy occurs from the molecular to the laser-cooled atomic species by the Coulomb interaction. The bicomponent Coulomb

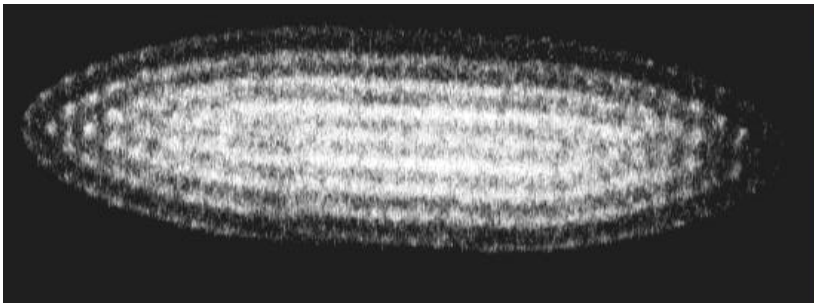

Figure 1.1: Experimental Ca^+ Coulomb crystal recorded using the linear Paul trap at a trapping voltage, V_{rf} of 140 V and endcap voltage, U_{dc} of 4 V.

crystal that results has two different ionic components, both of which adopt an ordered structure with ordered structure. Baba and Waki [15] in 1996 demonstrated the first sympathetic cooling experiments of molecular ions by laser-cooled ions. The research groups of Drewsen, Schiller, Softley, Thompson and Willitsch [16–20] have subsequently refined and extended this sympathetic cooling technique. Sympathetic cooling of molecular ions into Coulomb crystals opens up the possibility of using Coulomb crystals as a tool for studying the reaction of cold molecular ions. The principles of sympathetic cooling are discussed in detail in Chapter 6, and hence are not discussed here.

Reactions can be studied in Coulomb crystals, provided the kinetic energy of a given product ion is below the trap depth, to ensure the product ions remain trapped. In some cases, reactions are studied by tracking the change in shape of the Coulomb crystal – when the sympathetically cooled reacting ion species is heavier than the laser cooled ions, it forms a "dark" outer shell around the laser-cooled ions in the crystal and when it is lighter it forms inner dark core of the crystal. Further discussion of the ways in which such reactions can be monitored are outlined in Chapter 6.

Drewsen and co-workers demonstrated in 2000 the reaction of $^{24}Mg^+$ in a Coulomb crystal with H_2/D_2,[16] as given in reactions 1.10 and 1.11. MgH^+/ MgD^+ ions formed a dark shell outside the fluorescing Mg^+ and the crystal framework changed shape. Monitoring the change in shape of the crystal allowed the reaction to be monitored with time. For this reaction, the kinetic energy of the products was $\sim$0.1 eV, significantly lower than the

trap depth ($\sim$ 1 eV).

$$Mg^+ + H_2 \rightarrow MgH^+ + H \tag{1.10}$$

$$Mg^+ + D_2 \rightarrow MgD^+ + D \tag{1.11}$$

Drewsen and co-workers subsequently demonstrated a reaction of sympathetically cooled ions with an external reactant, in contrast to the previous reaction in which the laser-cooled ions were the reactant species. $^{24}Mg^{2+}$ ions (produced by non-resonant multi-photon ionization of laser-cooled $^{24}Mg^+$) were sympathetically cooled into the $^{24}Mg^+$ Coulomb crystal, where they formed a non-fluorescing core, and subsequently reacted with gaseous O_2, forming $^{24}Mg^+$ and O_2^+, as given in equation 1.12.[21]

$$Mg^{2+} + O_2 \rightarrow Mg^+ + O_2^+ \tag{1.12}$$

Drewsen and co-workers also probed isotope effects in chemical reactions using single ions in an ion-trap.[22] They studied the isotopic branching ratio of bimolecular single-ion reactions of excited state Mg^{+*} with HD, as given in equation 1.13 (channel 1) and 1.14 (channel 2). They followed the reaction process by monitoring product ion formation through the resonant-excitation mass spectrometry technique (discussed in detail in Chapter 6).

$$Mg^{+*} + HD \rightarrow MgH^+ + D \tag{1.13}$$

$$Mg^{+*} + HD \rightarrow MgD^+ + H \tag{1.14}$$

A similar study was undertaken with a single aniline ion ($C_6H_5NH_2^+$), which was sympathetically cooled into a Ca^+ single ion Coulomb crystal, forming a two-ion bi-component crystal.[23] The sympathetically cooled aniline ion was then subjected to photodissociation and resonant excitation mass spectra were recorded at fixed time intervals to periodically measure the mass of the dark ion. It was observed that the aniline ion underwent a series of consecutive photodissociation and isomerization reactions as given by the flowchart in 1.15:

$$C_6H_5NH_2^+ \Rightarrow C_5H_6^+ \Rightarrow C_5H_5^+ \Rightarrow C_3H_3^+. \tag{1.15}$$

Schiller and co-workers used a Be^+ Coulomb crystal to study the reaction between the ultracold triatomic hydrogen molecular ion, H_3^+, and room temperature O_2, as given in reaction 1.16. H_3^+ ions were produced by a two-step process: H_2^+ ions were first formed (by electron impact ionisation) and incorporated into a Be^+ Coulomb crystal. Subsequently, the H_2^+ ions reacted with neutral H_2, forming H_3^+ ions as an inner dark core in the Be^+ Coulomb crystal. As O_2 was leaked in, the inner dark core shrank and a dark outer shell formed outside the Be^+, indicating formation of HO_2^+. The observed reaction rates were in agreement with the Langevin rate.[24]

$$H_3^+ + O_2 \rightarrow HO_2^+ + H_2 \tag{1.16}$$

Schiller and co-workers demonstrated trapping of HD^+ into a Be^+ Coulomb crystal. The ultrahigh vacuum (UHV) conditions of the experiment enabled them to probe the rotational temperature of HD^+. They used laser spectroscopy to measure the rotational distribution of HD^+ ions (sympathetically cooled into the mK regime) and established that the effective rotational temperature was close to room temperature and independent of the translational temperature.[25]

In the above reactions, the sympathetically cooled and laser-cooled ionic reactants were translationally cold but rotationally hot. However, the neutral reactants were generally at room temperature – both translationally and rotationally hot, typically leaked into the chamber via a leak valve.

A new experimental method was demonstrated by Softley and co-workers for the study of reactive ion-molecule processes at low collision energies, $E_{\text{collision}}/k_B$ = 1 K, with single-particle sensitivity.[18] The reaction studied is given by 1.17,

$$Ca^+ + CH_3F \rightarrow CaF^+ + CH_3. \tag{1.17}$$

Here, the source of Ca^+ was a Ca^+ Coulomb crystal held in a linear Paul trap, and the source of the neutral reactant, translationally cold CH_3F, was a bent quadrupole guide velocity selector. The principles of quadrupole velocity selection are discussed briefly in section 1.3. The slowest neutral molecules were separated from a Maxwell-Boltzmann (thermal)

distribution of CH_3F at 298 K. Though the reactants were tranlationally cold (a few K), they were still internally warm, with a thermal distribution of rovibrational states.

The progress of the reaction was monitored by the disappearance of Ca^+ ions from the fluorescence images taken as a function of reaction time. The product ion, CaF^+, formed a dark shell outside the fluorescing Ca^+ ions and as the reaction progressed there was a visual flattening of the crystal. The kinetic energy of the product was less than the trap depth and the products thus remained trapped and were sympathetically cooled. The rate of decrease of the number of Ca^+ ions, $N(t)$, was found to follow a pseudo-first order rate law given by equation 1.18.

$$N(t) = N_0 e^{\left(-N_{CH_3F} k_{bi} t\right)} \tag{1.18}$$

Here, N_0 was the initial number of Ca^+ ions, N_{CH_3F} was the number density of CH_3F molecules at the trap centre and k_{bi} was the bimolecular reaction rate constant. The relative number of unreacted Ca^+ ions, $N(t)/N_0$ was plotted against time and the rate constant was extracted.

The rate constant was found to be dependent on the temperature of the collision: k_{bi} = 1.3×10^{-9} cm^3/s at low collisional energy, k_{bi} = 4.2×10^{-10} cm^3/s at 298 K. The room temperature rate constant was significantly lower than the predicted Langevin rate constant ($k_{Langevin}$ = 9.4×10^{-10} cm^3/s), and was attributed to existence of a low-lying "submerged" potential-energy barrier along the reaction coordinate.

The above reaction technique was extended to measure rate constants for chemical reactions of laser-cooled Ca^+ ions and the neutral polar molecules CH_2F_2 and CH_3Cl at low collision energies ($\langle E_{coll} \rangle$ = 5 - 243 K).[26] As in the previous experiment, trapped Ca^+ ions were reacted with translationally cold molecular beams of CH_3F (produced by a quadrupole velocity selector) or with room-temperature gas admitted into the vacuum chamber through a leak valve.

The role of the Ca^+ electronic state was modelled by solving the optical Bloch equations for an eight-level system. The laser cooling scheme for Ca^+ is given in Chapter 5, figure 5.13. The steady-state population of the Ca^+ ion states (^2S, ^2P, ^2D) was varied

systematically, by varying the cooling laser detuning and bimolecular rate constants were extracted for reactions of CH_3F, CH_2F_2 and CH_3Cl with laser-cooled Ca^+, for which Ca^+ was in either the ground state ($^2S_{1/2}$) or the combined excited state ($^2D_{3/2}$ and $^2P_{1/2}$). The ground state rate constant was found to be suppressed for CH_3F and CH_3Cl, explained by the presence of a submerged or real barrier on the ground state potential surface. The reactions of the excited states of Ca^+ were in agreement with capture theory.

The combination of a quadrupole velocity selector with an ion-trap has been extended further to study the reaction between sympathetically cooled OCS^+ and velocity selected ND_3 molecules in a Ca^+ Coulomb crystal.[27] A charge transfer process takes place between OCS^+ and ND_3, as given in reaction 1.19.

$$OCS^+ + ND_3 \rightarrow OCS + ND_3^+ \tag{1.19}$$

Here, OCS gas was leaked into the vacuum chamber through a leak valve ($\sim 10^{-8}$ mbar) and subsequently ionized to OCS^+ by (2 + 1) resonance-enhanced multiphoton ionization (REMPI). The OCS^+ ions formed were sympathetically cooled into the crystal, forming a dark layer around the Ca^+ ions, resulting in the flattening of the crystal. The sympathetically loaded OCS^+ ions reacted with a room temperature sample of ND_3 and velocity selected sample of ND_3. As ND_3 reacted with the OCS^+, a dark core formed in the Coulomb crystal, indicating the formation of ND_3^+ (see figure 1.2). Relevant molecular dynamics simulations enabled the determination of the number of each type of ion in the multi-component Coulomb crystal, by comparing simulated images with experimental images. The room temperature rate constant was found to be $k = 1.8\times10^{-9}$ cm^3/s and the rate constant evaluated for reaction with guided ND_3 (corresponding to an effective translational temperature of 5 K) was $k = 2.0\times10^{-9}$ cm^3/s.

In the reactions studied, the reactants were translationally cold, but internally hot; the molecular reactants had an approximately Boltzman distribution of rovibrational population. As such, the reactions were not studied under truly "cold" conditions. To observe quantum effects in a reaction, the reactants necessarily need to be both translationally and internally cold.

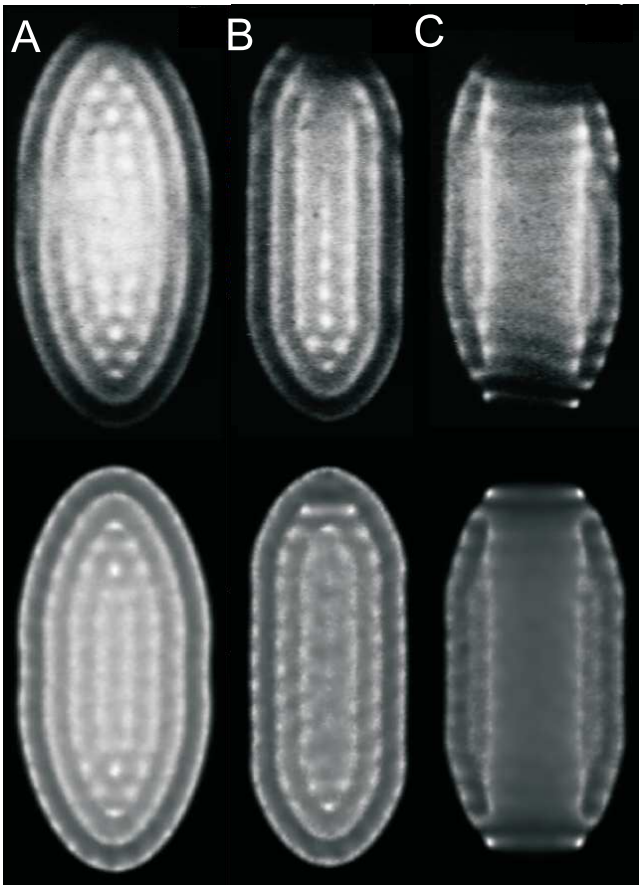

Figure 1.2: Experimental (top) and simulated (bottom) Coulomb crystal images showing the progress of the reaction between velocity-selected ND_3 and sympathetically-cooled OCS^+ ions. (A) Ca^+ Coulomb crystal images before sympathetic loading, (B) OCS^+ sympathetically-cooled into the Ca^+ Coulomb crystal, before the reaction (t = 0 s) and (C) tri-component Coulomb crystal, where ND_3 has charge transferred with some of the OCS^+ ions in the crystal (t = 65 s). Experimental images and simulations were supplied by Alex Gingell.

Drewsen and co-workers attempted to rotationally cool translationally-cold (sympathetically cooled) molecular ions. They demonstrated rovibrational cooling of MgH^+, which was sympathetically cooled into a Mg^+ Coulomb crystal, by using blackbody radiation (BBR)-induced laser cooling and achieved a rovibrational ground-state population of $\sim$35%.[28] A more detailed discussion on this experiment is given in Chapter 2.

Schiller and co-workers demonstrated rovibrational cooling of HD^+, by using BBR-induced rotational laser cooling schemes described in Chapter 2, and achieved 78% rovibrational ground-state population.[25] Adopting the approach of Schiller could facilitate the study of state-selected ion-molecule reactions with HD^+ ions.

Willitsch and co-workers prepared sympathetically cooled N_2^+ ions in selected states in a Ca^+ Coulomb crystal.[29, 30] They generated N_2^+ in selected vibrational and rotational states using threshold photoionization, and reported that $> 90\%$ of N_2^+ ions were in the rovibrational ground state. As N_2^+ is a non-polar diatomic species, it does not interact with BBR and thus rovibrational state lifetimes are limited only by collisions with background gas molecules. The lifetime of the ions produced in the rovibrational ground state was measured to be on the order of 15 minutes. They studied the influence of collisional and radiative processes on the population redistribution dynamics. This approach could be adopted for the study of cold ion-molecule reactions under controlled collision energy conditions, together with a source of velocity selected molecules (for instance, a Stark decelerator). However, for a polar ionic species, the interaction with BBR would dominate the lifetime of state selectivity; for most molecular ions this technique would not be suitable.[30] BBR-induced laser cooling schemes are useful for rovibrationally cooling the molecular ions, and rovibrational cooling schemes for a variety of diatomic and polyatomic ions is detailed in Chapters 2 and 3.

Several research groups of have recently developed cold ion trap – cold atom trap experiments.[31–38] Willitsch and co-workers studied the chemical reaction between laser-cooled Ca^+ ions and ultracold Rb atoms in an ion-atom hybrid trap, with a collisional energy range of E_{coll}/k_B= 20 mK - 20 K.[39] The product branching ratio $CaRb^+$:Rb^+ was monitored by resonance-excitation mass-spectrometry. Willitsch and co-workers also reported a study of cold reactive collisions between N_2^+, which was sympathetically cooled into a Ca^+ Coulomb crystal and laser-cooled Rb atom in an ion-atom hybrid trap at low collisional energies. The reaction (given by reaction 1.20) was monitored by observing the decrease in the number of N_2^+ ions in the Coulomb crystal over time. They found the reaction rate to be dependent on the internal state of Rb.[40]

$$N_2^+ + Rb \rightarrow N_2 + Rb^+ \tag{1.20}$$

In a very innovative experiment Willitsch and co-workers studied the reaction of conformationally selected 3-aminophenol (3AP) molecules with Ca^+ in a Coulomb crystal.

They were able to separate the two rotational conformers of 3AP molecules by spatially separating the two components of the molecular beam by electrostatic deflection, using inhomogenous electric fields. This technique made use of the difference in dipole moment between cis and trans 3AP, which differ from each other in the relative orientation of the O–H bond with respect to the NH_2 group. The cis and trans conformers have dipole moments of 2.33 D and 0.77 D respectively, giving rise to their different Stark interactions with an electric field.[41–43]

They found a two-fold larger rate constant for the cis conformer compared to the trans. The experimental observation was explained by conformer specific differences in the long-range ion-molecule interaction potential arising from the different dipole moments. Though the reactants were internally cold, they were translationally hot and demonstrate another interesting application of Coulomb-crystallised ion-molecule reactions.

1.2.2 Experimental studies of cold neutral – neutral reactions

A small number of approaches to studying cold neutral-neutral reactions have been developed including merged beam, crossed beam and ultracold experiments.

Costes and co-workers [44] developed a crossed supersonic molecular beam experiment with a very narrow crossing angle (12.5°). They studied the bimolecular inelastic collisions between ground-state O_2 and H_2 in the collision energy region of $\sim$ 5 K and reported state-to-state cross-section for rotational excitation of O_2 (N = 1, J = 0) to O_2 (N = 1, J = 1).

In merged beams methods, two molecular beams are combined to yield a single beam with a collision angle of zero. The relative velocity of the reactants in the moving frame of reference is the difference between the two beam speeds. A relative velocity of zero can be achieved, even at high beam velocities, if the merged beams are perfectly collinear and velocity matched. Thus slowing the molecules is not absolutely necessary for the study of cold chemical reactions.

Collision energies $\leq$ 5 K had been reached by merged beams of atomic ions and small

neutral species several decades ago.[45, 46] Narevicius and co-workers have recently demonstrated a merged beam technique with neutrals for the first time,[47, 48] demonstrating quantum behaviour in the Penning ionization (PI) of H_2, D_2 and Ar at milliKelvin temperatures. In PI, the collision of a metastable species with a ground state species leads to ionization of the ground state species and relaxation of the metastable species. Usually the metastable species is a rare gas in an electronically excited state.

The PI processes studied by Narevicius and co-workers include:

$$\mathrm{He}^* + \mathrm{H_2} \rightarrow \mathrm{He} + \mathrm{H_2^+} + e^-, \tag{1.21}$$

$$\mathrm{He}^* + \mathrm{D_2} \rightarrow \mathrm{He} + \mathrm{D_2^+} + e^-, \tag{1.22}$$

$$\mathrm{He}^* + \mathrm{HD} \rightarrow \mathrm{He} + \mathrm{HD^+} + e^-, \tag{1.23}$$

$$\mathrm{He}^* + \mathrm{Ar} \rightarrow \mathrm{He} + \mathrm{Ar^+} + e^-. \tag{1.24}$$

Narevicius and co-workers [47, 48] merged the two supersonic beams using a curved magnetic quadrupole. As only the He^* was magnetically guided, the other reactant (either isotopologues of H_2 or Ar) was unaffected. This merged beam approach enabled collisions to be studied at temperatures down to 10 mK. At energies < 1 meV (12 K), collisions enter the quantum regime. Orbiting (shape) resonances were observed in the above PI reaction of argon and molecular hydrogen with metastable helium; dramatic increases in the ionization rate were reported in the energy range of a few K down to 10 mK at these resonant collision energies.

Osterwalder and co-workers,[49, 50] in a similar merged beam experiment, have demonstrated the PI of NH_3 and ND_3 with Ne^*. Over the low-temperature range (100 mK – 250 mK) studied, Osterwalder and co-workers concluded that the Langevin capture model does not properly describe the Ne^*+ NH_3 reaction, and a clear transition from a process that is dominated by long-range forces at low collision energies to one where the short range forces dominate is observed at collision energies above $\approx$ 100 K.

However, in such merged molecular beam experiments, the reactants and products cannot be trapped, which is in contrast to the techniques involving slowly moving and trapped

cold/ultracold species, hence the observation time for the chemical processes is significantly shorter.

Ye and co-workers,[51–54] used an optical dipole trap to confine a near-quantum degenerate mixture of fermionic ^{40}K atoms and bosonic ^{87}Rb atoms. They report experimental evidence for exothermic atom-exchange chemical reactions of ultracold ^{40}K^{87}Rb molecules. A magnetic-field tunable Fano-Feshbach resonance (at 546.7 G) was used to associate the ultracold atoms into extremely weakly bound diatomic KRb molecules, in highly excited vibrational states. An ultracold, dense gas of KRb was then produced by a stimulated Raman adiabatic passage (STIRAP) with two-frequency laser irradiation; weakly bound fermionic KRb molecules, in a Feshbach resonance state, could then be coherently transferred to the rovibrational ground state of either the triplet or the singlet electronic ground molecular potential. Spin-polarized molecules in the single hyperfine state of either $|\ -4, 1/2\rangle$ or $|\ -4, 3/2\rangle$ (lowest hyperfine state) at various temperatures ranging from 200 nK – 900 nK were prepared.

The inelastic and reactive collisions between KRb molecules were subsequently probed. The molecule-molecule collisions can have the following outcomes:

$$\mathrm{KRb} + \mathrm{KRb} \rightarrow \mathrm{K_2} + \mathrm{Rb_2}, \tag{1.25}$$

$$\mathrm{KRb} + \mathrm{KRb} \rightarrow \mathrm{K_2Rb} + \mathrm{Rb}, \tag{1.26}$$

$$\mathrm{KRb} + \mathrm{KRb} \rightarrow \mathrm{KRb_2} + \mathrm{K}. \tag{1.27}$$

It was established that the rate of reaction was dominated by the p-wave angular momentum barrier for collisions of molecules prepared in the same quantum state; the reaction arises from tunneling through the angular momentum barrier followed by a short-range chemical reaction with a probability ≈ 1 (the chemical reaction barrier was below the collision energy). There was an enhancement of the reaction rate by a factor of 10 – 100 as a result of s-wave scattering, when these molecules were prepared in two different internal states. This process does not have a centrifugal barrier, and the rate constant was found to be independent of temperature.

This reaction was studied under ultracold conditions, but it is difficult to get to such low temperatures for ionic reactants. Also, these procedures are very specific to a particular molecule rather than a range of molecules like the case of Coulomb crystals and sympathetic cooling.

1.3 Generating cold molecules

Methods for generating cold neutral molecules are crucial for the study of cold ion-molecule reactions. There is no single method that is suitable for cooling every species. A variety of techniques are now available to generate cold molecules, with the most appropriate method for a given species dependent on the properties of the species involved and the final temperature necessary for the experiment. Cold molecule production can be divided into two main categories: direct methods and indirect methods.

Indirect methods involve the generation of cold/ultracold molecules from cold atoms or from the dissociation of larger molecules. Photoassociation and magnetoassociation of ultracold atoms can produce ultracold diatomic molecules. Magnetoassociation occurs through the use of Feshbach resonances followed by a stimulated Raman passage to produce ground state species. For further details on direct methods see the review by Bell *et al.*[3]

Direct methods cool molecules without changing their chemical composition. Supersonic expansion through a small orifice has historically been used to create a high velocity, unidirectional beam with a low internal velocity distribution, which can be used as a starting point for decelerating methods. There are many techniques used to cool the translational degrees of freedom of molecules, with those most relevant to this work including Stark deceleration,[55] Zeeman deceleration,[56, 57] velocity selection using a quadrupole electrostatic guide,[58] buffer gas cooling,[59, 60] mechanical slowing using a rotating nozzle,[61] kinematic cooling by momentum cancellation,[62, 63] laser cooling of atoms and molecules [64] and BBR assisted laser cooling.[65–67] A detailed discussion of the individual techniques is beyond the scope of this thesis. Only Stark deceleration and velocity selection using a bent quadrupole guide are briefly discussed, as these are being used

in combination with the ion trap to study reactions under controlled collisional energy conditions at Oxford. Please see reference [3] for a more general review of cold molecule production.

Stark Decelerator

The first Stark decelerator was developed by Meijer and co-workers [55] to decelerate polar molecules in low-field seeking Stark states. Parallel elctropolished pairs of stainless steel cylindrical rods are arranged in a linear array, such that the adjacent rods are perpendicular to each other, see figure 1.3. In the Oxford device, the rods are 3 mm in diameter and a 2 mm gap separates each pair; the distance between consecutive electrode pairs is 5.5 mm. Alternate electrode pairs are maintained at $\pm$10 kV, while the remaining electrodes are grounded. A time-varying inhomogenous electric field along the decelerator axis (necessary for Stark deceleration) is achieved by rapidly switching the high voltages between consecutive electrode pairs, such that the originally grounded electrode pairs gain the high voltage and this process is repeated. The principle employed is illustrated in figure 1.3.

In our laboratory, the decelerator was 131 stages and is capable of decelerating low-field seeking polar molecules to a tunable velocity. As the molecules enter the high electric field region, potential energy is gained by the molecules in 'low-field seeking' quantum states. Low-field seeking molecules exhibit a positive Stark effect, whereby a positive shift of energy with field occurs. The molecules (typically ND_3) gain potential energy at the expense of kinetic energy, and are thus subsequently slowed when this potential energy is permanently removed by switching the high voltages to the next pair of electrodes. The process is repeated 131 times (along the axis of the decelerator), with a precisely timed pulse sequence coordinating the high-voltage switching to match the decreasing molecular velocity.

The position of the molecule when the fields are switched and the strength of the external field determine the amount of kinetic energy removed at each stage. During the operation of the Stark decelerator, only molecules in a selected quantum state are decel-

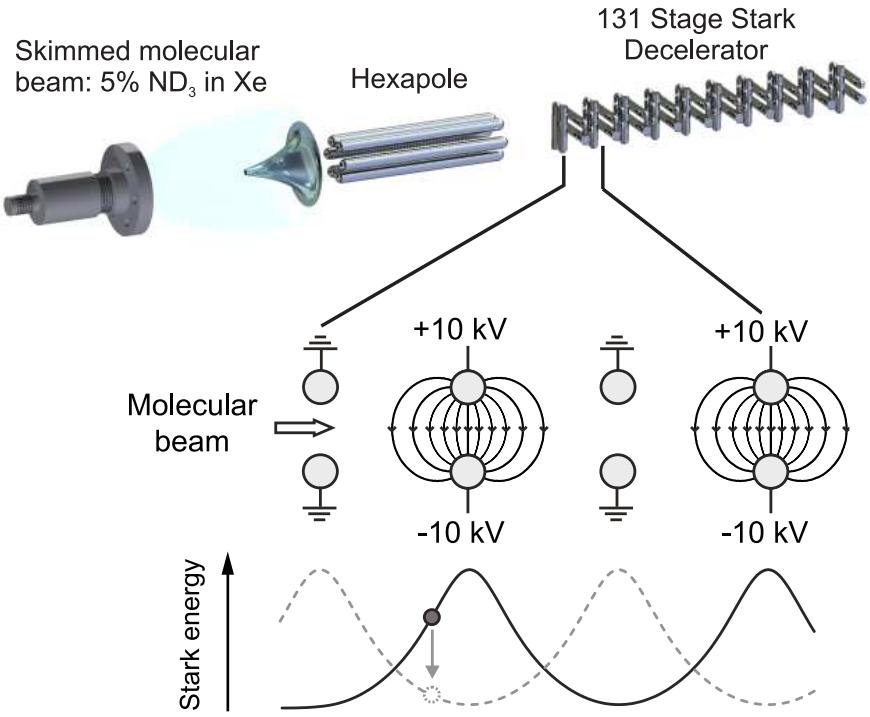

Figure 1.3: A schematic representation of the Stark decelerator. The decelerator has only the first 20 stages shown. The voltage applied to the electrodes is illustrated, along with the change in Stark energy of the molecule upon switching of the fields. This figure has been reproduced from Lee Harper's thesis.[68]

erated and focussed by the final hexapoles into the ion trap; molecules in other quantum states remain largely unaffected, because the pulse sequence is tailored for one quantum state and its Stark shift. Stark deceleration thus can produce molecules in a single quantum state with a tunable velocity. ND_3 molecules exiting the decelerator are state-selected, occur in packet(s) of $\sim 10^6$–10^8 molecules/cm^3, and have a very narrow velocity distribution centred on a tunable final velocity. The decelerated ND_3 molecules and the undecelerated molecules are separated by a mechanical shutter. ND_3 molecules have been decelerated from 360 m/s to 175 m/s, removing 75 % of the kinetic energy.[68, 69]

Quadrupole velocity selector

The velocity spread in a thermal gas from an effusive source is described by the Maxwell-Boltzmann distribution and is shown in figure 1.4 (A). There is always a small proportion of the velocity distribution which has a low velocity; even at room temperature, typically

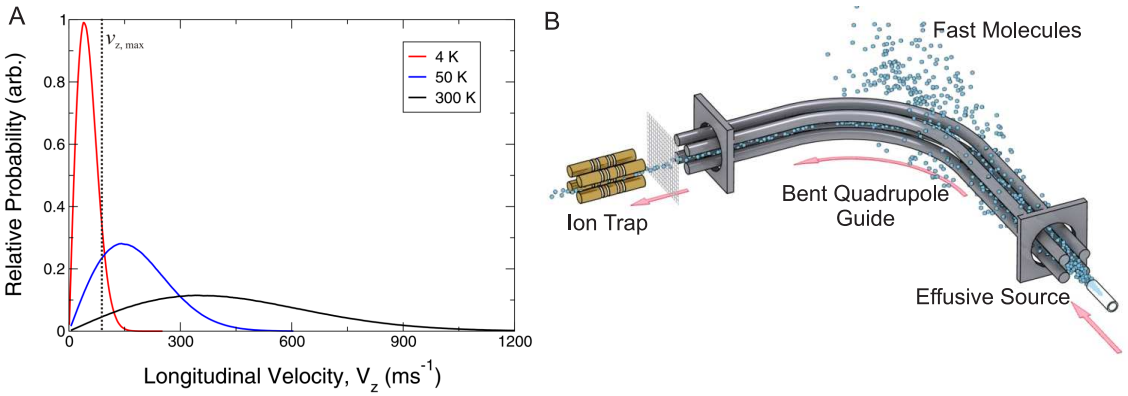

Figure 1.4: (A) Distribution of velocity for ND_3 molecules at different temperatures: 300 K (black line), 50 K (blue line) and 4 K (red line). v_{max} is the velocity of the molecules, below which ND_3 molecules get guided around the bend of the quadrupole velocity selector, under experimental conditions. (B) A representative bent electrostatic quadrupole velocity selector. This figure has been reproduced from Lee Harper's thesis.[68]

0.1% of the molecules have velocities less than 10% of the mean.[58] Due to the Stark effect, dipolar molecules in low-field seeking rotational states and with low velocities can be guided around the bend and selected out from the distribution. In our laboratory, ND_3, CH_3F, CH_3Cl, CH_2F_2, CH_3CN and CH_3NO_2 have been successfully velocity-filtered using a bent quadrupole velocity guide, and typically translational temperatures of few Kelvin can be reached. The final translational temperature attained is dependent on the bend radius and the applied voltage. It should be noted, however, that the rotational temperature is not addressed by this method, and the translationally cold molecules remain internally hot. For internally cold molecular beams, our research group has recently reported the combination of a buffer gas cell with a quadrupole guide, yielding an internally and translationally cold molecular beam of ND_3 [70] (also previously demonstrated by Rempe *et al* [58]).

The combination of either a Stark decelerator or a buffer-gas cell - velocity filter with an ion trap will facilitate the study of internally cold ion-molecule reactions at low collision energies. BBR-induced rotational laser cooling of diatomic and polyatomic ions in an ion trap, which has been discussed in detail in Chapters 2 and 3, can preserve the quantum state of the ions in an ion trap for the duration of the reactions ($\sim$ 15 – 20 minutes).

1.4 Outline of this thesis

The aim of the thesis is to break new ground in studying cold ion-molecule reactions involving polyatomic species such as that between $C_2H_2^+$ and ND_3, where both the reactants are state-selected. To achieve this, there are four main barriers to overcome: first, the production of ions and molecules in a specific quantum state; second, storing the ions for sufficiently long time for reaction with a neutral source; third, preserving the internal quantum state of the ion for the full duration of the reaction, typically 15 – 20 minutes; fourth, quantitatively monitoring the reaction and formation of products.

In our laboratory, Coulomb-crystallised ions have been used to study ion-molecule reactions.[18, 27, 68, 69, 71] The ionic reactant and ionic products are sympathetically cooled into Ca^+ Coulomb crystals, with the change in shape of the Coulomb crystal monitored and reaction kinetics extracted. This is discussed in detail in Chapter 5. Reactants or products lighter than Ca^+ form a dark core, and ions heavier than Ca^+ form a dark outer shell; only the ions directly addressed by laser-cooling (Ca^+) fluoresce. Unfortunately, visually monitoring a reaction in this way is useful only when reactants and products are heavier (lighter) and lighter (heavier) than the main laser-cooled ions of the Coulomb crystals (Ca^+ in this case). This is because the technique is insensitive to the different components of the dark inner core or the dark outer shell – it cannot detect impurities or multiple dark species of similar masses. A more species-sensitive technique is required for accurate calculation of reaction rates and branching ratios for reactions in general.

Previous experiments, described in section 1.2.1, have been carried out with translationally cold but internally warm molecular reactants (or, in some of the Willitsch group's work, internally cold but translationally hot molecular reactants).

By implementing schemes to selectively prepare and to control the internal quantum state of the molecular ions, and developing techniques to monitor a variety of reactions, it will be possible to study chemical collisions under highly controlled conditions in an ion trap. This thesis looks into theoretically and experimentally investigating several reactions in cold environments, in particular the reaction between $C_2H_2^+$ and ND_3, where both the

reactants are state selected. This work has made significant contributions to the field of cold state-selected ion-molecule reactions, in the areas set out below.

Most molecular ions produced in a selected rovibrational state will exhibit a lifetime of only a few seconds before redistribution of the population across several rovibrational states occurs, arising from interaction with the ambient BBR. Chapter 2, entitled "Rotational cooling schemes in MgH^+, DCl^+, HCl^+, LiH and CsH", theoretically investigates laser cooling schemes for several diatomic species. This chapter proposes ways to overcome the technical challenge of cryogenic cooling of the ion trap through the use of lasers to pump the rovibrational population towards the rovibrational ground state. The theoretical model is validated by comparing the results of the code (developed in this work) with available experimental results for BBR-assisted laser cooling in MgH^+.[28] A thorough *ab initio* analysis of the vibrational dipole moment of MgH^+ is performed, at different levels of theory. The model achieves an excellent match with the experiments performed by Drewsen and co-workers.[28] Similar cooling schemes are applied to other molecules in the same electronic ground state ($^1\Sigma$), including CsH and LiH. A comprehensive discussion on the effect of the rotational constant and the dipole moment on the cooling scheme efficiency is made. Two further diatomic species, DCl^+ and HCl^+ (in $^2\Pi$ electronic ground state), are considered, with cooling schemes proposed and the effect of isotopic substitution discussed. The effect of the BBR temperature and a hybrid approach (with some cooling of the apparatus in addition to laser-based schemes) is also proposed.

This approach is extended to an important linear polyatomic ion, $C_2H_2^+$, in Chapter 3, entitled "Rovibrational cooling schemes for linear polyatomic ions – $C_2H_2^+$". The interaction of the non-polar polyatomic $C_2H_2^+$ ion with BBR is investigated. Possible laser cooling schemes – both idealised and experimentally viable – are proposed. One might initially assume that a linear non-polar ion would be insensitive to the effects of BBR. In fact, two of the five acetylene vibrational modes are IR active and one of them, the cis bending mode (ν_5) overlaps with the peak of the BBR radiation at 300 K. $C_2H_2^+$ thus interacts with BBR very efficiently at 300 K. $C_2H_2^+$ is a linear ion with a $^2\Pi$ electronic ground

state, and is challenging to study as it has complicated angular momentum interactions, the most notable being the Renner-Teller interaction, which arises from the interaction of the vibrational angular momentum with the electronic angular momentum. This angular momentum interaction, along with spin-orbit coupling leads to a very complicated energy level splitting; the $1 \leftarrow 0$ ν_5 vibrational system is split into eight vibronic levels. This chapter elucidates these detailed energy level splittings and proposes possible rovibrational transitions that could be utilised in laser cooling schemes to preferentially populate the ground rovibrational states(s). The rotational transition intensities are derived and discussed in detail. The lifetimes of ions produced in a specific quantum state(s) is calculated, and possible BBR-assisted laser cooling schemes are presented. The effect of temperature on the BBR-assisted decay of the ion from a specific quantum state is investigated, with the behaviour at 77 K examined explicitly. Finally, an extension of this scheme to CO_2^+ is discussed.

The theoretical work presented in Chapter 3 has been complemented by experimental investigations into the state-selected production of $C_2H_2^+$ in selected states presented in Chapter 4, entitled "Production and detection of $C_2H_2^+$ in selected vibrational states". Appropriate (2+1) REMPI schemes are used to produce $C_2H_2^+$ in specific vibrational states, some of which are understood to be IR inactive and thus inert to BBR-induced decay. This chapter identifies vibrational states of $C_2H_2^+$ that could be produced by REMPI and are sufficiently long lived to enable the study of reactions in the ion trap with decelerated ND_3. (1+1) Resonance Enhanced Multiphoton Dissociation (REMPD) schemes are explored for detection of the ions in specific quantum states.

In Chapter 5, entitled "Ion trapping, laser cooling and Coulomb crystals", a comprehensive discussion of the principles of ion trapping with sinusoidally and digitally time-varying trapping voltages is provided. The stability region and the trap depth is compared for the two trapping waveforms. In this context, the depth of the digital trap is derived and the relationship between the digital trap depth and τ (fractional pulse width) is examined. The dependence of the stability region on trapping frequency and the τ for a digital trap is discussed. The possibility of co-trapping multiple species in a digital trap is investigated at the

experimental trapping conditions. General principles of laser cooling and Coulomb crystallisation are also provided, along with an experimental description of the two different ion trap apparatuses used in this work.

One of the aims of the thesis is to develop a more generally applicable detection technique to ascertain the constituent ions in a given Coulomb crystal. Chapter 6 entitled "Mass spectrometry in a digital ion trap" introduces a novel mass spectrometric technique that allows the contents of the trap to be ejected via a time-of-flight (TOF) tube onto MCPs, by converting the quadrupole ion trap into an extractor-repeller pair. This is achieved by switching off the trapping voltages and sending an ejection pulse to the electrodes. Clean ejection of the trap using sinusoidal voltages is not possible because of the persistent ringing present after the trapping voltage is switched off. The technique is developed using a digital rf trapping voltage rather than the traditional sinusoidal trapping voltage. The TOF trace obtained on ejecting the contents of the ion trap is thoroughly characterised, and the relationship between the number of ions in the crystal and the TOF peak intensity is established.

Ions are sympathetically cooled into Ca^+ Coulomb crystals in a digital trap and the contents of the multicomponent crystals are ejected onto MCPs for analysis. The mass resolution of the technique is demonstrated by ejecting multi-component Coulomb crystal of Ca^+ – $CaOH^+$ – $CaOD^+$. Finally, bicomponent CaF^+ – Ca^+ crystals are systematically analysed to validate the relationship between the number of ions of each species in the crystal to their respective MCP response. This digital ejection technique would, for the first time, allow us to study reactions with multiple products using Coulomb crystals (of particular interest the reaction between $C_2H_2^+$ and ND_3), something which has not been previously possible.

Chapter 2

Rovibrational Cooling Schemes in MgH^+, DCl^+, HCl^+, LiH and CsH

2.1 Introduction

Innovative techniques for producing cold and ultra-cold species have facilitated the investigation of reactive collisions in an increasingly diverse range of atoms, molecules and ions. As discussed in Chapter 1, ensembles of laser-cooled atomic ions contained within a radiofrequency ion trap can undergo a phase transition, adopting an ordered structure termed a Coulomb crystal. The exchange of kinetic energy between directly laser-cooled ions and co-trapped species (with appropriate properties) has been exploited to "sympathetically" cool molecular ions down to milliKelvin temperatures, yielding multi-component Coulomb crystals. This sympathetic cooling of molecular ions (including MgH^+, CaF^+, OCS^+ and ND_3^+) has expanded the scope of reactions that can be investigated in the cold and ultra-cold regime.[15, 18, 27, 28]

Ultra-cold atoms, molecules and ions (both atomic and molecular) can be held in traps for increasingly long periods of time. While these trapped species remain translationally cold, for molecules the absorption of ambient black-body radiation can result in rapid thermalisation of the rotational (and vibrational) degrees of freedom. At 300 K, internal state purity is lost typically on the order of tens of seconds, inhibiting the study of quantum state selected reactions. The goal of this chapter is to investigate the possibility of pumping the thermal population to its rovibrational ground state. In this chapter, blackbody-mediated

rovibrational laser cooling schemes in MgH^+, DCl^+, HCl^+, LiH and CsH will be discussed.

Resonance Enhanced Multiphoton Ionization (REMPI) or threshold ionization processes may be used to prepare molecular ions selectively in a single rovibrational state or in a small group of states. These quantum states are not affected by the sympathetic cooling collisions, and ions can be held in radiofrequency ion traps for extended periods of time, making it possible for reactions to be monitored over the course of minutes to hours. However, the lifetimes of the initially prepared quantum states of the molecular ions can be limited by thermalisation with the background blackbody radiation (BBR) field on this timescale.[72] Although the laser cooling of the host atomic ions in the crystal enables translational temperatures in the milliKelvin regime, the experimental apparatus (e.g., the ion trap itself) is typically kept at room temperature. The infrequency of inelastic collisions allows for rapid equilibration with the ambient BBR, with the loss of internal quantum state purity occurring typically on a timescale of seconds at room temperature. The thermalisation thus inhibits the investigation of quantum-state-selected collisions. To achieve internal state selection three approaches have been adopted to date. In the first approach, a molecular ion is chosen which has no electric-dipole-allowed transitions falling within the blackbody spectrum, such as N_2^+. In this case the populations produced by REMPI remain unperturbed almost indefinitely, allowing state-selected experiments on long time scales. [73] In the second approach, applicable to dipolar ions, the redistribution of population is utilised in combination with optical pumping to drive population towards the ground rovibrational state. This approach was first demonstrated experimentally for MgH^+ and HD^+, and similar cooling schemes have been proposed for species in a range of electronic ground states (including $^1\Sigma$, $^2\Sigma$, $^3\Sigma$ and $^2\Pi$). [25, 65, 72] A third possible approach is to cool the ion trap and its surrounds cryogenically to maintain low equilibrium rotational temperatures (and hence few states populated).[74] In this work calculations are presented that expand upon the cooling schemes previously studied and introduce new approaches to laser cooling by optical pumping. Excellent agreement is demonstrated between the previous experimentally recorded rovibrational populations of MgH^+ and those calculated with our model. Cooling

schemes for the diatomic hydrides LiH and CsH (both with $^1\Sigma$ electronic ground states) and the molecular ions HCl^+ and DCl^+ (with a $^2\Pi$ ground state) are presented, with the rovibrational populations modelled as a function of time. The inclusion of broadband excitation sources is considered in addition to the modelling of hybrid approaches (whereby optical pumping is employed in addition to low-temperature trap environments).

In this chapter a theoretical model is used to investigate laser-driven, blackbody-mediated, rotational cooling schemes for several $^1\Sigma$ and $^2\Pi$ diatomic species. The influence of the rotational constant, dipole moments and electronic state of the diatomics on the rotational cooling achievable is also considered.

2.2 BBR rate equation

The interaction of BBR with the rotational and vibrational degrees of freedom of a molecule can be established using the appropriate rate equations for the number density n_i in a level i,

$$-\frac{dn_i}{dt} = \sum_j B_{ij}\rho_T(\omega_{ij})n_i - \sum_j [B_{ij}\rho_T(\omega_{ij}) + A_{ij}]n_j] \tag{2.1}$$

ρ is the spectral density at the frequency ω, given (in the absence of additional light sources) by Plancks radiation law for the temperature of the surroundings:

$$\rho_T(\omega) = \frac{h\omega^3}{\pi^2 c^3 (e^{\frac{\hbar\omega}{k_b T}} - 1)} \tag{2.2}$$

If i represents a lower level $E^{''}$, $|v = 0, J^{''}\rangle$, and j an upper level $E^{'}$, $|v = 1, J^{'}\rangle$, (that is, $E^{'} > E^{''}$), the Einstein coefficients for spontaneous emission, A, and stimulated emission or absorption, B, are defined by

$$A_{v'J',v''J''} = \frac{\omega^3}{3\pi\epsilon_0\hbar c^3}\frac{S_{J',J''}}{2J'+1}\mu^2_{v',v''} \tag{2.3}$$

$$B_{v'J',v''J''} = \frac{1}{6\epsilon_0\hbar^2}\frac{S_{J',J''}}{2J'+1}\mu^2_{v',v''} \tag{2.4}$$

$$B_{v''J'',v'J'} = \frac{2J'+1}{2J''+1}B_{v'J',v''J''} \tag{2.5}$$

Primed states indicate the upper state of the transition, with the lower states denoted by a double prime; ω is the angular frequency of the transition; the $2J + 1$ terms account for rotational degeneracy.

In equations 2.3 and 2.4 the matrix elements of the dipole moment operator μ have been separated into vibrational and rotational components using

$$\Psi = \Phi^{el}.\Psi^{vib}.\Psi^{rot} = \Phi^{el}.\chi_N, \tag{2.6}$$

At room temperature, the BBR spectrum does not reach sufficiently high energies to induce electronic transitions and only vibrational and rotational contributions need to be considered, which allows the expression of the transition dipole moment as

$$\mu_{v'J'v''J''} = \langle \chi_N^{'} | \langle \Phi^{el} | \mu | \Phi^{el} \rangle \chi_N^{''} \rangle, \tag{2.7}$$

which may be further separated as

$$\mu_{v'J',v''J''} = S_{J',J''}\mu_{v',v''}. \tag{2.8}$$

The rotational line strength, $S_{J,J}$, is given for a symmetric top or diatomic molecule by

$$S_{J',J''} = (2J^{'} + 1)(2J^{''} + 1) \begin{pmatrix} J^{'} & 1 & J^{''} \\ -K^{'} & K^{'} - K^{''} & K^{''} \end{pmatrix}. \tag{2.9}$$

For transitions occurring within the same electronic state, $K^{'} = K^{''}$ (where K is the projection of J onto the molecular axis). For a diatomic species, K reduces to Ω (where $\Omega = \Lambda + \Sigma$; Λ is a projection of the orbital angular momentum onto the molecular axis; Σ is the projection of the spin angular momentum onto the molecular axis). For species in $^1\Sigma$ electronic states ($K = 0$), the selection rule is $\Delta J = \pm 1$ and Q branches are forbidden, while for molecules in Π states $\Delta J = 0, \pm 1$ and P, Q and R branches are present. For transitions within the same vibrational level (rotation-only transitions), $\mu_{v',v''}$ reduces to μ_0, yielding

$$\mu_{v'J',v''J''} = S_{J',J''}\mu_0 \quad (\Delta v = 0) \tag{2.10}$$

For transitions between vibrational levels, Taylor expansion of the dipole moment function $\mu(R)$ leads to

$$\mu_{v',v''} = \mu_0 \langle \Psi_{v'}^{vib} | \Psi_{v''}^{vib} \rangle + \left(\frac{d\mu}{dr} \right)_{R=R_{eq}} \langle \Psi_{v'}^{vib} | R | \Psi_{v''}^{vib} \rangle + ..., \tag{2.11}$$

but the first integral in equation 2.11 vanishes, and $\mu_{v',v''}$ can be written as

$$\mu_{v',v''} = \left(\frac{d\mu}{dr}\right)_{R=R_{eq}} \langle \Psi^{vib}_{v'} | R | \Psi^{vib}_{v''} \rangle \tag{2.12}$$

Thus, using the harmonic oscillator approximation,

$$\mu_{v',v''} = \sqrt{\left(\frac{v'}{2}\right)\left(\frac{\hbar}{m\omega_e}\right)} \left(\frac{d\mu}{dr}\right)_{R=R_{eq}} \tag{2.13}$$

It should be noted that equation 2.13 is valid only if the potential well is not strongly anharmonic; the dipole moment function is close to linear around R_{eq}; and rovibrational couplings are negligible.

In this work, equilibrium dipole moments μ_0 were evaluated using the Gaussian09 suite of quantum chemical packages [75] or taken from literature where accurate numbers were available. Coupled cluster calculations with single and double excitations and perturbative triple excitations (CCSD(T)) and Møller-Plesset second order perturbation theory (MP2) methods were employed, typically in combination with a cc-pVTZ basis set (as appropriate for the species of interest; see section 2.5). Vibrational transition dipole moments were either evaluated directly from the wave functions in the Gaussian09 suite or by using the dipole derivative (see below) and frequency as in equation 2.13. Henceforth the transition dipole moment calculated directly from the wavefunctions is specified as μ_{int} while that defined in equation 2.13 is denoted as μ_{lin}. For the latter case, the dipole moment derivative was determined using finite-field perturbation theory, via the Taylor series expansion of the energy of a species in the presence of small electric field

$$E \approx E^0 - \mu F_{\shortparallel} - \frac{1}{2}\alpha_{\shortparallel} F_{\perp}^2 \tag{2.14}$$

A field (of 1.0×10^{-3} au) parallel and anti-parallel to the bond can be applied in the calculations, and the resulting shift of the potential energy curve used to determine the dipole moment

$$E_{+z} \approx E^0 - \mu F_{+z} - \frac{1}{2}\alpha_{\shortparallel} F_{\perp}^2 \tag{2.15}$$

$$E_{-z} \approx E^0 - \mu F_{-z} - \frac{1}{2}\alpha_{\shortparallel} F_{\perp}^2 \tag{2.16}$$

Subtracting equations 2.15 and 2.16 above yields an expression for the finite-field dipole moment,

$$\mu = \frac{E_{-z} - E_{+z}}{2F_{+z}} \tag{2.17}$$

When considering a sample of N molecules initially at thermal equilibrium, the fractional population $f_{v,J}(T)$ of a particular rovibrational state $|v, J\rangle$ at temperature T is given by

$$f_{v,J}(T) = \frac{N_{v,J}}{N} = f_{0,0}(T)(2J+1)exp\frac{-E_{v,J}}{k_B T} \tag{2.18}$$

Integration of the coupled differential equations 2.1 (calculated in this work using the Expokit package in Fortran or expm in MATLAB) allows the evolution of population across rovibrational states to be calculated as a function of time.

The rate of BBR-induced decay of a given level is thus dependent on a number of molecular parameters: the rotational line strength; the permanent dipole moment μ_0 (governing rotational transitions); the vibrational transition dipole moment $\mu_{v',v''}$; the energy gap between states, which in turn depends on B and ω; and finally on the temperature of the blackbody – the variation of the BBR spectral function with temperature is illustrated in figure 2.1. As an example, the decay of population initially prepared in the rovibrational ground state is shown as a function of time, for several species of interest, in figure 2.2. The molecular constants used in the calculation of these curves are provided in table 2.1. It can be seen that species with a large dipole moment, such as CsH, LiH and MgH^+, couple most efficiently with the BBR. The higher residual populations (at equilibrium) of the ground state levels of HCl^+ and DCl^+ occur because of the larger splitting between the ground and lowest excited rotational states ($\sim 5B$) in the $^2\Pi_{3/2}$ electronic state compared to the $2B$ splitting in the $^1\Sigma$ molecules.

2.2.1 Comments on non-polar diatomic species

Non-polar diatomic (homonuclear) molecules have no electric dipole (E1) allowed transitions, as they have no dipole moment nor can $\left(\frac{d\mu}{dR}\right)_{r=r_{eq}}$ be non-zero. Consequently, BBR transitions will only occur from E1 "forbidden" transitions which are magnetic dipole (M1)

Table 2.1: Constants employed in the calculation of rovibrational population decay.

Species	μ_0 (D)	B (cm^{-1})	ω (cm^{-1})	$\mu_{v',v''}$	Reference
LiH	5.88	7.5	1405	0.21	[76]
CsH	8.33	2.7	891	0.548	[76]
MgH^+	3.916	6.4	1634	0.061	this work, [28], [77]
DCl^+	1.64	5.1	1918	0.18	this work, [78]
HCl^+	1.64	9.96	2674	0.193	[79]

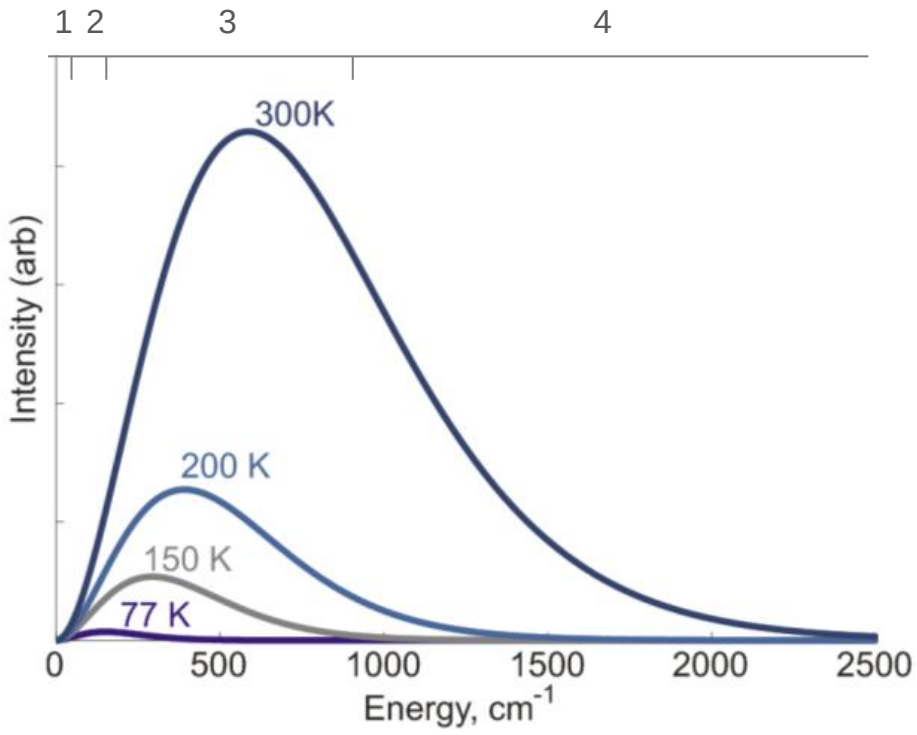

Figure 2.1: BBR curves at a range of temperatures. Typical energy ranges for rotational and vibrational transitions are indicated for heavy and light molecular ions; regions 1 and 2 indicate the rotational transition energies for heavy and light ions (respectively) and regions 3 and 4 indicate the vibrational transition energies for heavy and light ions (respectively).

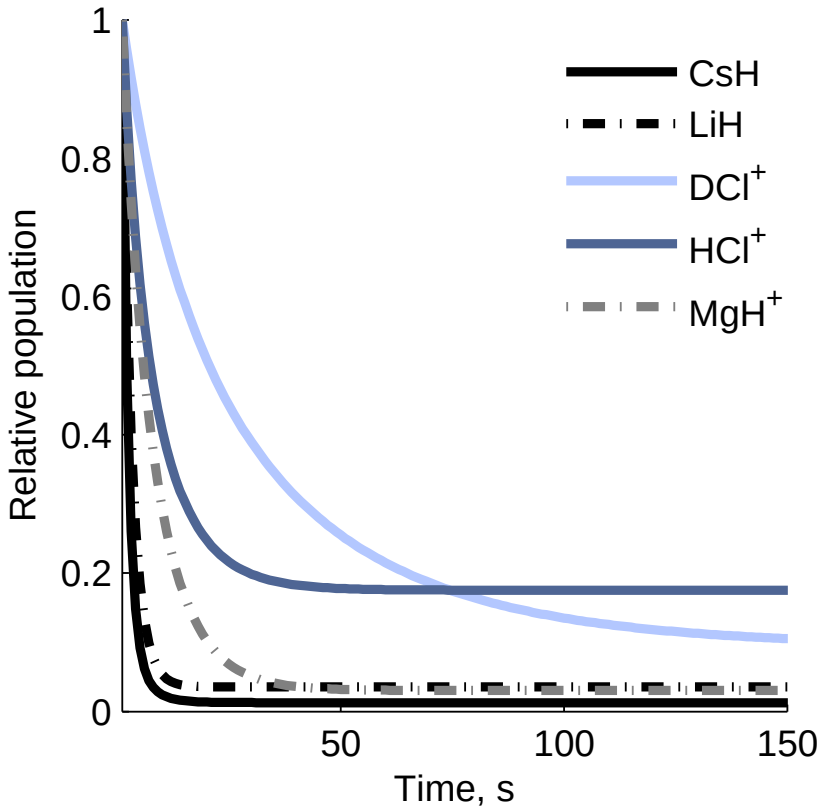

Figure 2.2: Decay of population in the rovibrational ground state of CsH, LiH, DCl^+, HCl^+ and MgH^+ as a function of time, arising from interaction with 300 K BBR.

or electric quadrupole (E2) allowed. E1-forbidden transitions are ≥ 5 orders of magnitude weaker in intensity than E1-allowed transitions: M1 transitions are typically 10^5 times weaker than E1-allowed transitions, with E2 transitions a further $\sim 10^3$ times less intense than M1.

Considering the components of the magnetic dipole moment, nuclear contributions are 10^3 times weaker than electronic contributions. Homo-nuclear diatomic ions with one unpaired electron (such as N_2^+ in the $X^2\Sigma_g^+$ state) have no possible J-conserved transitions induced by the electronic magnetic dipole. In such cases, the need to incorporate the nuclear spin contribution to the magnetic moment arises. The BBR rate equations returned by substituting an appropriate approximate value for the nuclear magnetic moment are too low to account for any observable population decay (on the order of $10^{-14} - 10^{-20}$ s^{-1}).

In general, there will be no significant BBR-mediated decay of quantum states in non-

polar diatomic species. While molecular collisions may still play a role in population redistribution, this will usually be a minor effect in experiments conducted under high and ultra-high vacuum conditions.

2.3 Incorporating laser excitation into the rate equation model

The increased spectral density arising from an external laser source was incorporated into the rate equation matrix to account for the laser-driven transitions. To evaluate the increased spectral energy density at the selected transition frequency or frequencies, properties of the laser including the pulse duration, spot size, repetition rate, spectral line-width and power must be accurately known. In the absence of these experimental details and to facilitate application of the model to systems where no experimental measurements have been undertaken the rate of laser-driven transitions required for saturation was found to be between 5×10^4 and 5×10^6 s^{-1}. The sensitivity of the cooling scheme to laser saturation was tested for MgH^+ by varying this transition rate from 5×10^2 to 5×10^4 s^{-1}.

For MgH^+, LiH, DCl^+ and HCl^+ the lowest 20 rotational states and first three vibrational states were considered in the rate equation model. For CsH, 30 rotational levels and three vibrational states were included in the cooling schemes. All of the diatomic species studied were almost exclusively in $v = 0$ at 300 K.

As is shown later, it is advantageous to pump more than one transition in many cases – this could either be achieved by using more than one laser, or alternatively by a single broadband laser if the transitions are sufficiently close in frequency and if the transitions to be pumped are not interspersed with transitions of another rotational branch or vibrational band. Two different representations of broadband pumping were investigated in this work. A Gaussian, centred at a selected frequency (to maximise cooling efficiency) and with a varied FWHM, was used to model a broad-bandwidth excitation source as might be provided by a short pulse (femtosecond) laser, as depicted in figure 2.3 (a). In contrast, Quantum Cascade Lasers (QCLs) have the potential to provide photons over a range of bandwidths

(to a limited extent) with a top-hat shaped spectral profile. They exhibit a step-like intensity drop-off in the fringes rather than the Gaussian-shaped profile of short pulse systems. In every case investigated here this offered enhanced cooling capabilities, because of the more equal pumping rate of the lines near the edge of the band. The calculations reported below all use the top hat spectral profile in figure 2.3 (b). For broadband excitation, the laser excitation was incorporated into the rate matrix elements for all allowed transitions whose frequency is under the laser bandwidth (weighted by the intensity of the laser at that frequency).

2.4 Investigation of BBR assisted laser cooling in MgH^+

Accumulation of population in the rovibrational ground state has been experimentally demonstrated in MgH^+, achieved through the combination of a laser-driven transition and BBR-mediated population redistribution.[28] To confirm the validity of our model, I initially simulated the population redistribution arising from BBR-assisted laser cooling in MgH^+.

In the experiments reported by Staanum *et al*, MgH^+ ions (initially produced in the vibrational ground state) were left to equilibrate for 120 seconds with the room temperature (293 K) BBR field.[28] The $|v = 0, J = 2\rangle \rightarrow |v = 1, J = 1\rangle$ transition was subsequently excited by a laser until a steady-state rotational distribution was achieved. Ultimately, this optical pumping process drove the population towards the rovibrational ground state $|v = 0, J = 0\rangle$. As illustrated in figure 2.4, the $|v = 1, J = 1\rangle$ state will spontaneously decay either directly to $|v = 0, J = 0\rangle$ or back to $|v = 0, J = 2\rangle$ (from which the population is continuously depleted). Population in levels $J = 3$ or higher is not directly pumped in this scheme, but BBR-induced rotational transitions transfer some of this population to J = 2. This population is then caught in the optical pumping cycle and thus the population is effectively trapped in the lower J levels. As in the work described in this chapter, Staanum *et al* incorporated the cooling laser into their rate calculations by altering the elements describing the $|v = 0, J = 2\rangle \rightarrow |v = 1, J = 1\rangle$ and $|v = 1, J = 1\rangle \rightarrow |v = 0, J = 2\rangle$ transitions such that these transitions were saturated.[28] However, their calculations only

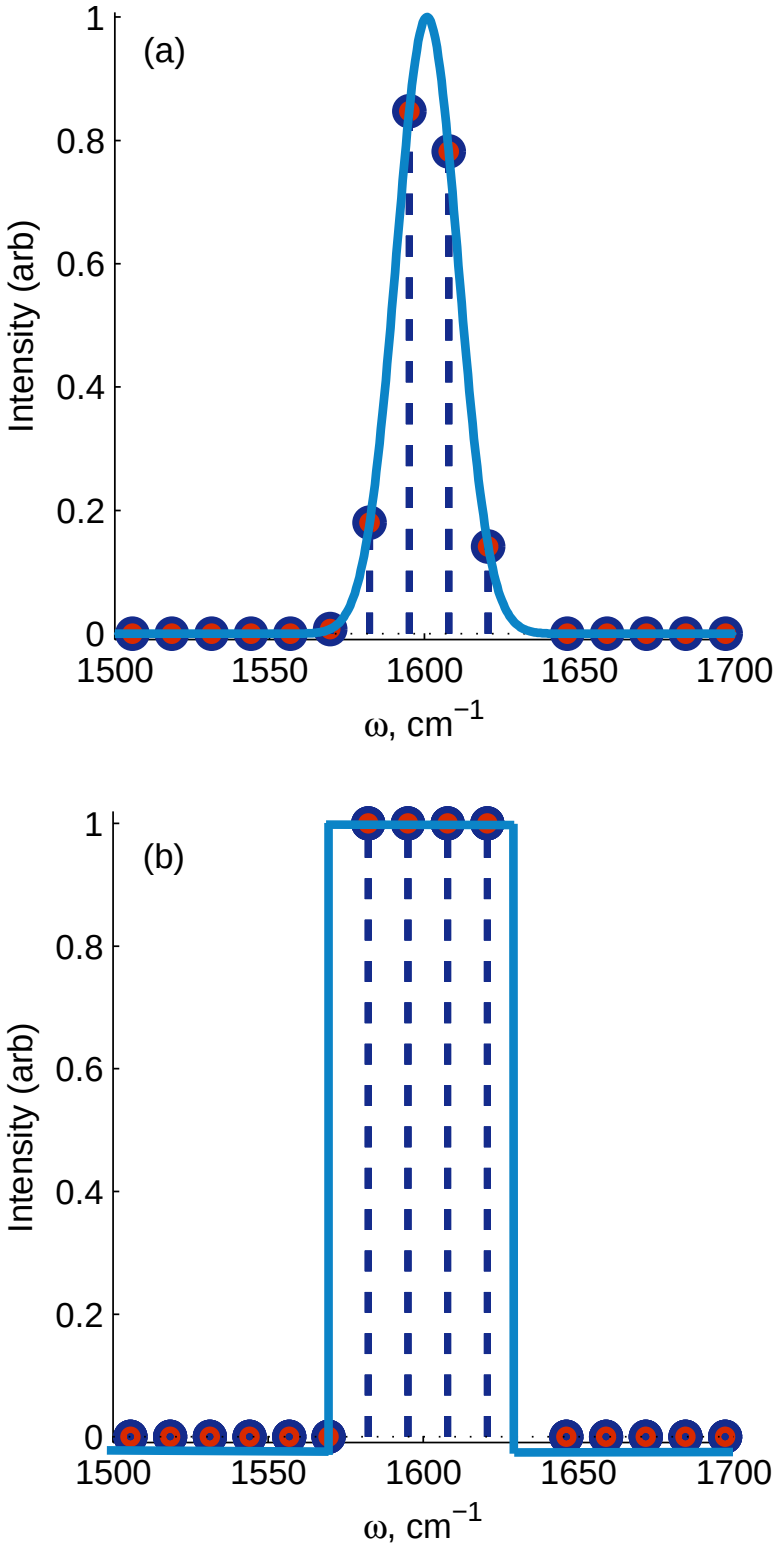

Figure 2.3: Schematic illustration of two laser pulses implemented in the cooling schemes for MgH^+ discussed in this work: (a) a Gaussian-shaped laser pulse, with four transitions excited; and (b) an idealised QCL-shaped pulse, again exciting four transitions but with equal intensity.

gave a rather approximate match to experiment in the final populations of the levels, a discrepancy that is investigated in more detail below.

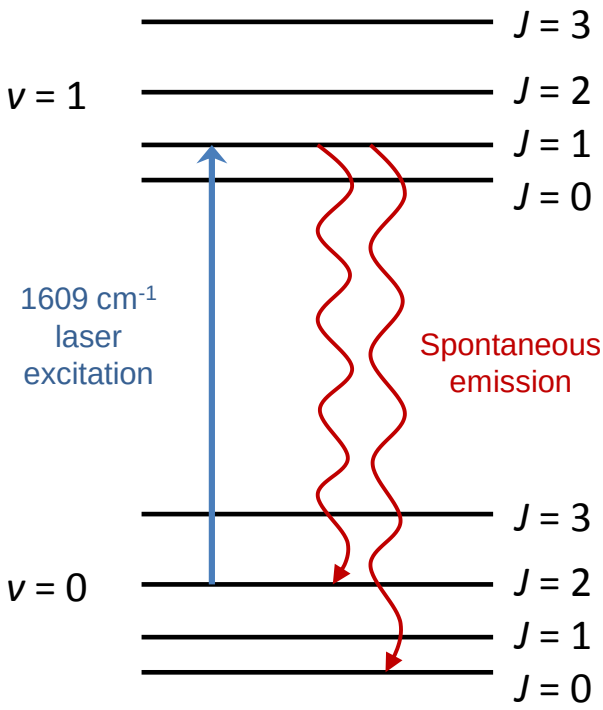

Figure 2.4: Schematic illustration of the rotational cooling scheme utilised in the experiments of Staanum *et al.*[28] The lowest vibrational and rotational states of $^1\Sigma$ MgH^+ are depicted, with the laser-driven excitation (blue, straight arrow) and allowed spontaneous emission (red wavy arrows) transitions depicted. BBR at 293 K further redistributes the rotational population (predominantly within each vibrational manifold).

Accurate simulation of the MgH^+ cooling scheme (as calculated in this work) requires knowledge of the rotational constant, B, vibrational constant, ω, the permanent dipole moment μ_0 and the transition dipole moment, $\mu_{v'J',v''J''}$ (comprising the vibrational transition moment and the rotational transition strength) of the ion.

2.4.1 MgH^+ dipole moment and potential energy surface calculations

Transition dipole moments were determined theoretically following characterisation of the electronic ground state potential and evaluation of the permanent dipole moment function. Calculations were performed at a number of different levels of theory using the Gaussian09

quantum chemistry package.[75] A series of correlation-consistent polarized valence n-tuple-zeta basis sets were employed. For Mg, cc-pVCxZ basis sets (where x = D, T, Q) were used as the addition of core potential improved convergence properties. An augmented basis set, aug-cc-pVxZ, was utilised for H to better account for the diffuseness of the MgH^+ charge distribution in the vicinity of the H. Complementing the series of correlation-consistent basis set calculations, complete basis set extrapolation calculations, as described by Taylor *et al*, were also performed.[80]

A potential energy curve was constructed for MgH^+ using a coupled cluster method, CCSD(T), in combination with the basis sets described above. Unrestricted calculations were performed for longer bond lengths, as the restricted method could not adequately describe the potential in this region.

The data obtained from these various approaches are summarised in table 2.2, alongside data reported by Aymer *et al* [81] (calculated using Configuration Interaction by Perturbation of a multi-configuration wave function Selected Iteratively, CIPSI). The dipole moment derivative (and hence the vibrational transition moment, μ_{lin} or μ_{int}) is highly sensitive to the basis set employed in the calculations. These data suggest that the transition moment falls in the range of 0.06-0.08 D.

The BBR-mediated population redistribution was calculated for MgH^+ using molecular constants calculated from each of the methods described. The best agreement with the experimental results of Staanum *et al* was achieved using data calculated at the CCSD(T)/CBS1 level of theory, with the vibrational transition dipole moment (of 0.061 D) determined using the finite field approach. All three CBS approaches returned μ_0 values that agreed within 1%. This is consistent with the findings of Taylor *et al*, where a comprehensive investigation found the three CBS extrapolations to perform comparably well in describing the characteristics of the NaH molecule.[80]

The calculations subsequently described for MgH^+ utilised μ_0 = 3.916 D and a vibrational transition moment of 0.0609 D, in combination with an experimentally obtained rotational constant, B = 6.387 cm^{-1}.[77] The frequencies of rovibrational transitions were

Table 2.2: Summary of the dipole moments and rotational constants calculated at different levels of theory.

Basis set	R_{eq} (cm^{-1})	ΔE (cm^{-1})*	B (cm^{-1})	μ_0 (D)	μ_{lin} (D)	μ_{int} (D)
DZ	3.161	1570.289	6.012	3.832	0.082	0.097
TZ	3.144	1619.792	6.091	3.893	0.067	0.08
QZ	3.136	1628.613	6.111	3.911	0.063	0.077
CBS1 (TZ-QZ)	3.136	1635.737	6.119	3.916	0.061	0.075
CBS2 (DZ-TZ-QZ)	3.144	1606.189	6.072	3.879	0.07	0.085
CBS3 (DZ-TZ-QZ)	3.144	1606.189	6.072	3.918	0.063	0.078
From [81]**	3.126	1636.514	6.192	2.9	0.09	0.12

* ΔE refers to the energy difference between $\langle v = 1, J = 0|$ and $\langle v = 0, J = 0|$.

** Data reported directly by Aymer *et al* [81] or calculated from their published potential energy curve and dipole moment function.

ascertained using the best available literature data.

2.4.2 Modelled population redistribution in MgH^+

The rotational population distribution in MgH^+ was modelled as a function of time in the presence of BBR at 293 K and no optical pumping. The initial population was assumed to be exclusively in the rovibrational ground state. As can be clearly seen in figure 2.5, internal quantum state purity is rapidly lost, with thermal equilibrium reached within 60 seconds. The equilibrium population in the rovibrational ground state was only 3.03% under these conditions.

As established experimentally, laser-excitation of the $|v = 0, J = 2\rangle \rightarrow |v = 1, J = 1\rangle$ transition, accompanied by spontaneous emission from the upper level, increases population in the rovibrational ground state.[28] The calculated change in the population of the states involved in this depletion cycle, $|v = 0, J = 0\rangle$, $|v = 0, J = 2\rangle$ and $|v = 1, J = 1\rangle$ (in addition to the $|v = 0, J = 1\rangle$ level), is plotted in figure 2.6 as a function of time. The population of the rovibrational ground state can be seen to rise steadily, reaching the equilibrium level of 46% within 120 seconds. This represents a 15-fold increase in the equilibrium population in the absence of any laser-driven transitions.

Initially at 12%, the population in the continuously depleted $|v = 0, J = 2\rangle$ level rapidly

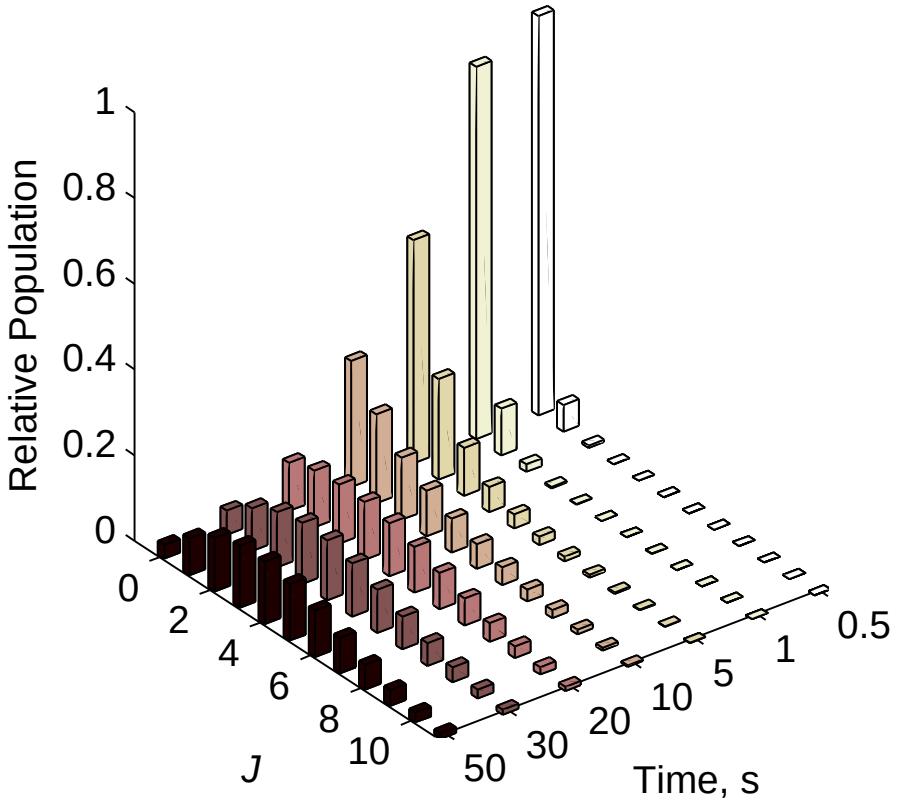

Figure 2.5: Distribution of MgH^+ rotational energy (in the vibrational ground state) as a function of time, in the presence of a 293 K BBR field, from an ensemble of ions initially exclusively in $J = 0$. At t = 0 population is exclusively in the rotational ground state ($J = 0$). Internal quantum state purity is rapidly lost, with thermal equilibrium reached within 60 seconds.

falls to a steady state of $< 4\%$. Population in the excited rovibrational level $|v = 1, J = 1\rangle$ spontaneously decays back to the $|v = 0, J = 0\rangle$ and $|v = 0, J = 2\rangle$ levels, and within a few seconds a steady-state population of 3.5% is reached. The increase in the population of the $|v = 0, J = 1\rangle$ level is due to an increase in BBR-mediated transitions from $|v = 0, J = 0\rangle$ and $|v = 0, J = 2\rangle$. As the $|v = 0, J = 1\rangle$ state is not directly addressed in the cooling scheme, an appreciable equilibrium population of 19% results.

It can be seen that the efficiency with which population is accumulated in the $|v = 0, J = 0\rangle$ state is limited by the rate of BBR-mediated population redistribution and the selected cooling transition.

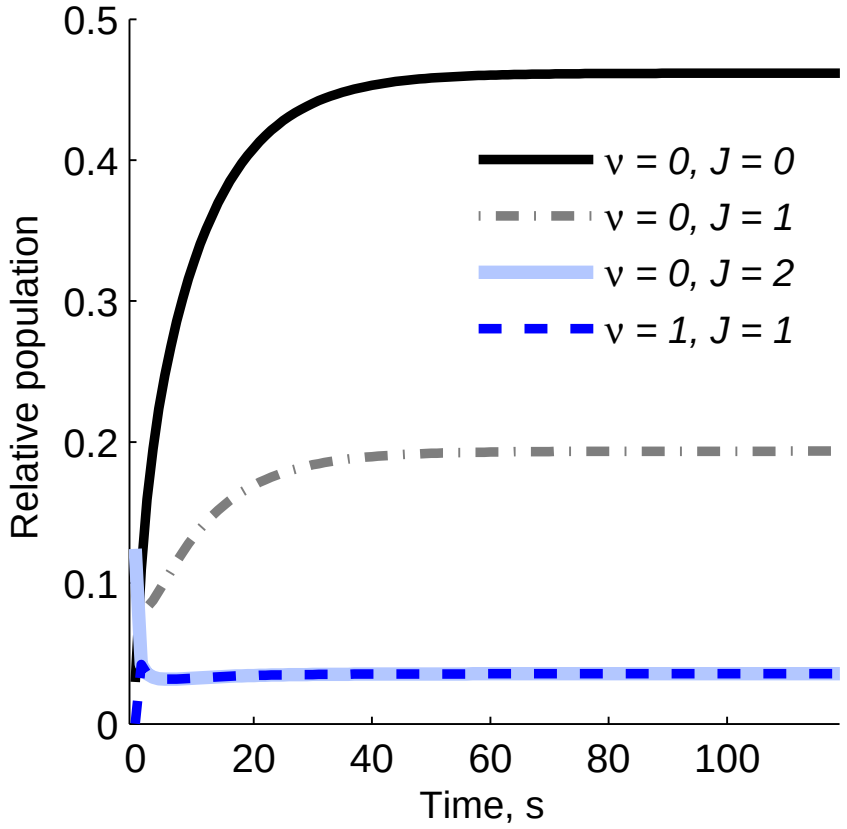

Figure 2.6: Change in the population of four rovibrational states of interest in MgH^+ as a function of time, following the application of a cooling laser (at t = 0) to a sample at thermal equilibrium (293 K).

The calculated equilibrium populations in the MgH^+ vibrational ground state with BBR-mediated laser cooling (as implemented experimentally by Staanum *et al*) [28] are shown in figure 2.7. Very good agreement can be seen between the populations calculated in this work and the experimentally observed populations. The timescale on which the population redistribution occurs in the experiments is also very well reproduced in the calculations. This near quantitative agreement serves to validate the methodology employed here and to provide confidence that it can be used to guide future experiments, predicting the efficiency of rotational cooling schemes in systems of interest. The calculations suggest that the previous discrepancy between theory and experiment in reference [28] is a consequence of sensitivity to the value of $\mu_{v',v''}$ in the calculations, rather than any unknown errors in experimental measurement.

The final population in the rovibrational ground state was surprisingly insensitive to changes in the laser-driven transition rate; the $|v = 0, J = 2\rangle \rightarrow |v = 1, J = 1\rangle$ transition was saturated at a rate of $\sim 5 \times 10^3$ s^{-1} (yielding 46.15% population in $|0, 0\rangle$), but a transition rate two orders of magnitude below this saturation point still achieved appreciable population in $|0, 0\rangle$ (44.92% with a transition rate of 5×10^1 s^{-1}). As such, if laser-driven transitions are not able to be saturated experimentally (as our model assumes), the rovibrational populations calculated here will still be reasonably accurate. It is also worth noting that the range of laser-driven transition rates considered was at least an order of magnitude greater than the rate of BBR-mediated redistribution or spontaneous emission (for the low J states of interest). Typically the rate of spontaneous emission dominates over BBR stimulated processes for vibrational transitions, whereas the rate of BBR stimulated processes dominates for rotational transitions.

2.4.3 Excitation of multiple cooling transition

The application of a single cooling laser is insufficient to accumulate a majority of the population in the rovibrational ground state of MgH^+; in part this is due to the population of the $J = 1$ level but also due to population in higher rotational states that is not driven towards $J = 0$ by the single frequency optical pumping; this higher J population only slowly diffuses towards the $J = 2$ level. The laser-excitation of multiple lines can enhance the population in the $|v = 0, J = 0\rangle$ state. While multiple, narrow-bandwith lasers could be employed to drive these multiple transitions, I propose that a single broadband laser source could achieve the same result. The first two transitions considered in MgH^+, $|v = 0, J = 2\rangle \rightarrow |v = 1, J = 1\rangle$ and $|v = 0, J = 3\rangle \rightarrow |v = 1, J = 2\rangle$, are only separated by $\sim$13 cm^{-1}, with a further two transitions ($|v = 0, J = 4\rangle \rightarrow |v = 1, J = 3\rangle$ and $|v = 0, J = 5\rangle \rightarrow |v = 1, J = 4\rangle$) within 39 cm^{-1}.

The calculations performed in this work show that simultaneous excitation of multiple P branch transitions in MgH^+ can increase the equilibrium population in the rovibrational ground state up to 58% at 293 K, as set out in table 2.3. This represents a significant (12%)

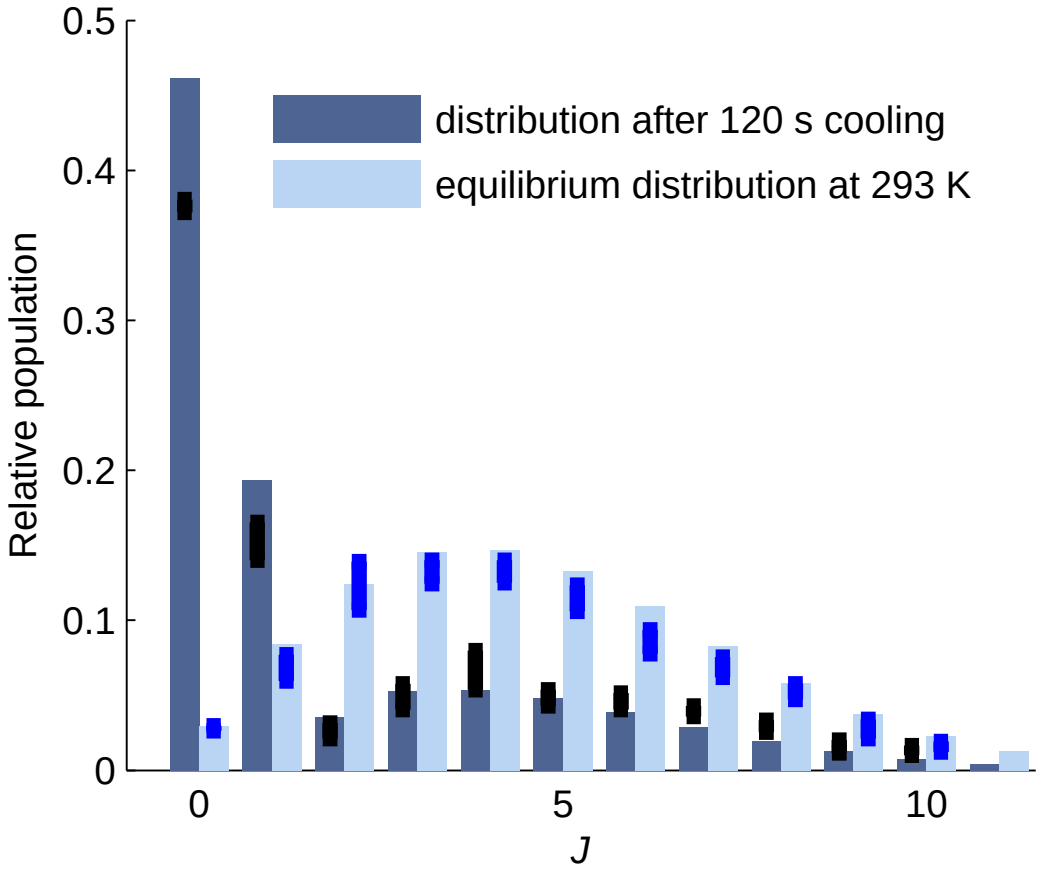

Figure 2.7: Comparison between the MgH^+ $v = 0$ rotational state populations calculated in this work (solid dark and light grey bars) and those experimentally recorded by Staanum *et al* (indicated in black and royal blue with reported error bars).[28]

enhancement over the population achieved when exciting a single laser-driven transition. The excitation of more than these four transitions yields diminishing returns. This is because up to 30% of total population accumulates in $|v = 0, J = 1\rangle$, placing an upper limit on the effectiveness of BBR-mediated laser-driven rotational cooling schemes for MgH^+ at 293 K. The inclusion of an additional narrow band laser driving an R branch transition to directly address the population accumulated in $|v = 0, J = 1\rangle$ was considered (in addition to the four transitions set out in table 2.3). While this did yield a lower population in the $|v = 0, J = 1\rangle$ state, the population in the rovibrational ground state was found to be $>$5% lower than the 58% achieved with just the four P branch transitions. To achieve the optimum laser pumping in this system a laser bandwidth of 30-40 cm^{-1} would be required,

which is within the typical gain profile of a QCL.

The sensitivity of the MgH^+ rovibrational ground state ($|0,0\rangle$) population to the laser-driven transition rate was tested with the excitation of multiple lines, extending the tests detailed above for a single laser-driven transition. Again, the final population calculated was not strongly dependent on the transition rates implemented. Saturation was achieved with transition rates of $\sim 5 \times 10^4$ s^{-1}. With transition rates two and three orders of magnitude lower than saturation (5×10^2 and 5×10^1 s^{-1}), the $|0,0\rangle$ state population was only 0.09% and 0.92% (respectively) below the maximum population achieved with saturated transitions. As such, the populations reported under multiple-transition cooling schemes are not strongly dependent on the assumption of laser saturation, and thus the use of broad-band sources such as QCLs is likely to be feasible.

It should be noted that, for effective BBR-assisted laser cooling, the transition rate for spontaneous emission from the laser-excited state to the ground state must be significantly larger than the rates of stimulated emission and absorption for rotational transitions within the excited vibrational state. The rapid rate of spontaneous decay prevents population from accumulating and spreading in the excited rovibrational state, allowing the population to be readily returned to $|v=0, J=0\rangle$ and the continuously laser-depleted state ($|v=0, J=2\rangle$ in MgH^+).

2.5 Cooling schemes for other $^1\Sigma$ electronic ground state species: LiH and CsH

Ultracold sources of alkali hydrides are of experimental interest as they possess large dipole moments. LiH, the lightest alkali hydride, has the potential to be Stark decelerated and loaded into a trap for further cooling and the accumulation of molecular density. Alternatively, it might be possible to form such molecules by photoassociation or magnetoassociation of ultracold Li and H atoms. CsH is potentially a more lucrative system for studying dipole-dipole interactions, as it has a larger dipole moment than LiH, but is likely to be more difficult to Stark decelerate. BBR-driven transitions will deplete any state-selected popula-

Table 2.3: Accumulation of population in $|v = 0, J = 0\rangle$ under different cooling schemes (assuming a QCL-shaped pulse for the excitation of multiple lines) for MgH^+, LiH and CsH. For MgH^+, calculations were performed at two temperatures: 293 K, for direct comparison with previous experimental work; and 77 K, to investigate the effect of temperature.

Pumped Transition	MgH^+			LiH		CsH	
	Transition freq. (cm^{-1})	Population in $\|0,0\rangle$ (%) at 293 K	at 77 K	Transition freq. (cm^{-1})	Population in $\|0,0\rangle$ (%) at 300 K	Transition freq. (cm^{-1})	Population in $\|0,0\rangle$ (%) at 300K
$\|0,2\rangle \rightarrow \|1,1\rangle$	1608.0	46.2	60.4	1374.0	59.6	879.6	34.3
$\|0,2\rangle \rightarrow \|1,1\rangle$	1608.0			1374.0		879.6	
$\|0,3\rangle \rightarrow \|1,2\rangle$	1595.1	54.8	68.7	1359.0	64.8	874.1	54.9
$\|0,2\rangle \rightarrow \|1,1\rangle$	1608.0			1374.0		879.6	
$\|0,3\rangle \rightarrow \|1,2\rangle$	1595.1			1359.0		874.1	
$\|0,4\rangle \rightarrow \|1,3\rangle$	1582.3	57.4	68.9	1344.0	65.9	868.7	63.3
$\|0,2\rangle \rightarrow \|1,1\rangle$	1608.0			1374.0		879.6	
$\|0,3\rangle \rightarrow \|1,2\rangle$	1595.1			1359.0		874.1	
$\|0,4\rangle \rightarrow \|1,3\rangle$	1582.3			1344.0		868.7	
$\|0,5\rangle \rightarrow \|1,4\rangle$	1569.6	57.7	68.9	1328.9	65.9	863.3	63.7

tion in both LiH and CsH inhibiting the build up of an appreciable density of cold, state-selected alkali hydride molecules in a trap. Complementing the calculations on MgH^+, similar calculations for the $^1\Sigma$ ground state LiH and CsH molecules is performed.

2.5.1 The effect of the rotational constant

Rotational cooling with a single laser-driven transition is most efficient for molecules with a high rotational constant, as in such systems the thermal distribution of rotational population spans comparatively fewer states. LiH fulfils this criterion, enabling a population of 59.6% to be built up in the rovibrational ground state with a single cooling laser exciting the $|v = 0, J = 2\rangle \rightarrow |v = 1, J = 1\rangle$ transition. This represents a near 17-fold increase in the ground state thermal population of 3.56%. As with the MgH^+ calculations, the effect of exciting additional transitions is considered (see table 2.3). In LiH, 65% of the population can be deposited into the ground rovibrational state with the inclusion of a second laser-driven transition. Exciting more than two transitions provides diminishing returns in the LiH cooling scheme, with the effectiveness of rotational cooling again limited by the accumulation of population in the $|v = 0, J = 1\rangle$ level.

In contrast to LiH (which has a rotational constant of 7.5 cm^{-1}), the smaller rotational constant of CsH (B = 2.7 cm^{-1}) hinders the build-up of population in $|v = 0, J = 0\rangle$ with the excitation of a single transition. The thermal distribution of CsH at 300 K spans some 25 J states, with the population in the rovibrational ground state of CsH is only 1.3% at 300 K. While this can be increased to 34% with the application of a laser driving the $|v = 0, J = 2\rangle \rightarrow |v = 1, J = 1\rangle$ transition, a cooling scheme where multiple transitions are excited (as set out in table 2.3) can yield a $J = 0$ population of up to 64%. As discussed with MgH^+, the employment of a broadband laser (or multi-wavelength QCL source), in this case with a bandwidth of around 16 cm^{-1} facilitating the simultaneous excitation of multiple transitions, would be beneficial in CsH; up to 30% more population could be accrued in $|v = 0, J = 0\rangle$ compared with what a single, narrow-frequency laser source could accomplish.

Furthermore, a molecule with a larger rotational constant has an enhanced overlap of its rotational transitions with the BBR spectrum at 300 K (see figure 2.1). The magnitude of the rotational constant thus influences the rate at which a steady state population is attained (given in table 2.4). This can be seen most clearly by comparing HCl^+ and DCl^+ (see section 2.6.1 for more details): both species have a $^2\Pi$ electronic ground state, with approximately the same dipole moment. However, as HCl^+ has a rotational constant which is almost double that of DCl^+, the rate at which equilibrium is attained is more than an order of magnitude faster in HCl^+.

2.5.2 The influence of the dipole moment

In addition to the rotational constant, the magnitude of the dipole moment also affects the timescale over which a steady state population is achieved under BBR-mediated, laser-driven rotational cooling. Table 2.4 provides the dipole moments of the species investigated in this work, along with the rotational constants and time taken for a steady state population to be reached in the rovibrational ground state. In each instance, only a single cooling transition is excited: the $|v = 0, J = 2\rangle \rightarrow |v = 1, J = 1\rangle$ transition in MgH^+, LiH and CsH; and the $|v = 0, J = 5/2\rangle \rightarrow |v = 1, J = 3/2\rangle$ line in HCl^+ and DCl^+ (see below).

In order to ascertain the influence of the dipole moment on the rotational cooling, μ_0 was varied while all other variables were kept constant. This enabled a direct relationship to be drawn between the dipole moment of a species and the rate at which rotational cooling is achieved: species with a larger dipole moment will reach a steady state population faster. However, the final equilibrium population in the rovibrational ground state for the molecules with larger dipole moments is typically lower than that calculated with a smaller dipole moment. This is because the equilibrium populations depend on the relative rates at which the ground state is populated and the rate at which it is depleted, the latter depending principally on the dipole moment.

These equilibrium populations are also dependent however on the vibrational transition dipole moment, i.e. the gradient of the dipole moment at equilibrium. A larger transition

Table 2.4: . The dipole moment, rotational constant and time taken for a steady state population to be attained (in the rovibrational ground state) for CsH, LiH, MgH^+, HCl^+ and DCl^+ following the excitation of a single cooling transition at 300 K.

Ground electronic state	Species	μ_0 (D)	B (cm^{-1})	time* (s)
$^1\Sigma$	CsH	8.33	2.7	31
	LiH	5.88	7.5	17
	MgH^+	3.916	6.4	48
$^2\Pi$	HCl^+	1.64	9.96	15
	DCl^+	1.64	5.1	425

* The time taken to reach an approximately steady state population (taken as 99% of the final equilibrium population) in the rovibrational ground state.

dipole moment yields a higher equilibrium population in the rovibrational ground state.

Taking these results together, we can infer that BBR-mediated, laser-driven rotational cooling will yield the highest populations in the rovibrational ground state and occur at the fastest rate for species with a large rotational constant and significant vibrational transition dipole moment. The complicated influence of the dipole moment means that a trade-off exists between reaching equilibrium rapidly (with a high dipole moment) and yielding a significant equilibrium population in the rovibrational ground state (best achieved with a lower dipole moment).

2.6 Considering the effect of electronic state

Species in Σ electronic states have no allowed Q-branch transitions. The most efficient single cooling transition for such species addresses the $J = 2$ level in the vibrational ground state, exciting to $|v = 1, J = 1\rangle$ as described earlier. Population will subsequently decay into $|v = 0, J = 0\rangle$ and $|v = 0, J = 2\rangle$. In the absence of Q-branch transitions, there is no efficient cooling transition that directly addresses the population in $|v = 0, J = 1\rangle$, however BBR-mediated rotational redistribution will continually transfer population into (and out of) this level. Accordingly, species in Σ electronic states can only accumulate $\leq 70\%$ of the total population in the rovibrational ground state even with several cooling transitions excited as an appreciable equilibrium population ($\leq 30\%$) will remain in the

$|v = 0, J = 1\rangle$ level.

Cooling schemes for species in Π electronic states, where Q-branch transitions are permitted, are significantly more effective; appropriate cooling schemes can accumulate $> 99\%$ of total population into the rovibrational ground state, as demonstrated in the DCl^+/HCl^+ system below.

2.6.1 $^2\Pi$ ground electronic state cooling scheme: DCl^+ and HCl^+

HCl^+/DCl^+ is a model system for investigating kinetic H/D isotope effects in reactions such as $HCl^+ + NH_3 \rightarrow NH_4^+ + Cl$.[82] The ions can also be readily formed state selectively by REMPI, and their quantum states detected state selectively by REMPD processes.[83, 84] HCl^+ is isoelectronic with the important OH and SH radicals. Furthermore, it has a $^2\Pi$ electronic ground state, in contrast to the $^1\Sigma$ systems investigated in section 2.5.

Cooling schemes for molecules in a $^2\Pi$ electronic state should explicitly consider spin-orbit coupling effects. Angular momentum interactions occuring in diatomic species are detailed in Appendix A. HCl^+/DCl^+ are examples of an inverted doublet, whereby the $^2\Pi_{3/2}$ component of the spin-orbit split $^2\Pi$ state is the lower in energy and the rotational ground state is $J = 3/2$. As HCl^+ falls into the pure Hunds case (a) coupling regime, transitions between the spin-orbit states are electric dipole forbidden; there will be no transitions between $^2\Pi_{3/2}$ and $^2\Pi_{1/2}$.

Transition moments were evaluated using the same approach detailed for MgH^+ above, with the exception that the MP2 method was used in place of CCSD(T), alongside a cc-pVTZ basis set. Other parameters were taken from literature (see table 2.1).[78, 79] Rotational energy levels for the $^2\Pi$ system were taken to be given by the pure Hunds case (a) formula,

$$E(v, J) = B[J(J + 1) - \Omega^2]. \tag{2.19}$$

DCl^+ species prepared exclusively in $|^2\Pi_{3/2}, v = 0, J = 3/2\rangle$ (the rovibrational ground state) take approximately 120 seconds to reach thermal equilibrium at 300 K (see figure 2.8). In this 300 K equilibrium distribution, only the ground vibrational state is populated,

Table 2.5: Population in the $|v = 0, J = 3/2\rangle$ rovibrational ground state of DCl^+ and HCl^+ (at 300 K) considering the effect of various cooling schemes (assuming a QCL-shaped pulse where multiple lines are excited).

	DCl^+		HCl^+	
Pumped Transition	Transition freq. (cm^{-1})	Population in $\|0,0\rangle$ (%)	Transition freq. (cm^{-1})	Population in $\|0,0\rangle$ (%)
$\|0,5/2\rangle \rightarrow \|1,3/2\rangle$	1893.2	92.0	2622.9	99.3
$\|0,7/2\rangle \rightarrow \|1,5/2\rangle$	1882.9	64.5	2603.3	66.4
$\|0,5/2\rangle \rightarrow \|1,3/2\rangle$	1893.2		2622.9	
$\|0,7/2\rangle \rightarrow \|1,5/2\rangle$	1882.9	99.7	2603.3	99.8
$\|0,5/2\rangle \rightarrow \|1,3/2\rangle$	1893.2		2622.9	
$\|0,7/2\rangle \rightarrow \|1,5/2\rangle$	1882.9		2603.3	
$\|0,9/2\rangle \rightarrow \|1,7/2\rangle$	1872.8	99.8	2583.7	99.8

with the rotational distribution spanning 15 J states. The thermal $|v = 0, J = 3/2\rangle$ population was calculated to be 9.5%. Following the excitation of a single cooling transition, $|v = 0, J = 5/2\rangle \rightarrow |v = 1, J = 3/2\rangle$, an equilibrium ground rovibrational state population of 92% was established (see table 2.5).

Given that Q-branch ($\Delta J = 0$) transitions are allowed in $^2\Pi$ DCl^+ the most efficient cooling transition involves exciting population from the second lowest J level (in $v = 0$) to the lowest J level in $v = 1$: $|v = 0, J = 5/2\rangle \rightarrow |v = 1, J = 3/2\rangle$. Population subsequently spontaneously decays from $|v = 1, J = 3/2\rangle$ to the states $|v = 0, J = 3/2\rangle$ and $|v = 0, J = 5/2\rangle$ (as no $\Delta J = -1$ transition is possible). The $|v = 1, J = 5/2\rangle$ state is continuously laser-depleted, resulting in a considerable enhancement of population in the rovibrational ground state with only one cooling transition. The calculated evolution of rotational population distribution is shown in figure 2.8.

As alluded to above, excitation of the equivalent transition in $^1\Sigma$ species ($|v = 0, J = 1\rangle \rightarrow |v = 1, J = 0\rangle$) is not an effective cooling mechanism because the absence of $\Delta J = 0$ transitions in $^1\Sigma$ states means that the population can only spontaneously emit back to $|v = 0, J = 1\rangle$. Driving the $|v = 0, J = 7/2\rangle \rightarrow |v = 1, J = 5/2\rangle$ transition in DCl^+ (equivalent to the most efficient single laser-driven transition in $^1\Sigma$ species, $|v = 0, J = 2\rangle \rightarrow |v = 1, J = 1\rangle$), yields a rovibrational ground state population of 64%

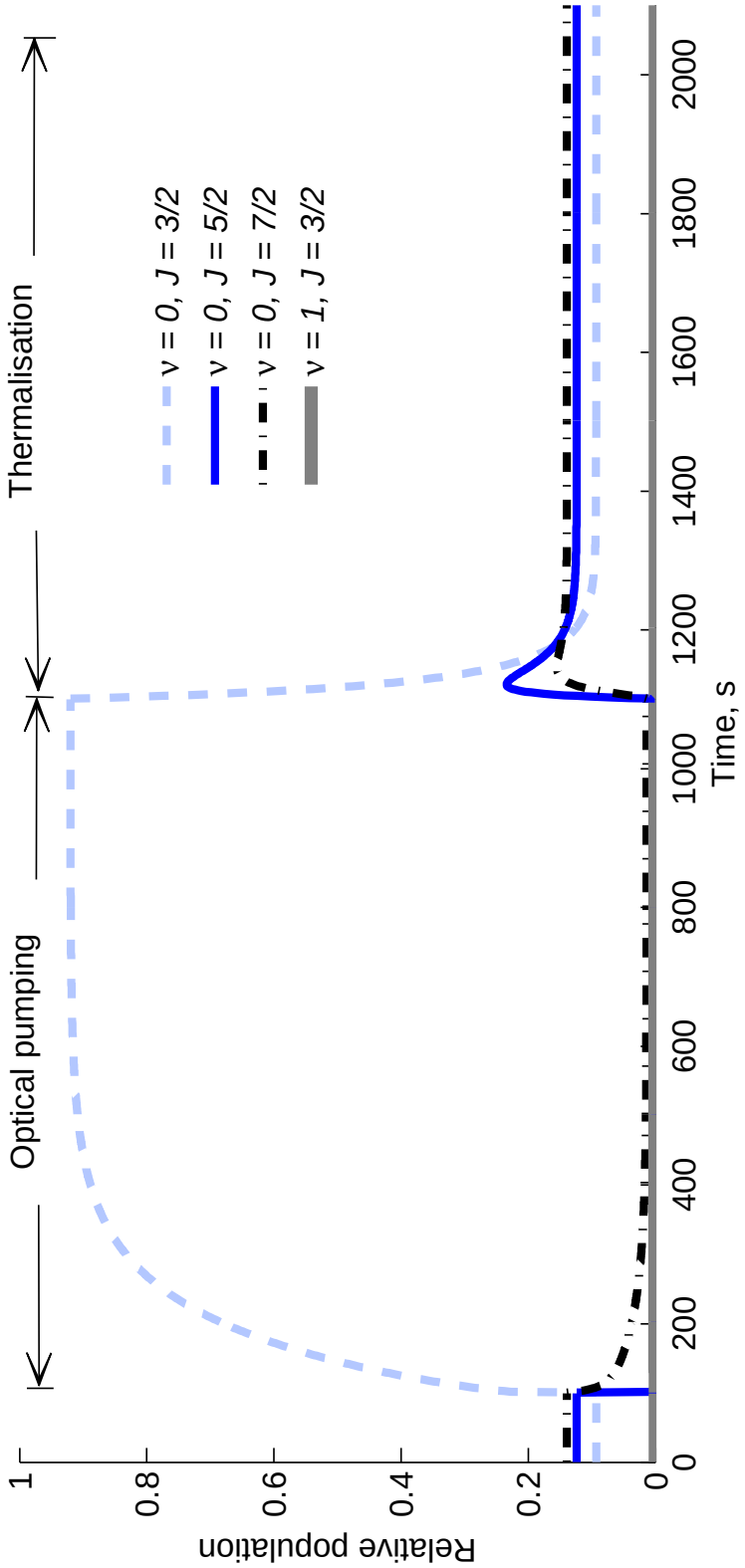

Figure 2.8: Change in the population of four rovibrational states of interest in DCl^+ as a function of time, following the application of a cooling laser (from t = 100 to 1100 seconds, the optical pumping period) exciting the $|v = 0, J = 5/2\rangle \rightarrow |v = 1, J = 3/2\rangle$ line in a sample at thermal equilibrium (300 K). At t = 1100 s the cooling laser is turned off, and re-thermalisation occurs rapidly.

in DCl^+. As seen in the $^1\Sigma$ systems, population will decay from $|v = 1, J = 5/2\rangle$ to the rovibrational ground state, $|v = 0, J = 3/2\rangle$, and the continuously depleted state, $|v = 0, J = 7/2\rangle$. However, in DCl^+ there will be an additional Q-branch transition to $|v = 0, J = 5/2\rangle$, which is not directly addressed in the cooling cycle (and accounts for the lower cooling efficiency of this single transition). Simultaneous excitation of the two cooling transitions with an appropriate laser source ($|v = 0, J = 5/2\rangle \rightarrow |v = 1, J = 3/2\rangle$ and $|v = 0, J = 7/2\rangle \rightarrow |v = 1, J = 5/2\rangle$; $\Delta\omega \sim 10.5$ cm^{-1}) effectively closes the cooling cycle, directly exciting population out of both $J = 5/2$ and $J = 7/2$. The result, depicted in figure 2.9, is >99% of total population accumulated in the rovibrational ground state.

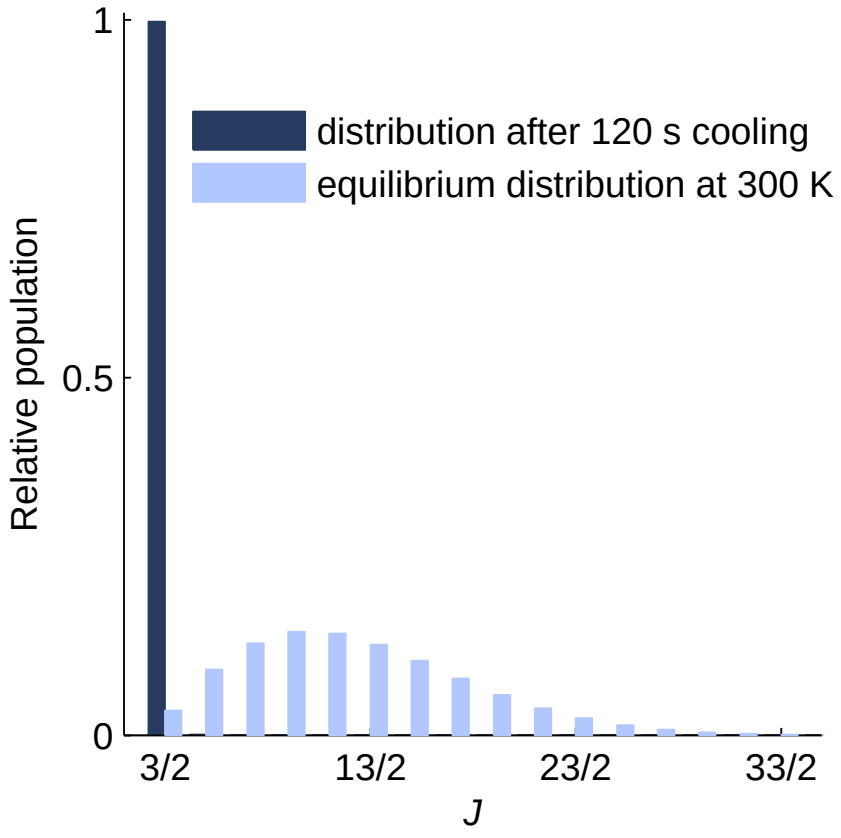

Figure 2.9: Equilibrium rotational population distribution in DCl^+, at 300 K thermal equilibrium and following excitation of the $|v = 0, J = 5/2\rangle \rightarrow |v = 1, J = 3/2\rangle$ and $|v = 0, J = 7/2\rangle \rightarrow |v = 1, J = 5/2\rangle$ transitions.

BBR-mediated population decay calculations were repeated for HCl^+ molecular ions exclusively in the ground rovibrational state at $t = 0$. As inspection of figure 2.2 reveals, there are significant isotope effects in both the rate of population decay and the resulting equilibrium level attained. The rovibrational ground state population in HCl^+ decays at a faster rate (with a 300 K lifetime of 6.6 seconds, compared with 20 seconds for DCl^+), but in the absence of laser cooling ultimately yields a higher equilibrium population of 19%, double the 9.5% calculated for DCl^+. Given the larger rotational constant (B) in HCl^+ compared with DCl^+ (see table 2.1) it is unsurprising that, with a single cooling laser exciting the $|v = 0, J = 5/2\rangle \rightarrow |v = 1, J = 3/2\rangle$ transition in HCl^+, 99.3% of population can be accumulated into the rovibrational ground state, >7% more than calculated for DCl^+.

2.7 The effect of temperature and hybrid approach of cooling

The rate of BBR-mediated population decay is dependent on the temperature of the black body (see figure 2.1). For a polar species (with a non-zero dipole moment), the rate of decay normally decreases with decreasing temperature. With the assistance of a cryogenic radiofrequency ion trap, Schwarz *et al* have experimentally demonstrated that state-selection is indeed maintained in MgH^+ when experiments are conducted at 4 K.[74] Our calculations indicate that state-selection will also be maintained for DCl^+ ions when exposed to BBR at (or below) 5 K, as shown in figure 2.10.

Maintaining an ion trap at $\leq$ 5 K represents a significant engineering challenge (and may also impose other experimental restrictions), which is why cooling schemes incorporating BBR-mediated optical pumping have been proposed for the diatomic species considered in this work.

Another option under consideration is to adopt a hybrid approach, whereby optical cooling schemes are implemented alongside traps operated at temperatures around 77 K; the rate of redistribution is likely to be substantially reduced at 77 K. This serves to enhance the maximum population that can be accumulated in the rovibrational ground state while

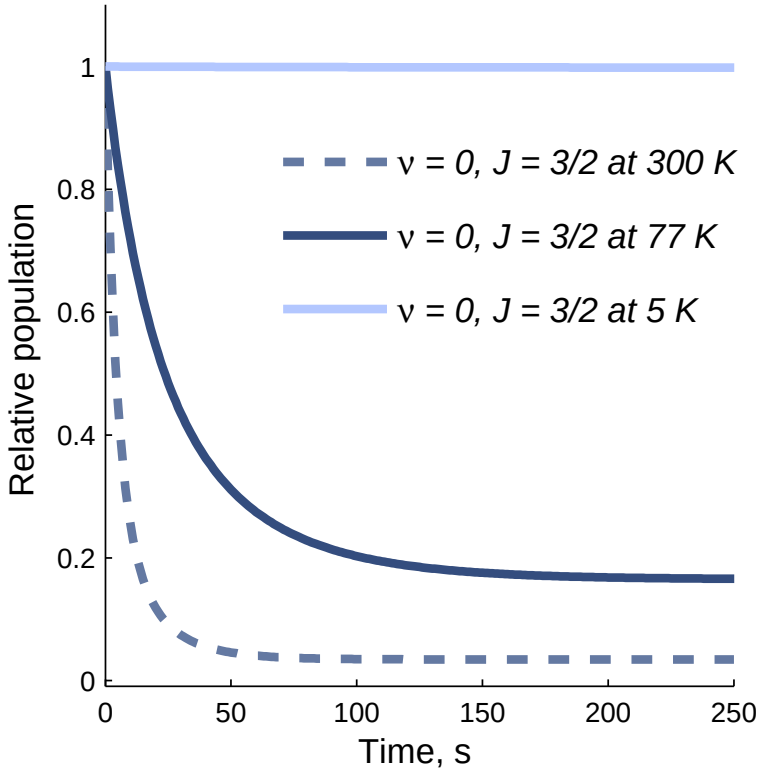

Figure 2.10: The rate of decay of state-selected $|^2\Pi_{3/2}, v = 0, J = 3/2\rangle$ DCl^+ at a range of BB temperatures: 300 K (dashed light grey-blue line); 77 K (solid dark grey-blue line); and 5 K (solid light grey-blue line). At temperatures $\leq$ 5 K the state purity is maintained for hundreds of seconds.

using a temperature range that is more easily attainable than the 4 K set-up implemented by Schwarz *et al*. Calculations on the MgH^+ system, set out in table 2.3, demonstrate the potential benefits of this hybrid methodology. A final population of 69% in the rovibrational ground state (under conditions of multiple rotational line excitation) was calculated at 77 K, well above the 58% achievable under room temperature conditions. Also noteworthy is that this population of 69% can be achieved with fewer cooling transitions excited, as the equilibrium rotational distribution at 77 K spans far fewer rotational levels than at 293 K.

2.8 Conclusion

Calculations to establish the effectiveness of laser-driven BBR-mediated optical cooling schemes for several diatomic species is performed. Close agreement with reported MgH^+

experimental results [28] demonstrates the validity of the methodology, but also its sensitivity to the dipole moment gradient. Optical pumping schemes involving several pumped transitions with broadband laser sources can accumulate populations of 57.7%, 65.9%, 63.7% and >99% in the rovibrational ground states of MgH^+, LiH, CsH and DCl^+/HCl^+ (respectively). For $^1\Sigma$ species, this represents a considerable enhancement (up to 29%) over the population accumulated following the excitation of a single transition. The inclusion of allowed Q-branch transitions in $^2\Pi$ species, such as DCl^+ and HCl^+, yields significantly higher rovibrational ground state populations (>90% with a single transition excited) compared with that attainable in $^1\Sigma$ species. The magnitude of the rotational constant, dipole moment and vibrational transition dipole moment were found to influence the rate at which equilibrium populations were attained under the rotational cooling schemes, and also the final equilibrium population achieved. The high sensitivity to the various parameters demonstrates that attempts to provide generalised cooling schemes for "similar" species [65] (such as molecules in the same electronic state) may have limited accuracy and applicability; with only the exchange of H for D, there is a significant alteration in the properties of the system. This emphasises the need for cooling schemes to be developed for, and tailored to, each system under consideration. Finally, a hybrid approach involving optical cooling in 77 K experimental environments is proposed. I believe that this approach will be best suited for polyatomic species, where optical cooling schemes are likely to be less efficient due to the more complicated energy level landscape.

Chapter 3

Rovibrational Cooling Schemes for Linear Polyatomic Ion- $C_2H_2^+$

3.1 Introduction

As the smallest alkyne, acetylene and its cation ($C_2H_2^+$) are simple enough species to be subjected to rigorous theoretical treatment, whilst also complex enough to have many of the properties of larger systems. The acetylene cation is of significant astrochemical interest in its own right, playing an important role in the chemistry of the interstellar medium (ISM). Ions such as $C_2H_2^+$ are abundant in the ISM, formed as a result of the intense radiation fields that prevail in such environments. Barrierless ion-molecule reactions of unsaturated hydrocarbon species are essential for the formation of conjugated hydrocarbons and clusters. Also, in the reactions of acetylene cations with N atoms or HCN, C-N bond formation is likely to be fast and of importance in building larger molecules. The reaction of $C_2H_2^+$ with molecular hydrogen has an unusual temperature dependence, with the opening of a new reaction channel at very low collision energies.[5] The long-lived collision complex influences the reaction dynamics of the system, and the experimentally observed rate constant has a strong negative temperature dependence below around 100 K. Simple extrapolation of trends from data recorded at temperatures down to 80 K simply cannot predict this behavior. These examples illustrate the importance of studying astrochemically-relevant ion-molecule reactions of the acetylene cation under cold conditions in developing our understanding of the fundamental chemistry of the ISM.

In order to experimentally investigate the reactions of $C_2H_2^+$ under astrochemically relevant conditions, in which rotational-vibrational temperatures are low, a mechanism for maintaining quantum state purity must be implemented. In the case of diatomic molecules, three approaches have been previously adopted to maintain the internal-state purity of trapped diatomic species. Firstly, if a homonuclear diatomic species is selected for study, such as N_2^+, [73, 85] such ions have no electric dipole-allowed transitions falling within the BBR spectrum, and lifetimes are extremely long (the main loss being due to collisions); however this approach is only applicable to a limited number of species. Secondly, the ion-trap apparatus can be cryogenically cooled, such that only the lowest rotational states are populated at thermal equilibrium.[74, 86] Finally, preferential population of the lowest rovibrational states can be achieved through a combination of optical pumping and BBR-mediated population redistribution. This technique has been explored both experimentally and theoretically for a number of diatomic species of interest,[25, 28, 65, 66] with rovibrational ground state populations in excess of 99% predicted for species such as HCl^+.

In this chapter my previous theoretical study of laser-driven, BBR-mediated, rotational cooling schemes in diatomic species of Chapter 2, is extended to a more complex polyatomic species of significant interest. A BBR-mediated rotational cooling schemes for $C_2H_2^+$ is proposed. The role of BBR in redistributing initially state-selected population is calculated at temperatures ranging from 77 to 300 K. The ability to achieve and maintain state selectivity in an ensemble of cold, trapped $C_2H_2^+$ ions will facilitate detailed experimental investigations into the reaction dynamics of this important species.

3.2 The Energy Levels and Vibrational Transition Intensities of $C_2H_2^+$

The acetylene cation, a highly symmetric linear species belonging to the $D_{\infty h}$ point group, has no net dipole moment ($\mu_0 = 0$) and hence pure rotational transitions are forbidden. Accordingly, one might initially expect that $C_2H_2^+$ would not interact with ambient BBR. While there is indeed no interaction within the ground vibrational state, there are two IR-

active vibrational modes, where the centre of symmetry of the $D_{\infty h}$ point group is broken. The asymmetric stretch (ν_3) has a frequency of $\omega_3 = 3136$ cm^{-1},[87] well above the range of the BBR spectral function at 300 K. The other IR active mode, a doubly degenerate cis bend (ν_5) shown in figure 3.1, has an experimentally measured frequency of ω_5 = 710 cm^{-1}.[87] This vibrational frequency is almost coincident with the peak of the 300 K BBR distribution (see figure 3.2). BBR-mediated rotational energy redistribution within the ground vibrational manifold therefore occurs rapidly, through the involvement of the $v_5 = 1$ manifold. At 300 K a large number of rotational states are populated, extending up to the first 20 J levels, owing to the small rotational constant, B (see table 3.1).

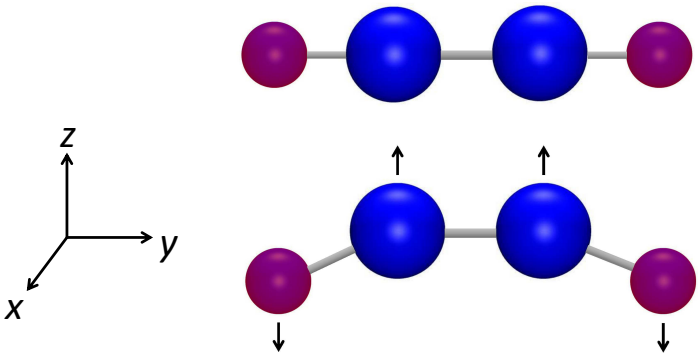

Figure 3.1: IR active cis bending mode of vibration (ν_5) in $C_2H_2^+$. The mode is doubly degenerate. The motion in $z-y$ plane is illustrated here. There is an equivalent degenerate mode in the $x-y$ plane.

3.2.1 Energy levels for the Renner-Teller states

The $^2\Pi$ electronic ground state of the $C_2H_2^+$ ion is split by spin-orbit coupling into $^2\Pi_{3/2}$ and $^2\Pi_{1/2}$ levels with a negative spin-orbit coupling constant (A) (see table 3.1) giving rise to an inverted doublet. In the excited vibrational levels, vibrational angular momentum arises from the doubly degenerate ν_5 bend precessing around the molecular axis, with projection quantum number l. The Renner-Teller effect couples the vibrational and electronic orbital angular momenta (projection quantum number Λ), giving rise to vibronic angular momentum with resultant projection quantum number $K = \Lambda + l$. This interaction further splits the vibrational energy levels (for $v_5 > 0$), yielding the states given in table 3.2 and illustrated in figure 3.3, where $K = 0, 1, \ldots$ is designated by the term symbol $\Sigma, \Pi, \ldots$. The subscript in

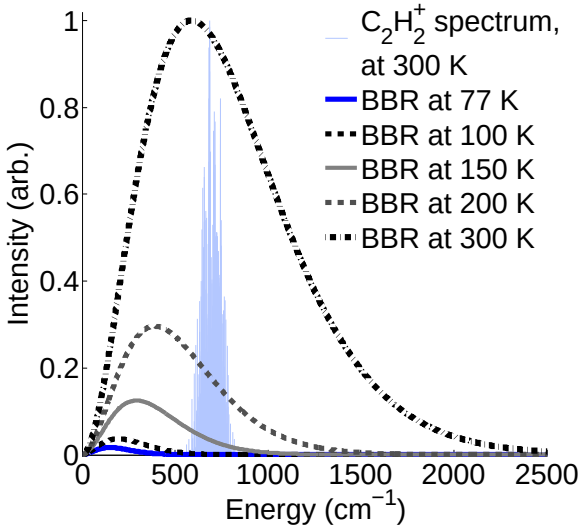

Figure 3.2: Simulated excitation spectrum of the ν_5 vibration in $C_2H_2^+$ at 300 K (light blue solid lines), superimposed with the BBR spectrum at a range of temperatures: 300 K (black dot dashed line), 200 K (dark grey dashed line), 150 K (light gray solid line), 100 K (black dashed line) and 77 K (blue solid line). At temperatures < 100 K there is minimal (if any) overlap between the peaks in the simulated ν_5 excitation spectrum and the blackbody spectra.

Table 3.1: Molecular parameters of $C_2H_2^+$.[87, 88]

Parameter	Value
μ_0	0.0 D
A	-30.91 cm^{-1}
B	1.1 cm^{-1}
ϵ for ν_5	0.032
ω_5	710 cm^{-1}
$\langle v_5 = 0 \vert \boldsymbol{\mu} \vert v_5 = 1 \rangle$	0.21 D

the vibronic term symbol gives the total projection quantum number P obtained by adding the spin projection quantum number Σ to K ($P = K + \Sigma$). The relative energies of allowed $v_5 = 0$ to $v_5 = 1$ transitions between the various rotational ground states of each vibronic component – spanning some 85 cm^{-1} – are indicated in figure 3.3. Details of the angular momentum interactions are given in appendix A.

The rovibrational energy levels and transition intensities in $C_2H_2^+$ can be obtained by diagonalization of the Hamiltonian including spin-orbit, Renner-Teller and rotational terms, using a Hund's case (a) type basis set $\mid \Lambda, l, K, S, \Sigma, P, J \rangle$, where the total angular mo-

Table 3.2: Renner-Teller rovibronic states in the first three ν_5 levels of $C_2H_2^+$ using the notation $^{2S+1}K_P$.

Vib. level, v_5	Rovibronic states
0	$^2\Pi_{3/2}$, $^2\Pi_{1/2}$
1	$^2\Sigma^-$, $^2\Sigma^+$, $^2\Delta_{5/2}$, $^2\Delta_{3/2}$
2	$^2\Phi_{7/2}$, $^2\Phi_{5/2}$, $^2\Pi^+_{3/2}$, $^2\Pi^-_{3/2}$, $^2\Pi^+_{1/2}$, $^2\Pi^-_{1/2}$

mentum quantum number J takes the values $P, P+1, \ldots$. Details of the relevant Hamiltonian matrices are given in the Appendix. The extent to which a species deviates from Hund's case (a) is indicated by the ratio of the spin-orbit constant to the rotational constant, $Y = A/B$. As shown by Hougen,[89] the rotational energies for the case when $v_5 = 0$ ($^2\Pi$) and $v_5 = 1$ (for $^2\Delta$ states) are given by equations 3.1 to 3.2, obtained from diagonalization of a 2×2 matrix (see the Appendix and also equation (47) of Hougen). The definitions of E_{vib}, B_{eff} and Y_{eff}, where $B_{\text{eff}} \approx B$ and $Y_{\text{eff}} \approx Y$, are provided in the Appendix.

$$E_{\text{vib+rot}} = E_{\text{vib}} + B_{\text{eff}}[(J+\frac{1}{2})^2 - K^2 \pm \frac{1}{2}\sqrt{4(J+\frac{1}{2})^2 + Y_{\text{eff}}(Y_{\text{eff}} - 4K)}\,], \text{for } J > (K-1) \tag{3.1}$$

$$E_{\text{vib+rot}} = E_{\text{vib}} - \frac{A}{2} + B_{\text{eff}}K, \text{when } J = K - \frac{1}{2}, \tag{3.2}$$

Each energy level has both $+$ and $-$ parity levels; while the parity has been explicitly considered in the intensity calculations, states with the same J but different parity are treated here as degenerate.

When considering the ($v_5 = 1$) $^2\Sigma$ states, the quantum number K is zero, and each $^2\Sigma$ component is composed of F_1 ($\Sigma = +1/2$, $J = N + 1/2$) and F_2 ($\Sigma = -1/2$, $J = N - 1/2$) sub-levels, yielding two sets of J quantum numbers for each $^2\Sigma$ vibronic level. (N is the total angular momentum quantum number excluding spin: $N = J - S$.) Equations 3.3 to 3.4, obtained by diagonalization of a 4×4 matrix (see Appendix, Herzberg[90] and also footnote 16 of Hougen[89]), are employed to calculate the rovibrational energy levels,

$$E(^2\Sigma) = E_{\text{vib}} + B_{\text{eff}}(J+\frac{1}{2})^2 \pm \frac{1}{2}\sqrt{\Delta\nu^2 \pm 4B_{\text{eff}}(J+\frac{1}{2})(v_5+1)\epsilon\omega_5 + 4B_{\text{eff}}^2(J+\frac{1}{2})^2} \tag{3.3}$$

$$\Delta\nu = A^*_{v_5,K=0} = \sqrt{A^2 + (v_5+1)^2\epsilon^2\omega_5^2} \tag{3.4}$$

where ϵ is the Renner-Teller parameter for ν_5, and E_{vib} and B_{eff} are as defined in the Appendix ($B_{\text{eff}} \approx B$). The $+$ and $-$ signs in front of the square root in equation 3.3 apply to the $^2\Sigma^+$ and $^2\Sigma^-$ states respectively, while the $+$ and $-$ signs inside the square root apply to the F_2 and F_1 components for $^2\Sigma^+$ and to F_1 and F_2 for $^2\Sigma^-$ respectively.[90]

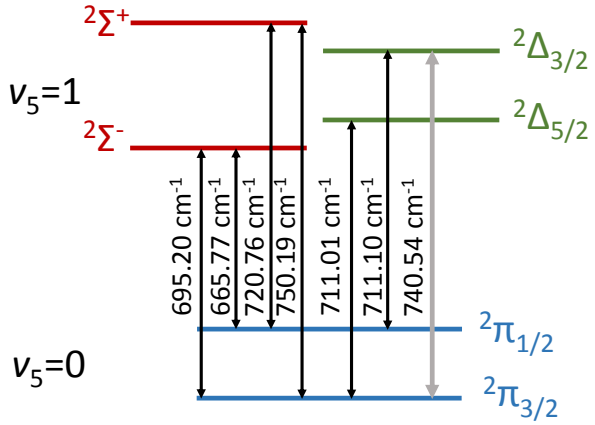

Figure 3.3: The energies of allowed $v_5 = 0$ to $v_5 = 1$ transitions (between the rotational ground states) are indicated, ranging from 665.77 cm^{-1} to 750.19 cm^{-1} as calculated in this work. The transition between $^2\Pi_{3/2}$ and $^2\Delta_{3/2}$ is only weakly allowed, and is thus shown in gray.

3.2.2 Transitions and rotational line strengths in the ν_5 fundamental band

Transitions between rovibronic levels must obey several selection rules: $\Delta J = 0, \pm 1$; $+$ parity $\leftrightarrow$ $-$ parity; $\Delta N = 0, \pm 1, \pm 2$; $\Delta K = \pm 1$; $\Delta P = 0, \pm 1$ (where P is the projection of J onto the molecular axis, and the ΔN selection rule derives simply from $J = N \pm 1/2$ in this system); and finally $\Delta v \neq 0$ (where v is the vibrational quantum number). This final selection rule arises from the zero dipole moment in the ground electronic state. Species classified as Hund's case (a) also obey an additional selection rule, $\Delta\Sigma = 0$. Due to state mixing in $C_2H_2^+$ this conservation of Σ is relaxed somewhat and transitions

nominally where $\Delta\Sigma \neq 0$ are considered (through the admixture of a $\Delta\Sigma = 0$ component). The strength of such transitions are guided by the ratio $Y = A/B$, and are weak in this system, i.e., for $^2\Pi_{3/2} \rightarrow {}^2\Delta_{3/2}$. Accordingly, the six main vibrational transitions are $^2\Pi_{3/2} \rightarrow {}^2\Delta_{5/2}$, $^2\Pi_{1/2} \rightarrow {}^2\Delta_{3/2}$, $^2\Pi_{3/2} \rightarrow {}^2\Sigma^{\pm}$ and $^2\Pi_{1/2} \rightarrow {}^2\Sigma^{\pm}$.

The rotational line strengths are obtained from the eigenfunctions of the diagonalized Hamiltonian matrices and the transition moments in the pure Hund's case (a) basis. Expanding each eigenstate m as

$$\psi_m = \sum_n C_{mn}\Phi_n^a, \tag{3.5}$$

where the a superscript indicates a pure Hund's case (a) state, leads to

$$S_{m'm''} = \mid \sum_{n'n''} C_{m'n'} \sqrt{{}^{\mathrm{a}}\boldsymbol{S}_{n'n''}}\, C_{m''n''} \mid^2, \tag{3.6}$$

where ${}^{\mathrm{a}}\boldsymbol{S}_{n'n''}$ is the pure case (a) rotational line strength connecting Hund's case (a) states $\phi_{n'}$ and $\phi_{n''}$, and $C_{m''n''}$ is an eigenfunction coefficient from the diagonalization. This equation gives the rotational line strength for a molecule/ion in an intermediate coupling case. The overall transition moment is then given by the product of the vibronic transition intensity and the rotational line strength

$$I_{K'K''m'm''} = \mu_{K'K''}^2 S_{m'm''}, \tag{3.7}$$

where $\mu_{K'K''}$ is the vibronic transition moment for a specific component of the transition (e.g., for $^2\Pi_{3/2} -^2 \Delta_{5/2}$). The values of this parameter were set equal for each of the 6 principal components allowed by the selection rules. The pure case (a) rotational line strengths that are necessary for the calculation are taken from Kovacs,[91] page 121. (Although the expressions are given there as rotational line strengths for pure case (a) diatomics, these are equally applicable to the Renner-Teller coupled states with the K and P quantum numbers equivalent to Λ and Ω for a diatomic.)

To validate the calculation of intensities, the calculated spectrum is compared with the experimental recording of the $C_2H_2^+$ ν_5-excitation action spectrum obtained in an ion trap by Schlemmer and coworkers.[87] Experimentally, the spectrum was obtained by monitoring $C_2H_3^+$ production from the reaction of $C_2H_2^+$ with H_2 at 90 K (where $C_2H_3^+$ products

could only be formed from vibrationally excited $C_2H_2^+$ reactants). A free-electron laser was utilized as the IR excitation source, yielding the spectrum depicted in figure 3.4 (inverted trace).[87] The restricted bandwidth of the free-electron laser limited the resolution of the experimental spectrum and individual rotational lines are not resolved. A ν_5 excitation stick spectrum has been calculated at 90 K, as shown in figure 3.4. Convolution of this 90 K stick spectrum with a $\sim$3 cm^{-1} FWHM Gaussian (to match the reported experimental resolution) yields the simulated spectrum presented in figure 3.4. My simulation reproduces the overall band profile and the features present in the experimental spectrum reasonably well. The transitions contributing to these main features can be identified: the most intense peak ($\sim$710 cm^{-1}) arises from the $^2\Pi_{3/2}$ to $^2\Delta_{5/2}$ and $^2\Pi_{1/2}$ to $^2\Delta_{3/2}$ bands; the peak at $\sim$695 cm^{-1} can be attributed to the $^2\Pi_{3/2}$ to $^2\Sigma^-$ band; the side feature at $\sim$720 cm^{-1} is due to the $^2\Pi_{1/2}$ to $^2\Sigma^+$ band; and the small peak at $\sim$740 cm^{-1} arises from the weak $^2\Pi_{3/2}$ to $^2\Delta_{3/2}$ band. The good agreement between my simulated spectrum and the experimentally observed spectrum serves to validate my theoretical approach, both in the calculation of the numerous energy levels and in my treatment of the transition line strengths.

3.2.3 Blackbody radiation-induced transitions and laser pumping of the acetylene ion

The method adopted to determine the rate of change of the population induced by laser pumping and by BBR has been detailed in a previous publication.[66] In brief, the evolution is calculated by numerical solution of the coupled rate equations

$$-\frac{dn_i}{dt} = \sum_j B_{ij}\rho_T(\omega_{ij})n_i - \sum_j [B_{ji}\rho_T(\omega_{ij}) + A_{ij}]n_j, \tag{3.8}$$

where ρ_T is the spectral density (including both effects of BBR and any applied laser pumping) and B_{ij} and A_{ij} are the Einstein coefficients for stimulated emission/absorption and spontaneous emission, respectively. The Einstein coefficients are proportional to the squared transition moments, which can be expressed as a product of a rotational line strength factor and the vibronic transition moment. In this work, the vibronic transition moment of 0.21D is used, which was estimated by Schlemmer and coworkers from the lifetime of the

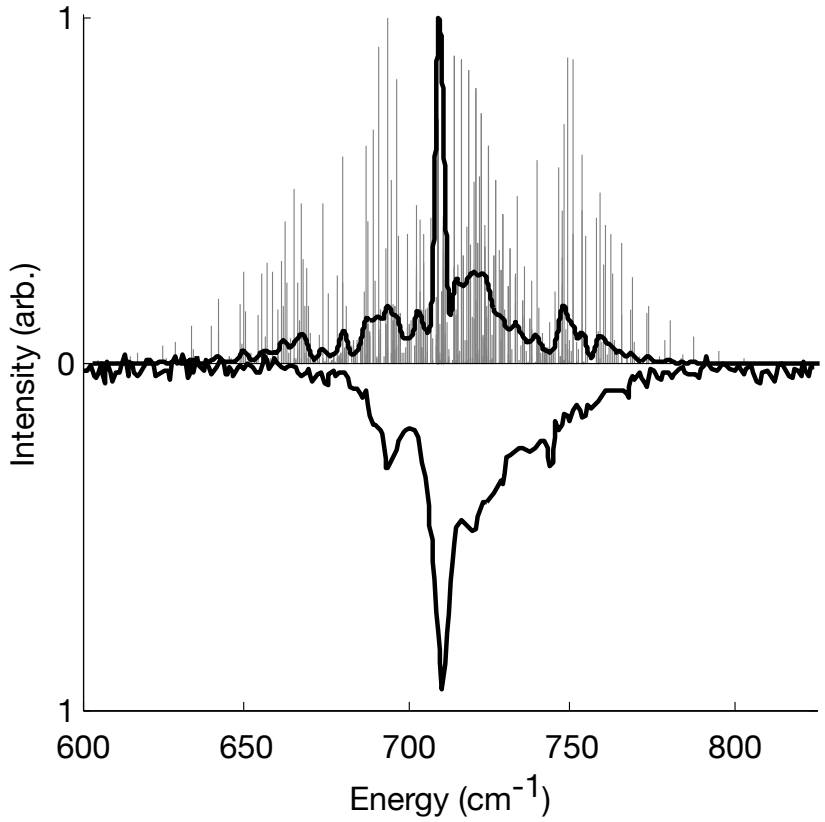

Figure 3.4: Calculated and measured spectrum of $C_2H_2^+$ at 90 K. The stick spectrum of rotational transitions is shown in gray; convolution with the $\sim$3 cm^{-1} resolution of the laser system yields the simulated spectrum (black, above). Inverted below this simulation is the experimental spectrum reported by Schlemmer *et al.*[87]

excited vibrational level.[87] For the rotational pumping the transition rate is set at a level sufficient to achieve saturation – generally above 10^3 s^{-1}.

When applied to the $C_2H_2^+$ ion, the coupled differential equations can be simplified; no pure rotational transitions ($\Delta v_5 = 0$) can occur as $\mu_0 = 0$. The rate of BBR-mediated population redistribution in $C_2H_2^+$ is thus dependent on: the line strength of the rovibrational transition; the vibrational transition dipole moment $\langle v_5 = 0|\boldsymbol{\mu}|v_5 = 1\rangle$; the energy difference between the states; and the blackbody temperature.

The BBR spectral function is shown at a range of temperatures in figure 3.2, overlaid with the calculated $C_2H_2^+$ stick spectrum at 300 K. The peak in the 300 K BBR spectrum is almost coincident with the peak in the calculated $v_5 = 0 \rightarrow v_5 = 1$ spectrum. As such, the BBR-mediated decay of state-selected population is expected to be rapid at 300 K. At lower blackbody temperatures ($T < 100$ K) this spectral overlap diminishes significantly,

Table 3.3: Lifetimes of selected $C_2H_2^+$ quantum states at 300 K and 77 K.

State	lifetime (s)	
	300 K	77 K
$\|v_5 = 0,^2\,\Pi_{3/2}, J = 3/2^+\rangle$	3.1	$>$ 10 hours
$\|v_5 = 0,^2\,\Pi_{3/2}, J = 3/2^-\rangle$	2.7	$>$ 10 hours
$\|v_5 = 0,^2\,\Pi_{1/2}, J = 1/2^+\rangle$	2.9	$>$ 10 hours
$\|v_5 = 0,^2\,\Pi_{1/2}, J = 1/2^-\rangle$	2.9	$>$ 10 hours
$\|v_5 = 1,^2\,\Delta_{5/2}, J = 5/2^+\rangle$	0.192	0.199
$\|v_5 = 1,^2\,\Delta_{5/2}, J = 5/2^-\rangle$	0.192	0.199
$\|v_5 = 1,^2\,\Delta_{3/2}, J = 3/2^+\rangle$	0.193	0.199
$\|v_5 = 1,^2\,\Delta_{3/2}, J = 3/2^-\rangle$	0.193	0.199
$\|v_5 = 1,^2\,\Sigma^-, J = 1/2^+\rangle$	0.109	0.114
$\|v_5 = 1,^2\,\Sigma^+, J = 1/2^-\rangle$	0.082	0.085

with the lifetimes of state-selected ions increasing accordingly.

The calculated decay of an initially quantum-state selected sample of $C_2H_2^+$ ions in the rotational ground states of the two spin-orbit components of the $v_5 = 0$ electronic ground state ($|v_5 = 0,^2\,\Pi_{3/2}, J = 3/2\rangle$ and $|v_5 = 0,^2\,\Pi_{1/2}, J = 1/2\rangle$) at 300 K is shown in figure 3.5. A Boltzmann distribution is reached within a few hundred seconds. The lifetimes of selected levels are presented in table 3.3, with the two rotational ground states exhibiting lifetimes on the order of 3 seconds at 300 K. The lifetime of an ion in the $|v_5 = 1,^2\,\Delta_{5/2}, J = 5/2\rangle$ level has been experimentally measured to be 200 ms at 90 K,[87] in quantitative agreement with my calculated value of 199 ms at 90 K, further validating my computational procedure.

Rotational population redistribution in the ground vibronic state is mediated by BBR-induced excitation to the $v_5 = 1$ manifold and emission back to the ground state. As such, the lifetimes of the lowest rotational states in $v_5 = 0$ increase with decreasing temperature. This relationship between temperature and the lifetime of ions in the $|v_5 = 0,^2\,\Pi_{3/2}, J = 3/2\rangle$ state is clearly demonstrated in figure 3.6. At 77 K, the population is almost frozen into the selected state, with lifetimes of several hours predicted for the $|v_5 = 0,^2\,\Pi_{3/2}, J = 3/2\rangle$ and $|v_5 = 0,^2\,\Pi_{1/2}, J = 1/2\rangle$ levels.

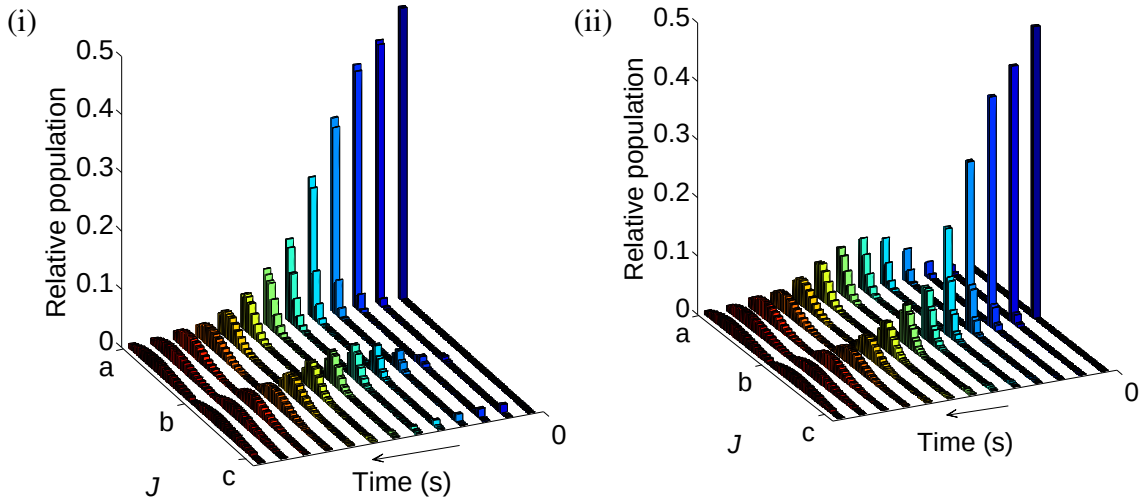

Figure 3.5: Interaction of $C_2H_2^+$ with BBR at 300 K, with the resulting decay of population initially prepared in (i) $^2\Pi_{3/2}$ J = 3/2 or (ii) $^2\Pi_{1/2}$ J = 1/2 shown as a function of time (0 s, 0.5 s, 1 s, 2.5 s, 5 s, 10 s, 15 s, 25 s, 50 s, 100 s, 125 s, 250 s and 500 s, with the time axis plotted right to left). The labels on the J axis are a: $v_5 = 0,^2\Pi_{3/2}, J$; b: $v_5 = 0,^2\Pi_{1/2}, J$; and c: $v_5 = 1,^2\Delta_{5/2}, J$.

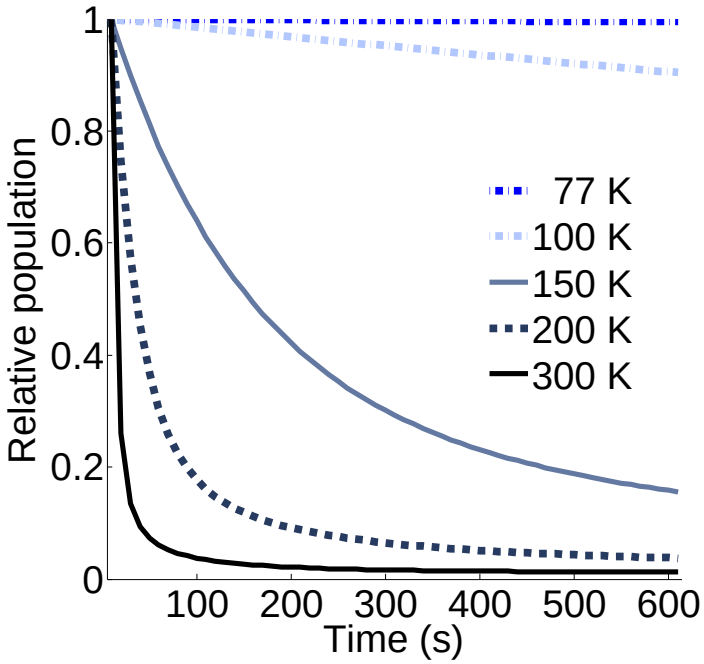

Figure 3.6: Decay of population initially prepared in the $v_5 = 0$, $^2\Pi_{3/2}$, J = 3/2 state at a series of temperatures, ranging from 77 to 300 K.

3.3 BBR-assisted laser cooling schemes

I have investigated several potential rotational cooling schemes for the $C_2H_2^+$ system. The presentation of these below follows a logical development: schemes found to be most effective in diatomic systems are initially explored in Section 3.3.1, with the effect of pumping P or Q branches and exciting multiple lines subsequently considered. In Section 3.3.2, experimentally feasible cooling schemes are detailed, culminating in the proposal of an efficient four-laser strategy yielding a $^2\Pi_{3/2}, J = 3/2$ rovibrational ground state population in excess of 70% at 300 K. Finally, the role of blackbody temperature is examined in Section 3.3.3, with the effects of conducting experiments in a 77 K environment discussed – it is shown that combining cooling to 77 K with the four-laser strategy provides the most generally efficient scheme.

3.3.1 Rotational cooling schemes at 300 K using narrow band laser excitation

The $C_2H_2^+$ energy level landscape is complex, particularly when compared with the simple energy level schemes of diatomic species. In the diatomic systems previously studied in my work, BBR-mediated redistribution via pure rotational transitions following the laser-driven excitation of a single vibrational transition yielded rovibrational ground state populations ranging from 34.3% (for CsH) to $> 99\%$ (in HCl^+).[66] In contrast, for the $C_2H_2^+$ system, the effect of a using a single narrow band laser to pump one rotational line is found to be negligible. As table 3.4 and figure 3.7 illustrate, the excitation of at least 5 transitions is required to accumulate a population of $\sim 30\%$ in the $^2\Pi_{3/2}$ rovibrational ground state. The population that can be accrued in $^2\Pi_{3/2}, J = 3/2$ saturates at approximately 40% when 10 or more $|v_5 = 0,^2\Pi_{3/2}\rangle \rightarrow |v_5 = 1,^2\Delta_{5/2}\rangle$ Q-branch transitions (or alternatively one Q-branch transition with 9 P-branch lines, as in figure 7) are excited concurrently. If the equivalent transitions are simultaneously excited from the $^2\Pi_{1/2}$ state (to the v_5=1, $^2\Delta_{3/2}$ excited state), up to 38% of the total population can be driven into the $^2\Pi_{1/2}, J = 1/2$ rotational ground state, with minimal interference to the population collected in the

$^2\Pi_{3/2}, J = 3/2$ level. In this idealized scenario, where 16 or more individual lines are excited, I calculate that $> 76\%$ of total population can be driven into the two rovibrational ground states ($^2\Pi_{3/2}, J = 3/2$ and $^2\Pi_{1/2}, J = 1/2$).

Schemes comprised exclusively of P-branch transitions were found to be most efficient in my study of diatomics.[66] In contrast, the most efficient rotational cooling schemes in $C_2H_2^+$ require at least one Q-branch transition. The main reason for this is the inability to use P-branch lines to directly address population in the $^2\Pi_{1/2}, J = 3/2$ and $^2\Pi_{3/2}, J = 5/2$ first excited rotational states; there are no P-branch transitions to the $^2\Delta$ manifold addressing population in the $^2\Pi_{1/2}, J = 3/2$ state, and the only P-branch transition from the $^2\Pi_{3/2}, J = 5/2$ level is very weak. As such, the excitation of at least one Q-branch transition is required to prevent population from accumulating in the $^2\Pi_{1/2}, J = 3/2$ and $^2\Pi_{3/2}, J = 5/2$ levels. When the appropriate Q-branch line exciting out of these states is combined with a series of P-branch transitions, appreciable population can be accumulated into the rovibrational ground states, as indicated in figure 3.7.

Schemes using only Q-branch lines are efficient in this molecule. There are no appreciable Q-branch transitions out of the rovibrational ground states: the $|v_5 = 0,^2\Pi_{3/2} J = 3/2\rangle \rightarrow |v_5 = 1,^2\Delta_{3/2} J = 3/2\rangle$ transition is very weak (as it is spin-forbidden) and the lowest J levels in the $^2\Delta_{5/2}$ and $^2\Delta_{3/2}$ states are $J = 5/2$ and $J = 3/2$, respectively, thus no possible Q-branch transitions exist from $^2\Pi_{3/2}, J = 3/2$ and $^2\Pi_{1/2}, J = 1/2$, respectively. As a result, population can accumulate in the $^2\Pi_{3/2} J = 3/2$ and $^2\Pi_{1/2} J = 1/2$ rovibrational ground states, even when pumping only Q-branch lines. In addition, the rotational line strength for the Q-branch transitions in a $^2\Pi$ - $^2\Delta$ system is relatively strong compared to P- or R-branches.

Overall, there is no appreciable difference in the cooling efficiency achieved by exciting a series of (predominantly) P-branch transitions and a single Q-branch line, compared with when exciting the same number of (exclusively) Q-branch transitions. However, one practical advantage of exciting only Q-branch lines in this system is the close energy spacing of sequential transitions. A fairly modest bandwidth laser – with a linewidth of, for example,

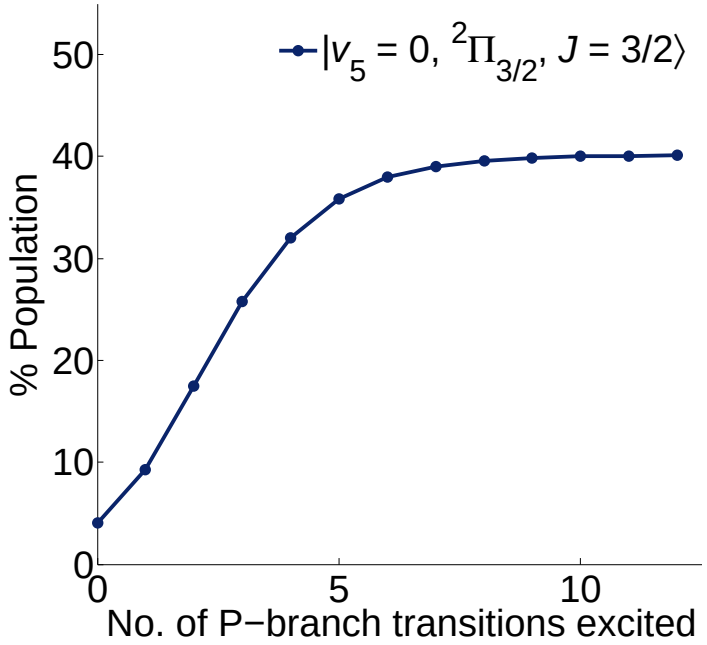

Figure 3.7: The increase in the population of $|v_5 = 0,^2\Pi_{3/2}, J = 3/2\rangle$ is presented at 300 K as the number of laser excited P-branch transitions is increased. In all instances the first Q-branch transition, $|v_5 = 0,^2\Pi_{3/2}, J = 5/2\rangle \rightarrow |v_5 = 1,^2\Delta_{5/2}, J = 5/2\rangle$, is also excited. The x-axis label '0' indicates that no P-branch lines are excited (i.e. only the one Q-branch transition is excited).

0.4 cm^{-1} – could drive multiple Q-branch lines with very little interference from undesirable transitions to other states. Some possible experimental cooling schemes for $C_2H_2^+$, exploiting this proximity of Q-branch transitions, are detailed below.

Enhanced quantum-state selectivity can be achieved through the additional excitation of transitions to the $^2\Sigma$ states. Direct transfer of population between the $^2\Pi_{3/2}$ and $^2\Pi_{1/2}$ states is forbidden, but this transfer can be achieved through the involvement of the $^2\Sigma^-$ or $^2\Sigma^+$ states, as indicated in figure 3.8. With the excitation of the $|v_5 = 0,^2\Pi_{1/2}, J = 1/2^+\rangle \rightarrow |v_5 = 1,^2\Sigma^+, J = 1/2^-, N = 1\rangle$ and $|v_5 = 0,^2\Pi_{1/2}, J = 1/2^-\rangle \rightarrow |v_5 = 1,^2\Sigma^+, J = 1/2^+, N = 0\rangle$ lines, in addition to the series of Q-branch transitions set out in table 3.4, 71.5% of total population can be driven into the $^2\Pi_{3/2}, J = 3/2$ rovibrational ground state. Exciting the most effective $^2\Sigma^-$ transitions from the $^2\Pi_{3/2}$ state, as set out in table 3.5, yields a population of 63.6% in the $^2\Pi_{1/2}, J = 1/2$ upper spin-orbit component of the ground state at 300 K.

Table 3.4: The effect of adding multiple pumping transitions at 300 K. Within each scheme, additional lines are cumulatively excited to yield the populations indicated. For example, in row 3 of scheme 1, the Q-branch transitions $|0,^2\,\Pi_{3/2},5/2\rangle \rightarrow |1,^2\,\Delta_{5/2},5/2\rangle$, $|0,^2\,\Pi_{3/2},7/2\rangle \rightarrow |1,^2\,\Delta_{5/2},7/2\rangle$ and $|0,^2\,\Pi_{3/2},9/2\rangle \rightarrow |1,^2\,\Delta_{5/2},9/2\rangle$ are all simultaneously excited.

No.	Pump Transition(s)	% Cumulative Population			
		at 300 K		at 77 K	
		$\lvert 0,^2\,\Pi_{3/2},3/2\rangle$	$\lvert 0,^2\,\Pi_{1/2},1/2\rangle$	$\lvert 0,^2\,\Pi_{3/2},3/2\rangle$	$\lvert 0,^2\,\Pi_{1/2},1/2\rangle$
1	$\lvert 0,^2\,\Pi_{3/2},5/2\rangle \rightarrow \lvert 1,^2\,\Delta_{5/2},5/2\rangle$	4.05	0.97	19.6	2.88
	$+\lvert 0,^2\,\Pi_{3/2},7/2\rangle \rightarrow \lvert 1,^2\,\Delta_{5/2},7/2\rangle$	9.25	2.01	39.11	5.32
	$+\lvert 0,^2\,\Pi_{3/2},9/2\rangle \rightarrow \lvert 1,^2\,\Delta_{5/2},9/2\rangle$	15.90	3.38	51.56	6.93
	$+\lvert 0,^2\,\Pi_{3/2},11/2\rangle \rightarrow \lvert 1,^2\,\Delta_{5/2},11/2\rangle$	22.87	4.83	58.14	7.79
	$+\lvert 0,^2\,\Pi_{3/2},13/2\rangle \rightarrow \lvert 1,^2\,\Delta_{5/2},13/2\rangle$	28.82	6.08	61.03	8.18
	$+\lvert 0,^2\,\Pi_{3/2},15/2\rangle \rightarrow \lvert 1,^2\,\Delta_{5/2},15/2\rangle$	33.17	6.99	62.39	8.35
	$+\lvert 0,^2\,\Pi_{3/2},17/2\rangle \rightarrow \lvert 1,^2\,\Delta_{5/2},17/2\rangle$	36.00	7.59	62.96	8.43
	$+\lvert 0,^2\,\Pi_{3/2},19/2\rangle \rightarrow \lvert 1,^2\,\Delta_{5/2},19/2\rangle$	37.76	7.96	63.23	8.47
	$+\lvert 0,^2\,\Pi_{3/2},21/2\rangle \rightarrow \lvert 1,^2\,\Delta_{5/2},21/2\rangle$	38.79	8.18	63.35	8.48
	$+\lvert 0,^2\,\Pi_{3/2},23/2\rangle \rightarrow \lvert 1,^2\,\Delta_{5/2},23/2\rangle$	39.40	8.31	63.41	8.49
		⋮			
	$+\lvert 0,^2\,\Pi_{3/2},39/2\rangle \rightarrow \lvert 1,^2\,\Delta_{5/2},39/2\rangle$	40.23	8.48	63.46	8.49
2	All the transitions of scheme 1				
	$+\lvert 0,^2\,\Pi_{1/2},3/2\rangle \rightarrow \lvert 1,^2\,\Delta_{3/2},3/2\rangle$	38.95	21.79	60.70	23.64
	$+\lvert 0,^2\,\Pi_{1/2},5/2\rangle \rightarrow \lvert 1,^2\,\Delta_{3/2},5/2\rangle$	38.26	31.47	58.39	35.59
	$+\lvert 0,^2\,\Pi_{1/2},7/2\rangle \rightarrow \lvert 1,^2\,\Delta_{3/2},7/2\rangle$	38.11	35.36	58.68	39.99
	$+\lvert 0,^2\,\Pi_{1/2},9/2\rangle \rightarrow \lvert 1,^2\,\Delta_{3/2},9/2\rangle$	38.10	36.84	57.43	41.50
	$+\lvert 0,^2\,\Pi_{1/2},11/2\rangle \rightarrow \lvert 1,^2\,\Delta_{3/2},11/2\rangle$	38.13	37.46	57.34	42.16
	$+\lvert 0,^2\,\Pi_{1/2},13/2\rangle \rightarrow \lvert 1,^2\,\Delta_{3/2},13/2\rangle$	38.16	37.74	57.30	42.43
	$+\lvert 0,^2\,\Pi_{1/2},15/2\rangle \rightarrow \lvert 1,^2\,\Delta_{3/2},15/2\rangle$	38.19	37.88	57.29	42.57
	$+\lvert 0,^2\,\Pi_{1/2},17/2\rangle \rightarrow \lvert 1,^2\,\Delta_{3/2},17/2\rangle$	38.21	37.95	57.28	42.64
	$+\lvert 0,^2\,\Pi_{1/2},19/2\rangle \rightarrow \lvert 1,^2\,\Delta_{3/2},19/2\rangle$	38.22	37.98	57.28	42.68
	$+\lvert 0,^2\,\Pi_{1/2},21/2\rangle \rightarrow \lvert 1,^2\,\Delta_{3/2},21/2\rangle$	38.23	38.00	57.28	42.70
		⋮			
	$+\lvert 0,^2\,\Pi_{1/2},37/2\rangle \rightarrow \lvert 1,^2\,\Delta_{3/2},37/2\rangle$	38.24	38.03	57.27	42.72

Table 3.5: Optimized laser pumping schemes at 300 K and 77 K.

No.	Transition(s)	% Population at 300 K		% Population at 77 K	
		$\|0,^2\Pi_{3/2},3/2\rangle$	$\|0,^2\Pi_{1/2},1/2\rangle$	$\|0,^2\Pi_{3/2},3/2\rangle$	$\|0,^2\Pi_{1/2},1/2\rangle$
3	all the transitions of schemes 1 and 2 (in table 3.4) $+\|0,^2\Pi_{1/2},1/2^+\rangle \rightarrow \|1,^2\Sigma^+,1/2^-,1\rangle$ $+\|0,^2\Pi_{1/2},1/2^-\rangle \rightarrow \|1,^2\Sigma^+,1/2^+,0\rangle$	71.52	1.57	99.99	0.0001
4	all the transitions of schemes 1 and 2 (in table 3.4) $+\|0,^2\Pi_{3/2},3/2^+\rangle \rightarrow \|1,^2\Sigma^-,3/2^-,2\rangle$ $+\|0,^2\Pi_{3/2},3/2^-\rangle \rightarrow \|1,^2\Sigma^-,5/2^+,3\rangle$	1.65	63.64	0.0002	99.99

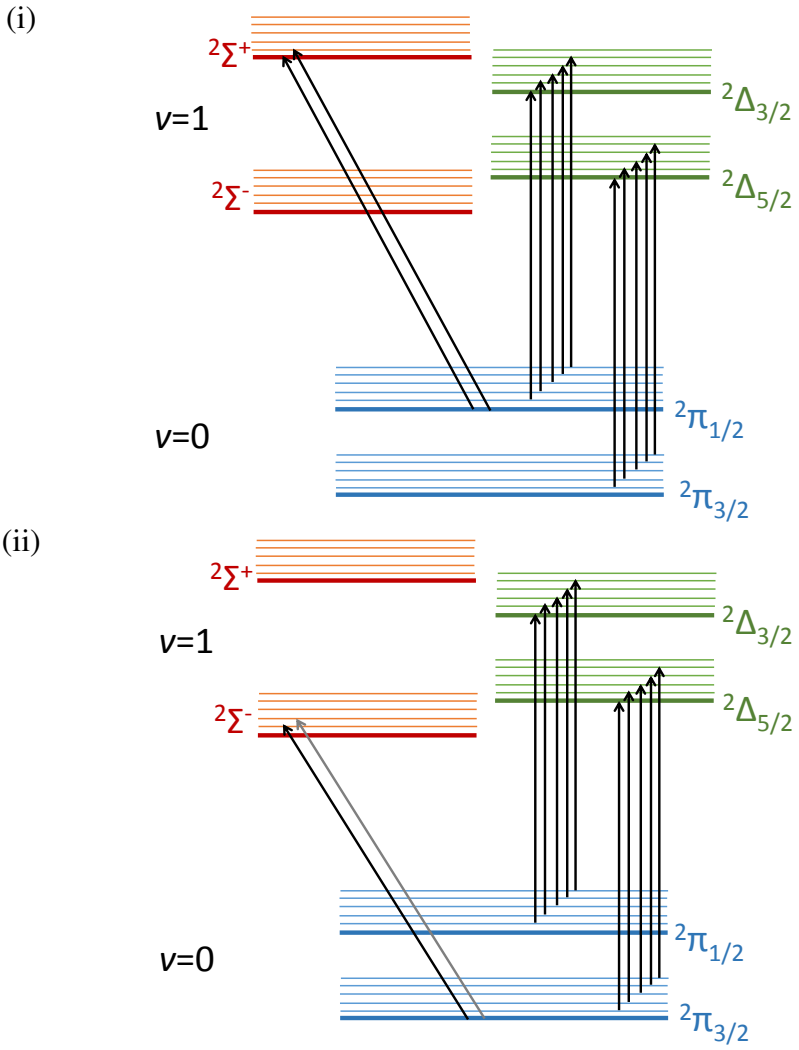

Figure 3.8: The most efficient BBR-assisted laser cooling schemes in $C_2H_2^+$: (i) the best transitions to pump the population to $|v_5 = 0, ^2\Pi_{3/2}, J = 3/2\rangle$, and (ii) the best transitions to pump the population to $|v_5 = 0, ^2\Pi_{1/2}, J = 1/2\rangle$. Energy levels are laterally translated for the sake of clarity.

3.3.2 Viability of implementing the cooling schemes at 300 K experimentally

The cooling schemes set out in tables 3.4 and 3.5, to achieve 71.5% population in the ground rotational level, require up to 38 separate narrow-bandwidth laser sources, which would be experimentally impractical. As indicated in table 3.6, in order to accrue populations $> 50\%$ in either of the $^2\Pi$ rovibrational ground states at least 12 lines must be explicitly excited: five $^2\Pi_{3/2}$ to $^2\Delta_{5/2}$ transitions, five $^2\Pi_{1/2}$ to $^2\Delta_{3/2}$ transitions and two additional $^2\Pi$ to $^2\Sigma$ lines. Even then, it is unrealistic to propose a cooling scheme requir-

ing so many laser sources for most experimental applications. I have thus investigated a more experimentally viable alternative, whereby multiple Q-branch transitions are excited with a single broadband laser source. As set out in table 3.7, a single laser with a 0.4, 0.75, 1.5 or 2 cm^{-1} bandwidth (centered at an appropriate wavelength) can lead to accumulation $\geq 41.76\%$ of population in the $^2\Pi_{3/2}, J = 3/2$ ground state. It is assumed in these calculations that all the transitions falling within a given bandwidth are exposed to the same spectral density. Similarly, a single laser with a bandwidth of 3 cm^{-1} spanning 704.75 – 707.75 cm^{-1} yields a population of 40.12% in the $^2\Pi_{1/2}, J = 1/2$ ground state. The proposed broadband laser excitation schemes exploit the close energetic spacing of sequential Q-branch transitions to excite multiple transitions. For example, the first nineteen $|v_5 = 0,^2\Pi_{3/2}\rangle \rightarrow |v_5 = 1,^2\Delta_{5/2}\rangle$ Q-branch transitions lie within 0.4 cm^{-1}. The power required for this broad band laser to saturate the transitions is on the order of 1 – 10 mW across the bandwidth.

With two broadband lasers centred at 706.0 cm^{-1} and 707.3 cm^{-1}, populations of 41.7% and 36.2% can be built up in each of the $^2\Pi_{3/2}$ and $^2\Pi_{1/2}$ rovibrational ground states (respectively), as presented in table 3.8. Adding two narrowband laser sources exciting selected $^2\Pi \rightarrow ^2\Sigma$ lines, as identified in tables 3.5 and 3.8, is predicted to yield a population in excess of 73% in $^2\Pi_{3/2}, J = 3/2$ or 53.4% in $^2\Pi_{1/2}, J = 1/2$. The driving of population into the $^2\Pi_{3/2}, J = 3/2$ state is extremely efficient with the broadband excitation scheme set out in table 3.8, predominantly due to the absence of any undesirable transitions falling within the 705.80 – 706.20 cm^{-1} window. While the scheme designed to drive population into the $^2\Pi_{1/2}, J = 1/2$ state is also effective, it yields $\sim 10\%$ less population than that achieved with the idealized scheme set out in table 3.5. This can be attributed to the presence of four undesirable transitions falling within the 707.00 – 707.60 cm^{-1} excitation range, resulting in the inadvertent excitation of the $|^2\Pi_{3/2}, J = 29/2^-\rangle \rightarrow |^2\Sigma^-, J = 29/2^+\rangle$, $|^2\Pi_{1/2}, J = 7/2^-\rangle \rightarrow |^2\Sigma^+, J = 5/2^+\rangle$, $|^2\Pi_{1/2}, J = 11/2^+\rangle \rightarrow |^2\Sigma^+, J = 9/2^-\rangle$ and $|^2\Pi_{1/2}, J = 27/2^-\rangle \rightarrow |^2\Sigma^+, J = 27/2^+\rangle$ lines.

These schemes suggest that BBR-mediated rotational cooling in $C_2H_2^+$ is both poten-

Table 3.6: Investigation of the number of Q-branch transitions required to pump the population towards $|v_5 = 0,^2\Pi_{3/2}, J = 3/2\rangle$ from a 300 K sample of $C_2H_2^+$. The number of transitions shown represents the sum of the transitions exciting out of $^2\Pi_{1/2}$ and $^2\Pi_{3/2}$ (for example, the 36 transitions comprise eighteen $^2\Pi_{1/2} \rightarrow {}^2\Delta_{3/2}$ Q-branch lines and eighteen $^2\Pi_{3/2} \rightarrow^2 \Delta_{5/2}$ Q-branch lines). Two further $^2\Pi \rightarrow {}^2\Sigma$ transitions are employed (in addition to the Q-branch transitions), as indicated in the table.

No of	% Population at 300 K			
Q-branch lines	$\|0,^2\Pi_{1/2}, \frac{1}{2}^+\rangle \rightarrow \|1,^2\Sigma^+, \frac{1}{2}^-, N=1\rangle$ $\|0,^2\Pi_{1/2}, \frac{1}{2}^-\rangle \rightarrow \|1,^2\Sigma^+, \frac{1}{2}^+, N=0\rangle$ also excited		$\|0,^2\Pi_{3/2}, \frac{3}{2}^+\rangle \rightarrow \|1,^2\Sigma^-, \frac{3}{2}^-, N=2\rangle$ $\|0,^2\Pi_{3/2}, \frac{3}{2}^-\rangle \rightarrow \|1,^2\Sigma^-, \frac{5}{2}^+, N=3\rangle$ also excited	
excited	$\|0,^2\Pi_{3/2}, 3/2\rangle$	$\|0,^2\Pi_{1/2}, 1/2\rangle$	$\|0,^2\Pi_{3/2}, 3/2\rangle$	$\|0,^2\Pi_{1/2}, 1/2\rangle$
36	71.52	1.58	1.65	63.64
24	71.40	1.57	1.65	63.47
20	71.10	1.56	1.64	63.05
16	70.09	1.54	1.60	61.64
10	61.85	1.36	1.34	51.09
6	38.42	0.82	0.74	27.37

tially achievable experimentally, and exceptionally effective at 300 K, despite the complex energy level structure of this ion.

3.3.3 Rotational cooling at 77 K

The cooling schemes explored thus far assume a blackbody temperature of 300 K. Under such conditions, BBR-mediated redistribution is rapid; from an initially state-selected

Table 3.7: Population that can be accumulated in the $^2\Pi$ rotational ground states at 300 K and 77 K using broadband laser systems.

Width	Range	% Population in $v_5 = 0$ at 300 K		% Population in $v_5 = 0$ at 77 K	
cm^{-1}	cm^{-1}	$\|^2\Pi_{3/2} J = 3/2\rangle$	$\|^2\Pi_{1/2} J = 1/2\rangle$	$\|^2\Pi_{3/2} J = 3/2\rangle$	$\|^2\Pi_{1/2} J = 1/2\rangle$
0.40	705.80-706.28	41.88	9.14	64.03	8.66
0.75	705.75-706.50	41.86	9.13	64.78	6.08
1.0	705.50-706.50	41.40	9.02	61.34	5.70
1.5	704.75-706.25	41.77	9.10	62.69	5.84
2.0	704.55-706.55	41.76	9.10	61.92	5.77
3.0	704.75-707.75	32.09	40.12	51.54	48.46
4.0	705.0-709.0	32.06	40.01	51.55	48.45
10.0	699.5-709.5	0.84	25.86	0.0	99.98

Table 3.8: The effect of using multiple lasers of different bandwidths.

Laser systems	% Population in $v_5 = 0$ at 300 K		% Population in $v_5 = 0$ at 77 K	
cm^{-1}	$\|^2\Pi_{3/2}, J = 3/2\rangle$	$\|^2\Pi_{1/2}, J = 1/2\rangle$	$\|^2\Pi_{3/2}, J = 3/2\rangle$	$\|^2\Pi_{1/2}, J = 1/2\rangle$
705.800–706.200 707.000–707.600	41.73	36.15	67.44	32.45
705.800–706.200 707.000–707.600 $\|0,^2\Pi_{1/2}, \frac{1}{2}^+\rangle \rightarrow \|1,^2\Sigma^+, \frac{1}{2}^-, 1\rangle$ $\|0,^2\Pi_{1/2}, \frac{1}{2}^-\rangle \rightarrow \|1,^2\Sigma^+, \frac{1}{2}^+, 0\rangle$	73.27	1.54	99.89	0.00
705.800–706.200 707.000–707.600 $\|0,^2\Pi_{3/2}, \frac{3}{2}^+\rangle \rightarrow \|1,^2\Sigma^-, \frac{3}{2}^-, 2\rangle$ $\|0,^2\Pi_{3/2}, \frac{3}{2}^-\rangle \rightarrow \|1,^2\Sigma^-, \frac{5}{2}^+, 3\rangle$	7.143	53.42	0.0	99.88

sample (with population exclusively in the $^2\Pi_{3/2}, J = 3/2$ rovibrational ground state), a Boltzmann distribution is attained within 500 seconds. In contrast, a similarly state-selected sample at 77 K will take over 83 hours to reach a Boltzmann distribution, attributable to the weaker overlap between the BBR spectral function and the energy of the $v_5 = 0 \rightarrow v_5 = 1$ transition.

Tables 3.4, 3.5, 3.7 and 3.8, suggest that laser-driven rotational cooling is more effective at accumulating population in the desired $^2\Pi$ rovibrational ground state at 77 K. For example, the optimal scheme set out in table 3.5 indicates that a population of $> 99.9\%$ could be accrued in the $^2\Pi_{3/2}, J = 3/2$ level at 77 K, compared with 71.5% at 300 K. However, without the aid of BBR to assist the redistribution of this population, the cooling process can be many orders of magnitude slower at 77 K. Consider the cooling scheme in table 3.6, where 16 Q-branch transitions are explicitly excited, yielding a population of 70.1% in the $^2\Pi_{3/2}, J = 3/2$ state at 300 K, attained within 2000 seconds. Utilizing the same laser cooling scheme at 77 K can result in a final population $> 99.7\%$. However, it would take in excess of 1000 hours for a population of 99.7% to be accumulated. Nevertheless, a population of 81.4% is built up at 77 K within 2000 s; the same time required for the fully equilibrated laser-cooled populations to be reached at 300 K.

Closer examination of the thermal rotational distribution at 77 K can account for the apparent disparity in these timescales. At 77 K, 58.8% of population is distributed amongst the first nine J states of the $^2\Pi_{3/2}$ manifold, with a further 28.4% in the first nine J levels of the $^2\Pi_{3/2}$ manifold: 87.2% of total population is thus either already in the $^2\Pi_{3/2}, J = 3/2$ state or is directly laser-excited by the scheme in table 3.6 where 16 Q-branch lines are explicitly addressed. Most of this directly excited population is rapidly driven into the ground rovibrational state, with the remaining $\sim 27\%$ of total population reliant on almost non-existent BBR-mediated redistribution. BBR redistribution at 77 K is so inefficient that accumulating the final $\sim 27\%$ of population into $^2\Pi_{3/2}, J = 3/2$ takes over 1000 hours. These calculations demonstrate the importance of BBR in rotational cooling schemes where only a finite fraction of the total population is directly laser-excited.

Interestingly, BBR-mediated redistribution is no longer required at 77 K when utilizing broadband excitation sources for rotational cooling in $C_2H_2^+$. Within the energy ranges 705.80 – 706.20 cm^{-1} and 707.00 – 707.60 cm^{-1}, more than 19 Q-branch transitions are directly excited from each of the $^2\Pi_{3/2}$ and $^2\Pi_{1/2}$ vibrational ground states. As such, at 77 K effectively all the population is directly laser-driven into the selected rovibrational ground state; 99.8% of population can be accumulated in either $^2\Pi_{3/2}, J = 3/2$ or $^2\Pi_{1/2}, J = 1/2$ within 120 seconds.

As table 3.3 illustrates, the $C_2H_2^+$ rovibrational ground states are so long lived at 77 K that an initially state-selected sample will remain state selected on the timescale of any experiments conducted. Consequently, if quantum state-selection could be achieved directly (through techniques such as REMPI or threshold ionization) it would be maintained without the need for laser-driven rotational cooling. Should one wish to start from a 77 K thermal distribution, then the rotational cooling schemes outlined in table 3.8 could drive $> 99.8\%$ of total population into either the $^2\Pi_{3/2}, J = 3/2$ or $^2\Pi_{1/2}, J = 1/2$ levels within 120 seconds.

3.4 Comments on other polyatomics: CO_2^+

The rotational cooling schemes outlined above for the acetylene ion can be extended to other linear polyatomics. For example, CO_2^+ is a linear, centro-symmetric ion with a $^2\Pi$ ground electronic state and a zero net dipole moment. As with the acetylene ion, CO_2^+ will have no rotational transitions within the ground vibrational state. Of the four vibrational degrees of freedom in this molecule, three are IR active: the doubly degenerate ν_2 bending mode (Π_u, $\omega_2 \simeq 513$ cm^{-1}),[92] and the ν_3 asymmetric stretch mode (Σ_u^+, $\omega_3 \simeq 1423$ cm^{-1}).[93] As such, BBR-mediated redistribution can occur via excitation of the ν_2 or ν_3 vibrational modes.

The ν_2 mode in CO_2^+ behaves in a similar way to the ν_5 mode of $C_2H_2^+$, insofar as $v_2 = 1$ is split into $^2\Delta$, $^2\Sigma^-$ and $^2\Sigma^+$ components by the Renner-Teller interaction. The $^2\Delta$ state is further split into $^2\Delta_{5/2}$ and $^2\Delta_{3/2}$ states as a result of spin orbit interactions. Spin orbit

coupling splits $v = 0$ into $^2\Pi_{3/2}$ and $^2\Pi_{1/2}$ components and also splits the ν_3 mode into two. As in $C_2H_2^+$, CO_2^+ has a negative spin-orbit constant ($A = -159.5\text{cm}^{-1}$),[94] yielding an inverted doublet ground state.

The complex splitting exhibited by the ν_2 mode results in an extended and congested vibrational spectrum, extending from $\sim$ 467 cm^{-1} ($^2\Sigma$, lower) to well beyond 700 cm^{-1} ($^2\Sigma$, upper). As with $C_2H_2^+$, the CO_2^+ bending mode overlaps very well with the BBR spectral function, implying that the rate of decay through the ν_2 vibrational mode would be rapid. Again similar to the $C_2H_2^+$ system, the overlap of the blackbody spectrum with the ν_2 vibrational mode will be very poor at temperatures $<$ 100 K.

The primary difference between CO_2^+ and $C_2H_2^+$ is the addition of an extra source of vibrational interaction: the ν_3 mode. This state is less complex than the ν_2 mode and exhibits a significantly higher vibrational frequency, but would still fall within the BBR spectral range at 300 K and thus would need to be incorporated into any theoretical modeling of rotational cooling in the CO_2^+ system. The effects of nuclear spin statistics would also need to be considered for CO_2^+ given that one half of the rotational levels do not exist (those for which the wavefunction is antisymmetric). In $C_2H_2^+$ there are actually two independent but almost degenerate radiative cycling processes, pumped by the scheme described, one of which is for the ortho spin states and one for the para states. For the $\Pi - \Delta$ bands each transition is doubly degenerate (one ortho, one para), while for the $\Pi - \Sigma$ bands two of the four transitions in Table 3.5 are ortho and two para. In CO_2^+ one of these two radiative cycles is absent but otherwise the arguments for $C_2H_2^+$ still apply. The ratio A/B is ~ -419.6 in CO_2^+, compared with -27.98 in $C_2H_2^+$, and as such, CO_2^+ would have more Hund's case (a) type character than $C_2H_2^+$, while still being classed as an intermediate case. Also noteworthy is the rotational constant in CO_2^+, which at $B = 0.38$ cm^{-1} is even smaller than that of $C_2H_2^+$.[94] The spacing between successive rotational lines in the Q branch will thus be very small in CO_2^+, with implications for the spread of rotational population (beyond the first 20 J levels, as was seen in $C_2H_2^+$ at 300 K) and also on possible experimental rotational cooling schemes employing broadband lasers.

3.5 Conclusion

In conclusion, this work has demonstrated the very different behavior of non-polar polyatomic ions in comparison with diatomic molecules and the key role played by low-frequency vibrations in facilitating black-body radiation induced population transfer. The complexity associated with the Renner-Teller effect and spin-orbit coupling in a linear polyatomic in a $^2\Pi$ ground electronic state is illustrated here; this is just one example of the complex vibrational and vibronic interactions that may take place in polyatomic molecules. My calculations show that good use can be made of the vibrational band systems available to devise pumping schemes that could lead to excellent control of the rotational population – the need to use a large number of laser frequencies could be overcome by using a moderately broadband source that overlaps multiple Q-branch transitions without interference from other transitions.

A number of laser-driven rotational cooling schemes are explored, yielding populations of up to 73.3% in the $^2\Pi_{3/2}, J = 3/2$ rovibrational ground state at 300 K. The methodology described in this work is broadly applicable to all linear polyatomic systems with no net dipole moment, including other species of astrochemical significance such as CO_2^+.

The study of low temperature ion-molecule collisions will undoubtedly benefit from the availability of schemes for producing quantum-state selected ions. For example, the reaction of $C_2H_2^+$ with ND_3 could be studied with trapped, sympathetically cooled $C_2H_2^+$ ions and state selected ND_3 from a Stark decelerator.

Chapter 4

Production and Detection of $C_2H_2^+$ in Selected Vibrational States

4.1 Introduction

The prodution of $C_2H_2^+$ in specific quantum states is crucial for studying the state-selective reaction of the acetylene cation with ND_3. In this chapter the production of $C_2H_2^+$ in selected vibrational states using appropriate (2+1) Resonance Enhanced Multiphoton Ionization (REMPI) schemes is described. We further discuss the possibility of state-selective ion detection using (1+1) Resonance Enhanced Multiphoton Dissociation (REMPD). Ultimately the aim is to use these processes in the ion-trap, but the initial study described here was carried out in a separate molecular beam chamber.

4.1.1 Principles of REMPI and REMPD spectroscopy

Coherent and simultaneous multiphoton transitions can occur if a molecule is exposed to an intense laser field where the absorption of multiple photons satisfies the resonance condition $E = nh\nu$, where n is an integer. An effcient and commonly employed technique is (2+1) REMPI, illustrated in figure 4.1. The probability of a three-photon excitation is greatly enhanced by the involvement of a real excited state in the neutral molecule. In figure 4.1, $|1\rangle$ is the ground electronic state of the neutral molecule and $|2\rangle$ is the excited state of the neutral molecule resonant with the two-photon energy, $2h\nu$. Together with the important condition of resonance for such a technique to work, it also is crucial to have a non-zero transition probablity for the transition: $|2\rangle \leftarrow |1\rangle$, and state $|2\rangle$ must be sufficiently long

lived for the subsequent one-photon ionization to be possible.

The excitation of this transition must obey several selection rules.[95] For linear molecules, $\Delta S = 0$ (spin selection rule), $+ \leftrightarrow +$ and $- \leftrightarrow -$ (parity selection rule for a two-photon transition), $\Delta\Lambda \leq n$, for n-photon excitation, and for symmetric molecules the overall transition symmetry must be $gerade$ ($ungerade$) for $n =$ even (odd). Here, S is the spin angular momentum and Λ is the projection of the electronic angular momentum onto the molecular axis.

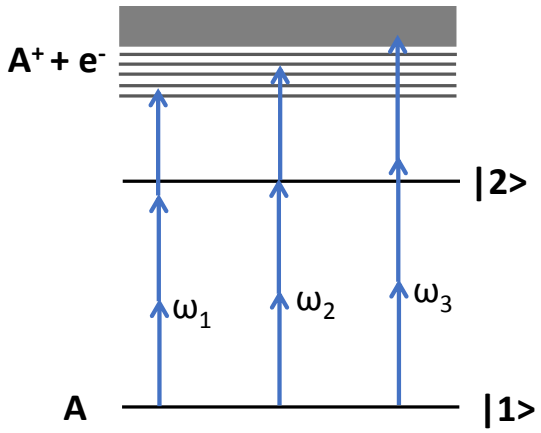

Figure 4.1: Schematic illustration of a (2+1) REMPI scheme, where the energy of two photons must be resonant with a bound excited state in the molecule. Photon ω_1 has insufficient energy and photon ω_3 has excessive energy to meet this requirement. Only the resonant photon, ω_2, ionises molecule A efficiently in this scheme.

4.1.2 REMPI of C_2H_2

Acetylene, C_2H_2, is a centrosymmetric molecule in the $D_{\infty h}$ point group with a $^1\Sigma_g^+$ electronic ground state. The $u \leftrightarrow g$ selection rule applies to excitations brought about using any odd number of photons, thus both one- and three-photon studies are only able to extract information about the *ungerade* excited states (whereas two-photon transitions excite to gerade states). In the Rydberg states, the antisymmetric acetylene core at low principal quantum number n ensures that the two-photon excitation $\pi_u^3 np_u^1 \leftarrow \pi_u^4$ gives rise to four singlet and four triplet states. *Ab initio* calculations performed by Perić and co-workers [96] show that $^1\Pi_g$ ($\pi_u^3 3p\sigma_u^1$), $^1\Delta_g$ ($\pi_u^3 3p\pi_u^1$), $^1\Sigma_g^-$ ($\pi_u^3 3p\pi_u^1$), $^1\Sigma_g^+$ and $\pi_u^3 3p\pi_u^1$ states constitute the singlet members of the "3p complex", listed in descending order of energy. These ex-

cited states are expected to have a linear geometry, but with extended C≡C bond lengths compared to the electronic ground state. Based on the above selection rules, and using a two-photon excitation scheme, it should be possible to excite transitions to any of the above mentioned states: $^1\Pi_g$, $^1\Delta_g$ and $^1\Sigma_g^+$.

The (2+1) REMPI scheme used in this work, illustrated in figure 4.2, has been previously reported [97, 98] and makes use of an intermediate vibrationless Rydberg state. It is because of the involvement of this state that the rotational substructure of the corresponding $\Delta_g - \widetilde{X}$ (or similarly the $\Sigma_g^+ - \widetilde{X}$ or $\Pi_g - \widetilde{X}$) transition cannot be resolved, due to lifetime broadening of the intermediate state. The rotational temperature distribution of the neutral ground state is reflected in the ionic ground state; the change of rotational quantum number J is small from initial to final state, thus the J distribution is largely unchanged in the ionic state. [97]

Though rotational discrimination is not possible due to the unresolved rotational structure in the excitation to the vibrationless intermediate state involved in the REMPI scheme, in principle it would be possible to populate different groups of rotational states (for example, low J or high J states) by tuning the laser to different parts of the band. It is further shown in Ashfold *et al* [97] that ions produced via this vibrationless Rydberg state yield exclusively ground state ionic species.

4.1.3 Detection of $C_2H_2^+$ by REMPD

Like the neutral acetylene molecule, $C_2H_2^+$ is linear in the ground state ($D_{\infty h}$ point group) but it has a $^2\Pi_u$ electronic ground-state configuration. The $u \leftrightarrow g$ selection rule applies to excitations brought about using any odd number of photons, as seen in the neutral species. REMPD involves the resonance-enhanced photodissociation of $C_2H_2^+$ to C_2H^+, where the C_2H^+ ion signal is monitored to ascertain the number of $C_2H_2^+$ parent ions, in different quantum states. This is a two-photon process, where the first photon resonantly excites the ion to the $\widetilde{A}(^2A_g)$ state, as depicted in figure 4.2. This state has a trans bent geometry of C_{2h} symmetry. A second photon of the same energy is then absorbed, promoting the species

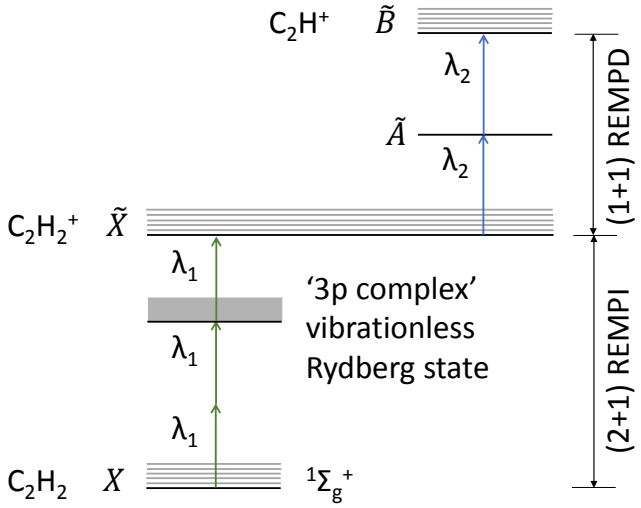

Figure 4.2: Excitation scheme for REMPI of C_2H_2 and REMPD of $C_2H_2^+$, where λ_1 is the REMPI wavelength and λ_2 is the REMPD wavelength.

into the dissociation continuum (the ionic $\widetilde{B}$ state) and yielding C_2H^+ fragment ions. The rovibrational population distribution in the $\widetilde{X}$ state of $C_2H_2^+$ is mapped onto the $\widetilde{A}$ state, thus monitoring C_2H^+ fragment ion production as a function of photon energy allows one to probe the population distribution of the ground ($\widetilde{X}$) state of $C_2H_2^+$.[98] It should also be noted that the $\widetilde{A}(^2A_g) \leftarrow \widetilde{X}(^2\Pi_u)$ excitation is complicated by the short lifetime of the $\widetilde{A}$ state (arising from non-radiative processes), resulting in lifetime broadening.[97]

4.2 Experiment

4.2.1 Experimental setup

Acetylene seeded in Ar is expanded through a pulsed valve (pulse width 10 μs) into a vacuum chamber (labelled as 'B' in figure 4.3) at an operating pressure of $1-5\times10^{-5}$ mbar. A pulse generator (Quantum+ model 9518) controls the time delays and length of each trigger sent to the pulsed valve and laser systems. The central part of the supersonic molecular beam (indicated by a dashed grey line) passes through a skimmer ('C') before entering the final vacuum chamber 'D', maintained at $\sim 4\times10^{-7}$ mbar (base pressure) by a turbo pump backed by a rotary pump. Chambers 'B' and 'D' are differetially pumped and are separated by the skimmer plate 'C'. Chamber 'D' has windows (labelled as 'E') for optical access.

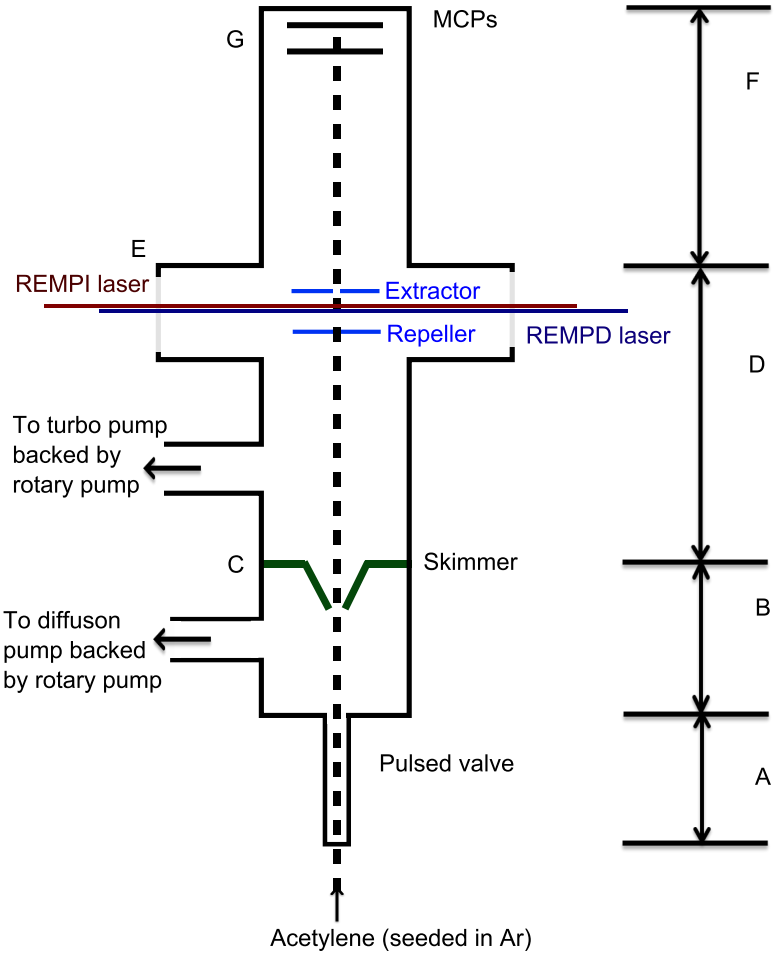

Figure 4.3: Schematic representation of the experimental apparatus used for the study of REMPI of C_2H_2 and REMPD of $C_2H_2^+$.

The laser intersects the molecular beam between the extractor-repeller plates, as shown in figure 4.3. A time of flight tube ('F') and multichannel plates (MCPs) enable mass-selective product detection. Ion current obtained from the MCPs is amplified by a custom-built boot-strap amplifier and is recorded by an oscilloscope. The MCP voltages used were: -1600 V, with a bias voltage of $+100$ V for the REMPI study and -1900 V with a $+100$ V bias for the REMPD study. The extractor and repeller plates were operated at 500 V and 2000 V, respectively.

4.2.2 Experimental procedure

4.2.2.1 Resonance Enhanced Multiphoton Ionization

(2+1) multiphoton ionization of the cold supersonic C_2H_2 molecular beam is brought about by a frequency tripled Nd:YAG pumped dye laser, the output of which is then frequency doubled by a BBO crystal. The dyes C540A and C503 were used to scan the frequency doubled ranges 262 – 276 nm and 260 – 262 nm, respectively. The laser beam is focussed by a 300 mm spherical lens onto the molecular beam, between the extractor-repeller pair as discussed in the previous section.

The resonant intermediate $^1\Delta_g$ or $^1\Sigma_g^+$ states lie at $\sim$72 753 cm^{-1} (two-photon energy) above the ground state. Ionization is brought about by the final ($\sim$36 376 cm^{-1}) one-photon excitation from this intermediate state. The rotational distribution of the neutral ground state is approximately reflected into the ionic ground state, because changes of J are relatively small.

4.2.2.2 Resonance-Enhanced Multiphoton Dissociation

$C_2H_2^+$ ions produced by REMPI can be dissociated to $C_2H^+ +$ H, as illustrated by the REMPD scheme in figure 4.2. C_2H^+ production is monitored by measuring the ion current at the MCPs as the photon energy is scanned. A frequency-tripled Nd:YAG pumped, frequency-doubled dye laser (C503 dye, BBO crystal) covers the wavelength range 235 – 270 nm with a pulse energy of 0.4 - 0.6 mJ. The dissociation laser is focused into the chamber with a 300 mm spherical lens, $\sim$2.5 mm downstream from the REMPI laser. The REMPD laser is fired a few μs after the REMPI laser, to maximise the dissociation of $C_2H_2^+$ to C_2H^+ and to reduce the probability of ionization of the neutral molecule by the REMPD laser. In the time delay of a few μs, $C_2H_2^+$ ions move downstream a few mm, thus focusing the REMPD laser a few mm downstream maximises the C_2H^+ ion current signal.

The first photon from the REMPD laser is absorbed by ground state ($\widetilde{X}$) $C_2H_2^+$ ions, taking them to the intermediate $\widetilde{A}$ state. A second photon from the same laser can then dissociate $C_2H_2^+$ to form C_2H^+ fragment ions in the ionic $\widetilde{B}$ state. The resulting ions enter

a field-free time-of-flight (TOF) tube before hitting the MCPs. The ion current obtained from C_2H^+ is monitored as a function of laser wavelength, yielding the REMPD spectra in figure 4.6.

To ensure that we are only considering C_2H^+ ions formed from $C_2H_2^+$, a LabView program (written by Dr. Chris Rennick) subtracts the C_2H^+ ion current in the absence of the REMPD laser from the ion current obtained when both the lasers are fired. Each data point is averaged ∼50 times.

4.3 C_2H_2 REMPI and $C_2H_2^+$ REMPD spectra

The REMPI spectrum of acetylene recorded in this work is presented in figure 4.4. Peak assignment is based on that of Ashfold *et al* [97] (established using photoelectron spectroscopy), as presented in table 4.1.

The REMPI spectra show some rotational substructure. By tuning the REMPI laser wavelength to particular regions of each vibrational band, it would be possible, in principle, to preferentially produce $C_2H_2^+$ ions in low or high J states. As discussed in Chapter 3, only two $C_2H_2^+$ modes of vibration are IR active: modes ν_5 (cis-bending) and ν_3 (asymmetric stretch). The presence of a centre of symmetry in a mode of vibration renders the mode IR inactive. Figure 4.5 illustrates the five different modes of vibration in $C_2H_2^+$; clearly ν_1, ν_2 and ν_4 have a centre of symmetry and are thus IR inactive. Ions produced in these vibrational modes are expected to be immune to BBR-mediated interactions and the state-selectivity could thus be preserved.

$C_2H_2^+$ ions produced with excitation in the ν_2 mode (peaks C and H in the REMPI spectrum shown in figure 4.4) are IR inactive, with respect to decay to the ground state. The lifetimes would thus be limited only by collisions with background gases. This suggests that $C_2H_2^+$ in v_2 = 1 and v_2 = 2 excited vibrational states are 'locked' states, with appreciable vibrational lifetimes.

Peaks 'C', 'F', 'G' and 'H' in figure 4.4 correspond to the excitation of single vibrational modes (see table 4.1). Peaks 'A', 'B', 'D' and 'E' in figure 4.4 involve the excitation of a

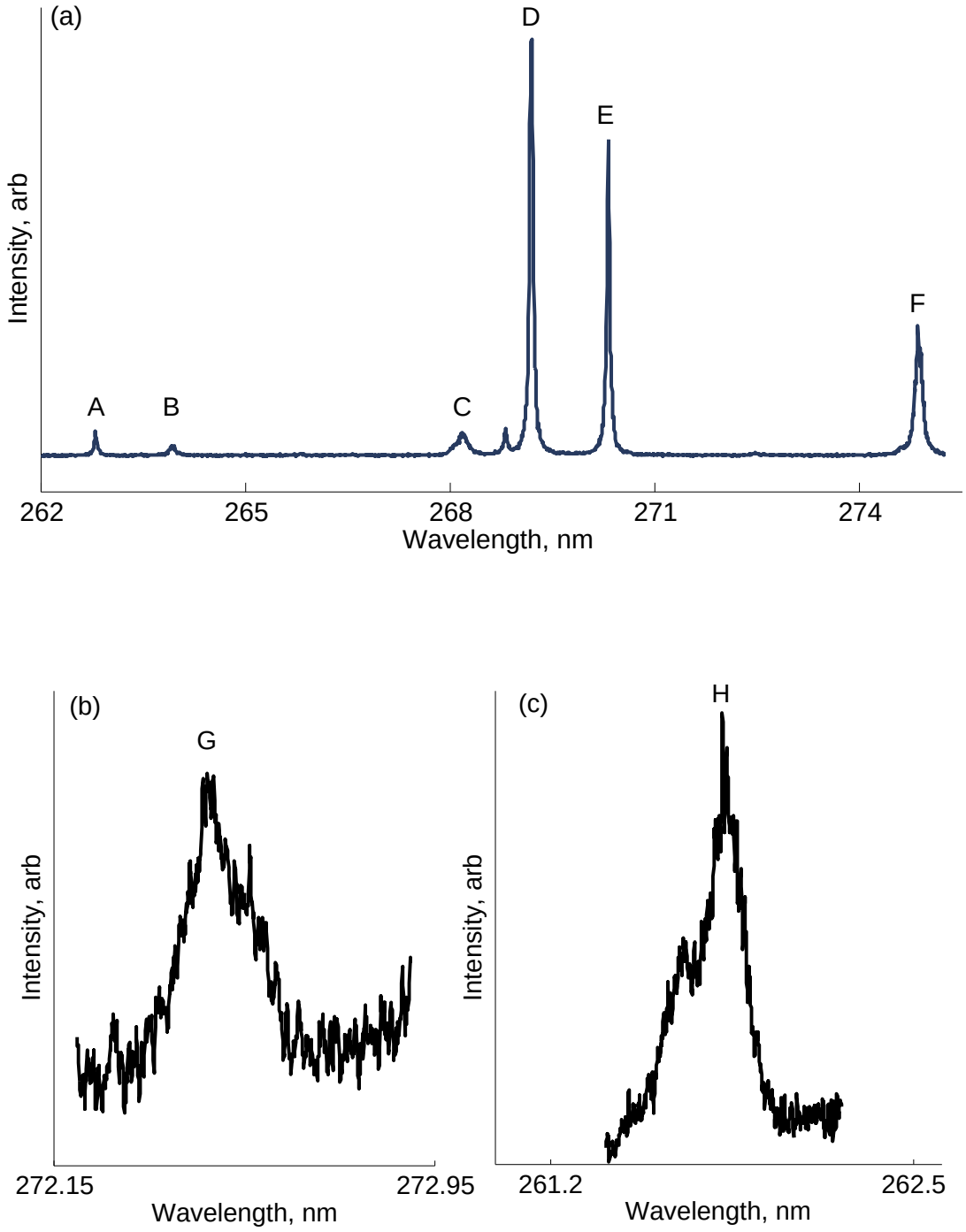

Figure 4.4: (a) REMPI spectrum of $C_2H_2^+$. Panels (b) and (c) are scans recorded with higher averaging and narrower step sizes for the peaks at 272.477 nm and 261.82 nm (respectively).

Table 4.1: Vibrational mode assignment of the peaks observed [97].

Peak label	Peak (nm)	$C_2H_2^+$ vib. assignment	Intermediate state
Figure 4.4 (c) H	261.8	2_0^2	$^1\Delta_g$, 2_0^2
Figure 4.4 (a) A	262.8	0_0^0+5_0^2	$^1\Sigma_g^+$, 2_0^1
Figure 4.4 (a) B	263.9	5_0^2+0_0^0	$^1\Delta_g$, 5_0^2, 2_0^1
Figure 4.4 (a) C	268.2	2_0^1	$^1\Delta_g$, 2_0^1
Figure 4.4 (a) D	269.2	0_0^0+ 5_0^2	$^1\Sigma_g^+$), 0_0^0
Figure 4.4 (a) E	270.3	5_0^2+0_0^0	$^1\Delta_g$, 5_0^2, 0_0^0
Figure 4.4 (b) G	272.5	–	$^1\Delta_g$, 4_0^1
Figure 4.4 (a) F	274.9	0_0^0	$^1\Delta_g$, 0_0^0

combination of two vibrational modes. Photoeletron spectroscopy performed by Ashfold *et al* [97] has established that, though these peaks are produced with the same combination band populated, 0_0^0 and 5_0^2 (through different intermediate states), the population distribution to each component of the combination band is different; the ratio of population in 0_0^0 and 5_0^2 varies. For instance, if we want to produce C_2H^+ ions with more population in ν_5 then we need to tune the REMPI laser to 263.9 nm or 270.3 nm; alternatively, if we want more population in 0_0^0, then we need to use a REMPI laser wavelength of 262.8 nm or 269.2 nm.

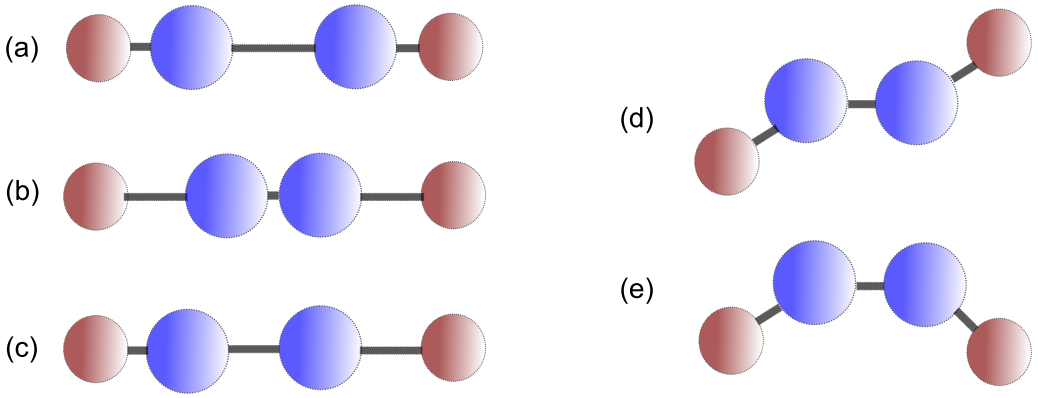

Figure 4.5: Modes of vibration in $C_2H_2^+$: (a) symmetric C–C stretch, ν_1; (b) symmetric C–H stretch, ν_2; (c) asymmetric C–H stretch, ν_3; (d) trans bend, ν_4 and (e) cis bend, ν_5.

The REMPD spectra obtained by plotting the C_2H^+ ion current against the REMPD laser frequency are shown in figure 4.6. While there is some rotational sub-structure present,

overall the spectral features are quite broad. The Drewsen group have demonstrated the use of REMPD as a useful tool for probing ions in a specific rovibrational state in their study of MgH^+.[28] The absence of a favourable intermediate state has rendered this approach less applicable to the $C_2H_2^+$ system.

REMPD spectra obtained at 268.2 nm and 269.2 nm REMPI wavelengths display broad peaks without any easily resolvable features. Figure 4.6 (c) shows the REMPD spectrum recorded with 274.9 nm REMPI excitation. This is the only spectrum with unambiguous structure obtained in this study and was found to be reproducible. Boesl and co-workers,[98] using a higher resolution laser (a UV bandwidth of 0.1 cm^{-1}, a pulse energy of 500 mJ, in steps of 0.04 cm^{-1}, averaging over 40 laser shots per step), were able to fully resolve the REMPD rotational structure and have assigned the constituent peaks accordingly. The labelling adopted in figure 4.6 (c) has been based on that of Boesl and co-workers.[98] The rotational structure at $\sim$255 nm was assigned to the electronic origin, 0_0^0.

In figure 4.6 (c), ν_4 is the trans bending mode, ν_{5a} is the out-of-plane cis bending mode and ν_{5b} is the in-plane cis bending mode. Excitation of the ν_4 mode can yield progressions $v = 0, 1, 2, 3....$ For the cis bending mode, ν_5, due to parity selection rules, only even number of quanta of vibration can be populated.[98]

Boesl and coworkers attributed the complexity of the spectrum to the involvement of the intermediate bent ionic $\widetilde{A}$ state, based on the predominance of the ν_4 mode in the REMPD spectrum (see spectrum in figure 4.6 c). The substructure at 250 nm, 246.3 nm and 243.3 nm in figure 4.6 (c) had been assigned as 4_0^1, 4_0^2 and 4_0^3 respectively. In figure 4.6 (c), the intensity of 4_0^2 peak is greater than 4_0^1 peak. This can be explained by the fact that the trans bent intermediate $\widetilde{A}$ state has a double minimum potential well. Consequently, the intensity of the REMPD peaks of the trans bending modes increases with increasing vibrational quantum number, as the the Franck-Condon overlap increases with the vibrational quantum number increases.[98]

Based on their rotational analysis together with the small Franck-Condon factors and long lifetime, Boesl and co-workers assigned the lowest frequency rotational structure ob-

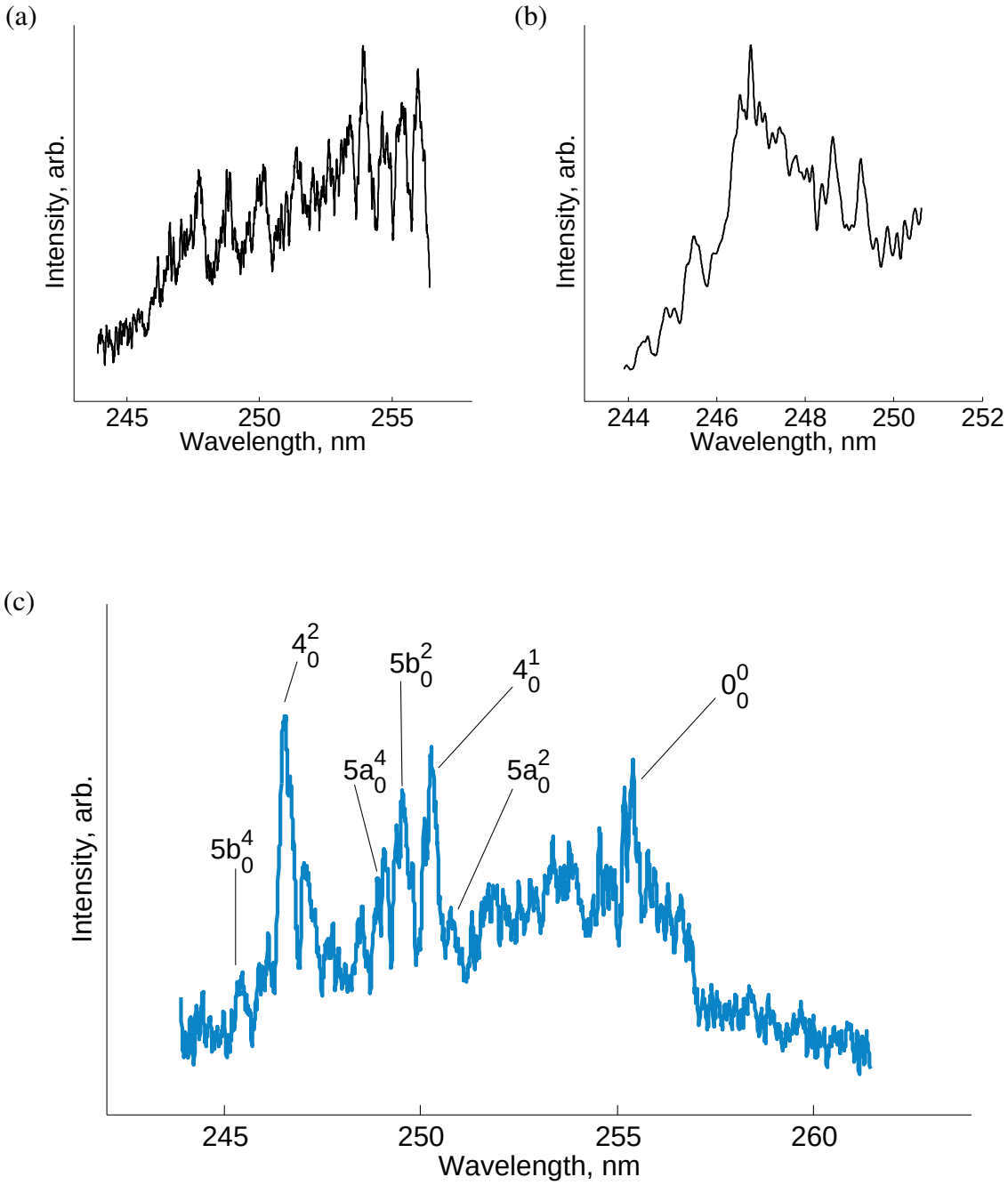

Figure 4.6: REMPD spectra of $C_2H_2^+$ recorded with (a) 268.2 nm, (b) 269.2 nm and (c) 274.9 nm REMPI wavelengths.

served to the out-of-plane bending vibration (υ_{5a}). The vibronic features in figure 4.6 (c) at 251 nm and 248.8 nm are assigned as $5a_0^2$ and $5a_0^4$ respectively. The in-plane cis bending mode ν_{5b} is assigned to the bands at 249.4 nm ($5b_0^2$) and 245.4 nm ($5b_0^4$).[98]

When comparing the results of Boesl and co-workers with the spectra we recorded, both our resolution and signal-to-noise ratio is lower. Should we wish to undertake these experiments in an ion-trap, the number of ions will be significacntly lower. It will thus be challenging to repeat the REMPD study in the ion-trap, and improvements in our laser systems (or detection apparatus) may be required.

4.4 Summary and future directions

In principle, it would be possible to produce $C_2H_2^+$ ions in low or high J states within a selected vibrational band, by tuning the REMPI laser wavelength to a particular part of the band. Applying this method to the ion-trap apparatus, it would be challenging to reproduce the REMPD spectra as the signal-to-noise ratio is already fairly low, and the number density would be even lower in the ion trap. Though we will not be able to obtain exact quantum state information, we could estimate the width of the rotational distribution by performing REMPD spestroscopy on trapped $C_2H_2^+$ ions.

One of the aims of this work was to experimentally establish how the rovibrational population of $C_2H_2^+$ ions evolved with time. Once $C_2H_2^+$ ions are produced in low or high J states, we have established that it would be possible to see the overall change in rotational state distribution with time, even though we cannot quantify the evolution of population absolutely. This could be achieved by recording REMPD spectra of Coulomb crystallised $C_2H_2^+$ ions in an ion-trap at different time intervals and observing the change in spectral features. If there is no change in the REMPD features this would imply that the population in the selected state is stable. This would also be useful if we wish to test the effectiveness of liquid nitrogen cooling; if features in the $C_2H_2^+$ REMPD spectra that changed over time when observed at 300 K can maintain their original profile at 77 K (under liquid N_2 cooling of the trap apparatus), this would confirm our theoretical predictions (see Chapter 3) and

facilitate the measurement of state-selected reaction rates in future experiments.

It is possible to produce acetylene ions in various selected vibrational states, as summarised in table 4.1. None of these schemes are rotationally selective with our laser system and apparatus, but should reflect the rotational distribution of the neutral acetylene molecule. The states produced via excitation through the v_2 = 1 and v_2 = 2 modes are IR inactive, implying that $C_2H_2^+$ ions produced in these states would be immune to BBR-mediated population redistribution. As such, decay to other vibrational states would occur through collisions with background gases only; thus the ν_1 and ν_2 states are expected to exhibit appreciable lifetimes. $C_2H_2^+$ ions can also be produced with population in two or more vibrational bands, as discussed in section 4.3. These combination bands are potentially interesting for the study of future vibrationally state-selected reactions in the ion trap.

We have established that $C_2H_2^+$ ions could be formed in a vibrationally state-selected manner and sympathetically loaded into a Coulomb crystal in an ion trap (see chapter 6), enabling their reaction with velocity-selected neutral ND_3 (from the Stark decelerator) to be studied. The challenges involved in examining such state-selected ion-molecule reactions at cold temperatures are detailed in Chapter 7 – along with suggestions as to how some of these experimental challenges could be overcome.

The dependance of reaction rates and branching ratios on the $C_2H_2^+$ vibrational state could potentially be established for the 0_0^0, 2_0^1 and 2_0^2 bands. The reaction of states produced via the combination bands, 5_0^2 + 0_0^0 (produced with different relative populations in 5_0^2 and 0_0^0), could also be examined and compared against the reactivity of the pure vibrational states. Additionally, by selecting different positions in the vibrational band, reaction rates at high or low J rotational levels with ND_3 could be studied for the vibrational REMPI peaks identified in this work.

Chapter 5

Ion Trapping, Laser Cooling and Coulomb Crystals

5.1 Introduction

In this chapter, the principles of ion trapping and laser cooling are discussed and the experimental set up described. We have developed a technique which enables one to eject the trapped ions through a time-of-flight (TOF) tube onto multichannel plates (MCPs) for detection. This is achieved by converting the ion trap electrodes to an extractor-repeller pair, as further detailed in Chapter 6. Such ejection is not possible with a sinusoidally varying rf voltage in our set up, as the resonant circuitry of the electronics in the trap hinders the clean switching from trapping voltages to extractor/ repeller voltages; ringing causes the ejection to be inefficient. A digital trap – an ion trap operating with a digitally varying rf voltage – does not have this problem. This chapter describes the development and characterisation of a digital ion trap, which is compared with the sinusoidal trap in respect to the trap depth and stability region for the species of interest.

5.2 Ion trapping

Electromagnetic fields can be used to manipulate species with an electric charge, namely ions. The challenge involves providing a deep electromagnetic potential well, such that the ions are stably trapped in three dimensions. In free space, the static electromagnetic potential, ϕ, obeys Laplace's equation ($\nabla^2\phi = 0$), and cannot be confined in all three

dimensions (Earnshaw's theorem).[99] At best the electric potential forms a saddle point, with a maximum in one direction along which ions can be lost. One way to address this is to switch the electric field between the two orthogonal orientations of the potential, such that the saddle point flips at each switch. Radio frquency (rf) fields are sufficient to achieve rotation of the potential fast enough to overcome the relative translational motion of the ions, making confinement of ions in three directions possible.[100]

Linear Paul traps, as employed in this work, use quadrupolar electrostatic fields and time-varying rf electric fields to trap ions. A variety of electrode geometries and electromagnetic field combinations can be utilised; Paul traps have also been designed using bladed [101] and hyperbolic [102] electrode geometries.

Penning traps, on the other hand, do not use time varying (switching) fields. Instead, Penning traps employ spatially homogenous magnetostatic fields and spatially inhomogenous electrostatic fields to achieve confinement.[103]

5.3 Linear Paul trap

5.3.1 Principle and Design

The ion trap used in this work is a linear Paul trap, comprising four parallel segmented cylindrical electrodes, each divided into three parts (see figure 5.1). The segments of the electrodes are insulated from each other; all twelve components can have voltages independently applied to them. The trap parameters are defined in table 5.1.

Table 5.1: Trap parameters

r_0	Radius of the interelectrode space
$2z_0$	Length of the centre peice of an electrode
V_{rf}	Peak to peak voltage
ω_{rf}	rf trapping frequency (angular)
U_{dc}	End cap voltage
$\phi(x, y)$	Electric potential

Charged particles in the inter-electrode space obey the transverse equation of motion

given by:

$$\ddot{u} + K_u = 0, u \in (x, y), \tag{5.1}$$

where $K_{x,y} = \pm 2emV_{\text{rf}}/r_0^2$. The quadrupoles are combined into a doublet, with the second having opposite polarity to the first, resulting in stability along the x direction and destabilising fields in the y direction. Thus to obtain transverse confinement in both directions a time varying periodic voltage V_{rf} is used – this is applied to each quadrupole rod such that diagonally opposite electrode rods are in the same phase but with a phase shift of 180° with respect to the nearest electrodes. The electrodes at all times have an applied rf voltage $\pm\frac{1}{2}V_{\text{rf}}\cos(\omega_{\text{rf}}t)$. The presence of four electrodes creates two rotating time varying saddle points in the potential thus giving radial confinement (x, y direction).[104] This configuration of the centre electrodes gives rise to an electric potential ($\phi(x, y)$) given by

$$\phi(x, y) = \frac{V_{\text{rf}}}{2}\left(\frac{x^2 - y^2}{r_0^2}\right). \tag{5.2}$$

The choice of waveform for the time-varying rf voltage is quite arbitrary,[105] and in this work both sinusoidal and pulsed (digital) waveforms are used, as shown in figure 5.2. Axial confinement is obtained by applying static (dc) voltages (U_{dc}) to the eight end pieces.

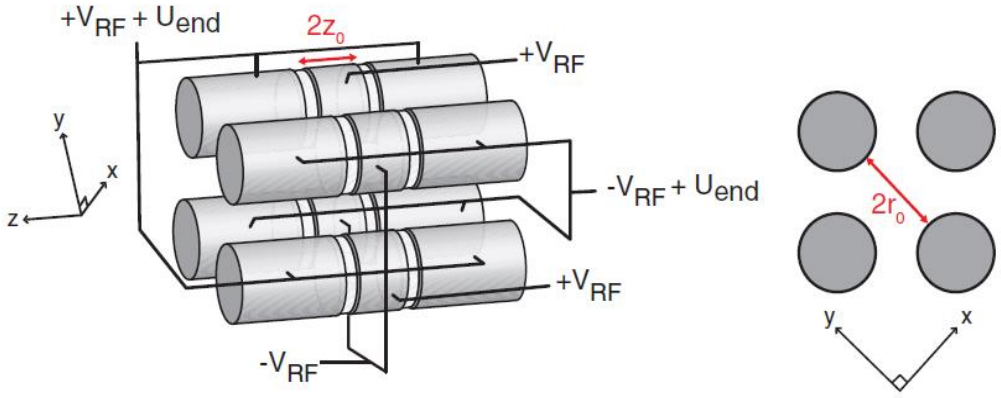

Figure 5.1: Design of the linear Paul trap used in this thesis. This figure has been reproduced from Alexander Gingell's thesis.[71]

The voltage applied to the electrodes varies as

$$\phi(x, y, t) = \phi(x, y)\phi(t) = \begin{cases} \frac{V_{\text{rf}}}{2}\left(\frac{x^2-y^2}{r_0^2}\right)\cos(\omega_{\text{rf}}t), & \text{for a sinusoidal trapping voltage} \\ \frac{V_{\text{rf}}}{2}\left(\frac{x^2-y^2}{r_0^2}\right)P_\tau(t), & \text{for a digital trapping voltage,} \end{cases} \tag{5.3}$$

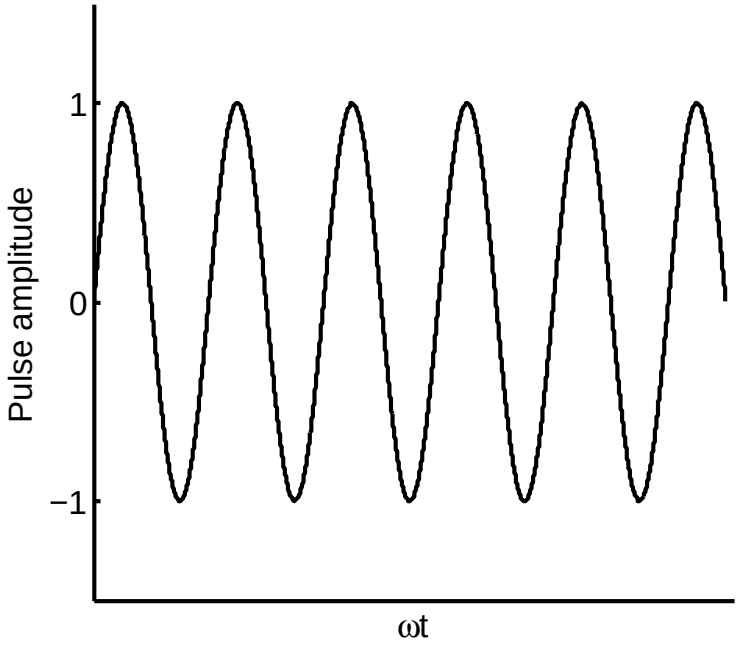

(a)

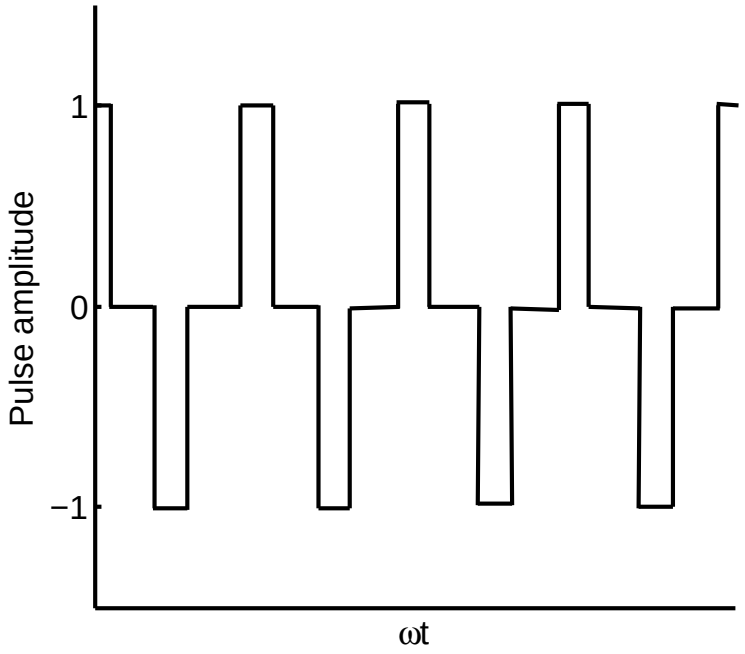

(b)

Figure 5.2: RF voltages used in this thesis: (a) a sinusoidal pulse, and (b) a digital pulse.

where V_{rf} is the peak-to-peak rf voltage and ω_{rf} is the angular radiofrequency, given by $2\pi/T$ where T is the time period. Taking τ as the fractional width of the non-zero part of the digital pulse (t/T, where T is the time period), $P_\tau(t)$ is given by,[104]

$$P_\tau(t) = \begin{cases} 1 & \text{if } |t| \leq \tau T/2 \\ 0 & \text{if } \tau T/2 < |t| \leq (1-\tau)T/2 \\ -1 & \text{if } (1-\tau)T/2 < |t| \leq T/2, \end{cases} \tag{5.4}$$

$$P_\tau(t+T) = P_\tau(t). \tag{5.5}$$

The digital trap voltages can be expressed as a Fourier expansion of $\cos(\omega t)$,

$$f_T = \sum_{n=1}^{\infty} a_n \cos(n\omega t) = \sum_{n=1}^{\infty} a_n \cos\left(\frac{2n\pi t}{T}\right), \tag{5.6}$$

where a_n is the Fourier coefficient obtained by Fourier decomposition of equation 5.6.

$$\begin{aligned} a_n &= -\frac{2}{n\pi}(-1+(-1)^n)\sin n\pi\tau \\ &= \frac{4}{n\pi}\sin(n\pi\tau) \text{ (where } n \in \text{odd)}. \end{aligned} \tag{5.7}$$

For the digital trap, axial confinement is again obtained by applying static (dc) voltages (U_{dc}) to the eight end pieces. The potential that arises from the static voltages is given by,

$$\phi_{\text{end}}(x,y,z) = \frac{\eta U_{\text{dc}}}{z_0^2}\left(z^2 - \frac{x^2+y^2}{2}\right). \tag{5.8}$$

Here η is the geometric factor for the trap, which has been measured to be 0.244. [71] The experimental trap parameters are provided in table 5.2. The total electric potential is thus given by:

$$\phi = \phi_{\text{rf}}(x,y,t) + \phi_{\text{end}}(x,y,z). \tag{5.9}$$

Table 5.2: Experimental trap parameters

Diagonal electrode surface separation	$2r_0$	7.0 mm
Endcap separation	$2z_0$	5.5 mm
Geometric factor	η	0.244
Electrode radius	R	4.0 mm

Motion of ions in a trap: The motion of ions in a linear Paul trap can be adiabatically divided into two contributions: a low frequency ion drift (secular motion), and a higher frequency oscillation (micromotion). The secular motion of the ions can be interpreted as the motion of the ions trapped with a time-averaged pseudo-potential in the trap. It is this motion that can be laser-cooled. By contrast, the micromotion is a driven oscillatory behaviour, induced by the rf switching. The extent of micromotion increases with radial distance from the trap centre, as the gradient of the radial potential increases.

Equations of motion for a single ion can be reduced to a set of decoupled one-dimensional Mathieu differential equations in an oscillating quadrupole field. This is advantageous because the solutions of the Mathieu equations are well understood, with the stability of a trajectory dependent on only two dimensionless parameters (Mathieu parameters, a and q) and not on the initial conditions of the ion.[104, 106–108] The Mathieu equation is of the form:

$$\frac{d^2u}{d\xi^2} + [a_u - 2q_u \cos(2\xi)] = 0,\ u \in \{x, y, z\},\ \text{for a sinusoidal trap, and} \quad (5.10)$$

$$\frac{d^2u}{d\xi^2} + [a_u - 2q_u P_\tau(t)] = 0,\ u \in \{x, y, z\},\ \text{for a digital trap.} \quad (5.11)$$

Here, the angular position ωt is expressed in terms of a reduced parameter 2ξ.

A particle of mass m and charge Q in an electric field given by equation 5.9 experiences a force given by,

$$F = ma = -QE = -Q\nabla\phi. \quad (5.12)$$

For an ion trap operating at a sinusoidal time-varying rf voltage, the Newtonian equations of motion may be writen as:

$$\ddot{x} + \left(\frac{-\eta Q U_{\text{dc}}}{m z_0^2} + \frac{Q V_{\text{rf}}}{m r_0^2}\cos\omega_{\text{rf}} t\right) x = 0 \text{ for sinusoidal voltages,} \quad (5.13)$$

$$\ddot{x} + \left(\frac{-\eta Q U_{\text{dc}}}{m z_0^2} + \frac{Q V_{\text{rf}}}{m r_0^2} P_\tau\right) x = 0 \text{ for digital voltages,} \quad (5.14)$$

$$\ddot{y} + \left(\frac{-\eta Q U_{\text{dc}}}{m z_0^2} - \frac{Q V_{\text{rf}}}{m r_0^2}\cos\omega_{\text{rf}} t\right) y = 0 \text{ for sinusoidal voltages,} \quad (5.15)$$

$$\ddot{y} + \left(\frac{-\eta Q U_{\text{dc}}}{m z_0^2} - \frac{Q V_{\text{rf}}}{m r_0^2} P_\tau\right) y = 0 \text{ for digital voltages,} \quad (5.16)$$

$$\ddot{z} + \left(\frac{2\eta Q U_{\mathrm{dc}}}{m z_0^2}\right) z = 0 \text{ for sinusoidal and digital trap.} \tag{5.17}$$

5.3.2 Trap depth

As noted in section 5.3.1, ions in a trap can undergo two adiabatically separated motions: higher frequency driven oscillation (micromotion) or a lower frequency drift, known as the secular motion. The micromotion does not occur on the trap axis but increases as ions move towards the rf electrodes. If the trajectory of motion of an ion is stable (stability is discussed in section 5.3.3), the secular motion of the ion can be interpreted in the context of a time independent effective potential, V^*, which arises from the adiabatic approximation. A brief derivation of this pseudo-potential for both sinusoidal and digital trapping fields is given in appendix C.

A constant c_1 is defined, where c_1 depends on whether the trap is operating with sinusoidal or digital voltages,

$$c_1 = \begin{cases} 1/2 & \text{for a sinusoidal trap,} \\ 1/2 \sum_{n=1}^{\infty} a_n^2/n^2 & \text{for a digital trap.} \end{cases} \tag{5.18}$$

This constant arises from the derivation of the trap depth (as detailed in appendix C). In the case of a digital trap, c_1 depends on the width of the pulse, τ. The numerical value of this quantity is plotted against τ in figure 5.3. It should be noted that at τ = 0.293 the value of the constant is 1/2.

The effective potential, V^*, of an ion of mass m and charge Q is given by,

$$V^*(R_0) \;=\; \frac{q^2 E_0^2}{2m\omega^2} c_1 + Q\phi_s, \text{ for both sinusoidal and digital traps.} \tag{5.19}$$

The first term in equation 5.19 is effectively a time-averaged potential resulting from the oscillating rf fields, with amplitude E_0 and angular frequency ω. ϕ_s in the second term represents the potential arising from the static fields.

The rf potential, $\phi(x, y, t)$, is given in equation 5.3. The pseudo-potential arising from

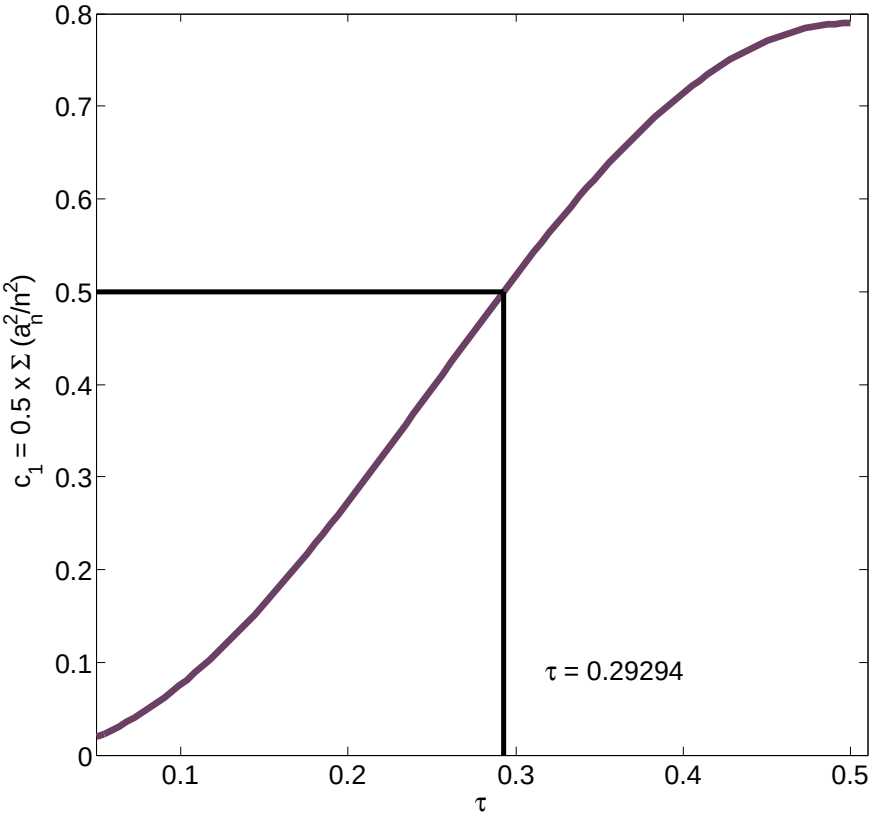

Figure 5.3: A plot of c_1 vs τ. It can be seen that the value of c_1 is 0.5 (the value of c_1 for the sinusoidal trap) when τ = 0.293.

equation 5.3 is radially harmonic and is given by:

$$\phi_{\text{ps}}(r) = \frac{Q^2}{m\omega_{\text{rf}}^2}\left(\frac{V_{\text{rf}}}{2r_0^2}\right)^2 (x^2+y^2) \text{ for a sinusoidal trap,} \tag{5.20}$$

$$\phi_{\text{ps}}(r) = \frac{Q^2}{2m\omega_{\text{rf}}^2}\left(\frac{V_{\text{rf}}}{r_0^2}\right)^2 \left(\frac{1}{2}\sum_{n=1}^{\infty}\frac{a_n^2}{n^2}\right)(x^2+y^2) \text{ for a digital trap.} \tag{5.21}$$

The derivations of the pseudo-potential are detailed in appendix C. Figure 5.4 is an illustration of the pseudo-potential inside the ion trap, in a transverse plane passing through the centre of the trap.

The trap depth, $\phi_{\text{ps}}(r_0)$, is defined as the value of pseudo-potential at $r = r_0$,

$$\phi_{\text{ps}}(r_0) = c_1\frac{Q^2}{2m\omega_{\text{rf}}^2}\frac{V_{\text{rf}}^2}{r_0^2}. \tag{5.22}$$

The secular trap depth, $\phi_{\text{sec}}(r_0)$, is thus given by,

$$\phi_{\text{sec}}(r_0) = c_1\frac{Q^2}{2m\omega_{\text{rf}}^2}\frac{V_{rf}^2}{r_0^2} - \frac{\eta Q U_{\text{dc}}}{z_0^2}\frac{r_0^2}{2}. \tag{5.23}$$

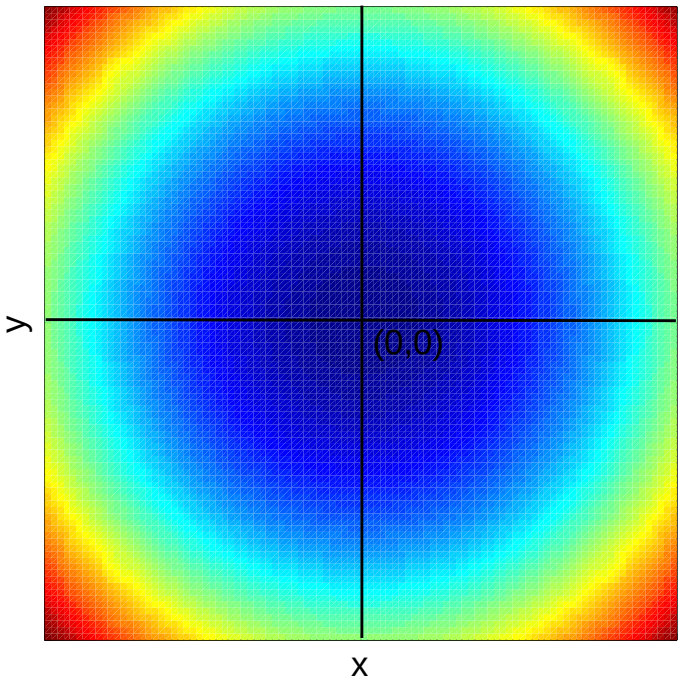

Figure 5.4: Contour plot of the pseudo-potential inside the ion trap, in a transverse plane passing through the centre of the trap. The corners of the square represent the positions of the electrodes which are generating the rf potential. Here, blue represents the most deep and red the least deep pseudo-potential.

The end cap potential, arising from the voltage U_{dc} applied to the end pieces of the electrodes, is given by equation 5.8. The secular potential, ϕ_{sec} is the sum of the pseudo-potential ($\phi_{\text{ps}}(r)$) and the potential energy from the end cap potential, $\phi_{\text{end}}(x, y, z)$ given by equation 5.8 can be writen as:

$$\begin{aligned}
\phi_{\text{sec}} &= \phi_{\text{ps}}(r) + Q\phi_{\text{end}}(x, y, z) && (5.24)\\
&= c_1 \frac{Q^2}{2m\omega_{\text{rf}}^2} \left(\frac{V_{\text{rf}}}{r_0^2}\right)^2 (x^2 + y^2) + Q\frac{\eta U_{\text{dc}}}{z_0^2}\left(z^2 - \frac{x^2 + y^2}{2}\right) && (5.25)\\
&= \left(c_1 \frac{Q^2}{2m\omega_{\text{rf}}^2} \left(\frac{V_{\text{rf}}}{r_0^2}\right)^2 - \frac{1}{2}\frac{Q\eta U_{\text{dc}}}{z_0^2}\right)(x^2 + y^2) + Q\left(\frac{\eta U_{\text{dc}}}{z_0^2}\right) z^2. && (5.26)
\end{aligned}$$

Figure 5.5 shows how the trap depth varies with τ in the digital trap, with V_{rf} = 50 V and U_{dc} = 1 V. The blue dashed line in the plot is the trap depth at which the sinusoidal trap in our laboratory operates (V_{rf} = 160 V, U_{dc} = 4 V and $\omega_{\text{rf}} = 2\pi\times$3.85 MHz). ϕ_{sec} = 1.36 eV is the secular trap depth for the digital trap at τ = 0.293; this is the value of the secular trap depth equivalent to a sinusoidally-varying voltage, with other trapping conditions the same

as in the sinusoidal trap.

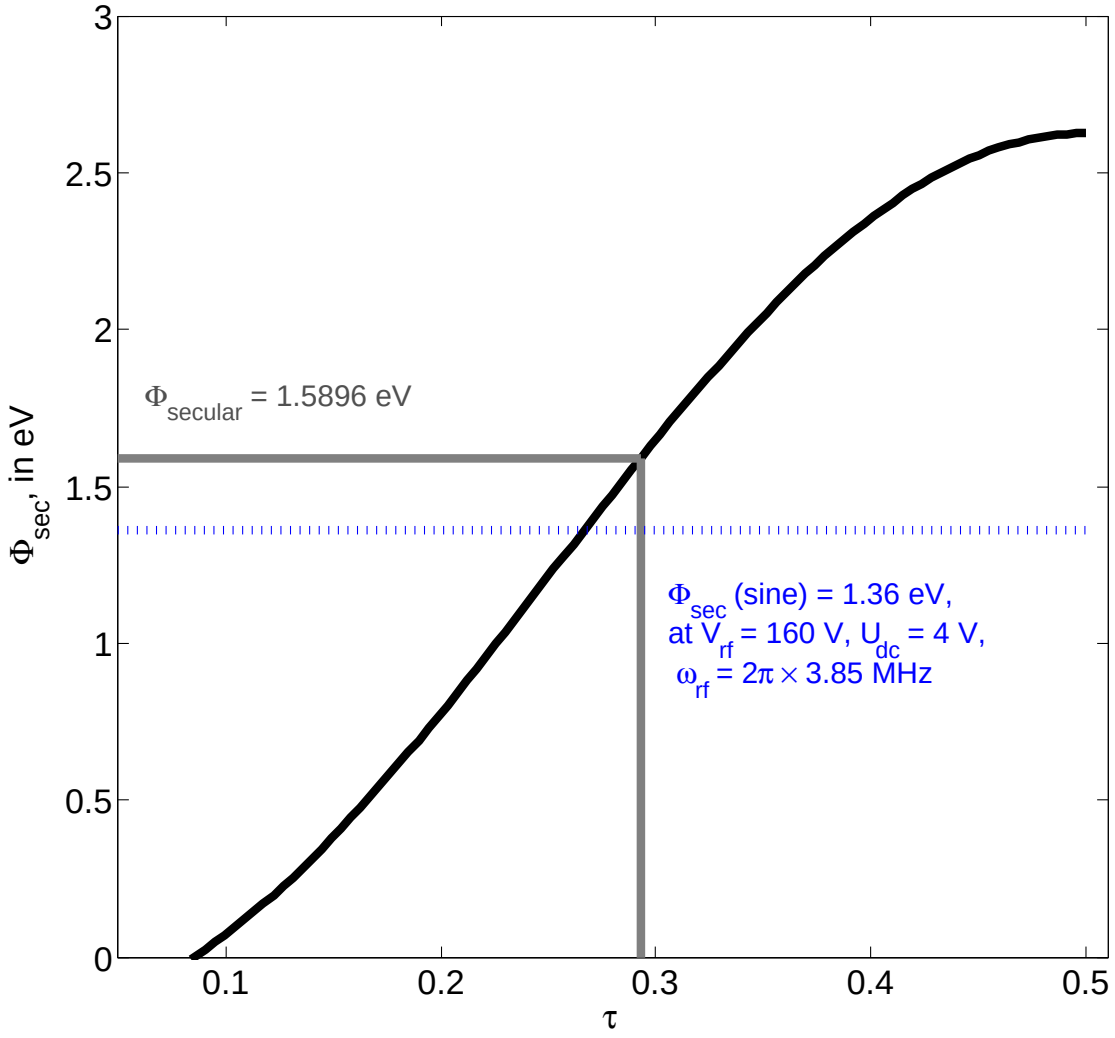

Figure 5.5: Secular trap depth ϕ_{sec} plotted against τ (V_{rf} = 50 V, U_{dc} = 1 V). The black curve shows the variation of ϕ_{sec} with τ, the blue dashed line is the trap depth at which the sinusoidal trap typically operates. The grey line indicates the trap depth of the digital trap at $\tau = 0.293$, the value of τ for which the constant c_1 of the digital trap is the same as c_1 in the sinusoidal trap.

Equation 5.26 can also be expressed in terms of the harmonic oscillation frequencies ω_j (z is the axial distance from trap centre):

$$\begin{aligned} \phi_{\text{sec}} &= \frac{1}{2}m\omega_r^2 r^2 + \frac{1}{2}m\omega_z^2 z^2, \\ &= \frac{1}{2}m \sum_{j=x,y,z} \omega_j^2 j^2, \end{aligned} \tag{5.27}$$

where,

$$\omega_{\text{axial}}^2 = \omega_z^2 = 2\frac{Q}{m}\frac{\eta U_{\text{dc}}}{z_0^2} \tag{5.28}$$

$$\begin{aligned}\omega_{\text{radial}}^2 &= \omega_x^2 = \omega_y^2 \\ &= \frac{c_1 Q^2}{m^2\omega_{\text{rf}}^2}\left(\frac{V_{\text{rf}}}{r_0^2}\right)^2 - \frac{Q\eta U_{\text{dc}}}{mz_0^2}.\end{aligned} \tag{5.29}$$

The plasma frequency is given by,

$$\omega_{\text{plasma}}^2 = \omega_z^2 + 2\omega_r^2, \tag{5.30}$$

The pseudo-potential frequency, ω_{ps} is derived from: force $= -\nabla U = -\omega_{\text{ps}}^2 x$,

$$\omega_{\text{ps}}^2 = \omega_{\text{radial}}^2 + \frac{\omega_{\text{axial}}^2}{2} = c_1\left(\frac{QV_{\text{rf}}}{m\omega_{\text{rf}}r_0^2}\right)^2. \tag{5.31}$$

In the equations for harmonic frequency, 5.20 – 5.31, the charge-to-mass ratio Q/m occurs in the numerator. Ions with a large charge-to-mass ratio (low mass singly charged ions) experience a larger radial trapping potential than ions with a smaller charge-to-mass ratio; lighter ions reside nearer to the trap axis.

Along the z-coordinate the particle undergoes simple harmonic motion. The behaviour is more complex along along the x- and y- coordinates. The dynamic switching of the rf potential causes ions moving away from the trap axis to undergo rapid oscillations, known as micromotion as described in section 5.3.1.

The experimental trap parameters used in the Oxford ion trap are given in table 5.3. For typical experimental parameters of V_{rf} = 160 V and U_{dc} = 4 V (with the sinusoidal trap), the characteristic frequencies of the secular harmonic motion of an ion in the trap are $2\pi\times$125.5 kHz (axial) and $2\pi\times$116.5 kHz (radial). For the digital trap operating at V_{rf} = 50 V, U_{dc} = 1 V and τ = 0.25 the secular frequencies are $2\pi\times$62.8 kHz and $2\pi\times$110 kHz, axial and radial (respectively). The digital trap is operated at a plasma frequency of $2\pi\times$ 167.7 kHz.

The pseudo-potential trap depth (given by equation 5.22) and secular trap depth, given by equation 5.23 for a sinusoidal trap operating at $\omega_{\text{rf}} = 2\pi\times$3.85 MHz, V_{rf} = 160 V, U_{dc} = 4 V, are 2.15 eV and 1.36 eV respectively. For an ideal digital trap ($\omega_{\text{rf}} = 2\pi\times$1.32 MHz, V_{rf}

Table 5.3: Experimental parameters used for the trapping experiments.

Trapping parameter	Sinusoidal trap	Digital trap
V_{rf}	100-250 V	45-55 V
ω_{rf}	$2\pi\times$3.85 MHz	$2\pi\times$1.32 MHz
U_{dc}	1.0 - 4.0 V	0.5 - 2.0 V
η	0.244	0.244
τ	-	0.25

= 50 V, U_{dc} = 1 V, τ = 0.25) the pseudo-potential trap depth is 1.41 eV and the secular trap depth is 1.21 eV.

Figure 5.6 shows the real digital voltage pulse that is used in the digital trapping experiments. The area under the waveform is equivalent to that of an idealised rectangular pulse with τ = 0.25 [109] and we assume that the characteristics of the real digital trap are well described by the idealised behaviour. The experimental digital waveform exhibits a non-zero pulse decay time, and thus deviates from the ideal digital waveform described above. Molecular dynamics simulations – in which the measured digital waveform can be directly utilised – indicate that this deviation from ideality has only a very minor impact on the trap depth.

5.3.3 Stability diagram

For poorly chosen values of the Mathieu parameters a_u and q_u, the micromotion is unstable and increases exponentially until ions are lost from the trap. In this section, the region in the $(V_{\text{rf}}, U_{\text{dc}})$ plane where stable trapping is possible is established.

Introducing the reduced parameter $\xi = \omega t/2$, and substituting into equations 5.10 and 5.11 yields the following reduced Mathieu equation:

$$\frac{d^2u}{d\xi^2} + (a_u - 2q_u f(\xi))u = 0, u \in x, y \tag{5.32}$$

where,

$$f(\xi) = \begin{cases} \cos(2\xi) & \text{for a sinusoidal trap} \\ \widetilde{P_\tau}(\xi)_\tau(\xi) & \text{for a digital trap.} \end{cases} \tag{5.33}$$

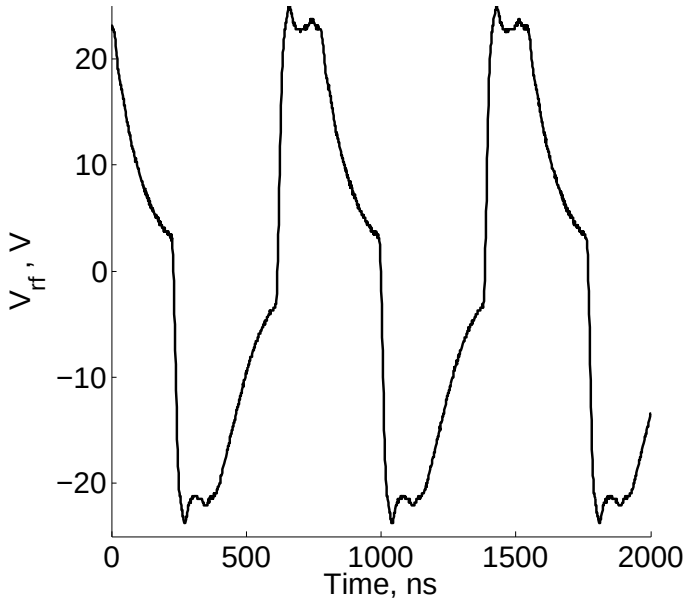

Figure 5.6: Experimental time-varying pulse generated by the experimental digital voltage generator.

Here, $\widetilde{P}_\tau(\xi)$ is the reduced transformation of $P_\tau(t)$ given by equation 5.4 to the reduced parameter space

$$\widetilde{P}_\tau(\xi) = \begin{cases} 1 & \text{if } |\xi| \leq \frac{1}{2}\tau\pi \\ 0 & \text{if } \frac{1}{2}\tau\pi < |\xi| \leq \frac{1}{2}(1-\tau)\pi \\ -1 & \text{if } \frac{1}{2}(1-\tau)\pi < |\xi| \leq \pi/2, \end{cases} \tag{5.34}$$

and

$$\widetilde{P}_\tau(\xi + \pi) = \widetilde{P}_\tau(\xi). \tag{5.35}$$

Comparing equation 5.13 to 5.16 with the form of Mathieu equation in 5.32, we can define the dimensionless Mathieu parameters:

$$a_x = a_y = -\frac{a_z}{2} = -\eta\frac{4QU_{\text{dc}}}{mz_0^2\omega_{\text{rf}}^2}, \tag{5.36}$$

$$q_x = -q_y = -\frac{2QV_{\text{rf}}}{mz_0^2\omega_{\text{rf}}^2}; q_z = 0. \tag{5.37}$$

The properties of Mathieu equations have been studied in detail and the behviour is well understood. [104, 110] The (q_u, a_u) plane is divided into stable and unstable regions by characteristic curves. For (q_u, a_u) in a stable region, the solutions to Mathieu equations are bound. In an unstable region, the solutions for positions tend to infinity with time. For overall transverse stability, both (q_x, a_x) and (q_y, a_y) need to fall within stable regions.

To determine the stable regions, equation 5.32 can be rewritten as

$$\frac{d^2u}{d\xi^2} + \widetilde{K_u}(\xi)u = 0, u \in x, y. \tag{5.38}$$

Here, the coefficient $\widetilde{K_u}(\xi) = a_u - 2q_u f(\xi)$ is a piece-wise constant function. The theory developed in reference [107] addresses the time-varying pulsed electric field that emulates the transverse dynamics of charged particles in the spatially varying magnetic field of a strong focussing lattice. Equation 5.32 can be solved from a vector containing the initial conditions using matrix multiplication,

$$\begin{bmatrix} u(\xi) \\ u'(\xi) \end{bmatrix} = M_u(\xi|\xi_0) \begin{bmatrix} u(\xi_0) \\ u'(\xi_0) \end{bmatrix} \tag{5.39}$$

where $u(\xi_0)$ and $u'(\xi_0)$ are initial values at $\xi = \xi_0$. $M_u(\xi|\xi_0)$ is the 2×2 transfer matrix from ξ_0 to ξ and is calculated by successive matrix multiplication of the transfer matrices for all the intervals of $K_u(\xi)$ between the initial (ξ_0) to final ($\xi_0 + \pi$). The details of this matrix multiplication are provided in appendix D. The solution of equation 5.39 is stable if $|TrM_u(\xi|\xi + \pi)| < 2$ and unstable if $|TrM_u(\xi|\xi + \pi)| > 2$. [107] The stability diagram is obtained by plotting the values of a_u and q_u that lead to stable single particle motion.

A typical single ion stability diagram is shown in figure 5.7. Here, the stability diagram is for Ca^+ at $\tau = 0.25$ and $\omega_{\text{rf}} = 2\pi \times 1.32$ MHz in a digital trap. It should be noted that only a portion of this stability region is accesible experimentally. For all subsequent stability diagram figures, only a small portion of the stability plot representing the experimentally feasible conditions is presented. The a vs q stability plot can be also expressed as a U_{dc} vs V_{rf} stability plot by expressing a_u and q_u (equations 5.36 and 5.37) as U_{end} and V_{rf}, as given below:

$$\begin{aligned} U_{\text{dc}} &= -a_x \frac{mz_0^2\omega_{\text{rf}}^2}{4\eta Q} = -a_y \frac{mz_0^2\omega_{\text{rf}}^2}{4\eta Q} \\ V_{\text{rf}} &= -q_x \frac{mr_0^2\omega_{\text{rf}}^2}{2Q} = q_y \frac{mr_0^2\omega_{\text{rf}}^2}{2Q}. \end{aligned} \tag{5.40}$$

Figure 5.8 shows the stability diagram for Ca^+ in a sinusoidal trap, plotted both as a

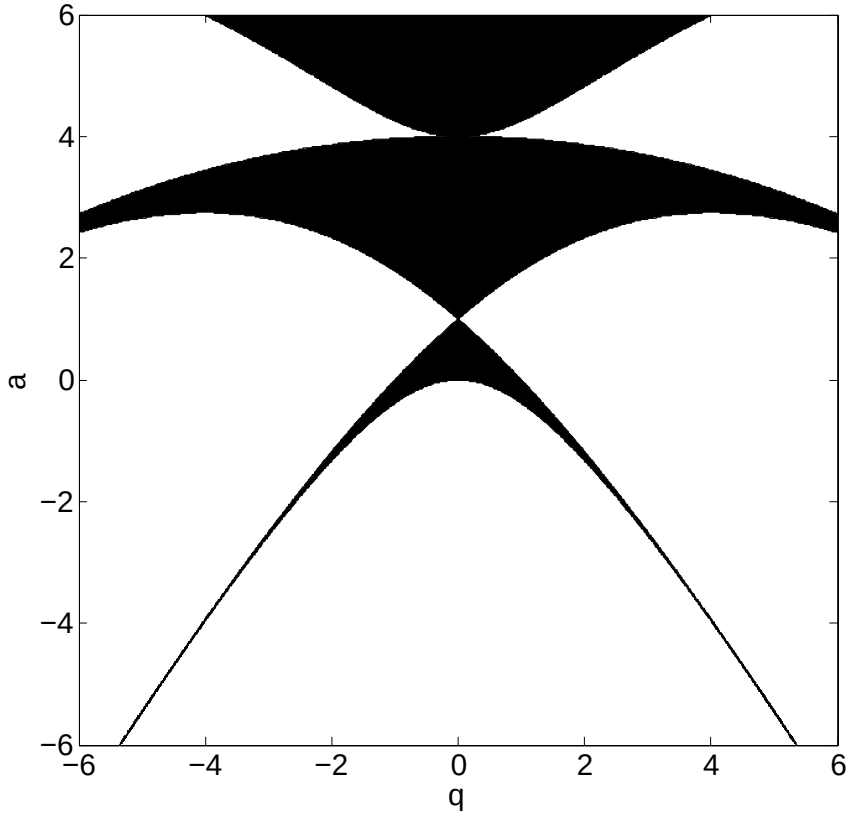

Figure 5.7: A typical stability diagram for Ca^+ in a digital trap operating at τ = 0.25 and $\omega_{\text{rf}} = 2\pi\times1.32$ MHz. The stability zone is coloured in black; it is in this region that the requirements for stablity are met.

function of a vs q and U_{dc} vs V_{rf}, at a trapping frequency of $2\pi\times3.85$ MHz. The stability region in the latter also includes a contour plot indicating the trap depth in eV.

The digital trap in our laboratory operates at $\omega_{\text{rf}} = 2\pi\times1.32$ to $2\pi\times1.42$ MHz. The "real" voltage (V_{rf}) pulse used (depicted in figure 5.6) is similar to that of an ideal digital pulse of τ = 0.25.

Figure 5.9 depicts the single ion Ca^+ U_{dc} vs V_{rf} stability diagram at experimental trapping parameters for a digital trap at τ = 0.25 and $\omega_{\text{rf}} = 2\pi\times1.32$ MHz. The trap depth (eV) is also shown on this plot. A black rectangle in the upper left hand corner of figure 5.9 indicates the region we typically operate experimentally.

The region of stable trapping depends on the frequency of trapping, ω_{rf}. This is true for both the sinusoidal and digital trap. Figure 5.10 is the U_{dc} vs V_{rf} stability diagram for Ca^+ for a digital trap at a range of trapping frequencies with τ = 0.25.

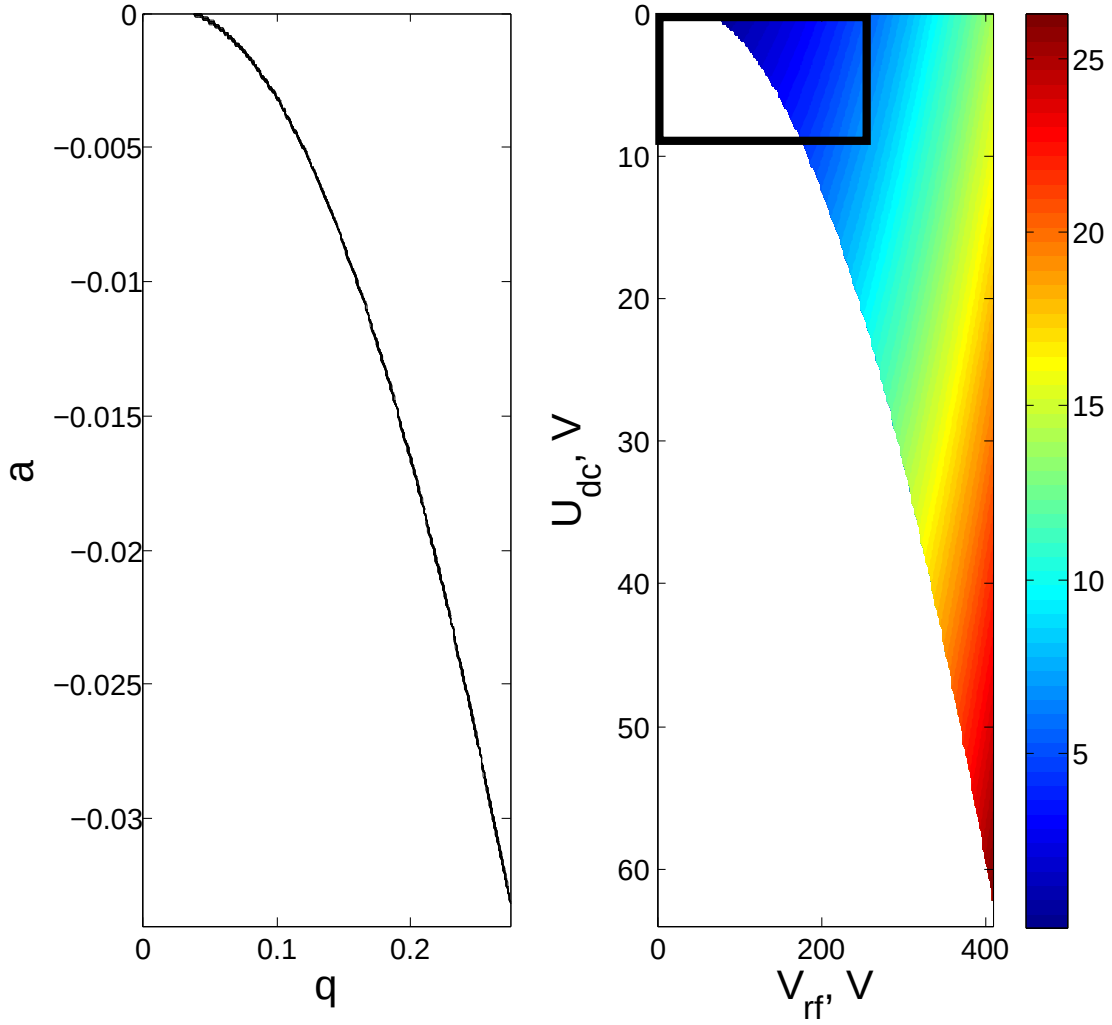

Figure 5.8: (left) The a vs q stability diagram for Ca^+ in an ion trap operating at $\omega_{rf} = 2\pi \times 3.85$ MHz; and (right) the corresponding U_{dc} vs V_{rf} plot, with the region of stability also including a contour plot illustrating the trap depth. The colour bar shows the trap depth in eV. A black rectangle in the upper left hand corner of figure indicates the region we typically operate experimentally.

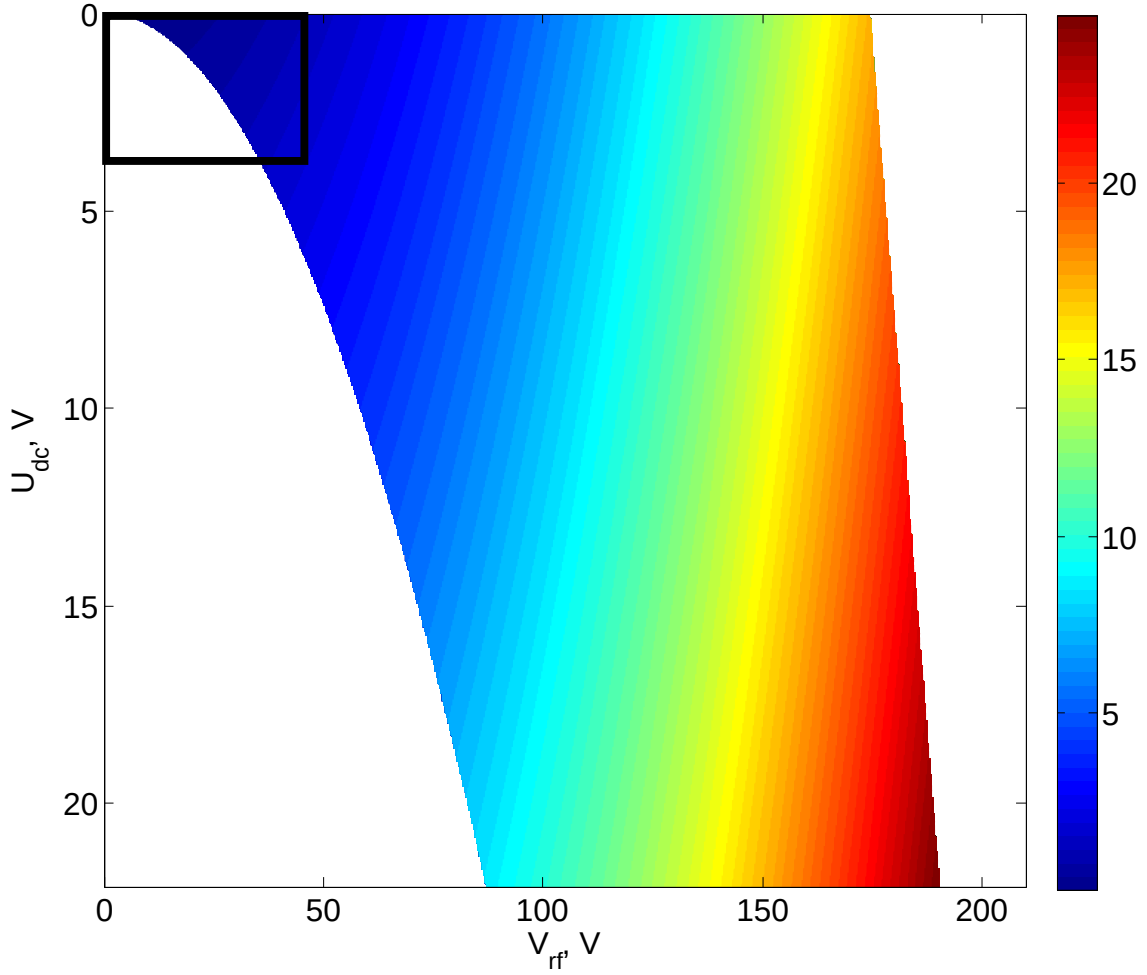

Figure 5.9: Stability diagram for Ca^+ in a digital trap operating at V_{rf} = 50 V, U_{dc} = 1 V, τ = 0.25 and $\omega_{\mathrm{rf}} = 2\pi\times 1.32$ MHz. The colour bar shows the trap depth in eV. A black rectangle in the upper left hand corner of figure indicates the region we typically operate experimentally.

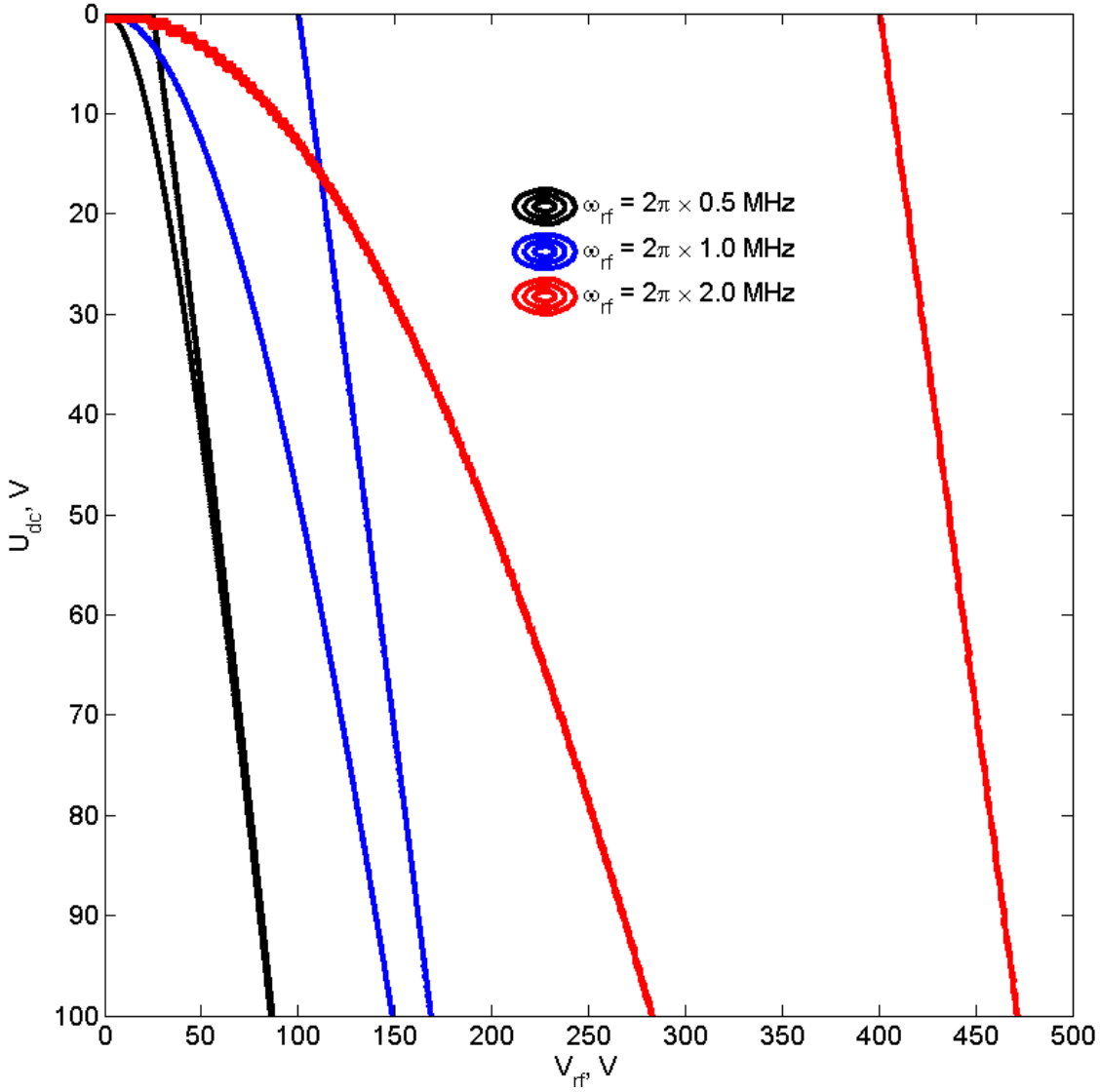

Figure 5.10: Stability diagram for Ca^+ in a digital trap, with τ = 0.25 at $\omega_{rf} = 2\pi\times0.5$ MHz (black), $\omega_{rf} = 2\pi\times1.0$ MHz (blue) and $\omega_{rf} = 2\pi\times2.0$ MHz (red). The region of stable trapping lies between the curve of same colour in each case.

For a digital trap, the region of stable trapping of Ca^+ in the U_{dc} vs V_{rf} stability diagram depends on τ. Figure 5.11 shows the U_{dc} vs V_{rf} plot at $\omega_{rf} = 2\pi \times 1.32$ MHz at three different values of τ. The blue, red and black curves are for $\tau = 0.4$, 0.25 and 0.1 respectively. The region enclosed within curves of the same colour represents the stability region for the specific τ chosen.

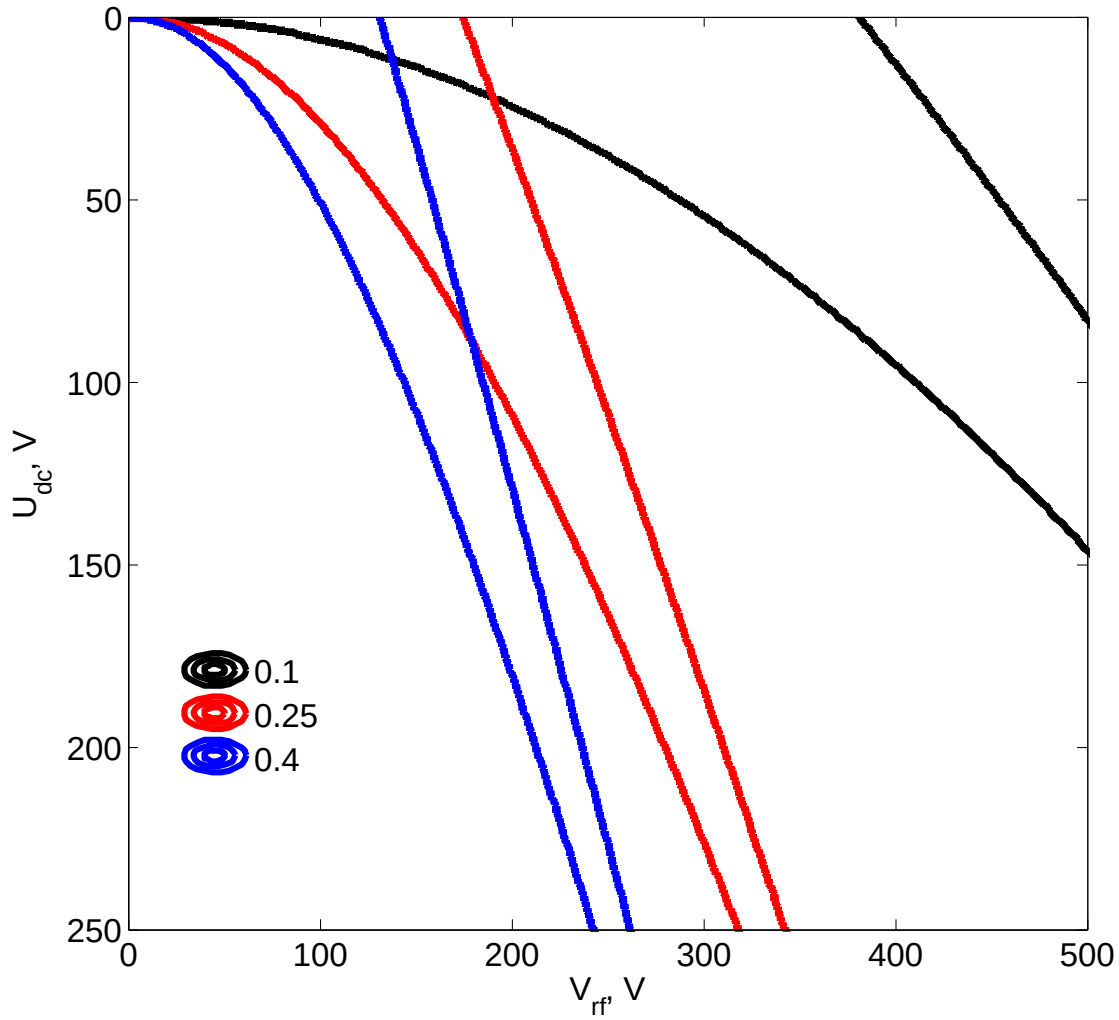

Figure 5.11: The U_{dc} vs V_{rf} stability diagram (digital trap) is plotted for Ca^+ at a trapping frequency of $2\pi \times 1.32$ MHz at three different values of τ. Here, the blue, red and black curves are for $\tau = 0.4$, 0.25 and 0.1 respectively. The region of stable trapping lies between the curve of same colour in each case.

Different ions can be trapped simultaneously, provided they have an overlapping region of stability which is experimentally accessible. Figure 5.12 shows the possibility of co-

trapping ions of multiple mass-to-charge ratios at the trapping parameters used in this thesis for a digital trap (at $\tau = 0.25$ and $\omega_{rf} = 2\pi \times 1.32$ MHz). In the figure, only the stability region of Ca^+ is shaded black; for all other ions the region enclosed within curves of the same colour is the region of stable trapping for that mass. Any species which can be trapped in similar stability region as Ca^+ could, in principle, be sympathetically cooled into a Ca^+ Coulomb crystal. Clearly, $C_2H_2^+$ and ND_3^+ can be co-trapped together in a Ca^+ Coulomb crystal.

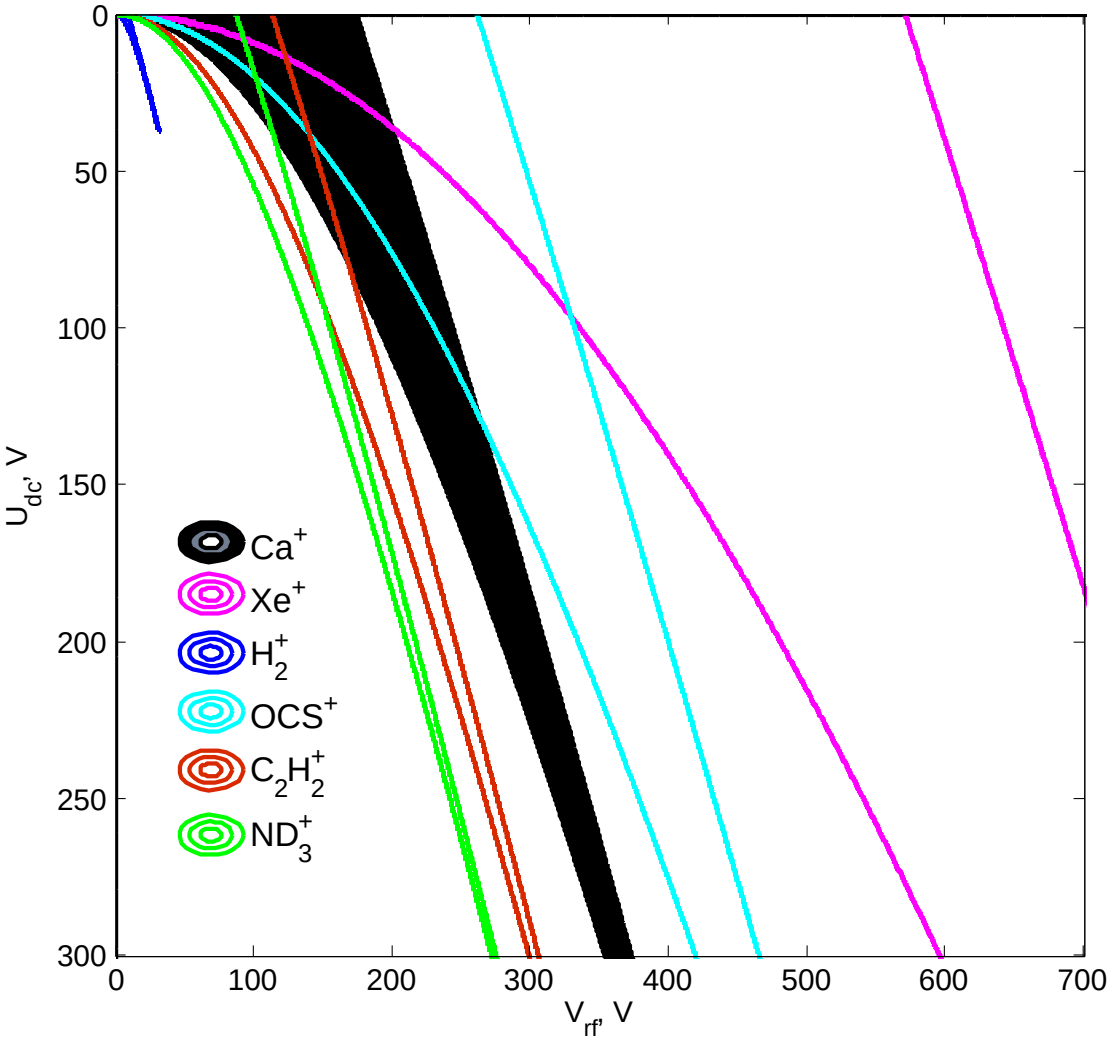

Figure 5.12: Stability diagram for various species, ranging from H_2^+ to Xe^+, in a digital trap operating at $\tau = 0.25$ and $\omega_{rf} = 2\pi \times 1.32$ MHz. This plot show the regions in the stability diagram where masses could be co-trapped; royal blue is H_2^+, green is ND_3^+, red is $C_2H_2^+$, black is Ca^+, aqua is OCS^+ and pink is Xe^+. The region enclosed within curves of the same colour is the region of stable trapping for the relevant mass; only the stability region of Ca^+ is shaded black.

5.3.4 Summary

The sinusoidal and digital trapping fields are comprehensively compared with respect to trap depth and stability regions. The trap depth has been derived for both digital and sinusoidal trapping fields.

It was observed that as τ increases, the trap depth of a digital trap increases. Programs have been developed to calculate the stability regions for different ions under varying experimental conditions. For $\tau = 0.293$, the trap depth and stability diagram for both sinusoidal and digital trapping fields would be equivalent. The digital pulse generator used in our experiments did not generate idealised pulses; the area under the waveform is equivalent to that of an idealised rectangular pulse with $\tau = 0.25$.[109] We assume in trap depth and stability calculations that the characteristics of the trap are well described by the idealised digital fields.

The trap depth at which the sinusoidal trap operates experimentally in our research group is $\sim$ 1.36 eV. In contrast, the exerimental parameters at which the digital trap operates generates a trap depth of 1.21 eV. The trap depth of the digital trap is quite low and consequently the crystals would be expected to be hotter than the ones obtained in a sinusoidal trap.

Stability diagram obtained for various species, ranging from H_2 to Xe^+, has also been deduced for digital trap at experimental conditions of $\tau = 0.25$ and $\omega_{rf} = 2\pi \times 1.32$ MHz.

5.4 Translationally cold, spatially confined Ca^+ Coulomb crystals

An ion trap allows one to generate a spatially confined ensemble of typically (initially) translationally hot ions. Ions can have significant kinetic energy, present as both secular motion and micromotion. The large amplitude secular motion can be removed by a laser-cooling scheme using continuous wave (CW) diode lasers. Laser cooling can be applied to a small range of neutral and ionic species, subject to the availability of a closed cooling cycle. Laser cooling is also referred to as Doppler cooling, as it makes use of the Doppler

effect. The laser cooling schemes employed for $^{40}Ca^{+}$ ions is discussed in the subsequent sections.

5.4.1 Laser cooling of trapped $^{40}Ca^{+}$ ions

If a photon is resonant with an electronic transition, it can be absorbed, producing an electronically excited ion. Photon absorption (or emission) leads to a change in momentum of the ion, as implied by the laws of conservation of momentum. Using photons of a perfectly resonant wavelength, an equal number of ions will be accelerated or decelerated, depending on whether their z velocity component is aligned with or opposed to the direction of laser propagation. If a laser is detuned to a wavelength longer than the resonant wavelength, (termed red-shifting) an overall cooling of the ions can be achieved. This takes advantage of the Doppler effect; only photons propagating in the opposite direction to the ions are absorbed, thus leading to a net reduction of ion momentum on absorption, as photons are then emitted in all directions when the ion spontaneously relaxes back to the ground state from the excited state. Given a sufficiently large number of laser cooling cycles, mK translational temperatures are readily achieved. The ions can be detected by imaging the fluorescence resulting from photon emission using a microscope objective lens and a charge couple device (CCD) camera.

The Ca^{+} ions are produced by photoionisation of a thermal beam of Ca atoms using the frequency-tripled output (355 nm) of a pulsed Nd:YAG laser. The laser cooling scheme used in this thesis for $^{40}Ca^{+}$ was first described by Ritter, *et al.* [111] and is illustrated in Figure 5.13. A diode laser drives the $^{2}S_{1/2} \rightarrow {}^{2}P_{1/2}$ primary cooling transition at 397 nm. The lifetime of $^{2}P_{1/2}$ state is around 7 ns,[112] with a spontaneous decay to the $^{2}S_{1/2}$ state. However, the $^{2}P_{1/2}$ state can also decay spontaneously to the $^{2}D_{3/2}$ metastable state, with a branching ratio of around 1:12 in favour of the ground $^{2}S_{1/2}$ state.[71] The transition from the $^{2}D_{3/2}$ state to the ground state is electric-dipole forbidden, and the decay is slow with a lifetime of just over a second.[113] The population in the metastable state becomes large over many cooling cycles, preventing effective laser cooling. Introduction of a second diode

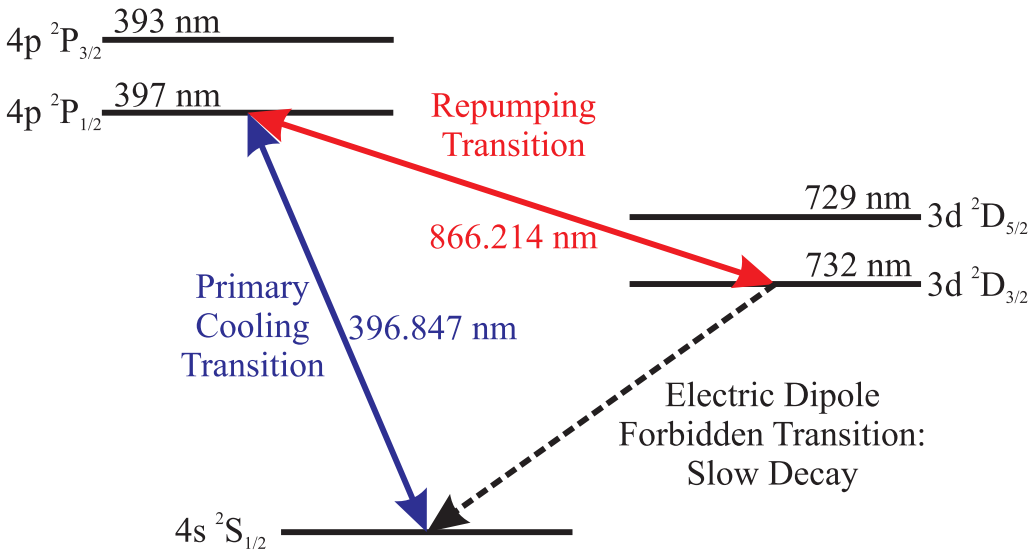

Figure 5.13: The relevant low-lying electronic states of the $^{40}Ca^+$ ion, neglecting spin orbit coupling. The laser induced electronic transitions are shown. The wavelengths shown correspond to energies relative to the ground state. This figure has been reproduced from Lee Harper's thesis.[68]

laser in the near IR (at $\approx$ 866 nm) continuously repumps the metastable population back into the $^2P_{1/2}$ state. In our experiments, the cooling lasers are aligned along the longitudinal axis of the trap. Thus, although cooling only takes place directly along one dimension, the Coulomb interactions between multiple ions in a trap lead to coupling (and hence cooling) of motion in all dimensions. For later experiments, the diodes were retro-reflected giving bi-directional cooling.

The lowest translational temperature that could be achieved by the Doppler cooling scheme for Ca^+ is given by the formula,

$$T_{\text{min, Doppler}} = \frac{\hbar\Gamma}{2k_B}, \tag{5.41}$$

where, Γ is the linewidth of the laser-cooling transition. For the laser-cooling scheme used in this thesis a minimum translational temperature of 0.5 mK can be attained. The zero-point kinetic energy (corresponding to the motional frequencies ω_{axial} and ω_{radial} given by equations 5.28 and 5.29, repectively) of the motion of the ion in the potential of the ion trap limits the minimum achievable temperature.

The calcium source used in these experiments contains all of the naturally occurring

calcium isotopes, with $^{40}Ca^{+}$ accounting for 96.94%. [114] It is not possible to laser cool all of these isotopes simultaneously with a single diode laser system, as the isotopic shifts in the electronic transitions are orders of magnitude larger than the transition linewidths. Calcium ions are non-resonantly ionised in our experiments; other isotopes may be trapped alongside the $^{40}Ca^{+}$ ions and can be sympathetically cooled along with $^{40}Ca^{+}$ ions into the resulting Coulomb crystal, appearing as dark ions in experimental fluorescence images. The diode lasers might also emit some photons at 393 nm, exciting $^{40}Ca^{+}$ ions to the $^{2}P_{3/2}$ state.[68, 71] This state can decay to the $^{2}D_{5/2}$ metastable state, which is not repumped. Calcium ions that become trapped in this state may also appear as dark calcium ions in any fluorescence images.

5.4.2 $^{40}Ca^{+}$ Coulomb crystals

An ensemble of laser cooled ions, discussed above, can form a strongly interacting cold plasma within the ion trap. The behaviour of this plasma is governed by the balance of the Coulombic repulsion between the positive ions, their effective translational energy or the secular kinetic energy, and the effective trapping potential/forces experienced by the ions within the trap. At low translational temperatures, the Coulombic repulsion between the ions dominates, and the ions cannot freely move past each other, thus restricting the secular motion. The ions tend to remain localised at the effective potential minimum and the ensemble of ions resembles a fluid-like state. A phase transition occurs as the secular temperature is lowered further, giving rise to an ordered three-dimensional lattice structure known as a Coulomb crystal. Within the crystal structure, for typical trapping parameters, ion spacings are of the order of 10 – 20 μm. A Coulomb crystal is sometimes alternatively referred to as a "Wigner crystal".

The crystallization occurs when the plasma coupling parameter, Γ, is greater than 150. The plasma coupling parameter is the ratio of potential energy (E_{P}) to secular kinetic energy (E_{k}) of the ions and is used to describe the thermodynamic state of a plasma:

$$\Gamma = \frac{E_{\mathrm{P}}}{E_{\mathrm{k}}} = \frac{q^2}{4\pi\epsilon_0 a_{\mathrm{WS}} k_{\mathrm{BT}}}, \tag{5.42}$$

where a_{WS} is the Wigner-Seitz radius, which gives the average inter-ion distance from the density of ions at zero temperature in the plasma (n_0):

$$1/n_0 = \frac{4}{3}\pi a_{\mathrm{WS}}^3, \tag{5.43}$$

for the particle charge, q, and the ensemble temperature, T.

Ion densities in the trap are limited by Coulomb repulsion to approximately 10^8 ions/cm^3. [69] Based on equation 5.42 the phase transition to the crystalline state occurs at or below $T \approx$ 100–150 mK.[21, 71] Such low temperatures can only be attained by laser-cooling. A Coulomb crystal comprised of a single species has a uniform density.[115]

The crystal structure is determined by the actual trapping potential and the number and quantity of ionic species trapped. According to theory (in the limiting case of infinite crystals), [116] a one-component Coulomb crystal in an effective harmonic potential is expected to have an ideal body-centered-cubic (bcc) crystalline structure. Such an ideal structure is observable only for very large crystals ($> 10^5$ ions). Ions in smaller crystals are organized in a near-hexagonal structure inside concentric spheroidal shell. For a bicomponent crystal, the two different species will be radially separated. Ions with lower mass-to-charge ratios remain closer to the trap axis and ions with a larger mass-to-charge ratio form a surrounding shell structure with a spheroidal outer boundary.

Ions diffuse throughout the lattice structure in the crystalline state. Along with the ion micromotion, this results in a contribution to the blurring of experimentally imaged ion fluorescence. The images captured represent an ion spatial probability density; each of the bright spots observed in experimental Coulomb crystal images indicates a lattice position rather than a single ion.

Temperature of Coulomb Crystal

Of the two different types of motion – secular and micromotion – only the secular motion is addressed by the laser-cooling schemes describes in section 5.4.1; micromotion remains constantly driven by the rf fields. The sample of ions in the crystal do not have a uniform temperature distribution (or kinetic energy distribution) as the rf field strength

increases linearly from the trap axis. The equivalent temperature is minimum at the trap axis and can be as high as tens of Kelvin, depending on the rf amplitude and the distance of the ion from the trap axis.

The assignment of temperature, in this thesis, refers to the effective average kinetic energy of the crystal, expressed in units of Kelvin:

$$T = \frac{\langle E_{\mathrm{K}} \rangle}{k_{\mathrm{B}}}. \tag{5.44}$$

For crystals of a few hundred ions, the average micromotion energy is generally used to define the crystal temperature, as it is typically several orders of magnitude larger than the secular temperature.

5.4.3 Molecular dynamics simulations of Coulomb crystals

The structure, properties and dynamics of ion Coulomb crystals can be theoretically studied with molecular dynamics simulations. Such simulations enable us to ascertain crystal ion numbers, both of fluorescing and dark components. Simulations are performed using CCMD, a set of programs written in-house by Dr. Martin Bell and extended by Dr. Chris Rennick.

The total force experienced by an ion, i, in an ensemble can be given by:

$$\boldsymbol{F}_{\text{total,i}} = \boldsymbol{F}_{\text{trap}} + \boldsymbol{F}_{\text{Coulomb}} + \boldsymbol{F}_{\text{laser}} + \boldsymbol{F}_{\text{heat}} \tag{5.45}$$

$\boldsymbol{F}_{\text{trap}}$ is the harmonic trapping force on ion i, and corresponds to the Mathieu equations. It is derived from the time-dependent trap potential:

$$\boldsymbol{F}_{\text{trap},i} = q_i \left(\frac{V_{\text{rf}} \cos\left(\omega_{\text{rf}} t\right)}{r_0^2} (x_i - y_i) + \frac{\eta U_{\text{dc}}}{z_0^2} [2z_i - (x_i + y_i)] \right). \tag{5.46}$$

The Coulomb interaction is taken into account using pairwise addition of all of the inter-ionic forces:

$$\boldsymbol{F}_{\text{Coulomb},i} = \sum_{i \neq j} \frac{q_i q_j}{4\pi \epsilon_0 r_{ij}^2} \hat{\boldsymbol{r}}_{ij}, \tag{5.47}$$

where $\boldsymbol{r}_{ij}$ is the displacement vector.

The laser cooling force is formulated as:

$$\boldsymbol{F}_{\text{laser},i} = \beta \dot{\boldsymbol{z}}_i. \tag{5.48}$$

Since laser cooling occurs along the longitudinal axis of the trap, only the z axis is considered in the viscous damping term. Here, β is a damping coefficient.

The stochastic heating term, $\boldsymbol{F}_{\text{heat,i}}$, is designed to model photon recoil and background collisions which provides random velocity kicks to every ion at each time step, and adjusting it allows for control of the final temperature of the crystal. It is introduced to take into account the heating of the ions caused by collisions and by imperfections in the trap geometry and rf fields.

Simulated fluorescence images of the Coulomb crystal can be generated from the trajectories of the ions. A three-dimensional histogram containing the positions of all of the ions in the crystal is output by the MD simulations. Simulated images are compared with experimental images to determine the ion numbers of the experimental crystal. The visible spots in the final image corresponds to a slice through the three-dimensional distribution. The experimental crystal can be compared with simulated crystals generated with the appropriate trapping conditions, and the number of ions in the experimental crystal can be determined.

A higher secular temperature causes increased mobility of ions and leads to blurring of the image captured. The amplitude of micromotion is too small to be observed by the imaging system (resolution ~ 1 μm) and as such, the effective kinetic energy cannot be directly inferred. MD simulations offer one method for estimating the crystal temperature, and this is done by adjusting the value of the stochastic heating term in the CCMD code.

5.5 Experimental apparatus and procedure

Ion trapping experiments described in this thesis have been performed using two ion trap chambers. One ion trap apparatus (hence forth referred to as the ‘old ion trap’) is adapted from a set-up previously designed by Alex Gingell.[71] The experimental apparatus in two

complementary view points is illustrated in figures 5.14 and 5.15. The second ion trap apparatus (hence forth referred to as the 'new ion trap') has recently been designed by Laura Pollum.[117] A schematic representation of the new ion trap chamber is given in figure 5.16.

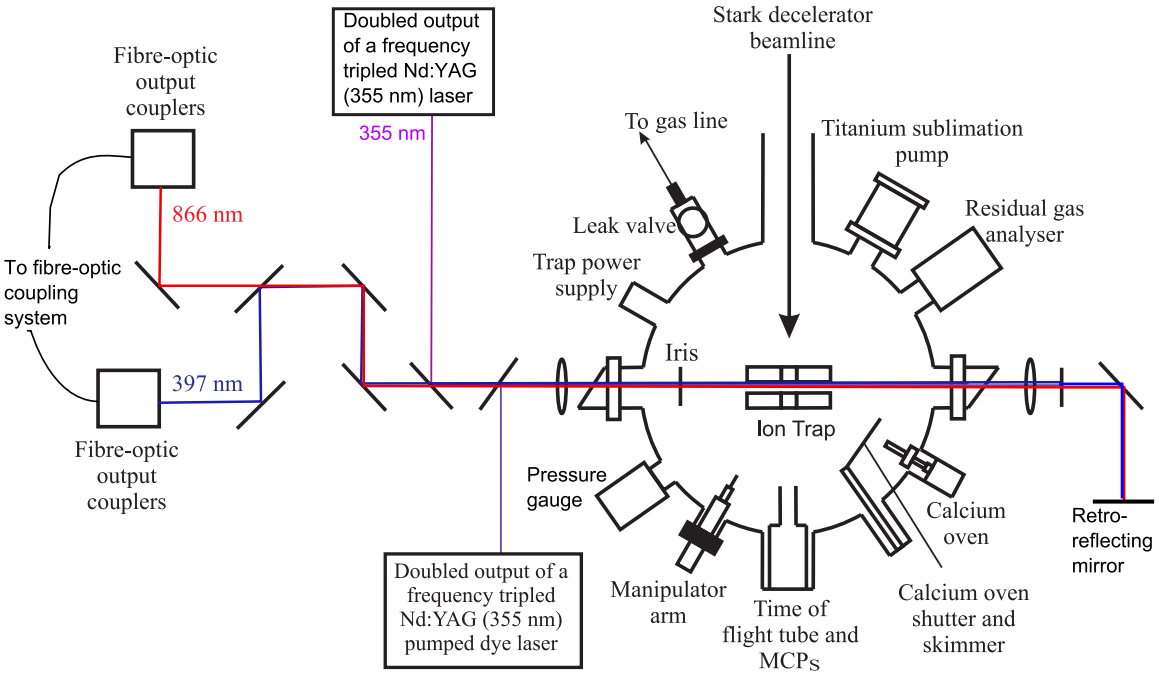

Figure 5.14: Representative top view of the 'old' ion trap chamber and the accompanying optical set-up. This figure has been adapted from Lee Harper's thesis.[68]

5.5.1 Experimental procedure

The ion trap is placed in the centre of an ultrahigh vacuum (UHV) chamber, maintained at 5×10^{-10} mbar and $2-3\times10^{-9}$ mbar, achieved using a turbo pump backed up by a rotary pump, for the old and new ion trap chambers respectively. The specifications of the ion trap are detailed in section 5.3.1. Radiofrequency voltages are applied to all segments of the trap electrodes; typically a peak-to-peak voltage (V_{rf}) of 100 –250 V is used for sinusoidal trapping and 45 – 55 V for digital trapping. An additional static voltage, U_{dc}, is applied to the twelve outermost segments of the trap electrodes and typically endcap voltages of 1 – 4 V (sinusoidal trapping) and 0.1 – 2 V (digital trapping) are applied to confine the ions along the trap axis. The trapping frequency (ω_{rf}) used is $2\pi\times3.85$ MHz for sinusoidal trapping

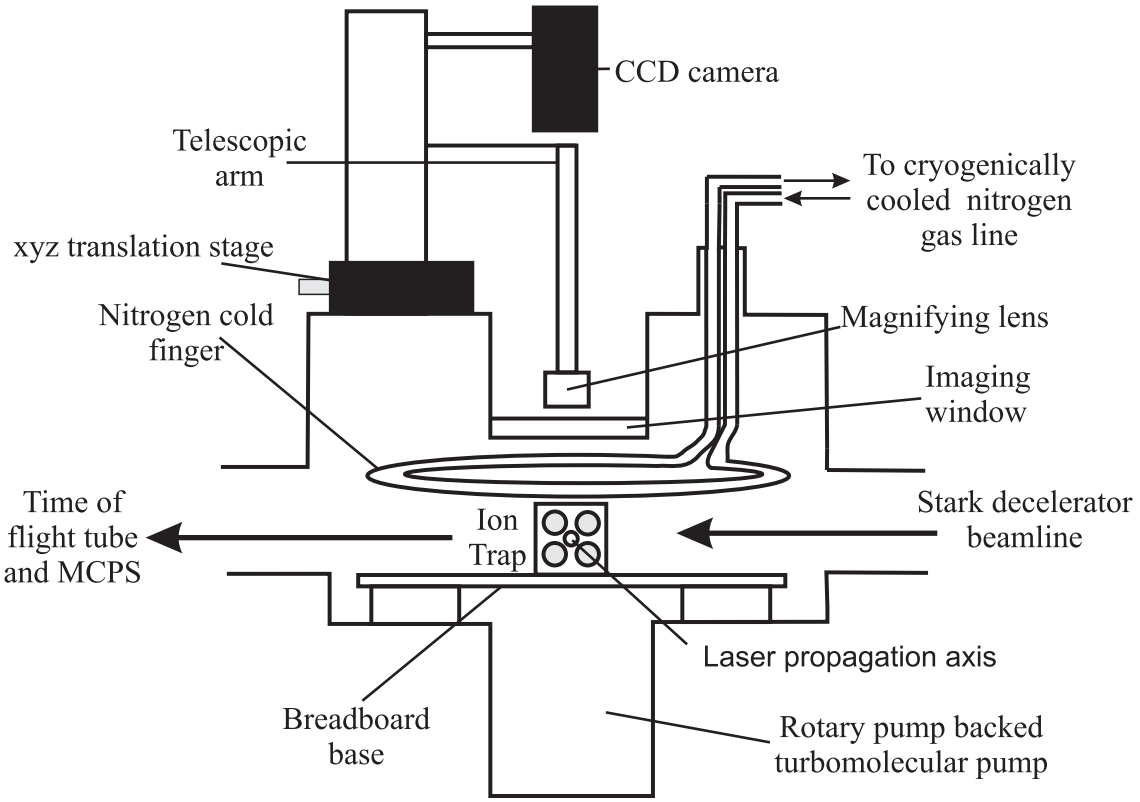

Figure 5.15: Representative side view of the 'old' ion trap chamber, viewed along the laser propagation axis. The figure has been reproduced from Lee Harper's thesis.[68]

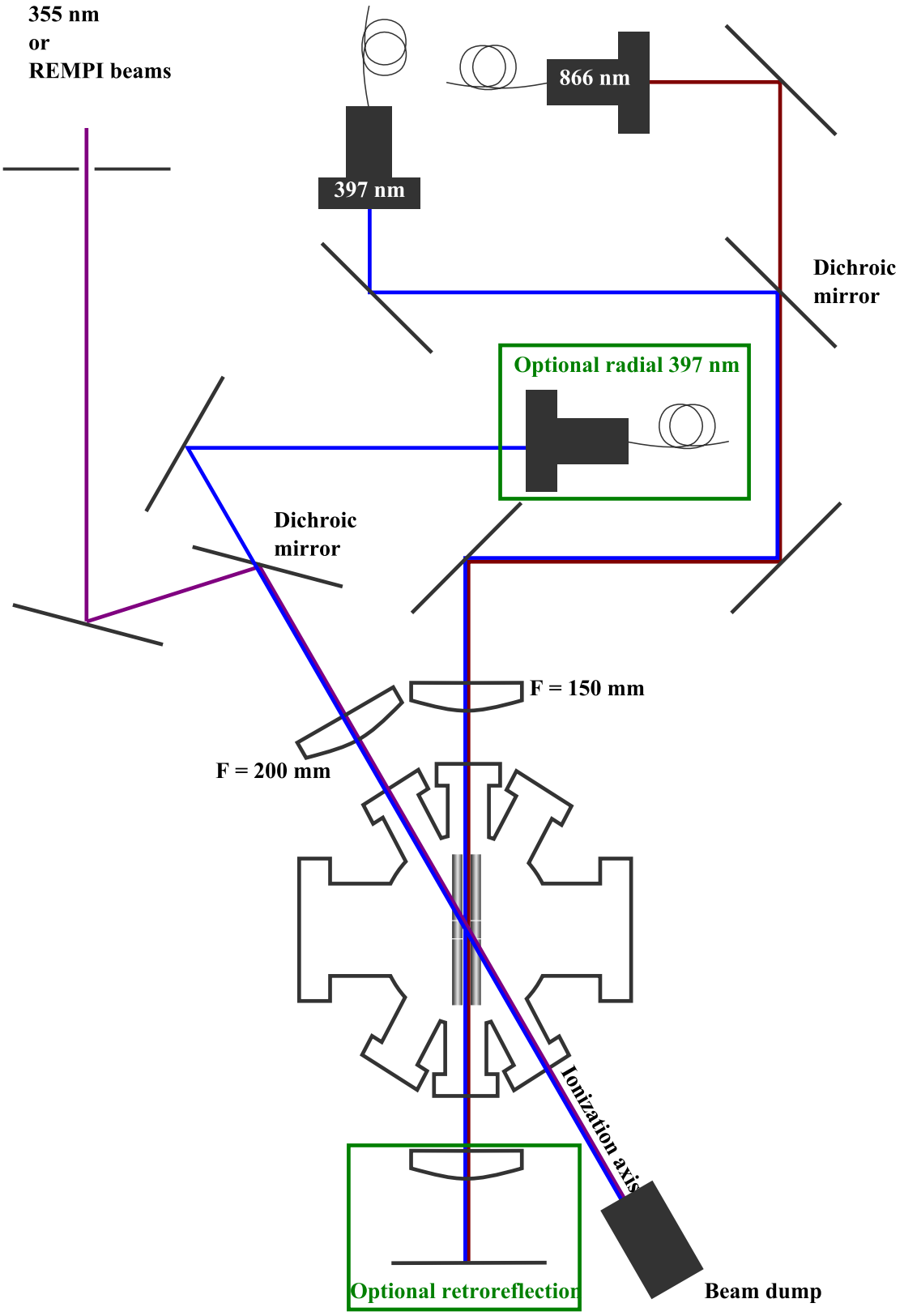

Figure 5.16: Representative top view of the 'new' ion trap chamber and the accompanying optics. The figure has been reproduced from Laura Pollum's thesis.[117]

and $2\pi\times1.32$ – $2\pi\times1.42$ MHz for digital trapping.

An effusive calcium atom beam, emitted from an oven, is collimated with a skimmer and subsequently ionized at the trap center in a two-photon nonresonant process using a 355 nm frequency-tripled Nd:YAG laser. A shutter is used to block the effusive calcium atom beam when the ion trap is not being loaded, to prevent calcium deposition on the electrodes and thus the potential development of patch potentials.

The $^{40}Ca^{+}$ ions formed are initially translationally hot and are laser-cooled, as discussed in section 5.4.1. 397 nm and 866 nm cw diode lasers are fibre coulped to improve their beam profiles (and to enable sharing between two chambers). The 397 nm diode laser output (Toptica DL 100 Pro, $\leq$ 18 mW) and 866 nm diode laser (Toptica DL 100, $\leq$ 50 mW) are fibre-coupled. The 866 nm and 397 nm cooling lasers are in continuous use and are retro-reflected to ensure cooling from both directions of the z coordinate ($\pm z$). The laser linewidths are of the order of several MHz.

A wavemeter (High-Finesse WS-U) simultaneously monitors both diode laser frequencies by virtue of a fiber-switcher (Leoni M1$\times$2 SI50/125). Dr. Chris Rennick has written a LabView program to facilitate efficient locking of the diode lasers at our desired detunings. It has been observed that appropriate locking of the laser frequencies leads to more stable, colder Coulomb crystals. Figure 5.17 is a good example of successfully "locked" cooling laser fluctuations. The primary cooling laser is detuned by approximately 40 – 45 fm for sinusoidal trapping and 10 – 15 fm for digital trapping.

The 397 nm fluorescence emitted by the laser-cooled Ca^{+} ions is focused with a 10$\times$ magnification lens, which then is projected onto a charge coupled device (CCD) camera system to yield a two dimensional projection image. The CCD camera is mounted perpendicular to the ion trap and the Coulomb crystal is viewed perpendicular to the trap axis. Through a Brewster quartz window that provides a line of sight for the camera to 'see' and capture the Coulomb crystal ion fluorescence. In the case of the new ion trap the camera is mounted on the side (rather than above), however the crystal view remains perpendicular.

A time-of-flight (TOF) tube is attached to the chamber, allowing the contents of the trap

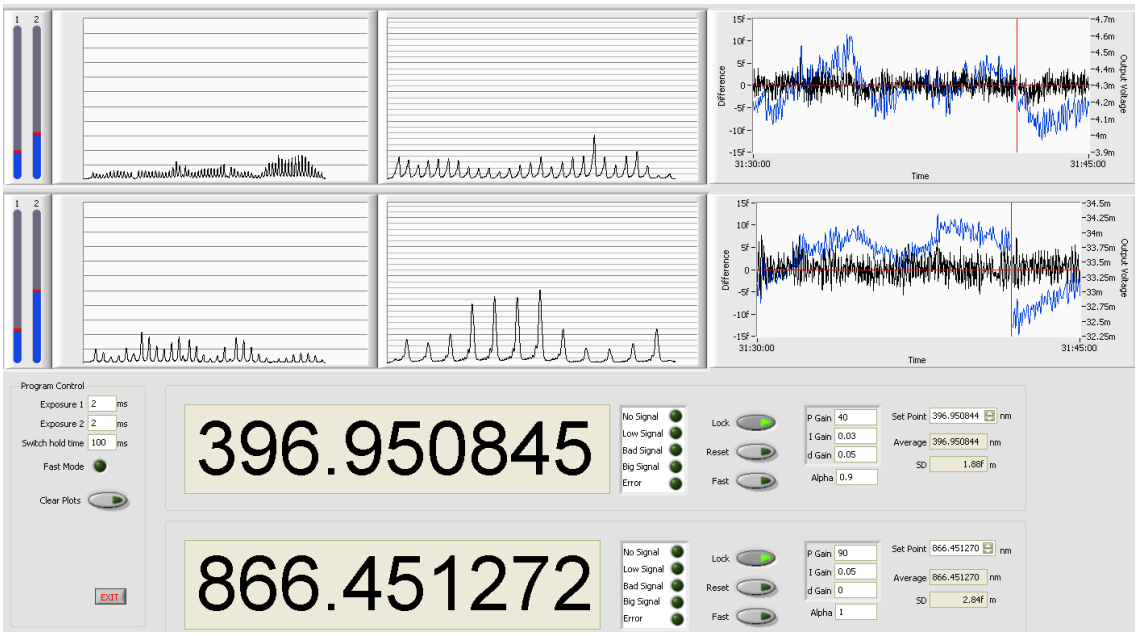

Figure 5.17: Snapshot of the laser control software. The black traces in the right hand window(s) is the laser wavelength fluctuations, and the blue is the voltage applied to control the wavelength. The top window is for the 397 nm diode and the bottom is for the 866 nm diode.

to be ejected onto MCPs by converting the ion trap into an extractor-repeller pair. This is detailed in Chapter 6.

Key difference between the old and new ion trap apparatus

In the old ion trap chamber, a nitrogen cold finger consisting of a double coil of copper tubing has been installed in the chamber. A stream of nitrogen gas, which has been pre-cooled by passing through an external liquid nitrogen heat-exchange reservoir, is flowed through the chamber, facilitating the freezing out of contaminents such as pump oil.

The new ion trap chamber (see figure 5.16) was designed to be attached to a buffer gas cooled source and electrostatic guide apparatus. The chamber is much smaller compared to the old apparatus and is provided with an improved cold finger which allows liquid nitrogen to flow through it. Unlike the old apparatus, this apparatus has a radial ionization/cooling axis. This axis makes radial cooling possible and strings of ions and single ions can be

trapped for significantly longer times. Also, the new oven requires a relatively low current to produce the neutral calcium beam. Another important difference is the imaging system; a photo multiplier tube (PMT) is mounted such that it can be used simultaneously with the CCD camera (rather than interchangeability, as in the old ion trap).

5.6 Experimental Ca^+ Coulomb crystals

A well-centred crystal looks symmetrically elliptical, with symmetric shells of ions containing no dislocations on varying $V_{\rm rf}$ and $U_{\rm dc}$. Digital ion crystals are less stable, and retro-reflecting the cooling lasers is essential. Typically, 500 μW of 397 nm and 1.2 – 1.6 mW of 866 nm are the optimal cooling laser powers utilised. The digital crystal is less forgiving to the cooling laser alignment, with both the 397 nm and 866 nm beams needing to propagate through the trap centre parallel to the trap axis. The fibre optic output couplers have horizontal and vertical degrees of freedom to provide more control on the overlap of the 397 nm and 866 nm cooling lasers. The overlap of the two cooling lasers is checked before and after the ion chamber. To ensure absolute overlap, a webcam is positioned at an equivalent position to the ion trap centre and the beams are deflected onto the webcam to check the overlap at the position of the crystals.

Ca^+ Coulomb crystals have been formed, stably trapped and stored for extended periods of time in both sinusoidally and digitally time-varying trapping fields. Images of Coulomb crystals of different sizes, obtained in the old ion trap apparatus, with both sinusoidal and digital trapping voltages are given in figures 5.18 and 5.19.

In figure 5.18, the centre image is a string of ions in the digital trap obtained at low axial trapping voltages ($U_{\rm dc}$ = 0.5 V). The ions are strongly localized and every bright spot indicates the position of a single Ca^+ ion. Similarly, the right most image in figure 5.19 is a string of ions held in a sinusoidal trap at $U_{\rm dc}$ = 0 V. It is quite clear that the digital ions were hotter.

Figure 5.20 illusrates the effect of varying end cap voltage on a digital crystal trapped at $V_{\rm rf}$ = 50 V and $\omega_{\rm rf} = 2\pi\times1.32$ MHz, with variation of the end cap voltage from 0.2 V to

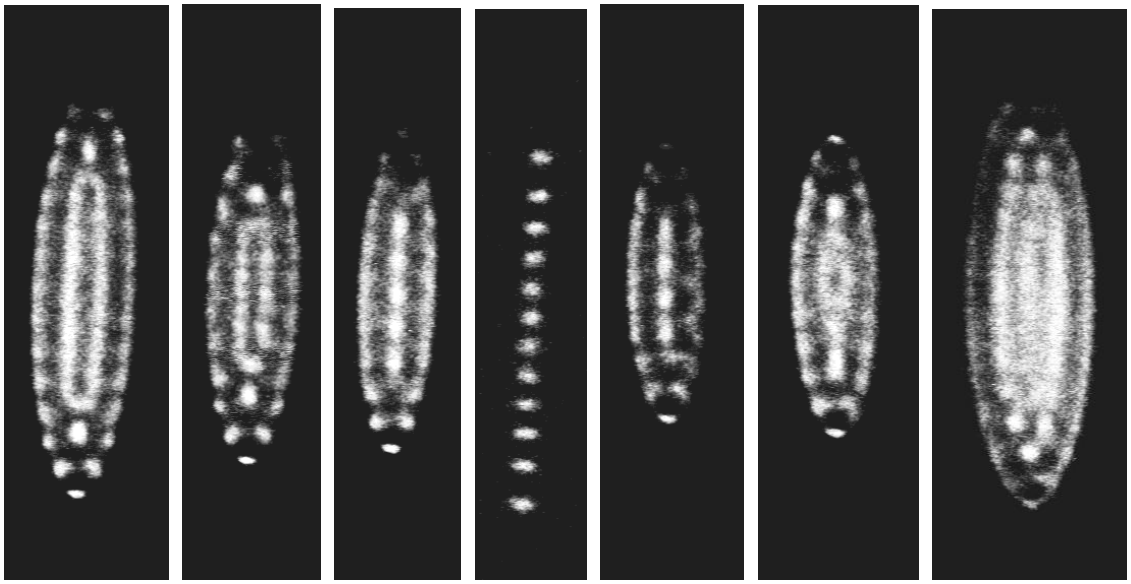

Figure 5.18: Coulomb crystals obtained in the old ion trap with a digital trapping voltage, V_{rf}, of 50 V and a trapping frequency, ω_{rf}, of $2\pi\times1.32$ MHz. The string of ions are trapped at 0 V end cap voltage, U_{dc}; the Coulomb crystals to the left of the string of ions are trapped at U_{dc} of 0.6 V and the three Coulomb crystals to the right at 0.5 V.

2.0 V. It is clearly seen that as the end cap voltage is increased (moving from right to left), the crystal assumes a more spheroidal shape.

Figure 5.21 shows the Coulomb crystals obtained in the new ion trap apparatus. The difference in the appearance of the crystals is due to the different imaging systems used in the two set-ups.

5.7 Conclusions

This chapter introduces the concept of digital ion trapping for ejection of particles onto MCPs. A comprehesive comparison between sinusoidal and digital trapping fields has been performed with respect to trap depth and stability regions. The trap depth has been derived for both digital and sinusoidal trapping fields and the derivation is given in appendix C. The dependence of the stability region on trapping frequency and τ for a digital pulse has been shown. The possibility of co-trapping multiple species has been investigated by plotting stability diagrams for several species, with mass-to-charge ratios ranging from 2 amu (H_2^+) to 131 amu (Xe^+), at the experimental trapping conditions. Species with overlap-

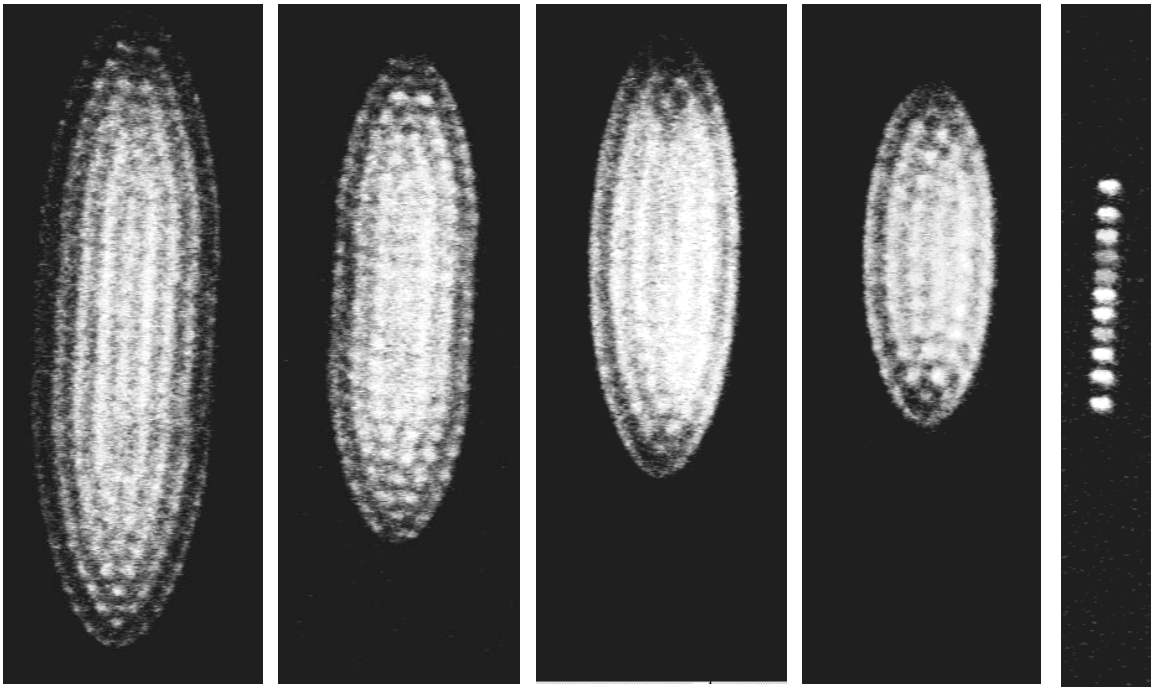

Figure 5.19: Coulomb crystals obtained in the old ion trap with a sinusoidal trapping voltage, V_{rf}, of 160 V, an axial trapping voltage, U_{dc}, of 4 V and a trapping frequency, ω_{rf}, of $2\pi\times3.82$ MHz. The string of ions (final image) is obtained at zero end cap voltage.

ping stability regions could be, in principle, co-trapped simultaneously. Also, it was seen that the regions of stability for Ca^+, $C_2H_2^+$ and ND_3^+ overlap each other in experimentally achievable regions.

Ca^+ Coulomb crystals have thus been formed, stably trapped and stored for extended periods of time in sinusoidally and digitally time-varying trapping fields (in both the old and the new ion trap apparatus).

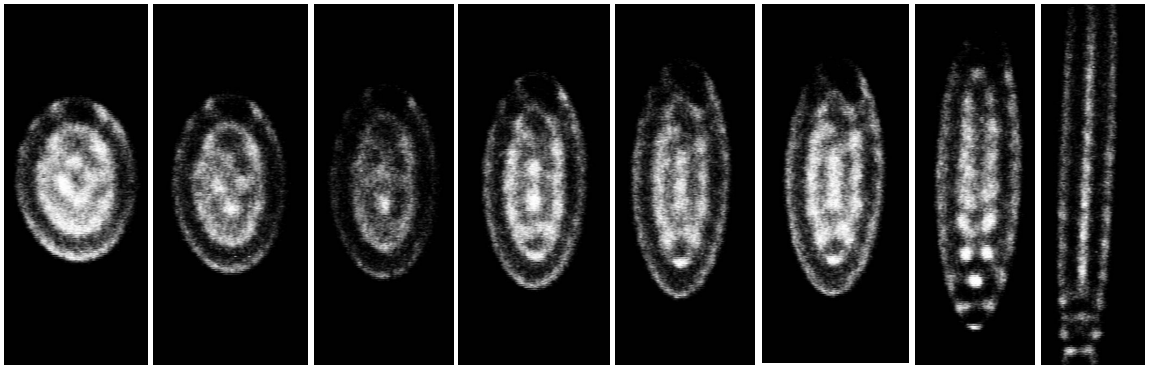

Figure 5.20: A single Coulomb crystal at $V_{\mathrm{rf}} = 50$ V, a digital trapping frequency of $2\pi \times 1.32$ MHz and varying U_{dc} (2.0 V, 1.8 V, 1.6 V, 1.4 V, 1.2 V, 1.0 V, 0.8 V and 0.2 V, from left to right respectively).

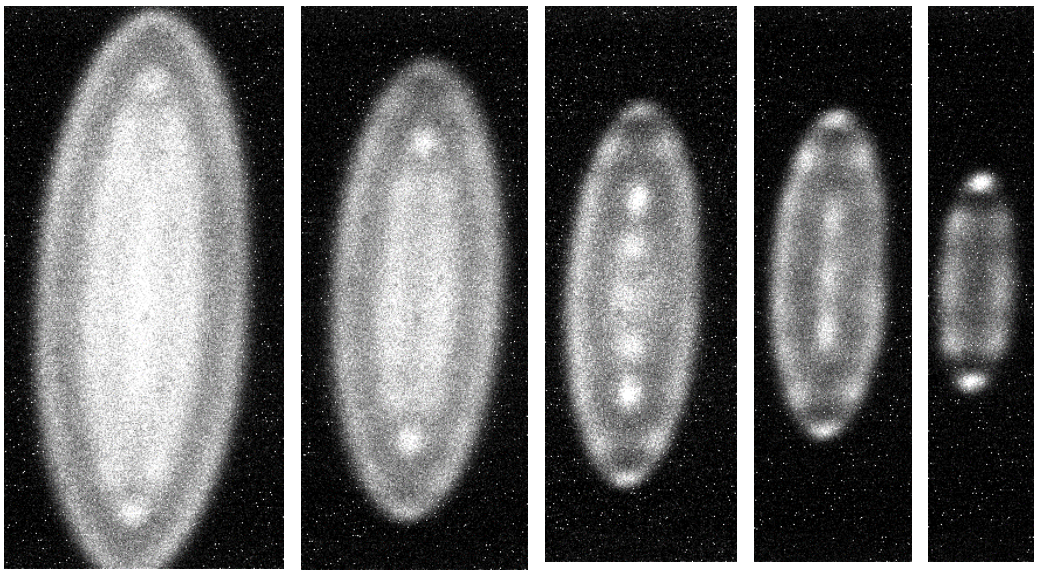

Figure 5.21: Coulomb crystals of various sizes obtained in the new ion trap at a digital trapping voltage, V_{rf}, of 50 V, with a axial trapping voltage, U_{dc}, of 1 V and a trapping frequency, ω_{rf}, of $2\pi \times 1.32$ MHz.

Chapter 6

Mass Spectrometry in a Digital Ion Trap

6.1 Introduction

Coulomb crystals are a useful tool for the study of cold ion-molecule reactions involving sympathetically cooled molecular ions. When the mass of the reactant molecular ion is higher (lower) than calcium (the laser-cooled ion in our experiments) and the mass of the product ion is lower (higher) than calcium, then the reaction can be monitored by observing the change in the shape of the Coulomb crystal. An example of such a chemical process studied in our laboratory is,

$$OCS^+ + ND_3 \rightarrow ND_3^+ + OCS.$$

Such a technique for monitoring a reaction is not effective for a reaction where the reactant(s) and product(s) are both either lighter or heavier than calcium. One such example of this is the charge transfer reaction between $C_2H_2^+$ and ND_3:

$$C_2H_2^+ + ND_3 \rightarrow C_2H_2 + ND_3^+.$$

As both $C_2H_2^+$ and ND_3^+ are lighter than Ca^+, and have similar masses, reaction progress cannot be (easily) monitored by visual changes in the crystal. The above reaction can however be monitored by a novel destructive technique – ion trap ejection. Ejection of the (multi-component) Coulomb crystal into a time-of-flight (TOF) mass spectrometer allows the masses and relative abundances of the ions within the Coulomb crystal to be established. This enables unambiguous determination of the constituents of the dark ions in the

Coulomb crystal, providing an alternative technique for monitoring a reaction by establishing the relationship between the number of ions in the crystal and the response obtained by ejecting the Coulomb crystal into the TOF tube (for detection by the MCPs). By ejecting the Coulomb crystals at different time steps, for a series of crystals, the reaction rate could be monitored. This will enable the study of reactions where both reactant and product ions are lighter (or heavier) than calcium.

Resonant mass excitation spectrometry offers an alternative, non-destructive technique [71, 118] for detecting the masses of ions within a crystal, typically used for small numbers of ions. The technique establishes the resonant frequencies at which the crystal heats up, and these frequencies are dependent on the masses of the ions. As discussed in Chapter 5, the secular frequency of any ion in an ion trap is dependent on its mass and by measuring the secular frequency of the ion it is possible to deduce the masses of the constituent ion(s).[119] The secular frequency can be experimentally measured by applying an additional, scanned rf drive voltage to the ion trap electrodes. When it is in resonance with the frequency of oscillation of the ions in the ion trap the relevant motion is excited and the ions are ejected from the trap if the drive amplitude is sufficiently high.[120]

Baba and Waki [15] developed a non-destructive version of the resonant excitation technique described in the previous paragraph. In Baba and Waki's approach, the secular motion of the laser-cooled ions (Coulomb crystal) in an ion trap is excited by scanning the rf drive frequency, causing the intensity of the fluorescence of the Coulomb crystal to modulate. When the secular motion of trapped ions is excited, a transfer of kinetic energy to the laser-cooled ions occurs by the Coulomb interaction, as a result of which the laser-cooled ions heat up and are consequently Doppler-shifted out of their laser-cooling resonant frequency. This Doppler-shift results in a loss of fluorescence intensity, which is easily noticeable in the images captured by the CCD camera. By measuring the fluorescence yield as a function of the drive frequency, a mass spectrum is obtained. The frequencies corresponding to minima in the fluorescence yield curve represent the motional frequencies of the ions. This technique is not destructive, as only a weak rf drive voltage frequency is employed and the

ions are not ejected out of the trap. They may be temporarily heated however, which could affect the reaction rate.

Schiller and co-workers developed a variant of the technique suggested by Baba and Waki,[15] whereby the cooling laser is far detuned, and resonant excitation Doppler-shifts the absorption frequency of the ions closer to the laser-cooling transition. In this technique, the maxima in the fluorescence yield curve denote the resonant frequencies.[121]

In a multi-component Coulomb crystal, the positions and widths of the motional resonances are dependent on the trapping parameters, the number of ions and the composition of the sample. This is caused by the strong Coulomb coupling between the closely spaced ions in the crystal. The resonant-excitation mass spectra of larger many-component crystals are not well resolved, as has been observed in our laboratory, during the study of the reaction $Ca^+ + CH_3F \rightarrow CaF^+ + CH_3$.[26, 71] However, the circumstances are different for a two-ion crystal with one laser-cooled and one sympathetically-cooled ion – here the mass spectrum is well resolved, as demonstrated by Drewsen and coworkers.[122]

Of the six motional degrees of freedom available to a Coulomb crystal of two ions, two normal modes are directed along the trap axis, the centre-of-mass mode ν_- (ions oscillate in phase), and a breathing or symmetric stretching mode, ν_+. These frequencies can be expressed as,

$$v_{\pm}^2 = \left[\left(1 + \frac{m_1}{m_2}\right) \pm \sqrt{1 - \frac{m_1}{m_2} + \left(\frac{m_1}{m_2}\right)^2}\right] v_1^2, \tag{6.1}$$

in a harmonic trap potential, where m_1 and m_2 stand for the masses of the two ions and v_1 is the frequency of the single ion of mass m_1. By measuring ν_- and ν_+, the mass m_2 can be easily found out, as m_1 and v_1 represent the mass and resonant frequency of the laser-cooled ion, which is known.

Two different experimental approaches were employed by Drewsen and co-workers to determine ν_- and subsequently deduce m_2. The first approach involved using a conventional rf resonant-excitation scheme with laser-cooling fluorescence detection but was limited by the damping of the ion motion caused by the electric and optical fields. The second approach overcame the inadvertant damping effects by inducing resonant excitation through

optical forces and detecting only the component of the ion motion in phase with the periodic perturbation. Modulation of the laser-cooling force induced by chopping one of the cooling lasers at a variable frequency enabled the ion fluorescence in phase with the perturbing force to be measured. The mass of the sympathetically loaded ion could then be determined from the dispersion-shaped fluorescence signatures.

By employing pulsed excitation and analysis of the fluorescence of laser-cooled ions, Keller and co-workers [101] have developed a 'crystal weighing' technique to measure the secular motion of trapped ions. They measured the centre-of-mass mode frequency of single ions as well as for the entire ion crystals. Their technique is also based on the principle of resonant-excitation. The motion is excited by short voltage pulses, in contrast to the other methods described above, and is detected through the autocorrelation of the ions' fluorescence. Fourier transforming the autocorrelation determines the secular frequency. They have used this method to measure the mass of ions and observed charge exchange collisions between trapped calcium isotopes. This method is limited to systems which have few different components and where the product masses are known.

These mass-excitation techniques are most useful at the few ion level but fail to give the relative number of ions accurately in larger Coulomb crystals, though they can help provide a qualitative assessment of the identities of the ions in an ion trap. Also, a time study is not possible as the technique uses a frequency scan to detect the resonant frequency shift and hence cannot simultaneously establish the identities of all ions present at a given time.

In this chapter, the application of a digital or pulsed rf trapping potential to extract the contents of the trap onto a time-of-flight mass spectrometer (TOF-MS) is described. The primary advantages of this arrangement, arising from the clean switching off the rf field, is discussed in Chapter 5, section 5.1 and section 6.3.1 of this chapter. The use of the digital waveform, however, may also bring additional advantages. It is possible to include a dead time in the waveform (where the field is zero) for a controlled portion of the rf period. This could be useful, for example, when the ion trap is combined with the Stark decelerator to avoid interference between the rf field and the pulsed voltage applied

to the Stark decelerator. The zero-field conditions might also be desirable in experiments involving the generation and trapping of excited Rydberg states in selected ionic species.

6.2 Time-of-flight mass spectrometry

Time-of-flight mass spectrometers are based on a simple mass-separation principle. The velocities of ionised species starting from the same position at the same time, and accelerated by a constant homogeneous electrostatic field, are related to their mass-to-charge ratio. The relative masses of the species (assuming all are singly charged) can be deduced from their arrival time at a detector.

The first proposal for a MS based on the TOF principle was made by W. E. Stephens [123] and later improved by W. C. Wiley and I. H. McLaren, who introduced two acceleration regions.[124] Wiley and McLaren observed that ions of a particular mass-to-charge ratio would reach the detector with a spread in arrival times, due to the effects of uncertainty in the time of ion formation (temporal distribution), location in the extraction field (spatial distribution) and initial kinetic energy (kinetic energy distribution), limiting the resolution of a given mass peak.

The temporal distribution arises when two ions of the same mass are formed at different times with the same kinetic energy. The field-free region is traversed by each ion, maintaining a constant difference in time and space. Ions of the same mass, that are formed at the same time with the same initial kinetic energy, but are formed at different locations in the extraction field, experience a different change of potential on crossing the source region; they are accelerated to different kinetic energies, giving rise to a spatial distribution. Ions formed with different initial kinetic energies have different final velocities after acceleration and arrive at the detector at different times, giving rise to a kinetic energy distribution. Ions of the same kinetic energy but with velocities in different directions will also arrive at the detector at different times, corresponding to their turn around time in the source. The ability of the spectrometer to resolve masses despite the initial space distribution is called space resolution (space focussing). The time spread introduced by the initial kinetic energy

distribution is called energy resolution.[124] The mass resolution, $\Delta m/m$, is the largest mass, m, for which adjacent masses are completely separated.

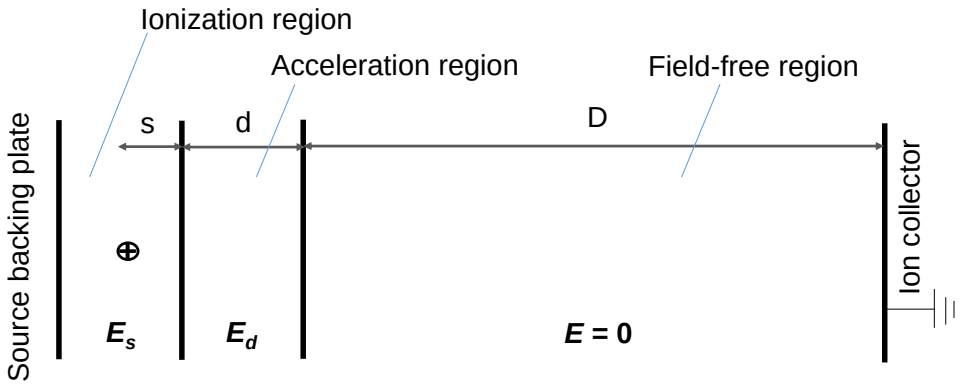

Figure 6.1: Schematic repesentation of a Wiley McLaren TOF-MS.

6.2.1 Flight time

The schematic representation of the path of the ion from the source to the detector is given in figure 6.1, where s is the distance of the ion (in the ionization region) from the first plate of the acceleration region, d is the length of the acceleration region and D is the length of the field-free region. In moving through the source, any ion with mass m and charge q with initial energy, U_0, increases its energy to value U, given by: [124]

$$U = U_0 + qsE_\mathrm{s} + qdE_\mathrm{d}, \tag{6.2}$$

where E_s is the field in the source region and E_d is the field in the acceleration region. The total time, t, taken by the ion to reach the detector is:

$$t = t_\mathrm{s} + t_\mathrm{d} + t_\mathrm{D}, \tag{6.3}$$

where t_D is the time in the field free time-of-flight region, t_d is the time in the acceleration region and t_s is the time in the initial ionization region and are given by:

$$t_\mathrm{s} = 1.02\frac{2m^{\frac{1}{2}}}{qE_\mathrm{s}}[(U_0 + qsE_\mathrm{s})^{\frac{1}{2}} \pm (U_0)^{\frac{1}{2}}], \tag{6.4}$$

$$t_\mathrm{d} = 1.02\frac{2m^{\frac{1}{2}}}{qE_\mathrm{d}}[U^{\frac{1}{2}} - (U_0 + qsE_\mathrm{s})^{\frac{1}{2}}], \text{ and} \tag{6.5}$$

$$t_{\mathrm{D}} = 1.02\frac{2m^{\frac{1}{2}}D}{2U^{\frac{1}{2}}}. \tag{6.6}$$

The $+$ and $-$ signs in t_{s} correspond to initial velocities directed away from and towards the collector, respectively. When $U_0 = 0$, $s = s_0$ (where s_0 is the average initial position of the ions) and,

$$U_{\mathrm{t}} = qs_0E_{\mathrm{s}} + qdE_{\mathrm{d}} \text{ and} \tag{6.7}$$

$$k_0 = \frac{(s_0E_{\mathrm{s}} + dE_{\mathrm{d}})}{s_0E_{\mathrm{s}}}. \tag{6.8}$$

The time-of-flight, t, is given by:

$$t = 1.02\left(\frac{m}{2U_{\mathrm{t}}}\right)^{\frac{1}{2}}\left(2k_0^{\frac{1}{2}}s_0 + \frac{2k_0^{\frac{1}{2}}}{k_0^{\frac{1}{2}}+1}d + D\right). \tag{6.9}$$

The higher resolution adjustibility achievable with the double-field source (the modification introduced by Wiley and McLaren) is due to the flexibility introduced by the two new parameters d and E_d/E_s, which are not available in the single-field source. The measurement of relative mass intensities is possible with increased precision.

6.3 Mass spectrometry in an ion trap

Mass spectrometry using a quadrupole ion trap can be achieved by converting the trap electrodes to act as an extractor-repeller pair. This is achieved by applying a slightly lower ejection (dc) voltage to the electrodes which are closer to the TOF tube (forming the extractor) than to the ones that are farther away (repeller). Ion traps have been used by several research groups, including our research group, to record REMPI spectra.

Recently, E. Hudson and co-workers [125] demonstrated "laser-cooling-assisted mass spectrometry" (LA-MS) to prepare assays of molecules for mass spectrometry. Their method showed reduced width of the initial phase-space distribution by sympathetically cooling the input molecules in an ion trap. They demonstrated improved mass resolution (from $\Delta m/m$ = 35 to $\Delta m/m$ = 500) over conventional MS and isotopic resolution at room temperature.

The LA-MS technique also showed an increased detection efficiency by over an order of magnitude.

The apparatus used in the Hudson experiment consists of a segmented linear quadrupole trap (LQT) and a TOF-MS, into which molecules can be radially extracted from the LQT. The LQT is driven asymmetrically; two diagonally opposing electrodes at rf voltage, the others at rf ground. The main laser cooled species used is Ba^+ or Yb^+; for Ba^+ (Yb^+), a Doppler cooling beam at 493 nm (369 nm) and a repump beam at 650 nm (935 nm) are required. The ions of interest are then sympathetically loaded into the trap, with the secular temperature estimated to be 1 – 100 mK.

The rf trapping voltage was turned off within a fraction of an rf cycle and the electrodes pulsed to high DC voltages with a 10% – 90% rise time of $\approx$ 250 ns. The high voltage is applied such that a two-stage electric field is established, which radially extracts the cold atoms and molecules from the LQT into the TOF-MS (extractor voltage of 1.2 kV, repeller voltage of 1.4 kV). The molecules are detected with a channel electron multiplier (CEM), which is shielded from the drift tube by a grounded stainless steel mesh.

Hudson and co-workers have demonstrated unit mass resolution in the resulting mass spectra and have detected the different isotopes of Yb, although the relative heights of the Yb peaks do not reflect the natural abundance of each isotope. They have not reported on any quantitative study of the detection efficiencies of different masses and crystal geometries. The work presented in this chapter (experimental descripton given in section 6.3.1) details the design, implementation and characterisation of a digital ion trap mass spectrometry method to quantitatively monitor reactions within Coulomb crystals. A relationship between the number of ions in the crystal and the response obtained by ejecting these into the TOF mass-spectrometer will be established in subsequent sections. The utility of the technique to help loading cleaner crystals is also discussed.

Ito and co-workers [126] demonstrated a buffer gas filled radio-frequency quadrupole ion cooling trap for multi-reflection time-of-flight mass spectrometry (MR-TOF), developed for use with short-lived nuclei. Their ion trap apparatus consists of two main compo-

nents: an asymmetric taper trap and a flat trap. The ions are cooled in 2 ms in the flat trap and then ejected orthogonally to the MR-TOF detector.

The flat trap operates on the same principle as a segmented Paul trap, however the flat trap design uses six strip electrodes and is constructed using two printed circuit boards (PCBs). While the quadrupole approximation is not suffcient for use as a mass filter, it is perfectly well-suited for ion storage and cooling. The PCBs are mounted on an aluminum block and each PCB consists of three strips divided into 7 segments. The central electrode of each board has a hole at its centre. By applying a potential difference between the centre electrodes of the PCBs, ions are extracted orthogonally. The taper trap electrodes are not parallel; the tapered structure produces an effective axial drag force. The pre-cooled ions are efficiently transported to the flat trap due to the drag force, and because of this the ions are ejected faster from the taper trap than from the parallel trap.

The ion trap system was developed for cooling ions in the flat trap before ejecting the ions orthogonally to the MR-TOF for precise mass measurement and analysis. They have shown that ejection from the taper trap gives a sharper mass spectrum. The efficiency of detection was were low: $\approx 27\%$ for $^{23}Na^{+}$ and $\approx 5.1\%$ for $^{7}Li^{+}$, though the cooling time was appreciably fast ($\sim$ 2 ms).

6.3.1 Experimental description

The conversion of the trap electrodes into an extractor-repeller pair is achieved in our research group by using a custom-built digital voltage generator, which has the ability to output digital trapping voltages or, when triggered, to apply ejection voltages to the ion trap electrodes. A slightly lower ejection (dc) voltage is applied to the “extractor” electrodes (which are closer to the TOF tube) than to the “repeller” electrodes. The schematics of this is represented in figure 6.2.

Sinusoidally time-varying trapping voltages cannot easily be switched off cleanly, as the use of resonant circuitry results in ‘ringing’ even after the trapping voltage is switched off. The use of digital trapping voltages eliminates these ringing issues. Figure 6.3 shows the

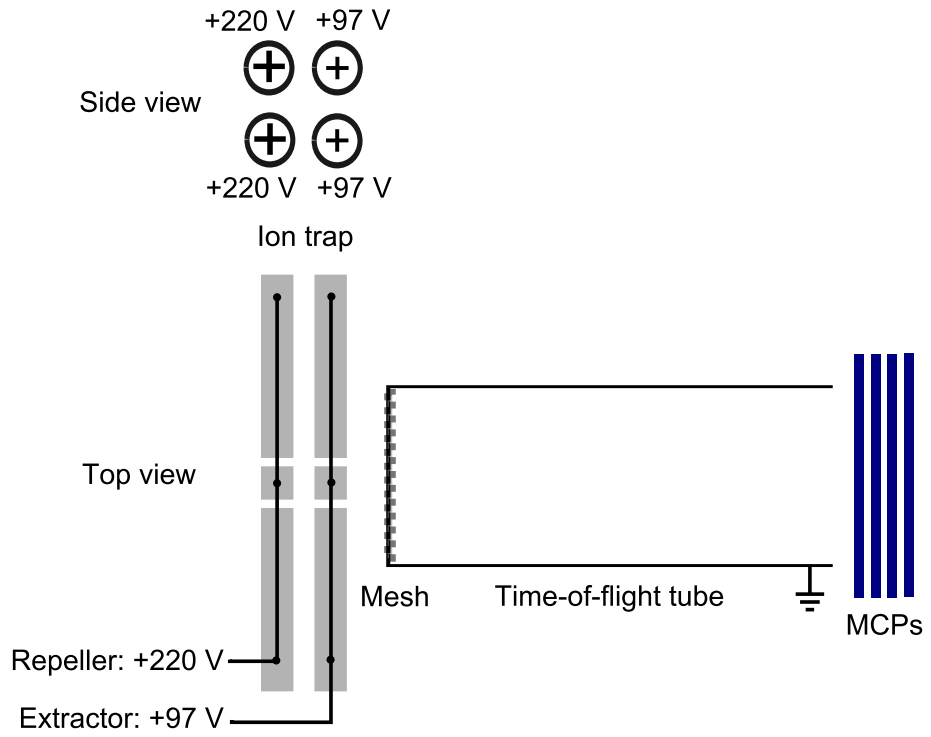

Figure 6.2: Schematic representation of the extractor-repeller pair and the time-of-flight apparatus.

real digital trapping voltages and extractor-repeller ejection pulses used experimentally. The ejection pulses are clean – there is no ringing – and the electrodes return to normal trapping voltages after ejecting the contents of the trap. Simulations performed by Alexander Smith [109] using MATLAB suggest that the time required for a Ca^+ ion to travel from the centre of the trap to the mesh at the start of the TOF tube is $\sim$1.5 μs; the minimum width of ejection the pulse should thus be greater than $\sim$1.5 μs to ensure all ions receive the same voltage "kick".

The time between switching off the trapping voltages and switching on the ejection voltages is the 'delay' time and can be varied in this experimental set-up from 0 μs – 1.15 μs. The width of the ejection pulse can be varied from 1.12 μs to 3.92 μs (repeller voltage) and 1.12 μs to 10 μs (extractor voltage). The larger width for the extractor pulse enables the field between the mesh and the second trap electrode pair to be maintained for longer. The delay time should be kept low to minimise Coulomb repulsion after the trapping voltage is turned off and thus to reduce the chances of obtaining broadened mass spectrometric peaks

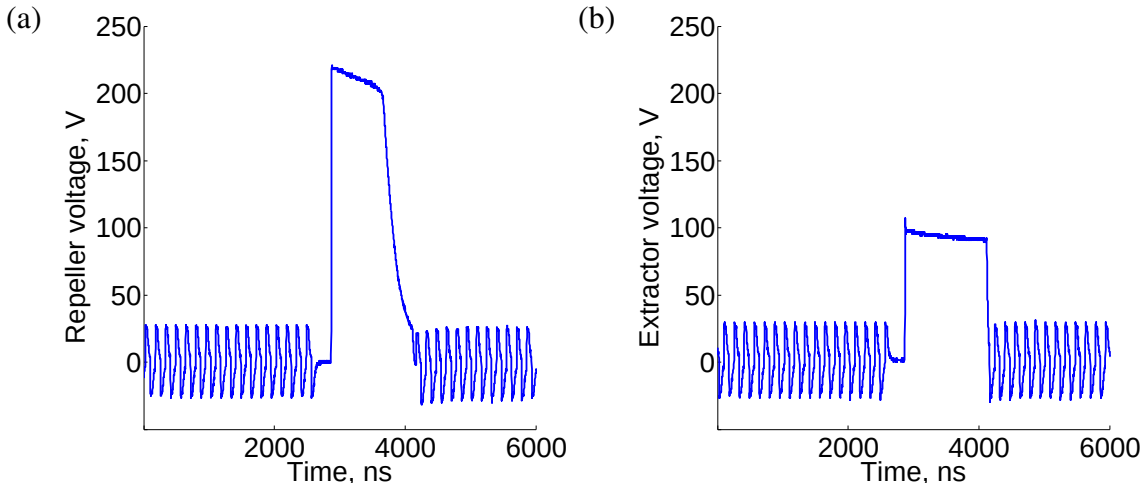

Figure 6.3: Real experimental ejection pulses. (a) A repeller voltage of 220 V and (b) extractor voltage of 97 V are typical experimental settings.

or ion loss.

Typically, a repeller voltage of 220 V and a extractor voltage of 97 V is applied. The MCPs were maintained at -1800 to -1900 V. A boot-strap amplifier (built in-house) is used to amplify the signal, and a bias voltage of +100 V is applied to the MCPs.

Coulomb crystals held in the trap are ejected (destructively) into the TOF mass-spectrometer and are detected by the MCPs. The mass spectrum obtained is saved for analysis. Before ejecting the Coulomb crystal, an image of the crystal is always captured and saved. The image is analysed to deduce the number of ions in the crystal and the TOF spectrum is analysed to get the corresponding signal intensity. The ultimate aim of this work is to establish a relationship between the number of ions ejected and the signal intensity recorded, so that quantitative data on reaction rates can be deduced.

6.3.2 Ion number fitting – deducing the number of ions in a crystal

The CCMD code described in section 5.4.3 is used to generate simulated images of crystals under the experimental conditions. Before ejecting any crystal into the TOF tube, an image of the crystal is captured and saved. The experimental image is then compared against simulated crystals and the ion number of each ejected crystal is evaluated.

For pure Ca^+ Coulomb crystals, simulations are performed for crystals consisting of 5

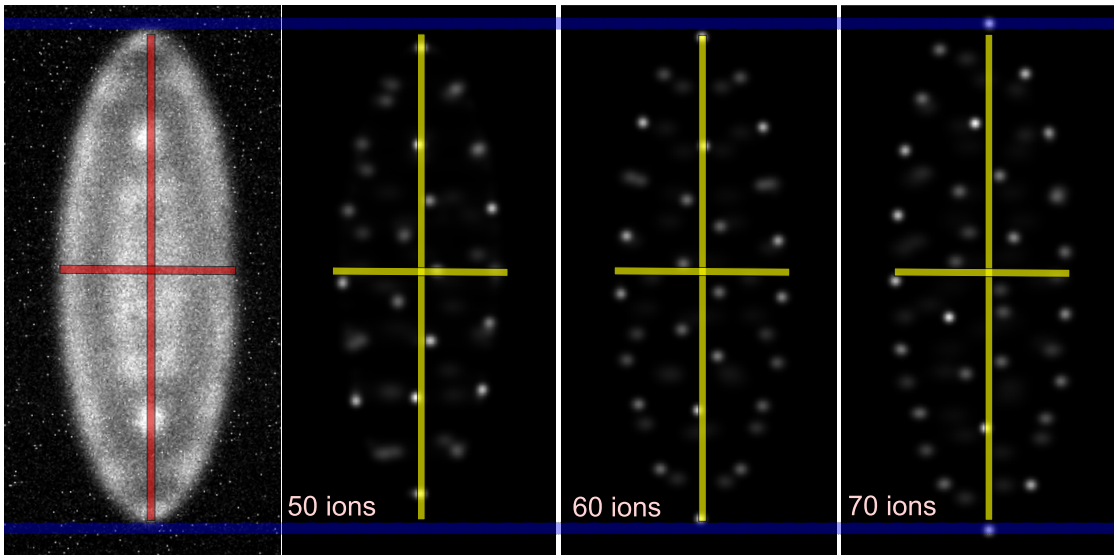

Figure 6.4: Establishing the number of Ca^+ ions in the experimental image (far left) through comparison with simulated crystals. As indicated by the vertical lines, a crystal with 50 ions is too small and 70 ions too large; a 60 ion crystal yields the best fit to experiment.

– 200 Ca^+ ions in step sizes of 5. For the multicomponent Ca^+ – CaF^+ Coulomb crystals, an array of simulated crystals of sizes ranging from 5 – 100 Ca^+ ions, and 5 – 100 CaF^+ ions (co-trapped along with Ca^+), have been generated.

Figure 6.4 illustrates how ion numbers are assigned to an experimental image of a pure Ca^+ Coulomb crystal. The left most crystal is the image captured before ejecting the Coulomb crystal into the TOF tube. The remaining three images are simulated Ca^+ Coulomb crystals generated at the same trapping conditions as the experimental image; the only parameter varied is the number of ions in the crystal. The vertical and horizontal semi-transparent lines are fitted to the experimental image to guide the eye. The positions of the ions in the experimental image are matched with the simulated images, achieved by overlaying the simulated crystals on the experimental crystal. In this way, the number of ions in a crystal can be established to within ± 5 ions.

6.3.3 Analysis of TOF trace

After ejecting a crystal from the ion trap, the resulting TOF trace is analysed by a code I developed where base line substraction is performed and the area under each peak is cal-

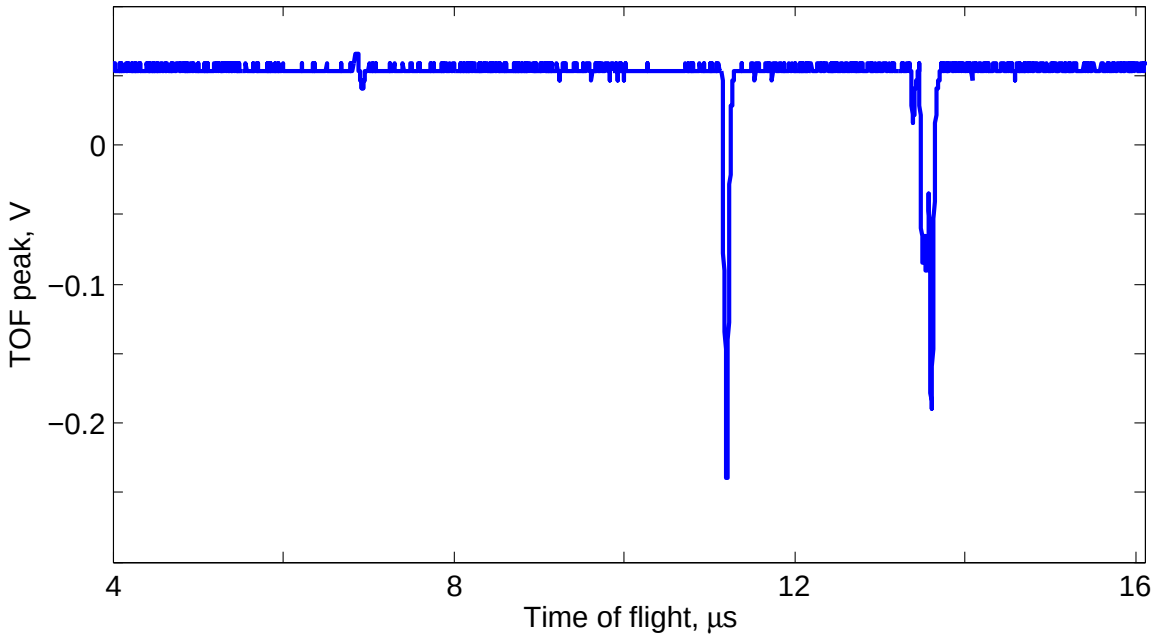

Figure 6.5: A representative TOF trace, obtained on ejecting a Ca^+–CaF^+ bi-component crystal.

culated. Figure 6.5 shows a representative TOF spectrum as recorded by the oscilloscope, obtained on ejecting a bi-component Ca^+ – CaF^+ Coulomb crystal. The area under each peak was calculated (after appropriate background substraction). The integrated peak intensity is plotted against the number of ions, and characterisation of these experiments is provided in section 6.5.

6.4 Investigating Ca^+ Coulomb crystals by ion ejection

The digital ion ejection technique is very useful in investigating the identity and number of ions loaded into the ion trap. Figure 6.6 shows two representative traces for "Ca^+ only" Coulomb crystals. One of the most common impurities that is formed inadvertantly along with calcium using a 325 nm ionization laser is pump oil. The pump oil peaks are obtained at masses 55 and 57 amu. Figure 6.6 (a) is the TOF spectrum obtained for a Ca^+ Coulomb crystal, where calcium has been ionized at 325 nm by a non-resonant process. The peak obtained at 6.6 μs is that of Ca^+ and the other peak at 7.92 μs is pump oil ion contamination. In contrast, Figure 6.6 (b) is the TOF spectrum obtained on ejecting a Coulomb crystal

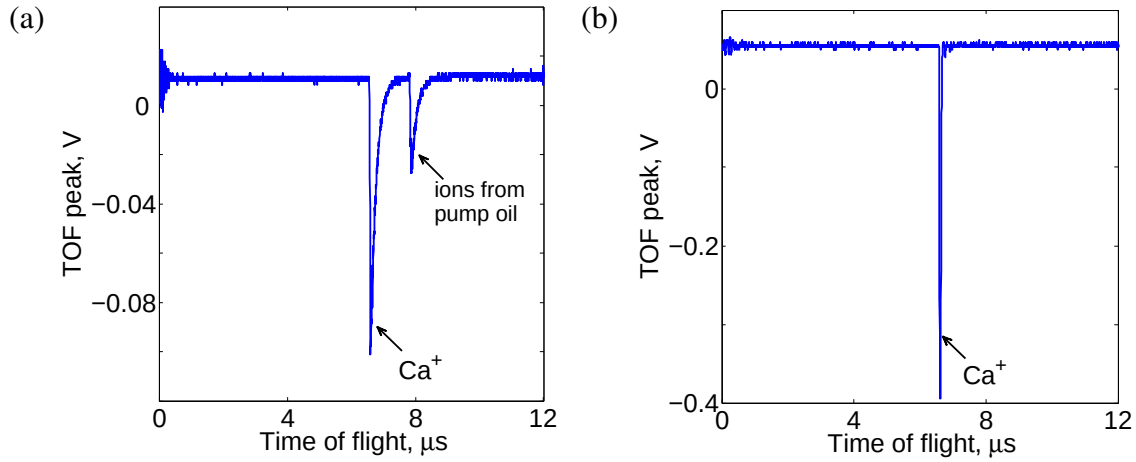

Figure 6.6: (a) Oscilloscope trace for a Ca^+ Coulomb crystal which has been ionized at 325 nm. The peak obtained at 6.6 μs is that of Ca^+ and the other peak at 7.92 μs is pump oil contamination. (b) Here the calcium ionization was achieved using a 355 nm laser, and the resultant crystals were consistantly found to be clean (free from pump oil contaminants). The width of the mass peaks for the two traces are not same because two different amplifiers were used for recording them; the amplifier corresponding to the figure on the right has a much faster response time.

where the calcium ionization was brought about by using a 355 nm laser (again a non-resonant process); the resultant crystals were consistently found to be clean.

Consequently, we are now using only 355 nm ionization of calcium in a bid to minimise the formation of any undesirable (contaminant) ions.

6.5 Analysis of Ca^+ Coulomb crystal ejection – the relationship between the integrated peak height of the TOF spectrum and the number of ions in the crystal

A quantitative analysis of pure Ca^+ Coulomb crystal ejection is undertaken, and the correlation between the number of Ca^+ ions in the crystal and the peak height of the TOF spectrum obtained is established. Conditions henceforth referred to as the 'standard conditions' indicate $V_{\rm rf}$ = 50 V, $U_{\rm dc}$ = 1 V. MCPs were maintained at -1900 V (bias voltage of +100 V) unless otherwise mentioned. The frequency of trapping fields used typically ranges between $2\pi\times$ 1.327 – $2\pi\times$ 1.427 MHz. Crystals have also been ejected at $U_{\rm dc}$ = 0 V and 2 V and the effect of MCP voltages has been studied.

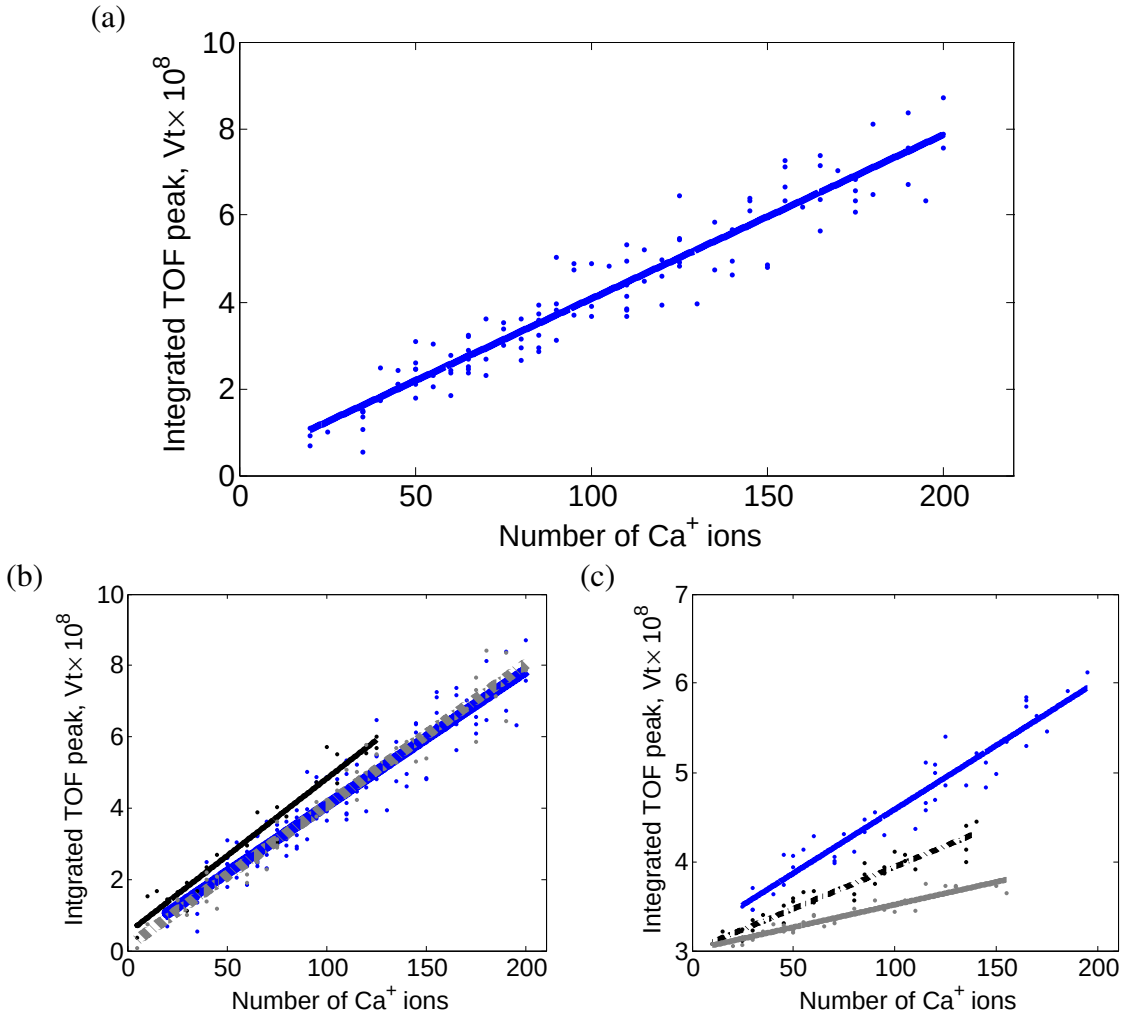

Figure 6.7: The relationship between the integrated TOF peaks and the number of Ca^+ ions in the ejected crystal. Experimental parameters are V_{rf} = 50 V and $\omega_{rf} = 2\pi\times$ 1.327 MHz and the MCP voltage is maintained at -1900 V unless otherwise mentioned. (a) Crystal ejected at U_{dc} = 1 V. (b) Comparison of ejection at U_{dc} = 0.1 V (black solid line), 1 V (blue solid line) and 2 V (grey dashed line). (c) Crystal ejection with U_{dc} = 1 V, at different MCP voltages: -1800 V (grey solid line), -1850 V (black dashed-dotted line) and -1900 V (blue solid line).

Figure 6.7 summarises the characterisation results obtained: subplot (a) shows the relationship obtained at standard conditions. A linear fit was found to give the best match to the data. The adjacent R^2 parameter for this fit was 0.912 with a slope of $3.79\times10^{-10}\pm0.11\times10^{-10}$, and 119 data points were used to generate this plot. The excellent fit to the linear trendline is very useful, enabling a simple and clear relationship between ion number and peak intensity to be established. The scatter obtained is mainly due to the uncertainty in the assignment of the number of ions in each crystal and the uncertainty in the calculation of the area under the TOF spectrum peak. More detailed comments on possible sources of error are given in section 6.8.

Figure 6.7 (b) shows the effect on the TOF peak height of varying the end-cap voltage at which the crystal is ejected. Here the crystal was trapped at U_{dc} = 0.1 V, 1 V and 2 V and ejected at these end-cap voltages. No significant difference is observed in the resultant TOF peak intensities. The effect of using different MCP voltages has been studied and in figure 6.7 (c), three different voltages were used: -1800 V, -1850 V and -1900 V. The slope of the best-fit line was found to be maximised for the highest MCP voltage. As expected, even at lower MCP voltages a clear linear relationship between the number of ions and integrated TOF peak exists. Simulations suggest that saturation effects are not likely to occur under these settings with < 200 ions.

For the above study the delay time between switching off the trapping voltage and applying the ejection pulse is kept to a minimum. A maximum width of the ejection pulses is used to ensure complete ejection.

Strings of ions (1 – 12 ions) were also ejected into the TOF tube to establish the sensitivity of the technique to small ion numbers (up to 10 ions). TOF peaks were detected, but the peak heights were erratic. The method is thus not sufficiently sensitive for small strings and single ion ejections.

Alexander Smith has carried out simulations of Ca^+ Coulomb crystal ejection in MATLAB, using SIMION to simulated the experimental fields.[109] Here, starting with a simulated crystal generated from the CCMD program, the ejection of Ca^+ Coulomb crystals

through the TOF tube and onto the MCPs was modelled. It was found out that under zero delay time (time between switching off the trapping voltage and switching on the ejection voltage), 98% of ions in a 500 ion Ca^+ crystal reached the MCPs; and with a delay of 1.16 μs the 97% of the ions reached the MCPs.

The simulations suggest that MCP channel saturation is not likely to be a major factor, by establishing the spatial distribution of ions on the detector. MCP detection efficiency for a 200 Ca^+ ion crystal at an endcap voltage (U_{dc}) of 0.1 V is 97.5%, at 1 V is 97% and at 2 V is 96%.

6.6 Investigation of bi-component Coulomb crystals

6.6.1 Sympathetic cooling

Sympathetic cooling is a useful technique employed to cool ions to the milliKelvin regime, for which no simple direct laser cooling scheme exists. Molecules cannot easily be laser cooled, because their complex energy-level structure and lack of a closed optical cycle makes implementation of laser cooling transitions impractical. Experimentally, laser cooling a species is limited by the number of laser transitions required and the availability of narrow-band lasers in that wavelength region. Sympathetic cooing is a very efficient alternative method for cooling molecular ions down to milliKelvin temperatures.

The Coulomb interaction that arises when molecular ions are simultaneously trapped with laser-cooled atomic ions efficiently transfers kinetic energy from the molecular to the atomic species, from which it is constantly removed by the Doppler (laser) cooling cycles. A bi-component Coulomb crystal is formed, where both laser-cooled and the sympathetically cooled ions form ordered structures, with secular temperatures down to milliKelvin. As they cool down, the dark (non-fluorescing) ions are incorporated into the Coulomb crystal, leading to a visible change in shape of the laser-cooled ion framework, confirmed using MD simulations (CCMD code).

Baba and Waki [15] performed the first sympathetic-cooling experiments on molecular ions with laser-cooled ions. The technique has been adopted, refined and extended by the

research groups of Drewsen, Schiller, Thompson, Willitsch and our research group. This process creates a multicomponent Coulomb crystal, where lighter ions are towards the trap axis and heavier ions are furthest from the trap axis. As discussed in Chapter 5, the secular frequency is dependent on the mass of the trapped ion, and ions with a larger mass-to-charge ratio than the fluorescencing ions experience a weaker trapping potential, and as such form an outer layer around the laser-cooled ions. This results in a compression of the upper and lower sides of the observed crystal image, and an expansion along the z-axis (along the length of the trap). Trapped ions with a lighter mass-to-charge ratio are trapped closer to the trap axis than the laser-cooled ions, forming an axially symmetric dark core in the crystal images.

Sympathetically-cooled dark ions can come from two different sources: ions can be generated inside the trap, for example by photoionization or electron-impact ionization of a neutral species introduced to the trap chamber, and subsequently sympathetically cooled into the crystal, such as Xe^+ or $C_2H_2^+$. Any ions produced via in situ chemical reactions can also be sympathetically cooled, for example CaF^+, $CaOH^+$ or $CaOD^+$, assuming that their kinetic energy is lower than the effective trap depth. For sympathetic loading, the trap depth has to be substantial, as otherwise the energy released during an exothermic reaction process can heat up the crystal and the crystal can be subsequently lost.

Sympathetic cooling can be performed for an extensive range of molecular ion species. For efficient sympathetic cooling and stable trapping to occur there must be a similar mass-to-charge ratio between the laser-cooled ions and the sympathetically-cooled ions. Ions of equal mass-to-charge ratio exhibit the most efficient energy transfer between laser- and sympathetically-cooled species. To ensure that sympathetic cooling is effective and the Coulomb crystal remains stable, the ratio of the mass of the sympathetically-cooled ions to the laser-cooled ions should be ideally within a factor of 0.4 – 2.5. Figure 5.12 in Chapter 5 illustrates clearly the masses that could be co-trapped with Ca^+.[120]

The heaviest species that have been sympathetically cooled are organic dye molecules with a mass exceeding 400 amu using Ba^+ as the laser-cooled "heat sink".[127] Be^+

Coulomb crystal had been used to sympathetically cool H_2^+ and H_3^+.[128] Sympathetically cooled molecular ions are usually in thermal equilibrium with the ambient black-body radiation field, as sympathetic cooling does not affect the internal degrees of freedom of the molecular species. This is because higher order interactions that could induce inelastic processes, for example charge-dipole coupling, are effective only at shorter separation between the ions. In a Coulomb crystal, the typical distance between the ions is tens of microns and all the short range interactions are neglected. Multi-component Coulomb crystals thus provide a powerful method for following the progress of low temperature ion-molecule reactions.

6.6.2 Expererimental procedure

An effusive calcium atom beam, emitted from an oven and collimated with a skimmer, is ionized at the trap center in a two-photon non-resonant process using a 355 nm (5 – 6 mJ/pulse) frequency-tripled Nd:YAG laser. The translationally hot $^{40}Ca^+$ ions formed in the trap are laser-cooled as discussed in Chapter 5.

The precursor gases for the ions that are generated inside the trap are introduced into the chamber (which already has a Ca^+ Coulomb crystal trapped) by a leak valve, with lasers used for ionization. Xenon is ionised by a (2+1) REMPI process, (accessing the $5p^5 6p\ ^2P_{3/2}$ intermediate state) with a pulsed 249 nm laser [129] (1 m J/pulse, obtained by frequency doubling the output of a dye laser, using Coumarin 503 dye, pumped by a frequency tripled Nd:YAG laser). Acetylene is ionised by a (2+1) REMPI process, described in Chapter 4, with a pulsed 269 nm laser (1 – 2 mJ/pulse, obtained by frequency doubling the output of dye laser using Coumarin 540A dye, pumped by a frequency tripled Nd:YAG laser).

For CaF^+ ions produced in situ by reaction, neutral CH_3F is introduced to the chamber using a leak valve. Reaction of Ca^+ with CH_3F produces CaF^+, which gets co-trapped with Ca^+. $CaOH^+$ and $CaOD^+$ are also loaded in a similar way, where H_2O (or D_2O) reach the chamber through leak valves and react directly with Ca^+ forming $CaOH^+$ or $CaOD^+$.

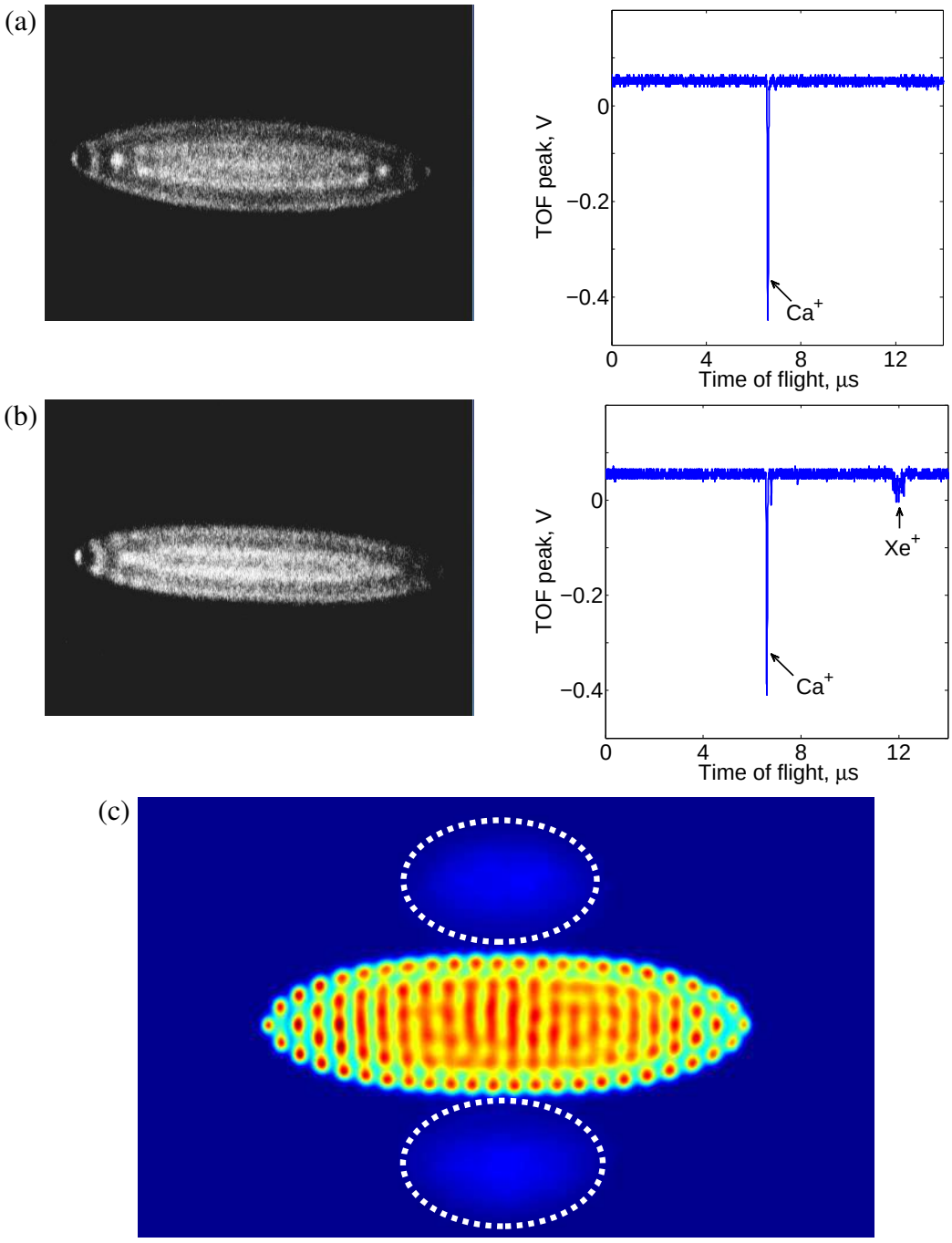

Figure 6.8: (a) A clean Ca^+ Coulomb crystal and corresponding TOF spectrum following ejection, (b) a Xe^+ – Ca^+ Coulomb crystal and corresponding TOF spectrum following ejection. (c) This figure has been reproduced from Lee Harper's thesis;[68] a simulated Ca^+ – Xe^+ Coulomb crystal made up of 500 laser-cooled calcium ions and 100 sympathetically-cooled xenon ions. This simulated image has been generated with false colour under a sinusoidal trapping voltage. The uncrystallised xenon ions are in a fluid plasma state and are denoted as faint amorphous patches above and below the calcium crystal image. The white dotted lines indicate the location of the diffuse xenon cloud.

6.6.3 Discussions on Ca^+ – Xe^+ bi-component crystal

Xe^+ is heavier than Ca^+ and thus forms a shell outside Ca^+ in the resulting bi-component Coulomb crystal, as shown in the simulation of figure 6.8 (c). The Xe^+ ions have a mass-to-charge ratio much higher than Ca^+, and are actually not cold enough to fully crystallise, remaining in a fluid plasma state. The uncrystallised xenon ions can be seen in the simulations as faint amorphous patches above and below the calcium crystal image. The Ca^+ crystal is itself slightly flattened. As discussed in section 6.6.1, for efficient sympathetic cooling the mass-to-charge ratio of the sympathetically cooled ion to the laser cooled ion should be less than 3; the mass-to-charge ratio of Xe^+ to Ca^+ ions is just outside this range. In reality, the Xe^+ ions sit so far away from the trap axis that the Coulomb exchange of kinetic energy (by elastic collisions) is inefficient. As a result, the Xe^+ ions remain uncrystallised. The same could also be predicted from figure 5.12 in Chapter 5.

Impurity ions, presumed to originate from hydrocarbons from pump oil in the vacuum chamber, are also formed inadvertantly and are heavier than Ca^+, sitting outside the Ca^+ ions in the crystal. Knowing the constituents of the dark ions is essential for any reaction kinetic measurements done with Coulomb crystals. The most common unwanted mass we observed during the optimisation process was around 59 amu, attributed to pump oil.

Loading of Xe^+ (sympathetically) into the Ca^+ Coulomb crystal has been optimised to ensure that a pure Xe^+ – Ca^+ crystal is loaded. It was observed that using a 249 nm ionization laser power of 1 – 2 mJ/pulse but allowing the laser through the chamber for a short duration of time results in clean xenon loading. Figure 6.8 (a) is the image and TOF spectrum ontained after ejecting a Ca^+ Coulomb crystal into the TOF mass-spectrometer, and figure 6.8 (b) is the same for a bi-component Xe^+ – Ca^+ Coulomb crystal, at V_{rf} = 50 V, U_{dc} = 0.6 V and $\omega_{\mathrm{rf}} = 2\pi\times1.35$ MHz. The broad peak obtained for Xe^+ is because sympathetically-cooled Xe^+ is not in a crystallised state, and is thus translationally hotter than Ca^+.

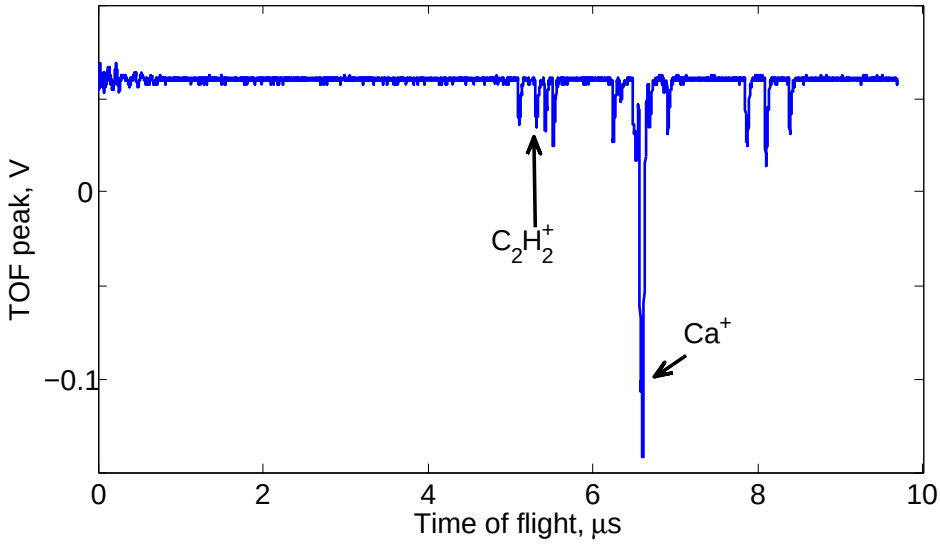

Figure 6.9: TOF spectrum obtained on ejecting Ca^+ Coulomb crystal, sympathetically loaded with $C_2H_2^+$.

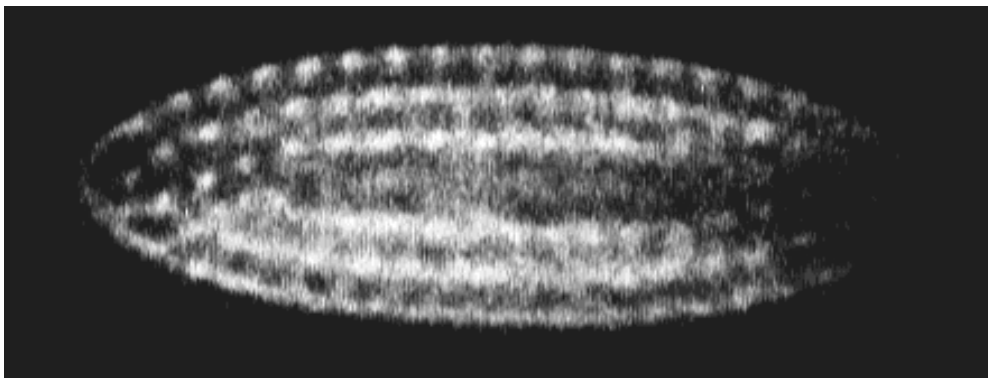

Figure 6.10: A Ca^+ Coulomb crystal, sympathetically loaded with $C_2H_2^+$.

6.6.4 Discussions on Ca^+ – $C_2H_2^+$ bi-component crystal

Acetylene was first leaked into the ion trap chamber, which was already loaded with a Ca^+ Coulomb crystal, to ensure that the neutral gas did not react with Ca^+. Control experiments were performed under both sinusoidal and digital trapping conditions and it was concluded that acetylene does not react with calcium ions.

A REMPI spectrum of acetylene was obtained in the ion trap chamber using the continuous extractor-repeller voltages on the ion trap electrodes. A ∼269 nm laser is used for ionizing acetylene, and REMPI peak corresponding to that of acetylene was obtained. This

confirmed the formation of $C_2H_2^+$ ions in the trap.

Loading acetylene ions into a Ca^+ Coulomb crystal is particularly challenging. Ejecting the resulting crystals into the TOF tube shows that a range of species are ionized and trapped along with mass 26 (acetylene). Figure 6.10 shows the resulting TOF spectrum. The masses lighter than calcium that get co-trapped inadvertantly are: 24, 27, 28, 36 and 37 amu. Possible sources of contamination could come from the acetylene cylinder, which contains acetone as a stabilising agent. Fragment ions from either CH_3COCH_3 (acetone) or $C_2H_2^+$ could account for some of these masses.

6.6.5 Mass resolution

Mass resolution can be defined as the largest mass for which two consecutive peaks differing by 1 amu can be completely separated in a mass spectrum. Here we investigate the mass resolution achieved with the digital ejection technique. Figure 6.11 illustrates the mass resolution of the technique for masses both higher and lower than calcium (40 amu).

Figure 6.11 (a) provides a TOF spectrum when trying to sympathetically load acetylene into Ca^+ Coulomb crystal, which clearly shows peaks corresponding to masses 26 amu, 27 amu and 28 amu. Resolution of the mass spectrum (defined by $m/\Delta m$, where Δm is the full width at half maximum of the mass spectrum peak) was 90 for a typical 100-ion Ca^+ crystal.

To obtain the TOF spectrum given in figure 6.11 (b), a systematic study was undertaken in the new ion trap. After loading calcium into the trap, gaseous H_2O is leaked into the chamber, whereby it reacts with Ca^+ forming $CaOH^+$ (see reaction 6.10), which is subsequently trapped. Gaseous D_2O is then leaked into the chamber, and in a similar way $CaOD^+$ (see reaction 6.11) is formed and co-trapped to yield a multicomponent Ca^+, $CaOH^+$ and $CaOD^+$ crystal.

$$Ca^+ + H_2O \rightarrow CaOH^+ + H \tag{6.10}$$

$$Ca^+ + D_2O \rightarrow CaOD^+ + D \tag{6.11}$$

This Ca^+ – $CaOH^+$ – $CaOD^+$ Coulomb crystal is allowed to cool for tens of seconds before

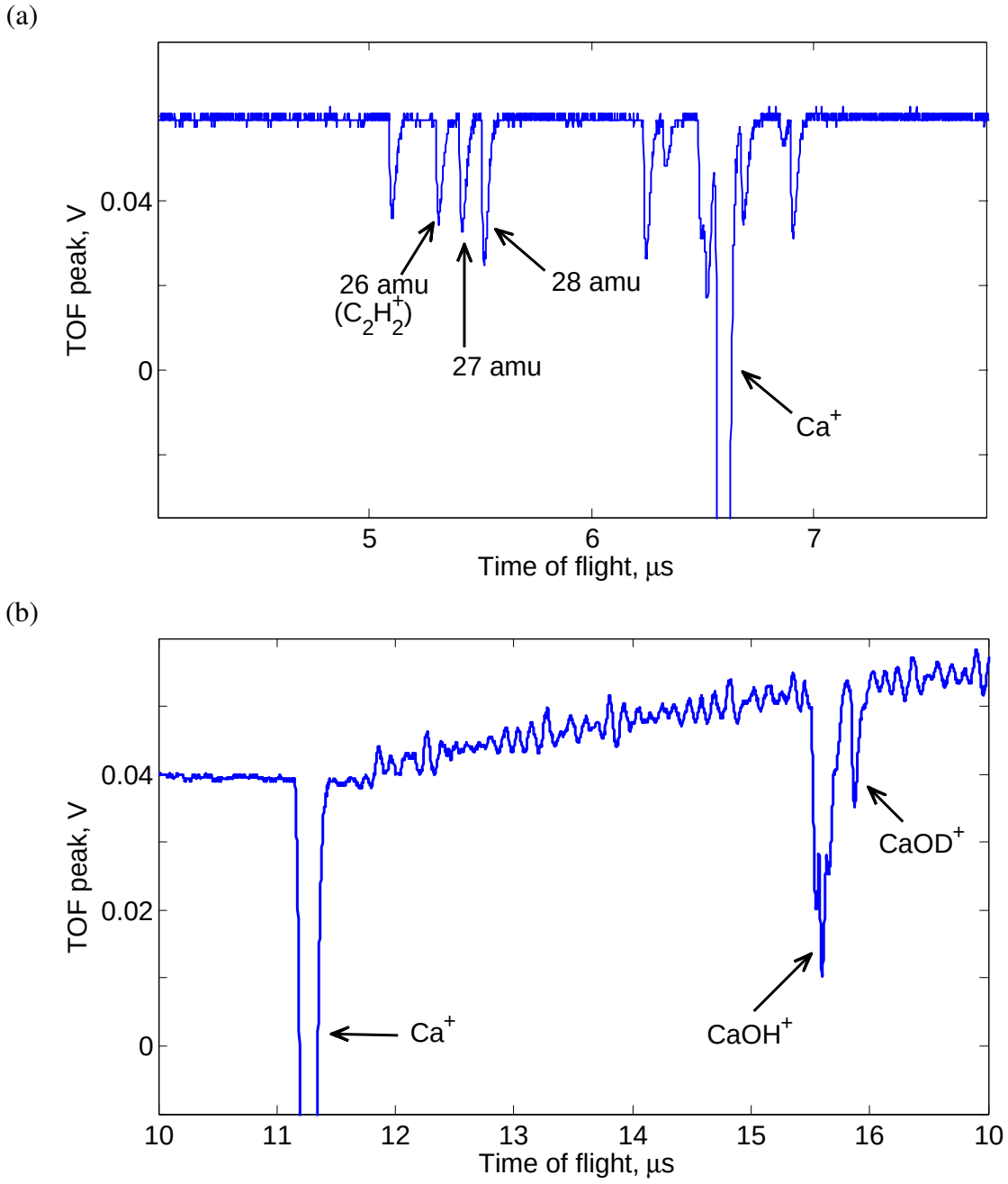

Figure 6.11: (a) TOF spectrum obtained trying to sympathetically load acetylene into a Ca^+ Coulomb crystal. The peak obtained at 6.6 μs is that of calcium (old ion trap) . (b) TOF spectrum obtained by ejecting a Ca^+ – $CaOH^+$ – $CaOD^+$ Coulomb crystal. Here the peak obtained at 11.2 μs is calcium (new ion trap). The difference in the time-of-flight for calcium is because the two studies (a) and (b) were undertaken in two different apparatus.

being ejected into the TOF tube and detected by the MCPs, with an example TOF spectrum shown in figure 6.11 (b). At masses higher than 40 amu (Ca^+), mass resolution is not very clear from the TOF trace – a split peak was observed for peaks corresponding to $CaOH^+$ (57 amu) and $CaOD^+$ (58 amu), making interpretation of the mass spectrum difficult.

Simulations of Ca^+–$CaOH^+$–$CaOD^+$ crystals ejected from the trap were perfomed by Alexander Smith [109] starting with a simulated crystal generated from the CCMD program, the ejection of Coulomb crystals through the TOF tube and onto the MCPs was modelled in MATLAB using SIMION to generate the experimental fields. The simulations show that the TOF spectrum obtained has split peaks for both $CaOH^+$ and $CaOD^+$ signals. Figure 6.12 (a) depicts the split peaks of $CaOH^+$ and $CaOD^+$ obtained by simulating the Ca^+–$CaOH^+$–$CaOD^+$ crystal ejection, under the same conditions as the real experiment was conducted. Clearly, the split peaks of $CaOH^+$ and $CaOD^+$ are overlapped. For the experimental mass spectrum (standard conditions, extractor voltage of 97 V and repeller voltage of 220 V), the simulations suggest that we are in fact observing the partially overlapping $CaOH^+$ and $CaOD^+$s peaks. The partial intersection of the split peaks accentuates the height of the middle peak. However, Ca^+–$CaOH^+$–$CaOD^+$ crystal ejection simulations undertaken at extractor and repeller voltages of 97 V and 160 V (respectively) showed clear separation of the mass peaks, as in figure 6.12 (b).

The repeller and extractor voltages, currently optimised for Ca^+, could instead be optimised for the molecular species of interest and thus provide mass resolution potentially well beyond 58 amu. Further crystal ejection simulations are being undertaken to establish the resolution limit of this new technique.

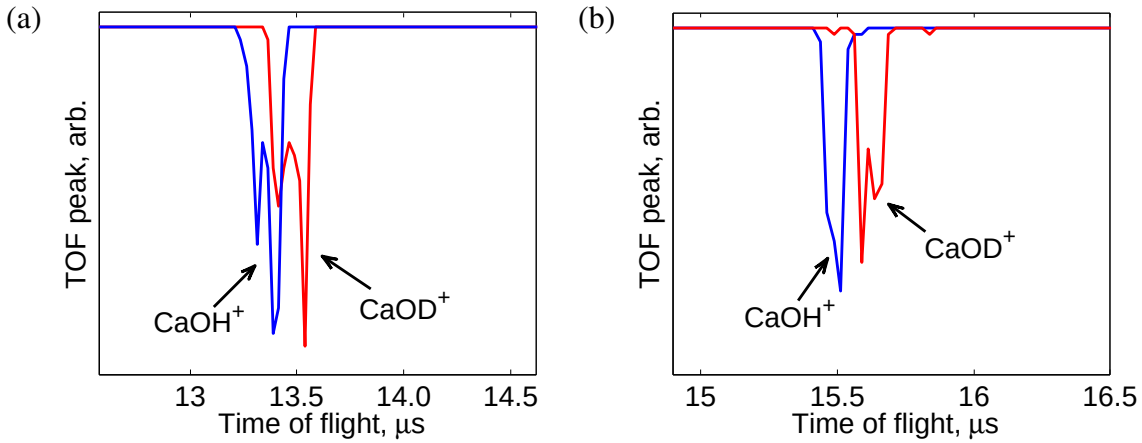

Figure 6.12: (a) Simulated TOF spectrum obtained on ejecting a Ca^+ – $CaOH^+$ – $CaOD^+$ Coulomb crystal at the experimental operating parameters, with extractor and repeller voltages of 97 V and 220 V. One of the split peaks of each of $CaOH^+$ and $CaOD^+$ overlaps. (b) However, when the extractor and repeller voltages were kept at 97 V and 160 V (respectively), the simulation predicted clear separation of the $CaOH^+$ and $CaOD^+$ peaks in the TOF spectrum, with minimised peak splitting. In both the figures, the blue line correponds to $CaOH^+$ and the red line to $CaOD^+$. This figure has been reproduced from Alexander Smith's Part II thesis.[109]

6.7 Analysis of Ca^+ Coulomb crystal with sympathetically cooled CaF^+ – Investigation of the relationship between the integrated peak heights of the TOF spectrum and the number of ions in the crystal

A Ca^+ Coulomb cystal is loaded into the new ion trap, followed by sympathetic loading of CaF^+. This is done by introducing CH_3F into the trap chamber through a leak valve, whereby CH_3F reacts with Ca^+ forming CaF^+ (see reaction 6.12). The CaF^+ is co-trapped with Ca^+ and is subsequently sympathetically cooled.

$$CH_3F + Ca^+ \rightarrow CaF^+ + CH_3 \tag{6.12}$$

After allowing sufficient time for the bi-component crystal to cool down, an image is captured with a CCD camera set-up. The crystal is then ejected into the TOF tube and the resulting TOF spectrum is obtained. Figure 6.13 shows three Coulomb crystals with differing Ca^+:CaF^+ ratios. It is quite clear that the relative ion numbers are qualitatively reflected in the peak heights of the TOF spectrum. In this section, the TOF peaks are quan-

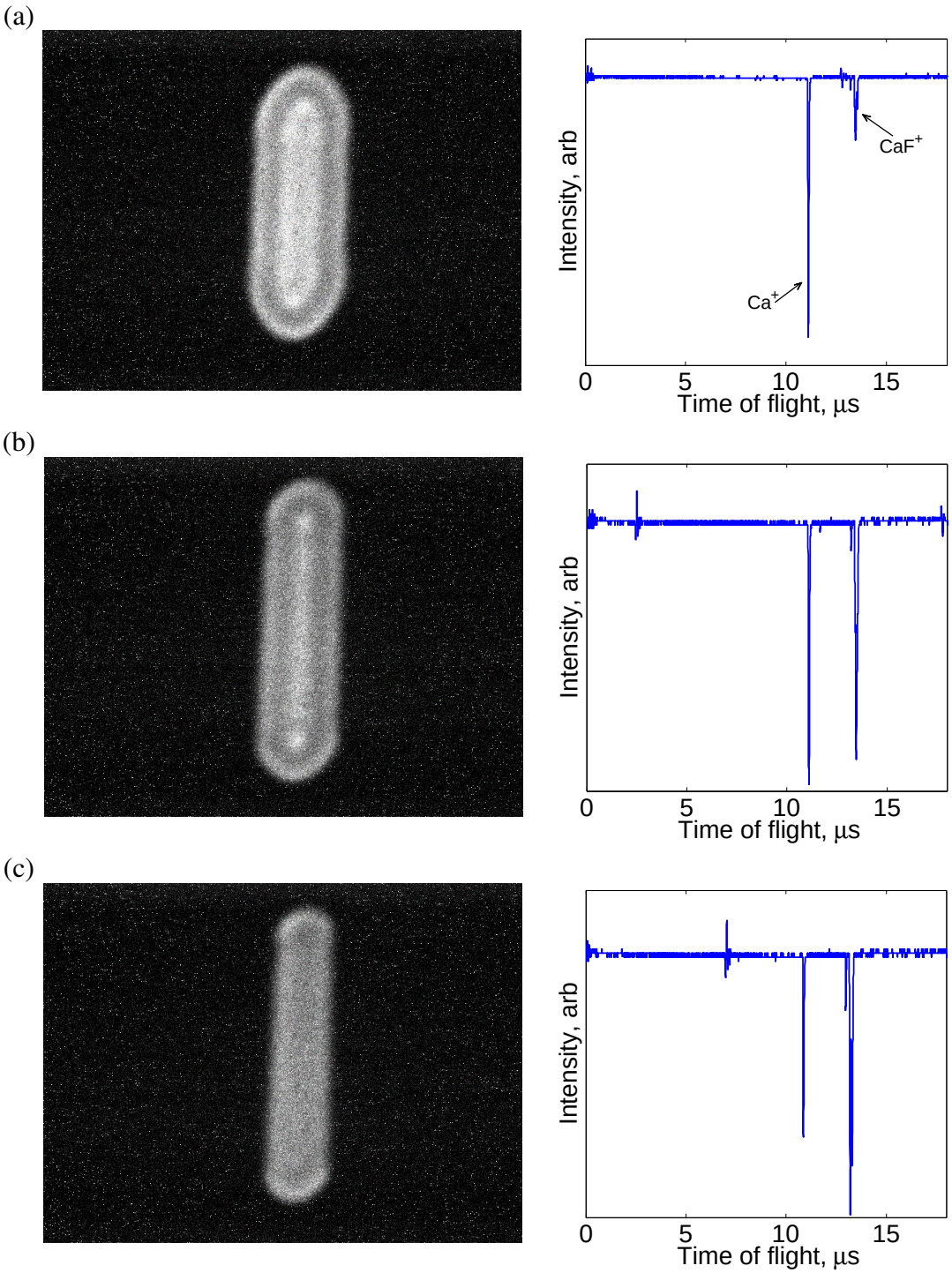

Figure 6.13: Three bi-component Ca^+ – CaF^+ Coulomb crystals. Each row has (left) the image of the crystal before ejection and (right) the TOF spectrum on ejection of the crystal. The peak at 11.1 μs corresponds to Ca^+ and the peak at 13.2 μs is that of CaF^+. In (a) Ca^+ is the largest component; in (b) there are approximately equal numbers of Ca^+ and CaF^+ ions; and in (c) CaF^+ is the main component.

titatively analysed and compared against the number of ions of Ca^+ and CaF^+ established from CCMD simulations.

The CCMD code described in section 5.4.3 is used to generate simulated images of crystals at V_{rf} = 50 V, U_{dc} = 1.0 V and a trapping frequency of $2\pi\times$ 1.427 MHz, reflecting the experimental conditions. Simulated mixed crystals of sizes ranging from 5 – 100 Ca^+ ions and 5 – 100 CaF^+ ions (co-trapped along with Ca^+) are generated using the CCMD code (in steps of 5). The experimental image is then compared against the simulated crystals and the ion numbers of each component in every crystal is established.

Figure 6.14 shows the correlation between ion number and the integrated TOF peak. 64 mixed crystals were ejected under standard conditions to obtain the plot. A linear fit was found to give the best fit to the integrated TOF peak vs ion number plot for Ca^+ ions (from the mixed crystals), with fitting parameter R^2 of 0.815. The slope of the fit to Ca^+ in the mixed crystal was found to be $3.57\times10^{-10} \pm 0.21\times10^{-10}$.

The relationship between the number of CaF^+ ions and the integrated TOF peak (for number of ions of CaF^+ less than 60), is found to be linear, with a gradient of 3.1×10^{-10} $\pm0.33\times10^{-10}$. This is in agreement with the slope obtained for Ca^+ from the mixed Ca^+–CaF^+ Coulomb crystals (within the standard error range). We have only reported the trend for upto 60 CaF^+ ions due to the lack of sufficient data points for crystals with $>$ 60 CaF^+ ions. As there is more uncertainty in fitting the number of heavy dark ions, many more crystals and ejection TOF traces must be analysed before trends can be established with any degree of certainty. For up to 60 CaF^+ ions, the linear trend observed for Ca^+ is reproduced. We expect this to be the case for all mixed crystals, where the mass-to-charge ratios are sufficiently close to that of Ca^+ (for efficient sympathetic cooling).

It should be noted that, due to water contamination of the MCPs, the gradients of the lines of best fit obtained for Ca^+ only and Ca^+ in mixed Ca^+–CaF^+ crystals are not directly comparable. While the MCPs were baked after water contamination, the response did not return to the pre-contamination level. This illustrates the importance of regular calibration of the MCP response and resulting TOF peak area.

(a)

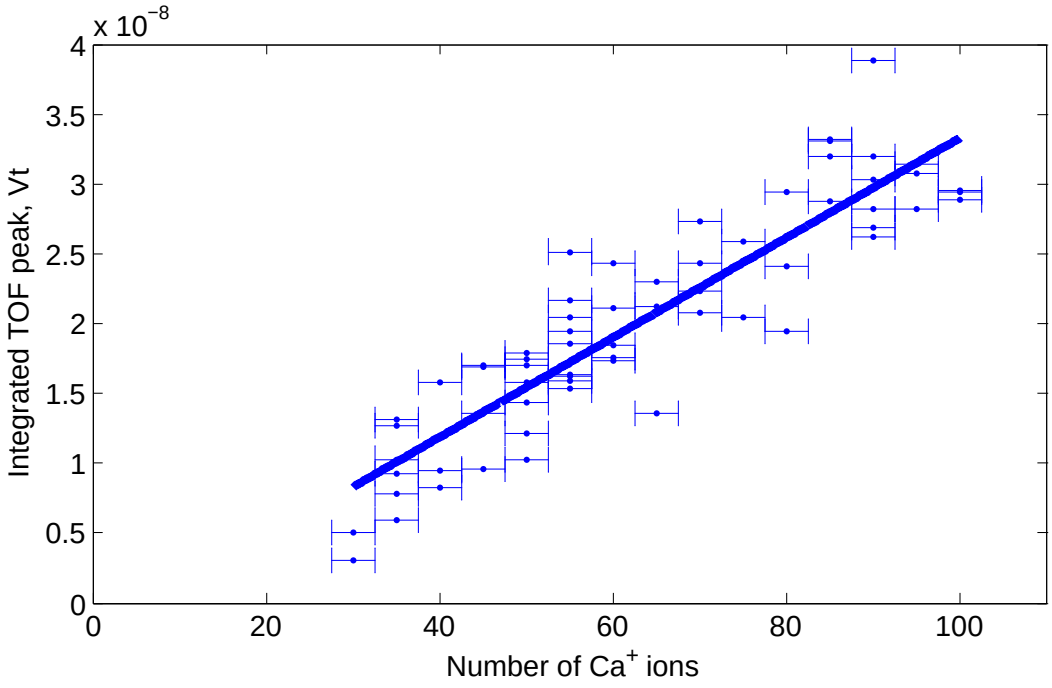

(b)

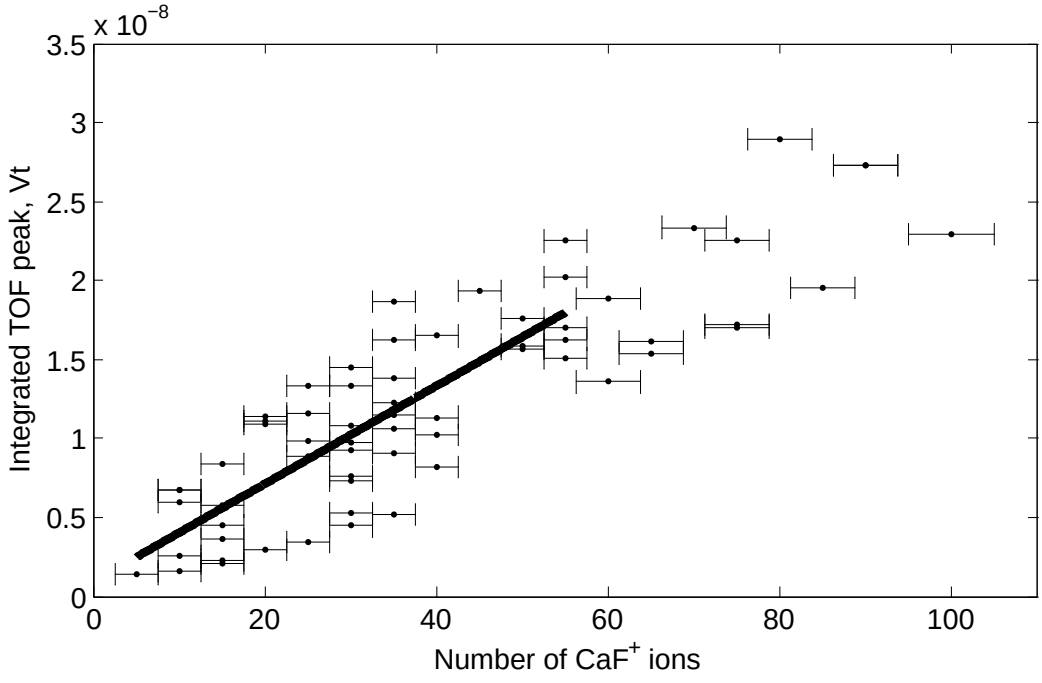

Figure 6.14: Bi-component Ca^+ – CaF^+ crystal ejection analysis. The number of ions of (a) Ca^+ and (b) CaF^+ are plotted against the integrated TOF peaks obtained by ejecting 64 mixed crystals at V_{rf} = 50 V, U_{dc} = 1 V and $\omega_{rf} = 2\pi\times$ 1.427 MHz. The MCPs were maintained at -1900 V.

Overall, a linear relationship between the TOF peak and the number of ions ejected exists, such that the TOF spectrum obtained is directly proportional to the number of ions ejected. This is a very important result and establishes the ejection technique as a useful tool for monitoring reactions in Coulomb crystals.

6.8 Sources of possible errors

The fitting of experimental Coulomb crystals to evaluate the number of ions is not sensitive beyond a certain point. Simulated crystals differing by sizes of less than 5 ions are visually very similar and difficult to distinguish. Thus there is typically an error bar of ± 5 ions in the fitting of experimental images to simulations. Although there is always a possibility of impurity ions getting sympathetically loaded into the Coulomb crystal (by charge exchange with other ions), that would be evident from the TOF spectrum obtained and is thus not expected to be significant.

Also, although crystal images are captured and saved just before ejection, the time required for this is on the order of a few seconds and there could be minor losses of ions from the crystal during this time. This would mean we are fitting to an upper bound on the number of ions in the ejected crystal.

The mesh used at the beginning of the TOF tube (see figure 6.2) is reported to have 88% transmission. So, there is loss of ions as they pass through the mesh towards the MCPs, and the number of ions that are ejected from the trap and number of detected ions is not same. However the transmission should be independent of the ion species.

Alexander Smith has done relevant calculations and simulations of crystal ejections, which show that MCP channel saturation is not likely to be a major factor. Ion detection efficiency for a 200 Ca^+ ion crystal at an endcap voltage (U_{dc}) of 0.1 V is 97.5%, at 1 V is 97% and at 2 V is 96%. However, the cascade of electrons generated each time the ions hit the MCPs varies, which could affect the TOF spectrum observed, especially at low signal levels. As such, multiple ejections of similar sized crystals is required to reduce the uncertainty in the MCP response.

The noise in the TOF spectrum makes the actual evaluation of the area under the mass peak difficult. The background substraction applied to the TOF traces might sometimes be over- or under-substracting the noise, contributing to the scatter on either side of the line of best fit.

Another possible source of error is the boot-strap amplifier used to amplify the MCP signal. Dr Atreju Tauschinsky (in our research group) has performed simulations that suggests that for TOF peaks (after ampliflication) below 2 V, the amplification is linear. All our observed TOF peaks were below 2 V.

6.9 Conclusion and future directions

Digital ejection has been proven to be a useful tool in the characterisation of multi-component Coulomb crystals. The technique enables the determination of both the masses of the ions ejected and also the relative ion numbers. There is a linear relationship between the number of ions ejected and the TOF peak area. The slopes of Ca^+ and CaF^+ in the mixed crystal agree with each other within the standard error range, for CaF^+ ion number < 60 (beyond which uncertainty in the ion number assignment makes the data statistically insignificant).

Simulations carried out by Alexander Smith confirm the efectiveness and efficiency of this digital ejection technique. For a small Ca^+–CaF^+ bicomponent crystal consisting of 100 Ca^+ ion and 40 CaF^+ ions, under standard conditions, the calculations predict that 100% of both Ca^+ and CaF^+ ions reach the MCPs, after being ejected. When the delay time was increased to 2 μs the detection efficiency (the number of ions reaching the MCPs after the ions are ejected from the trap) of CaF^+ dropped to 99%, however, the Ca^+ detection efficiency remained at 100%. For larger Ca^+–CaF^+ crystals (under standard conditions) of 500 Ca^+ ions and 200 CaF^+ ions the detection efficiency was predicted to be 98% for Ca^+ and 90% for CaF^+. In the experiments described in this thesis, the bicomponent crystal analysis was done with < 100 ions each of Ca^+ and CaF^+. For a Ca^+–Xe^+ bicomponent crystals, a detection efficiency of 100% and 97.5% was calculated for a crystal consisting of 100 Ca^+ and 80 Xe^+ respectively.

Though the technique is destructive, by generating a calibration plot indicating the integrated TOF peaks for a given number of ions of a given type, a reaction can be studied. Ejecting crystals at different time intervals will allow the extent of reaction– and thus the reaction rate – to be calculated. Since the process is destructive, several crystals would need to be loaded, and ejected, for accurate measurements.

A range of reactions can be studied using this technique, as long as the ionic reactants and products can be co-trapped in the Coulomb crystal. For instance, the reaction between $C_2H_2^+$ and ND_3 could be studied with this novel technique. There are several reaction pathways leading to different products, as set out for $C_2H_2^+$ and NH_3 in reaction 6.13. Most of the charged products – which could be co-trapped in the Coulomb crystal – are lighter than calcium, as is $C_2H_2^+$. Reactants and products would thus both form in the inner dark core.

$$\begin{aligned} C_2H_2^+ + NH_3 &\rightarrow C_2H + NH_4^+ \text{ (proton tranfer)} \\ &\rightarrow C_2H_2 + NH_3^+ \text{ (charge tranfer)} \\ &\rightarrow CH_3NCH^+ + H \text{ (H-elimination)} \\ &\rightarrow CH_3CNH^+ + H \text{ (H-elimination)} \\ &\rightarrow CH_3CN^+ + H_2 \text{ (H_2-elimination)} \\ &\rightarrow CH_2CNH^+ + H_2 \text{ (H_2-elimination)} \\ &\rightarrow C_2H_3^+ + NH_2 \text{ (H-atom abstraction)} \end{aligned} \tag{6.13}$$

All the reactions are exothermic, with the exception of H-atom abstraction.[130] The reaction between $C_2H_2^+$ and ND_3 would be even more complicated, with more available pathways and products owing to the distinguishability of H and D atoms. The ejection technique demonstrated and developed in this chapter would be very useful for the study of reactions with multiple products. The change of crystal shape alone cannot establish the extent of reaction if multiple components comprise the dark core or the dark outer shell.

There are several other ion-molecule reactions of astrophysial interest that could be

studied, such as HCl^+/DCl^+ and ND_3. Even ion-molecule reactions that could be studied by monitoring the change in shape of the Coulomb crystal, such as the reactions given in 6.14 and 6.15,

$$OCS^+ + ND_3 \rightarrow OCS + ND_3^+, \tag{6.14}$$

$$Xe^+ + ND_3 \rightarrow Xe + ND_3^+, \tag{6.15}$$

can be more accurately studied with the ejection technique developed. This is because the change in the Coulomb crystal shape can be due to reactant/product ions or undesired contaminants, with the most common contaminant we observed identified as pump oil impurities.

We have already used this ejection techique to optimise our calcium ion loading process. Calcium was ionized using two different lasers: at 325 nm and 355 nm. Both the ionization procedures were non-resonant, and it was seen that 355 nm ionisation consistently produced cleaner Ca^+ Coulomb crystals. With the 325 nm pulsed laser, pump oil impurities were sometimes inadvertantly loaded along with the Ca^+. It has been established as a useful technique for testing the purity of bi-component Coulomb crystals, where Xe^+, $C_2H_2^+$ and CaF^+ were sympathetically cooled, into the crystals. The broad Xe^+ peak in the TOF spectrum confirms that Xe^+ ions are hot and are uncrystallised, in a fluid plasma state. The ejection of '$C_2H_2^+$ – Ca^+' crystals indicated that the proportion of $C_2H_2^+$ in the dark core was only a fraction of the volume of the dark core; a number of undesired impurities were co-trapped along with $C_2H_2^+$.

The digital ejection technique could be refined by improving the digital pulse generator. Care should be taken to make sure the rf trapping voltages sent to the four electrodes are properly synchronised, as otherwise they tend to heat up the crystals. The noisy pulse generated, together with imperfect synchronisation, results in a shallower trap depth and thus less cold crystals. Improving the pulse shape and synchronisation would result in colder crystals, which would be much easier to fit to simulated crystals, resulting in more accurate ion number analysis. A shallow trap depth also makes it difficult to study exothermic ion-molecule reactions. Additionally, the mesh used in the TOF tube (at present with 88%

transmission) could possibly be replaced with one of higher transmission ($> 95\%$).

Dr Atreju Tauschinsky has recently designed a sinusoidal ejection technique that has addressed the ringing issue. A fast switch in the rf voltage driving circuity is introduced that turns off the input of the sinusoidal drive voltages into the electrodes. This leads to a fast decay of the trapping voltages on the electrodes, with a time constant of 1 μs. The amplitude of the electrode ringing reduces to a tenth ($1/e^2$) of the initial value after two time periods. Simulations have shown that the efficiency of detection remains similar to a digital trap on ejecting after two time periods (2 μs). This is illustrated in figure 6.15, where at t = 4 μs the trapping voltage is turned off and at t = 6 μs (after 2 μs), the ringing has reduced to 10% of its initial amplitude, when the ejection pulses are applied. The ejection voltages are clean and thus the sinusoidal ejection could be a possible viable method of pursuing such experiments in the future.

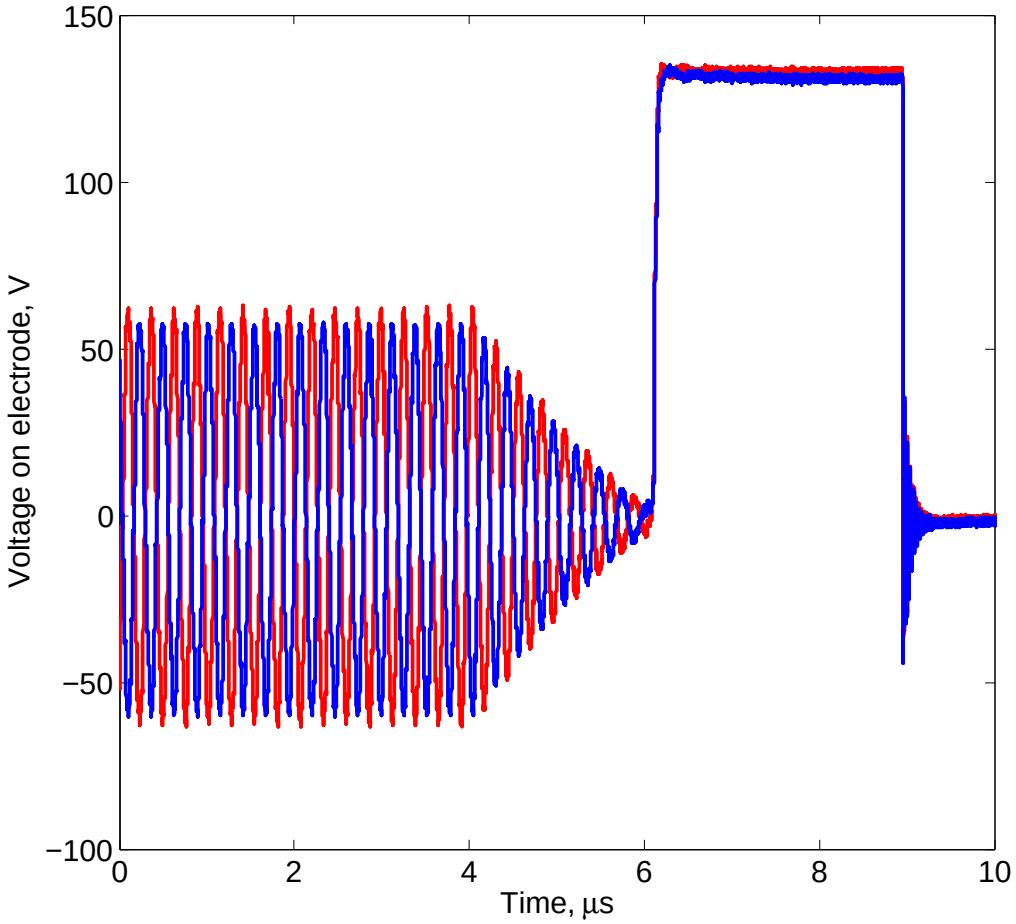

Figure 6.15: Simulated results for sinusoidal ejection. The two colours indicate the extractor and repeller electrodes.

Chapter 7

Conclusions and Future Directions

7.1 Conclusions

The thesis has broken new ground in the experimental investigation of state-selected ion-molecule reactions in the cold regime.

Sympathetic cooling of molecular ions, as demonstrated here and elsewhere with species such as MgH^+, CaF^+, OCS^+, $C_2H_2^+$ and ND_3^+, in a radio-frequency ion trap has expanded the scope of reactions that can be investigated in the cold and ultra-cold regime. However, molecular ions in a Coulomb crystal are typically translationally cold but are not rotationally and vibrationally cold. The main challenges in moving towards fully state-selected ion-molecule reactions involve preserving the state populations of trapped molecular ions for 15 – 20 minutes (the time typically required for kinetics measurements) and developing appropriate techniques to monitor the reactions. The thesis details the significant progress made towards experimentally realising state-selected reactions between $C_2H_2^+$ and ND_3 at low collisional energies.

Laser cooling schemes were theoretically explored in this thesis to rovibrationally cool species which are translationally cold. By implementing schemes to selectively prepare or to control the internal quantum state of the molecular ions, and developing techniques to study a variety of reactions, it will be possible to investigate chemical collisions under highly controlled conditions in an ion trap.

Calculations were performed to model the interaction of ambient blackbody radiation (BBR) with several diatomic species and to establish the effectiveness of laser-driven BBR-

mediated optical cooling schemes for several diatomic species. BBR-induced laser cooing schemes developed in this thesis had good agreement with reported MgH^+ experimental results,[28] demonstrating the validity of the methodology. The sensitivity of such a model to the dipole moment gradient was also explored; in this respect rigorous *ab initio* calculations were performed using the Gaussian09 quantum chemistry package to determine the dipole moment gradient of MgH^+.

Optical pumping schemes involving multiple pumped transitions with broadband laser sources were found to be efficient, and could accumulate populations upto 57.7%, 65.9%, 63.7% and >99% in the rovibrational ground states of MgH^+, LiH, CsH and DCl^+/HCl^+, respectively. While for species in a $^1\Sigma$ electronic state (MgH^+, LiH, CsH), the cooling scheme was found to be less effective, a considerable enhancement of population – up to 29% greater than the population accumulated following the excitation of a single transition – was still observed. The rate at which equilibrium populations were attained under the rotational cooling schemes, and also the final equilibrium population achieved, were found to be influenced by the magnitude of the rotational constant, dipole moment and vibrational transition dipole moment. The high sensitivity to the various parameters demonstrated that attempts to provide generalised cooling schemes may have limited accuracy and applicability for "similar" species (such as molecules in the same electronic state). For example, a significant alteration in the properties of the system was observed with only the exchange of H for D in HCl^+. This emphasised the need for cooling schemes to be developed for, and tailored to, each system under consideration. A hybrid approach involving optical cooling in 77 K experimental environments was also considered, which yielded more population in the rovibrational ground state.

An extension to a linear polyatomic species, specifically the $C_2H_2^+$ ion, was subsequently investigated, with a combination of cold trap environments (at 77 K) and optical pumping schemes examined. $C_2H_2^+$ ion is a linear non-polar polyatomic species in a $^2\Pi$ electronic ground state. The complexity associated with the Renner-Teller effect and spin-orbit coupling in this species was considered – just one example of the complex vibrational

and vibronic interactions that may take place in polyatomic molecules. My work demonstrated that this non-polar polyatomic ion displays a rather different behaviour compared to diatomic species, and demonstrated the key role that low-frequency vibrations play in facilitating BBR-induced population decay and transfer. Calculations showed that good use can be made of the molecular vibrational bands to devise pumping schemes that could lead to excellent control of the rotational population. Rotational transitions within the same vibrational level ($\Delta v = 0$) are spectroscopically forbidden because this is a non-polar ion. Out of the five modes of vibrations the ion has, only the asymmetric stretch mode (ν_3) and the cis bending mode (ν_5) are IR active. However, the lifetime of this species produced in a specific quantum state was found to be very low, on the order of a few seconds. Population decay occurred through the involvement of other vibrational states – the $1 \leftarrow 0$ band of the ν_5 vibration ($\sim$ 700 cm^{-1}) was found to overlap strongly with the peak of the BBR spectrum at 300 K. On the other hand, the lifetime of $C_2H_2^+$ ions were found to be $>$ 10 hours at 77 K, as the overlap of the 1$\leftarrow$0 vibrational band with 77 K BBR is poor. A rotational-cooling scheme was proposed that involved simultaneous pumping of a set of closely spaced Q-branch transitions in the $^2\Delta_{5/2}$ – $^2\Pi_{3/2}$ band, together with two $^2\Sigma^+$ – $^2\Pi_{1/2}$ transitions. It was shown that this should lead to $>$70% of total population in the lowest rotational level at 300 K and over 99% at 77 K (albeit on a long time scale). In principle, the multiple Q-branch lines could be pumped with just two broad-band ($\sim$ ν = 0.4 – 3 cm^{-1}) infrared lasers. In addition to this, an extension of this scheme to CO_2^+ was suggested.

The study of low temperature ion-molecule collisions would undoubtedly benefit from the availability of schemes for producing quantum-state selected ions. For example, the reaction of $C_2H_2^+$ with ND_3 could be studied with trapped, sympathetically cooled and internally cold $C_2H_2^+$ ions and state-selected ND_3 from a Stark decelerator. Restricting the quantum states of the reactants enables more stringent tests of quantum mechanical reaction rate calculations, as well as enhancing the probability of observing effects such as scattering resonances.

The production of $C_2H_2^+$ ions in different vibrational states using REMPI schemes was

investigated, with the ions successfully produced in different vibrational states: 0_0^0, 2_0^1, 2_0^2 and the combination band $0_0^0 + 2_0^2$. Some of these states were 'locked' states (such as those involving 2_0^n), where the lifetime of the state would only be limited by collisions with background gases as opposed to BBR-mediated redistribution. The combination bands would also be interesting to study in a reaction with ND_3. The REMPI peaks exhibited some rotational sub-structure, which indicated that tuning the laser to those regions would produce ions in low (or high) rotational states. It has been demonstrated that rovibrational states of $C_2H_2^+$ are preserved at 77 K. It would thus be possible to study reactions of these with velocity-selected ND_3 molecules, from the decelerator, in a cryogenically cooled ion trap. The possibility of detecting the ions in specific quantum states was also explored with REMPD spectra obtained for several states of $C_2H_2^+$ ions. The signal to noise ratio, however, was too low and application of the detection technique to the ion trap would be challenging as the molecular density would be significantly lower.

The concept of digital ion trapping was introduced for ejection into a time-of-flight mass spectrometer. A comprehensive comparison between sinusoidal and digital trapping fields was performed with respect to the trap depth and stability regions. The trap depth was derived for both digital and sinusoidal trapping fields. It was observed that as the fractional pulse width, τ, of the digital pulse increased, the trap depth of a digital trap also increased. Programs were developed to calculate the stability regions for different ions under varying experimental conditions. At τ = 0.293, the trap depth and stability region for both sinusoidal and digital trapping fields was found to be equivalent (at similar trapping parameters). The trap depth at which the sinusoidal trap operates experimentally in our research group is $\sim$ 1.36 eV. In contrast, the experimental parameters at which the digital trap is operated generates a trap depth of 1.21 eV. The dependence of the stability region on trapping frequency and the τ for a digital trap was investigated. The possibility of cotrapping multiple species was explored for several species, with mass-to-charge ratios ranging from 2 amu (H_2^+) to 131 amu (Xe^+), at the experimental trapping conditions.

Using sinusoidally and digitally time-varying trapping fields, Ca^+ Coulomb crystals

were formed, stably trapped and stored for extended periods of time. The sympathetic cooling of a diverse range of ions into Ca^+ Coulomb crystals was demonstrated, again using both sinusoidal and digital trapping fields.

A mass spectrometry technique was developed using digital ion trapping and ejection onto a detector. Ejection was achieved by switching off the trapping voltage and converting the quadrupole trap into an extractor-repeller pair by providing the ion trap electrodes with appropriate ejection pulses. Ejection when using a sinusoidal trapping field was not possible as the resonant circuits used in the construction of the sinusoidal pulse generator induced ringing in the electrodes when the trapping voltages were turned off and ejection pulses were applied. Digital ion trapping did not have this problem, and the ejection of the contents of the trap, into the time-of-flight mass spectrometer, was clean (without residual ringing).

This mass spectrometric technique is considered to be potentially very useful in the monitoring of reactions studied in an ion trap using Coulomb crystals. It extends the application of Coulomb crystals to the study of low-temperature reaction dynamics for complex reactions. Coulomb crystals, both pure Ca^+ and sympathetically-cooled multicomponent crystals, were ejected from the ion trap and the TOF trace obtained was recorded using an oscilloscope. When the integrated, base-line subtracted TOF peak was plotted against the number of ions in a Ca^+ crystal, a linear relationship was obtained. Similar linear relationships were obtained for sympathetically-cooled Ca^+ – CaF^+ Coulomb crystals, where the integrated TOF peak of both the Ca^+ and CaF^+ ions was plotted (separately) against the number of ions deduced by comparison with mixed crystal simulation results. Simulations carried out by Alexander Smith, in our research group, confirmed the effectiveness and efficiency of the technique. Though the technique is destructive, by generating a calibration plot indicating the MCP response for a given number of ions, a reaction could be studied, by ejecting crystals at different time intervals. Several crystals would need to be loaded, and ejected, for accurate measurements.

This technique would enable one to monitor a reaction in a Coulomb crystal where the reactant and product species were both either lighter or heavier than calcium, such

as the reaction between $C_2H_2^+$ and ND_3. In this case there are several possible reaction pathways leading to different products: proton transfer, charge transfer, H-elimination, H_2-elimination and D-atom abstraction.[130] Most of the charged products are lighter than calcium; the reactant and product ions would both form in the inner dark core. This digital ejection technique would facilitate unambiguous assignment of the ion masses and relative quantities – something not possible (or very difficult) with existing mass identification methods when dealing with large, multi-component Coulomb crystals.

In addition to this, we have already used this technique to optimise our calcium ion loading technique. It was observed that 355 nm ionisation consistently produced "cleaner" Ca^+ Coulomb crystals (compared with 325 nm ionisation). The purity of bi-component Coulomb crystals, where Xe^+, $C_2H_2^+$ and CaF^+ were sympathetically cooled (into Ca^+ Coulomb crystals) was able to be established with this technique. The broad Xe^+ peak in the MCP trace confirmed that Xe^+ ions were hot and uncrystallised, as anticipated from simulations. The ejection of '$C_2H_2^+$– Ca^+' crystals indicated that the proportion of $C_2H_2^+$ in the dark core was only a fraction of the volume of the dark core (with several undesired impurities inadvertently co-trapped along with $C_2H_2^+$). Importantly, this work also demonstrated that C_2H_2 does not react directly with Ca^+, suggesting that our target reaction, $C_2H_2^+$ + ND_3, can be investigated in Ca^+ Coulomb crystals.

The combination of computational and experimental work undertaken and described in this thesis paves a concrete path for observing and analysing the state-selected $C_2H_2^+$ + ND_3 reaction in an ion trap.

7.2 Future directions

This thesis introduces new theoretical and experimental methods for the study of cold ion-molecule reactions. Many aspects of this work could be further developed and improved.

The digital ejection mass spectrometry technique could be refined by improving the digital pulse generator, by ensuring that the radio frequency trapping voltages sent to the four electrodes are properly synchronised and less noisy, as otherwise they tend to heat up the

crystals. Improving the pulse shape and having better synchronisation would result in colder crystals which would be much easier to fit to simulated crystals, resulting in more accurate ion number analysis. The shallow trap depth also makes it difficult to study exothermic ion-molecule reactions. Dr Atreju Tauschinsky, in our research group, has already designed an ejection technique with sinusoidal trapping fields, where the ringing of the electrodes was addressed. Simulations suggested that detection efficiency similar to that of the digital ejection could be obtained on ejecting the contents of the trap, even ater a delay of ~ 2 μs, where the amplitude of ringing reduces to a tenth of its initial value.

Ions from pump oil have consistently been an undesired contaminant, inadvertently sympathetically cooled into Coulomb crystals, either during ionization process or by charge transfer with sympathetically cooled ions. The probability of such processes occurring could be significantly reduced by using dry backing pumps, instead of the oil-based rotary pump that is used in our laboratory.

DCl^+ or HCl^+ can, in principle, be sympathetically-cooled into a Ca^+ Coulomb crystal, and it would be interesting to investigate the reactions of these experimentally. Appropriate lasers – at wavelengths established from our calculations – could rotationally cool the already translationally cold ions. Efficient REMPI and REMPD schemes already exist for DCl^+ and HCl^+ [131] and the REMPD schemes could be used to monitor the number of DCl^+/HCl^+ ions in specific quantum states. The translationally cold molecular ions (in a specific ro-vibrational quantum states) could then react with velocity selected (and rotationally selected) ND_3 molecules from the decelerator. Such a process would represent a fully-state-selected, low collision energy reaction, fulfilling our initial objective.

The loading of acetylene ions into a Ca^+ Coulomb crystal requires further studies. One way of optimising the procedure could be by using a clean source of acetylene gas (and possibly purifying the sample further in the laboratory). The laser cooling schemes developed in this thesis could be used to rotationally cool a translationally-cold sample of acetylene ions in a multi-component Coulomb crystal. In addition, cryo-cooling the ion trap would enhance the $C_2H_2^+$ rotational state lifetimes. The internally cold $C_2H_2^+$ could

subsequently react with velocity selected (and rotationally selected) ND_3 molecules from the Stark decelerator, with the reaction able to be monitored by the mass spectrometry ejection technique introduced in this thesis. The reaction between vibrationally selected $C_2H_2^+$ and velocity selected ND_3 could also be studied (as few vibrational states are locked) and could give interesting results on the influence of vibrational state on the rate of reaction. Hybrid cooling approaches discussed in this thesis could be implemented, with a combination of cryo-cooling the ion trap and using laser-cooling schemes to rotationally cool the trapped molecular species.

Ultimately, it would be desirable to detect the quantum states of product ions. This would require the developement of appropriate REMPD schemes, such as are already known for reactant ions such as MgH^+ and $C_2H_2^+$. For the ND_3 + $C_2H_2^+$ reaction, for example, detection of ND_3^+ and ND_3H^+ (or ND_4^+) would be highly desirable in order to achieve the goal of a fully state-to-state collision experiment. Reactions between HCl^+ and ND_3 or $C_2H_2^+$ and ND_3 are of astrophysical interest, as all three reactants are relevant to the chemistry of the interstellar medium (ISM). Studying state selected reactions will assist in improving our understanding of astrophysical processes. State-selected reactions with these reactants, with their multiple branching ratios, can also be studied. Light hydrides are easy to prepare and isotope substitution reaction can be performed to observe the kinetic isotope effect. In addition, *ab initio* quantum mechanical calculations could be performed on these light hydrides to verify any experimental findings.

The study of state-selected ion-molecule reactions at low temperature and low collisional energy would also help us to understand fundamental processes underlying the reaction; the quantum nature of ion-molecule reactions, which is otherwise averaged out at ambient temperature would be unveiled. Such a study would help shed light on phenomena such as quantum tunnelling and resonances, and challenge the existing classical model, theories and assumptions. Many of the concepts and techniques introduced in this work could be applied to numerous ion-molecule reactions, potentially enabling the experimental investigation of such systems in the cold regime for the first time.

Appendix A

Angular Momentum Interactions

Descriptions provided in this appendix is based on the work of Hougen *et al* [89] and Zare *et al*.[132]

Table A.1: Definition of various symbols used

$\boldsymbol{G}$	Vibrational angular momentum
ℓ	Projection of **G** onto molecular axis
$\boldsymbol{L}$	Electronic orbital angular momentum
Λ	Projection of **L** onto molecular axis
$\boldsymbol{S}$	Electronic spin angular momentum
Σ	Projection of **S** onto molecular axis
K	$\lvert \pm \Lambda \pm \ell \rvert$
P	$\lvert K \pm \Sigma \rvert$
Ω	$\lvert \Lambda \pm \Sigma \rvert$
$\boldsymbol{R}$	Rotational angular momentum, $\boldsymbol{R} = 0, 1, 2, 3, ...$
$\boldsymbol{J}$	Total angular momentum
$\boldsymbol{N}$	$\boldsymbol{J} - \boldsymbol{S}$, total angular momentum excluding electronic spin

A particle of mass m and velocity $\boldsymbol{v}$ located at a position $\boldsymbol{r}$ from some origin has a linear momentum $\boldsymbol{p}$ (given by classical mechanics) of $m\boldsymbol{v}$ and an angular momentum given by $\boldsymbol{r} \times \boldsymbol{p}$. In quantum mechanics, the angular momentum operator is given by $(\hbar/i)\boldsymbol{\nabla}$, where $\boldsymbol{\nabla}$ is the del operator whose cartesian components are $\frac{\partial}{\partial x}\hat{\boldsymbol{x}} + \frac{\partial}{\partial y}\hat{\boldsymbol{y}} + \frac{\partial}{\partial z}\hat{\boldsymbol{z}}$. The cartesian components of $\boldsymbol{p}$ are commonly expressed as $p_u = -i\frac{\partial}{\partial u}$, where $u \in x, y, z$.

A.1 Diatomic Species

In a diatomic species, the $\boldsymbol{L}$, $\boldsymbol{S}$, $\boldsymbol{N}$ and $\boldsymbol{R}$ angular momenta are coupled. The definitions of these symbols are given in table A.1. The angular momentum interactions are summarised in figure A.1.

In Hund's case (a) coupling, $\boldsymbol{L}$ and $\boldsymbol{S}$ precess about the molecule-fixed z-axis. The orbital angular momentum, $\boldsymbol{L}$, is strongly coupled to the molecular axis (z-axis) and the electronic spin angular momentum, $\boldsymbol{S}$, is coupled to $\boldsymbol{L}$ through spin-orbit coupling. Both $\boldsymbol{L}$ and $\boldsymbol{S}$ are tied to the molecular axis (z-axis) and thus have well-defined projections onto the molecular axis, Λ and Σ respectively. Their sum is defined as: $\Omega = \Lambda + \Sigma$. The angular momentum of the rotating nuclei, $\boldsymbol{R}$, is at right angles to the molecuar axis and couples with the vector $\boldsymbol{\Omega}$, which is pointing along the molecular axis, resulting in the total angular momentum $\boldsymbol{J}$. $\boldsymbol{J}$ makes a projection M onto the space-fixed Z-axis and the projection Ω on the molecule-fixed z-axis. The case (a) coupling case wavefunction is the symmetric top wavefunction $|\Lambda; S, \Sigma; v; J, \Omega, M_J\rangle$ and is valid for species with $A\Lambda \gg BJ$.

For diatomic species with very little or no spin-orbit coupling, $\boldsymbol{S}$ is no longer coupled to the internuclear axis. This decoupling of the spin angular momentum from the molecular axis leads to a new coupling case described by Hund's case (b). $\boldsymbol{L}$ precesses about the internuclear axis with well defined component Λ. Λ is coupled to $\boldsymbol{R}$ to form $\boldsymbol{N}$, the total angular momentum without the electronic spin. $\boldsymbol{N}$ then couples with $\boldsymbol{S}$ to give the total angular momentum $\boldsymbol{J}$. Basis function in the coupling scheme are written as $|\Lambda, N, S, J, M_J\rangle$. Species with $A\Lambda \ll BJ$ fall under this coupling scheme.

A.2 The Polyatomic Species $C_2H_2^+$

The doubly degenerate ν_5 mode of $C_2H_2^+$ precesses around the molecular axis (represented as $\boldsymbol{G}$, in figure A.2) to which it is strongly coupled and has a well defined projection ℓ onto the molecular axis. The Renner-Teller effect couples the vibrational and electronic orbital angular momenta, giving rise to vibronic angular momentum, which was absent in

the diatomic species discussed section A.1 ($C_2H_2^+$ has $^2\Pi$ electronic symmetry in the ground state) . Thus the simple Hund's case (a) and (b) classifications fail to describe the angular momentum coupling appropriately. Figure A.2 describes the coupling schemes in a linear polyatomic species in the $D_{\infty h}$ point group (with nonzero Λ). Hund's coupling cases can be extended to linear polyatomics, with the definition of Hund's case (a) 'type' and Hund's case(b) 'type' coupling regimes.

In the Hund's case (a) 'type' coupling scheme, $\boldsymbol{G}$, $\boldsymbol{L}$ and $\boldsymbol{S}$ are coupled strongly to the molecular axis. $\boldsymbol{G}$ is also coupled strongly to the electronic orbital angular momentum, $\boldsymbol{L}$ (due to Renner-Teller effect), giving rise to vibronic angular momentum. This vibronic angular momentum has a well-defined projection onto the molecular axis, K, and is often referred to as the Renner-Teller quantum number- $K = \Lambda + \ell = 0(\Sigma), 1(\Pi), 2(\Delta), 3(\Phi)....$, with the vibronic states that are formed as the result of the Renner-Teller interaction indicated in brackets. The vibronic angular momentum component $\boldsymbol{K}$ further couples with $\boldsymbol{\Sigma}$ to form $\boldsymbol{P}$, such that $P = \ell + \Lambda + \Sigma = K + \Sigma$. Similar to the diatomic species, the nuclear rotational angular momentum $\boldsymbol{R}$ is perpendicular to the molecular axis and couples with $\boldsymbol{P}$ to give rise to the total angular momentum $\boldsymbol{J}$. The projection of $\boldsymbol{J}$ onto the molecular axis (z-axis) is P. The basis set for such a coupling case is $|\Lambda, \ell, K, S, \Sigma, P, J\rangle$. $K, P, \ell, \Lambda, \Sigma$ and J are all 'good' quantum numbers.

When the molecule is rotating, Coriolis forces tend to uncouple the angular momenta $\boldsymbol{L}$, $\boldsymbol{G}$, and $\boldsymbol{S}$ from the molecular axis. In general, it is not possible for the Coriolis forces to produce any extensive uncoupling of the momenta $\boldsymbol{L}$ and $\boldsymbol{G}$ from the z-axis. The spin, however, may be almost completely uncoupled from the molecular axis, so that only the quantum number K is a good one during rotation, similar to Hund's case (b) for diatomics. Such a coupling case in a polyatomic species is described by Hund's case (b) 'type' coupling, as illustrated in figure A.2. Here, the vector $\boldsymbol{K}$ couples with $\boldsymbol{R}$ to form the $\boldsymbol{N}$, which then couples with $\boldsymbol{S}$ to give the total angular momentum $\boldsymbol{J}$. In this case, Σ is not a good quantum number, and the basis set is formed by: $|\Lambda, K, N, S, J, M_J\rangle$.

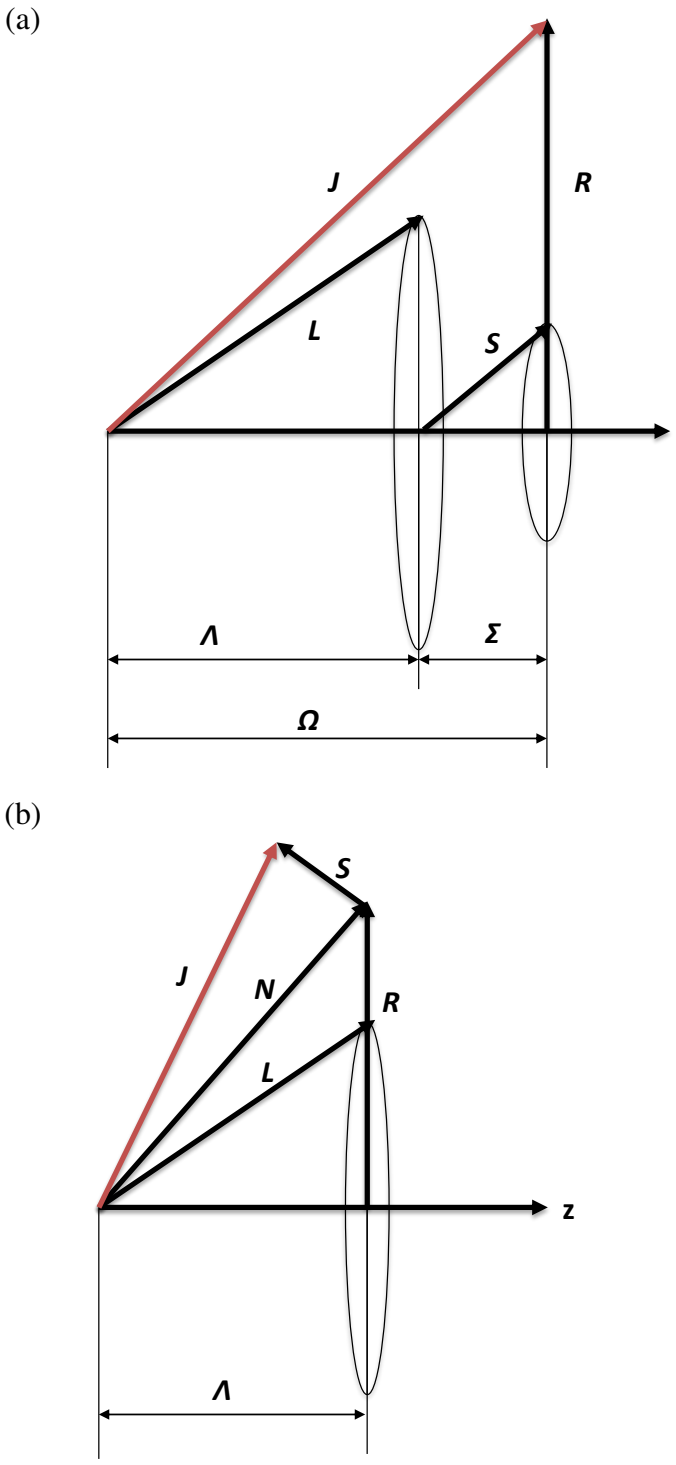

Figure A.1: Schematic illustration of the angular momentum interactions taking place in a diatomic species: (left) Hund's case (a) interactions, and (right) Hund's case (b) interactions.

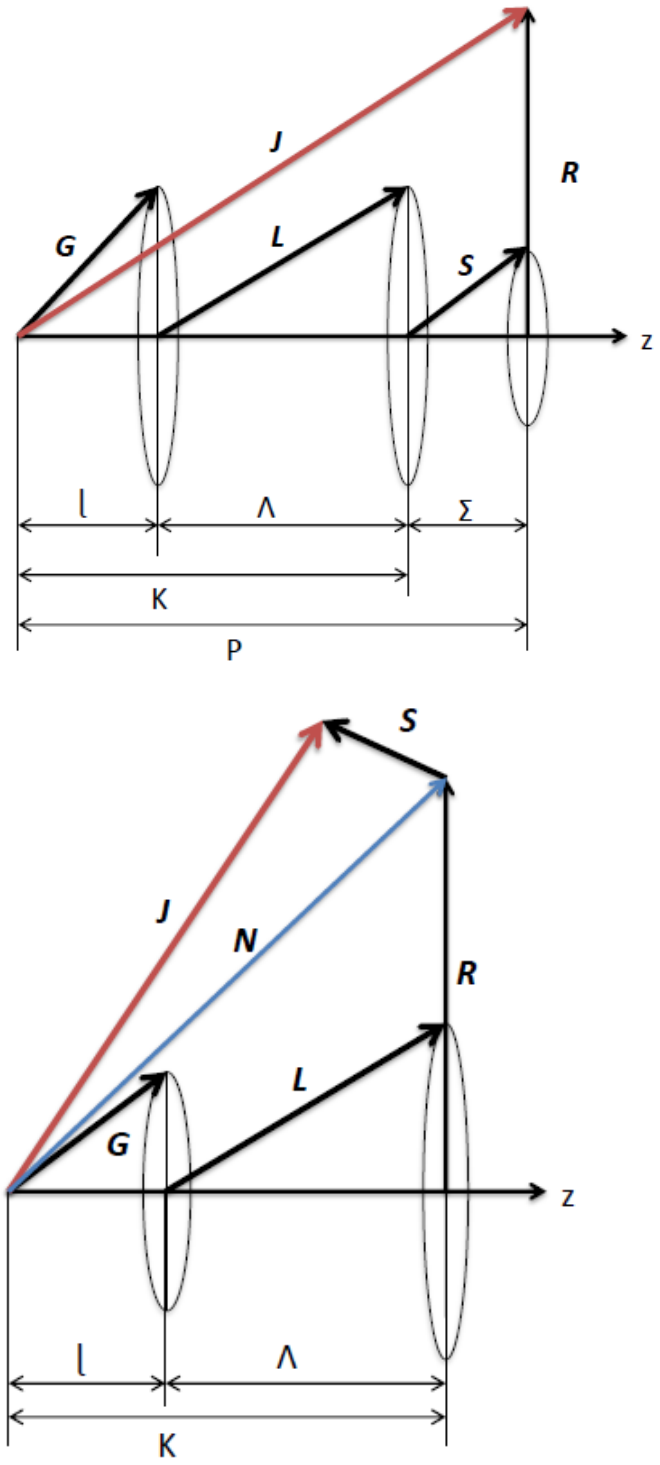

Figure A.2: Schematic illustration of the angular momentum interactions taking place in a polyatomic species in $^2\Pi$ elelectronic state. The interactions are (top) Hund's case (a) 'type' or (bottom) Hund's case (b) 'type' .

Appendix B

Rotational Energy and Rotational Line Strength for $C_2H_2^+$

Derivation of the $C_2H_2^+$ energy levels and transition intensities is achieved through diagonalization of the relevant Hamiltonian matrices. Using the harmonic approximation, the vibrational energy of the ν_5 cis-bending mode will be given by

$$E_{\text{vib}} = \omega_5(v_5 + \frac{d_5}{2}) = \omega_5(v_5 + 1), \tag{B.1}$$

where ω_5 is the vibrational frequency, v_5 is the vibrational quantum number, and d_5 is the degeneracy of the cis-bending mode, which is 2 in this case. Introduction of the Renner-Teller effect splits each of the vibrational levels into several vibronic levels.

In a Π electronic state, the K quantum number ($K = \Lambda + l$) takes the values $K = v_5 + 1, v_5 - 1, \ldots 0$ for an odd value of the vibrational quantum number v_5, or $K = v_5 + 1, v_5 - 1, \ldots, 1$ for an even value of v_5. Taking the Renner-Teller interaction into account the vibronic energy is given for $K = v_5 + 1$ by

$$E_{\text{vibronic}}(v_5, K = v_5 + 1, \Sigma = \pm 1/2) = \omega_5(v_5 + 1) \pm \frac{1}{2}A - \frac{1}{8}\epsilon^2\omega_5 K(K+1), \tag{B.2}$$

where ϵ is the Renner-Teller parameter for v_5 and Σ is the projection of the spin angular

momentum S on the internuclear axis.

For vibronic levels with $K < v_5 + 1$, the vibronic energies are given instead by

$$E^{+}_{\text{vibronic}}(v_5, K < v_5+1, \pm 1/2) = \omega_5(1 - \frac{1}{8}\epsilon^2)(v_5+1) + \frac{1}{2}A^* \mp \frac{\epsilon^2 A\omega_5 K(v_5+1)}{8A^*}, \quad \text{(B.3)}$$

$$E^{-}_{\text{vibronic}}(v_5, K < v_5+1, \pm 1/2) = \omega_5(1 - \frac{1}{8}\epsilon^2)(v_5+1) - \frac{1}{2}A^* \mp \frac{\epsilon^2 A\omega_5 K(v_5+1)}{8A^*}, \quad \text{(B.4)}$$

where $A^* = \sqrt{A^2 + \epsilon^2\omega_5^2[(v_5+1)^2 - K^2]}$.

The rotational Hamiltonian is given by

$$\begin{aligned}
\mathcal{H}_{\text{rot}} &= B[J(J+1) + S(S+1) - 2(K+\Sigma)\Sigma - JS_{\pm} \\
&\quad + K^2 + \frac{G_{\pm}}{2} + \frac{L_{\pm}}{2} + GL_{\pm} - 2(P-\Sigma)K + JSGL_{\pm}] \\
&= B[J(J+1) + S(S+1) - 2(K+\Sigma)\Sigma + K^2 - 2(P-\Sigma)K] + B[(J_+S_- + J_-S_+)] \\
&\quad + B[(G_+G_- - G_-G_+)/2] + B[((L_+L_- - L_-L_+))/2] + B[G_+L_- - G_-L_+] \\
&\quad - B[(J_+ - S_+)(G_- + L_-) - (J_- - S_-)(G_+ + L_+)], \qquad \text{(B.5)}
\end{aligned}$$

where G is the vibrational angular momentum associated with the degenerate bending motion and L is the electronic orbital angular momentum. The first term of equation B.5 is the zero-order Hamiltonian for pure case (a) type coupling, and this can be simplified as follows:

$$\begin{aligned}
\mathcal{H}_{\text{rot}} &= B[J(J+1) + S(S+1) - 2(K+\Sigma)\Sigma + K^2 - 2(P-\Sigma)K] \\
&= B[(J+1/2)^2 - K(K+2\Sigma)], \qquad \text{(B.6)}
\end{aligned}$$

where $S = 1/2$ and $J(J+1) = (J+\frac{1}{2})^2 - \frac{1}{4}, \Sigma = \pm\frac{1}{2}, \Sigma^2 = \frac{1}{4}$. The second term in B.5 contributes to the first-order correction to the energy. The third, fourth and fifth terms are

independent of J and contribute to an overall shift of energy. The final term,

$$B[(J_+ - S_+)(G_- + L_-) - (J_- - S_-)(G_+ + L_+)] = \\ B[(J_+ - S_+)G_- - (J_- - S_-)G_+] + B[(J_+ - S_+)L_- - (J_- - S_-)L_+], \quad \text{(B.7)}$$

connects states differing by one unit in l and Λ (see Zare,[132] page 302). Including the spin-orbit splitting adds a diagonal term $A\Lambda\Sigma$;

$$\langle\psi_P|\mathcal{H}_{\text{rot+SO}}|\psi_P\rangle = A\Lambda\Sigma + B[(J+\frac{1}{2})^2 - K(K+2\Sigma)] \quad \text{(B.8)}$$

(here, P denotes the states that result after spin-orbit coupling, so P can either be $K+1/2$ or $K-1/2$) and off-diagonal mixing is given by

$$\begin{aligned}\langle\psi_{K+1/2}|\mathcal{H}_{\text{rot+SO}}|\psi_{K-1/2}\rangle &= \langle\psi_{K+1/2}|B[J_+S_- + J_-S_+]|\psi_{K-1/2}\rangle \\ &= B\sqrt{(J+\frac{1}{2})^2 - K^2}. \end{aligned} \quad \text{(B.9)}$$

B.1 Discussion of $^2\Pi$ and $^2\Delta$ states

For the states $K = v_5 + 1$, i.e., the $^2\Pi$ rovibronic levels of $v_5 = 0$ and the Δ rovibronic levels for $v_5 = 1$, and when $A < 0$ (inverted doublet as in $C_2H_2^+$), states with $P = K - 1/2$ (or $\Sigma = -1/2$) are referred to as F_2 states and the states with $P = K + 1/2$ (or $\Sigma = +1/2$) as F_1 states. Hereafter we write these basis functions as $|\ 1\rangle \equiv|\ P = K + 1/2\rangle$ and $|\ 2\rangle \equiv|\ P = K - 1/2\rangle$.

The elements of the Hamiltonian matrix are

$$\mathcal{H}_{11} = \frac{A}{2} + B[(J+\frac{1}{2})^2 - K(K+1)],\ [\Lambda = 1,^2\Pi \text{ electronic state}] \quad \text{(B.10)}$$

$$\mathcal{H}_{22} = -\frac{A}{2} + B[(J+\frac{1}{2})^2 - K(K-1)], \tag{B.11}$$

$$\mathcal{H}_{12} = \mathcal{H}_{21} = B\sqrt{(J+\frac{1}{2})^2 - K^2}. \tag{B.12}$$

The solution for the above is

$$\begin{aligned} \mathcal{E}_{\pm} &= \frac{\mathcal{H}_{11}+\mathcal{H}_{22}}{2} \mp \sqrt{(\frac{\mathcal{H}_{11}-\mathcal{H}_{22}}{2})^2 + \mathcal{H}_{12}^2} \\ &= B[(J+\frac{1}{2})^2 - K^2 \pm \frac{1}{2}\sqrt{4(J+\frac{1}{2})^2 + Y(Y-4K)}\,], \end{aligned} \tag{B.13}$$

where $Y = \frac{A}{B}$. Equation B.13 is valid for all states except for the $J = K - 1/2$ state of $|P = K - \frac{1}{2}\rangle$ (such as $^2\Pi_{1/2}, J = 1/2$ and $^2\Delta_{3/2}, J = 3/2$). This is because an anomalous correlation arises in the absence of a corresponding state in $|P = K + \frac{1}{2}\rangle$, and the energy of this unique state is given by

$$E(J = K - \frac{1}{2}) = -\frac{A}{2} + BK. \tag{B.14}$$

For the ion under study, the upper sign in equation (B.13) would be for the lower *P* value in each vibronic component. This gives the energies of the innermost levels in the rovibronic splitting pattern and takes into account up to only the second order correction for energy. Note that in some texts, A_{eff} is used instead of A, where $A_{\text{eff}} = A[1 - \frac{1}{8}\epsilon^2 K(K+1)]$. The rotational levels of the molecule belong to case (a) when $|A_{\text{eff}}| \gg BJ$ and to case (b) when $|A_{\text{eff}}| \ll BJ$. In addition, we also use B_{eff} and Y_{eff} in place of B and Y (respectively), as set out by Hougen, [89] where $B_{\text{eff}} = B(1 \pm \frac{1}{Y_{\text{eff}}})$ and $Y_{\text{eff}} = |Y(1 - \frac{K(K+1)\epsilon^2}{8})|$. Given the molecular constants for $C_2H_2^+$, $B_{\text{eff}} \approx B$ and $Y_{\text{eff}} \approx Y$ for this system. The complete

energy of the above states can thus be written as follows:

$$E_{\text{vib}} = \omega_5(v_5+1), \tag{B.15}$$

$$E_{\text{vib+rot}} = E_{\text{vib}} + B[(J+\frac{1}{2})^2 - K^2 \pm \frac{1}{2}\sqrt{4(J+\frac{1}{2})^2 + Y(Y-4K)}\,], \tag{B.16}$$

$$E_{\text{vib+rot}} = E_{\text{vib}} - \frac{A}{2} + BK, \text{ when } J = K - \frac{1}{2}. \tag{B.17}$$

B.2 Discussion of $^2\Sigma$ states

The vibronic interaction giving rise to K = 0 will give two states denoted as $^2\Sigma^+$ and $^2\Sigma^-$. The Σ states are those with the highest and the lowest energy in the group of vibronic levels formed after the vibronic interactions (from a single vibrational level).

$K = 0$ can be formed from the following possible combinations represented by the basis $|\Lambda\ell\Sigma, J\rangle$: $|+1-1+1/2, J\rangle, |-1+1+1/2, J\rangle, |+1-1-1/2, J\rangle$, and$|-1+1-1/2, J\rangle$. We label the above basis functions for future reference accordingly:

$|+1-1+1/2, J\rangle \equiv |1\rangle$, $|-1+1+1/2, J\rangle \equiv |2\rangle$,

$|+1-1-1/2, J\rangle \equiv |3\rangle$, and $|+1-1-1/2, J\rangle \equiv |4\rangle$.

The 4×4 matrix is established in a similar way to the previous section, where the diagonal elements are given by

$$\langle\Lambda\ell\Sigma, J|\mathcal{H}_{\text{rot+SO}}|\Lambda\ell\Sigma, J\rangle = A\Lambda\Sigma + Bg(J, K+\Sigma), \text{where } K+\Sigma \text{ is } P$$

$$g(J, K+\Sigma) = J(J+1) - P^2 + \langle G_\perp^2\rangle_{\text{Avg}} + \langle L_\perp^2\rangle_{\text{Avg}} + \langle S_\perp^2\rangle_{\text{Avg}} \tag{B.18}$$

$$\langle G_\perp^2\rangle_{\text{Avg}} = G(G+1) - \ell^2 = 1, \tag{B.19}$$

$$\langle L_\perp^2\rangle_{\text{Avg}} = L(L+1) - \Lambda^2 = 1, \tag{B.20}$$

$$\langle S_\perp^2\rangle_{\text{Avg}} = S(S+1) - \Sigma^2 = 1/2. \tag{B.21}$$

Substituting the appropriate values for the angular momenta, the last three terms reduce to

a number that is constant for all levels, and just shifts the energy level:

$\langle G_\perp^2 \rangle_{\text{Avg}} + \langle L_\perp^2 \rangle_{\text{Avg}} + \langle S_\perp^2 \rangle_{\text{Avg}} =$ constant.

The energy contribution due to spin mixing will be given by

$$\mathcal{H}_{13} = \langle \Lambda\ell + \frac{1}{2}, J|\mathcal{H}_{\text{rot+SO}}|\Lambda\ell - \frac{1}{2}, J\rangle = -Bf(J, K - \frac{1}{2}) \text{ and } \mathcal{H}_{13} = \mathcal{H}_{31}, \tag{B.22}$$

$$\mathcal{H}_{24} = \langle \Lambda\ell - \frac{1}{2}, J|\mathcal{H}_{\text{rot+SO}}|\Lambda\ell + \frac{1}{2}, J\rangle = -Bf(J, K - \frac{1}{2}) \text{ and } \mathcal{H}_{24} = \mathcal{H}_{42}, \tag{B.23}$$

where $K - 1/2 = P$ and $f(J, K - 1/2) = \sqrt{[J(J+1) - P(P+1)]}$.

The next set of perturbative terms arise from the Renner-Teller interaction which gives rise to off-diagonal elements $\mathcal{H}_{12}, \mathcal{H}_{21}, \mathcal{H}_{34}, \mathcal{H}_{43}$. The mixing occurs between states of the same Σ but different Λ and ℓ values.

Substitution of the matrix elements gives the overall secular determinant

$$\begin{bmatrix} \frac{1}{2}A + Bg(J, K + \frac{1}{2}) & \frac{1}{2}(-1)^{J-\frac{1}{2}}\epsilon\omega_5 R(v, K) & -Bf(J, K - \frac{1}{2}) & 0 \\ \frac{1}{2}(-1)^{J-\frac{1}{2}}\epsilon\omega_5 R(v, K) & -\frac{1}{2}A + Bg(J, K + \frac{1}{2}) & 0 & -Bf(J, K - \frac{1}{2}) \\ -Bf(J, K - \frac{1}{2}) & 0 & -\frac{1}{2}A + Bg(J, K - \frac{1}{2}) & \frac{1}{2}(-1)^{J-\frac{1}{2}}\epsilon\omega_5 R(v, K) \\ 0 & -Bf(J, K - \frac{1}{2}) & \frac{1}{2}(-1)^{J-\frac{1}{2}}\epsilon\omega_5 R(v, K) & \frac{1}{2}A + Bg(J, K - \frac{1}{2}) \end{bmatrix} \tag{B.24}$$

where the functions g, f and R are defined above. The secular determinant formed in equation B.24 can be solved to give the energy of the four Σ vibronic states of given J and parity,

$$E_{\text{vib}} = \omega_5(v_5 + 1)(1 - \frac{1}{8}\epsilon^2) \tag{B.25}$$

$$E(^2\Sigma) = E_{\text{vib}} + B(J + \frac{1}{2})^2 \pm \frac{1}{2}\sqrt{\Delta\nu^2 \pm 4B(J + \frac{1}{2})(v_5 + 1)\epsilon\omega_5 + 4B^2(J + \frac{1}{2})^2}. \tag{B.26}$$

As noted previously, we use B_{eff} in place of B in equation A26, where $B_{\text{eff}} = B(1 \pm \frac{A^2 B}{A_{\text{eff}}^3})$, $A_{\text{eff}} = |\Delta\nu|$ and $\Delta\nu = \sqrt{A^2 + (v+1)^2\epsilon^2\omega_5^2}$, as defined by Herzberg. [133] (The +

sign in the expression for B_{eff} refers to the $^2\Sigma^+$ state, with the $-$ sign applying to the $^2\Sigma^-$ level.)

Appendix C

Pseudo potential Trap Depth Derivation

I have derived the pseudo potential for the digital trap, based on the derivation of the pseudo potential of the sinusoidal trap as described by D. Gerlich *et al* in reference [106].

A typical digital pulse is given by

$$P_\tau(t) = \begin{cases} 1 & \text{if } |t| \leq \tau T/2 \\ 0 & \text{if } \tau T/2 < |t| \leq (1-\tau)T/2 \\ -1 & \text{if } (1-\tau)T/2 < |t| \leq (1+\tau)T/2 \\ 0 & \text{if } (\tau+1)T/2 < |t| \leq (1-\tau/2)T \\ 1 & \text{if } (1-\tau/2)T < |t| \leq T, \end{cases} \tag{C.1}$$

where τ is the fraction of the time period the pulse has value 1.

Digital trapping voltages can be generated by a Fourier transformation of $\cos(\omega t)$,

$$f_T = \sum_{n=1}^{\infty} a_n \cos(n\omega t) = \sum_{n=1}^{\infty} a_n \cos\left(\frac{2n\pi t}{T}\right) = \sum a_n \cos(2n\pi\tau), \tag{C.2}$$

where a_n is the Fourier coefficient obtained by Fourier decomposition of equation C.2;

$$\begin{aligned} a_n &= -\frac{2}{n\pi}(-1+(-1)^n)\sin n\pi\tau \\ &= \frac{4}{n\pi}\sin(n\pi\tau) \text{ (where } n \text{ is odd).} \end{aligned} \tag{C.3}$$

A particle of charge q and mass m in an electromagnetic field $E(r,t)$ and $B(r,t)$ obeys the equation of motion (non-relativistic regime) given by,

$$m\ddot{r} = qE(r,t) + q\dot{r} \times B(r,t) = qE(r,t), \tag{C.4}$$

In equation C.4 the magnetic component is set to zero as the weak force exerted by the magnetic fields is discarded. The quasistationary electric field is composed of a static field $E_s(r)$ and a time dependent part, $E(r,t)$. $E(r,t)$ is given by:

$$E(r,t) = \begin{cases} E_0(r)\cos(\omega t) & \text{for a sinusoidal trap} \\ E_0(r)\sum\limits_{n=1}^{\infty} a_n \cos(n\omega t) = E_0 f_T & \text{for a digital trap.} \end{cases} \tag{C.5}$$

Here, E_0 is the peak electric field vector. The earliest treatment of the interaction of electrons with electromagnetic waves was Thomson's determination of an X-ray scaterring cross-section. His calculation is based on the classical non-relativistic motion of an electron in the field of a plane wave, which can be simply given by the equation of motion:

$$m\ddot{r} = \begin{cases} qE_0(r)\cos(\omega t) + qE_s(r) & \text{for a sinusoidal trap,} \\ qE_0(r)\sum\limits_{n=1}^{\infty} a_n \cos(n\omega t) + qE_s(r) = qE_0(r)f_T + qE_s(r) & \text{for a digital trap.} \end{cases} \tag{C.6}$$

Effective Potential and Pseudo Potential

To describe the motion of an ion in an inhomogenous field, the field is assumed to be only weakly inhomogenous and vary smoothly with r such that equation C.6 would still hold. The frequency is also assumed to be high enough to keep the amplitude given by

equation C.11 low. It can be expected that along the slow drift motion, the amplitude $a(t)$ and phase of the oscillatory motion vary slowly with time. Therefore, C.6 can be solved by adding a small drift term $R_0(t)$ and a rapidly oscillating motion $R_1(t)$:

$$r(t) = R_0(t) + R_1(t), \tag{C.7}$$

$$\text{where } R_1(t) = \begin{cases} -a(t)\cos\omega t \text{ for a sinusoidal trap,} \\ -a(t) f_T \text{ for a digital trap.} \end{cases} \tag{C.8}$$

A slow spatial variation of E_0 allows one to keep the first two terms in the Taylor expansion of $E[r(t)]$ about $R_0(t)$,

$$\begin{aligned} E[r(t)] &= E[R_0(t) - a(t)P_T], \text{ here } P_T \text{ is either } f_T \text{ or } \cos(\omega t) \\ &= E[R_0(t)] - (a.\nabla)E_0(R_0)P_T. \end{aligned} \tag{C.9}$$

C.1 Pseudo potential for a Sinusoidal Trap

The solution for differential equation C.6 in homogeneous fields independent of r, taking the static part to be zero is,

$$r(t) = r(0) - a.\cos(\omega t) \tag{C.10}$$

Here,

$$a = \frac{qE_0(r)}{m\omega^2} \tag{C.11}$$

where a is the amplitude vector.

Substituting equation C.9 into the equation of motion (equation C.6), $m\ddot{r}(t) = qE_0(r)\cos(\omega t))$. Solving first for the case of a sinusoidal trap:

$$m\frac{d^2}{dt^2}[R_0(t) - a(t)\cos(\omega t)] = q[E_0\{R_0(t)\} - (a.\nabla)E_0\{R_0(t)\}\cos(\omega t)]\cos(\omega t). \tag{C.12}$$

Here, it is assumed that the time variation of a and R_0 is slow, such that, $\dot{a} \ll \omega a$ and

$\ddot{R}_0 \ll \omega\dot{R}_0$. The left hand side (LHS) of equation C.9 simplifies to:

$$m\ddot{r} = m\frac{d^2}{dt^2}r(t) = m\ddot{R}_0(t) + ma(t)\omega^2\cos(\omega t). \tag{C.13}$$

Substituting this value in equation C.9,

$$m\ddot{R}_0(t) + ma(t)\omega^2\cos(\omega t) = q[E_0\{R_0(t)\}\cos(\omega t) - q(a.\nabla)E_0\{R_0(t)\}\cos^2(\omega t)]. \tag{C.14}$$

Assuming that the amplitude a changes in time only due to the motion along R_0, we can replace $a(t)$ with $a(R_0)$ – the amplitude $a(t)$ in equation C.14 can be replaced by $a(R_0)$ or a which is given in equation C.11, $a = qE_0(r)/m\omega^2$.

$$m\ddot{R}_0(t) = -q[a(t).\nabla]E_0[R_0(t)]\cos^2(\omega t). \tag{C.15}$$

Recalling the vector analysis relation,

$$\begin{aligned}(E_0.\nabla)E_0 &= \frac{1}{2}\nabla E_0^2 - E_0 \times (\nabla \times E_0) \\ &= \frac{1}{2}\nabla E_0^2.\end{aligned} \tag{C.16}$$

The second term disappears based on the quasi-static field condition. Also, the average of $\cos^2(\omega t)$ over a period is given by,

$$\langle\cos^2(\omega t)\rangle = \frac{1}{2\pi}\int_0^{2\pi}\cos^2(\omega t)dt = \frac{1}{2}. \tag{C.17}$$

Substituting equations C.16 and C.17 into C.15,

$$m\ddot{R}_0 = -\frac{q^2}{m\omega^2}\frac{1}{2}\nabla E^2[R_0(t)].\frac{1}{2} = -\frac{q^2}{4m\omega^2}\nabla E_0^2[R_0(t)]. \tag{C.18}$$

This equation of motion shows the time-averaged effect of the oscillatory field. Identifying

that an electrostatic force is the negative gradient of a potential, the force can be defined as

$$\text{Force, } F = m\ddot{R}_0 = -\nabla V^*(R_0). \tag{C.19}$$

V^*, is the effective potential and the pseudo potential is ϕ_{pseudo},

$$V^* = -\frac{q^2}{4m\omega^2}E_0^2(R_0). \tag{C.20}$$

E_0 is the field vector which is equal to $\nabla\phi(x,y)$. $\phi(x,y)$ for a quadrupole is $V_{rf}^2(x^2 - y^2)/2r_0^2$.

$$E_0^2 = (\nabla\phi(x,y))^2 = \frac{V_{rf}^2}{r_0^4}(x^2+y^2) \tag{C.21}$$

Therefore, the pseudo potential becomes,

$$\phi_{pseudo} = \frac{q^2}{4m\omega^2}\frac{V_{rf}^2}{r_0^4}(x^2+y^2) \tag{C.22}$$

C.2 Pseudo potential for a Digital Trap

Electric field for a digital trap, $E(r,t)$, is given in equation C.5. Recalling the equation of motion (equation C.6),

$$\begin{aligned} m\ddot{r} &= qE(r,t) \\ &= qE_0[R_0(t)]\sum_{n=1}^{\infty} a_n \cos(n\omega t). \end{aligned} \tag{C.23}$$

Solving for r,

$$\begin{aligned}
\ddot{r} &= \frac{q}{m}E_0(r)\sum_{n=1}^{\infty}a_n\cos(n\omega t) \\
\Rightarrow \dot{r} &= \frac{q}{m}E_0(r)\int\sum_{n=1}^{\infty}a_n\cos(n\omega t) \\
\Rightarrow r &= r_0+\frac{q}{m}E_0(r)\int\int\sum_{n=1}^{\infty}a_n\cos(n\omega t). \qquad \text{(C.24)}
\end{aligned}$$

The constants of motion are appropriately eliminated by shifting the origin. Switching the order of the integral and summation operators in the above equation,

$$\begin{aligned}
r(t) &= r_0-\frac{q}{m}E_0(r)\sum_{n=1}^{\infty}\int\int a_n\cos(n\omega t) \\
&= r_0-\left(\frac{qE_0(r)T^2}{4\pi^2 m}\right)\sum_{n=1}^{\infty}\frac{a_n}{n^2}\cos(n\omega t) \qquad \text{(C.25)} \\
r(t) &= r_0-\bar{A}\sum_{n=1}^{\infty}\frac{a_n}{n^2}\cos(\omega t). \qquad \text{(C.26)}
\end{aligned}$$

Here, $\bar{A}$ is the amplitude, and for a digital trap is given by:

$$\bar{A}=\frac{q\bar{E}(r)T^2}{4\pi^2 m}. \qquad \text{(C.27)}$$

Recalling the equation for electric field equation, similar to the sinusoidal trap treatment, a Taylor expansion of the equation gives,

$$\begin{aligned}
E[R(t)] &= E[R_0(t)]\sum_{n=1}^{\infty}a_n\cos(n\omega t) \\
&= E[R_0(t)-\bar{A}\sum_{n=1}^{\infty}\frac{a_n}{n^2}\cos(n\omega t)] \\
&= E_0[R_0(t)]-(\bar{A}\nabla)E_0[r_0(t)]\sum_{n=1}^{\infty}\frac{a_n}{n^2}\cos(n\omega t). \qquad \text{(C.28)}
\end{aligned}$$

Double differentiation of equation C.26 gives,

$$\ddot{R}(t) = \ddot{R}_0(t) + \bar{A}\frac{4\pi^2}{T^2}\sum_{n=1}^{\infty} a_n \cos(n\omega t). \tag{C.29}$$

Substituting equation C.28 into C.29,

$$m\ddot{R}(t) = qE[R_0(t)]\sum_{n=1}^{\infty} a_n \cos(n\omega t)$$

$$\Rightarrow m\ddot{R}_0(t) + \bar{A}\frac{4\pi^2 m}{T^2}\sum_{n=1}^{\infty} a_n \cos(n\omega t) = q\left[E_0[R_0(t)] - (\bar{A}\nabla)E_0[r_0(t)]\sum_{n=1}^{\infty}\frac{a_n}{n^2}\cos(n\omega t)\right]\sum_{n=1}^{\infty} a_n \cos(n\omega t). \tag{C.30}$$

As in the case of the sinusoidal trap, $\dot{\bar{A}} = 0$ and $\ddot{\bar{A}} = 0$. Equation C.30 simplifies to:

$$\begin{aligned} m\ddot{R}_0(t) &= -q(\bar{A}.\nabla)E_0[R_0(t)]\sum_{n=1}^{\infty}\frac{a_n}{n^2}\cos(n\omega t)\sum_{n=1}^{\infty} a_n \cos(n\omega t) \\ &= -\frac{q^2T^2}{4m\pi^2}\big(E_0[R_0(t)].\nabla\big)E_0[R_0(t)]\left[\sum_{n=1}^{\infty}\frac{a_n}{n^2}\cos(n\omega t)\sum_{n=1}^{\infty} a_n \cos(n\omega t)\right] \end{aligned} \tag{C.31}$$

To appropriately solve equation C.31, the average value of,
$\sum_{n=1}^{\infty}(a_n/n^2)\cos(n\omega t)\sum_{n=1}^{\infty} a_n \cos(n\omega t)$
over a time period has to be established (where $\theta = \omega t$).

$$\begin{aligned} \left\langle \sum_{n=1}^{\infty}\frac{a_n}{n^2}\cos(n\omega t)\sum_{n=1}^{\infty} a_n \cos(n\omega t)\right\rangle &= \frac{1}{2\pi}\int_0^{2\pi}\left[\sum_{n=1}^{\infty}\frac{a_n}{n^2}\cos(n\omega t)\right]\left[\sum_{n=1}^{\infty} a_n \cos(n\omega t)\right]d\theta \\ &= \frac{1}{2}\sum_{n=1}^{\infty}\frac{a_n}{n^2} \end{aligned} \tag{C.32}$$

Thus for a digital trap, the value of the time-averaged quantity containing the summation terms is dependent on τ, where τ is hidden in the Fourier coefficient a_n.

As $\big(E_0[R_0(t)].\nabla\big)E_0[R_0(t)] = \frac{1}{2}\big(\nabla E_0\big)^2$, equation C.31 can now be written as

$$\begin{aligned} m\ddot{R}_0(t) &= -\frac{q^2T^2}{4m\pi^2}\big(\frac{1}{2}(\nabla E_0)^2\big)\left[\frac{1}{2}\sum_{n=1}^{\infty}\frac{a_n}{n^2}\right] \\ &= -\frac{q^2}{2m\omega^2}\left[\frac{1}{2}\sum_{n=1}^{\infty}\frac{a_n}{n^2}\right]\nabla E_0^2. \end{aligned} \tag{C.33}$$

As noted previously, $F = -\nabla U$, and by comparison,

$$\phi_{\text{pseudo}} = -\frac{q^2}{4m\omega^2}\left[\sum_{n=1}^{\infty}\frac{a_n}{n^2}\right]E_0^2. \tag{C.34}$$

E_0 is given by $\nabla\phi$, and as before ϕ for a quadrupole trap is given by, $V_{\text{rf}}(x^2-y^2)/2r_0^2$. Thus

$$\phi_{\text{pseudo}} = \frac{q^2V_{rf}^2}{2m\omega^2r_0^4}(x^2+y^2)\left[\frac{1}{2}\sum_{n=1}^{\infty}\frac{a_n}{n^2}\right], \tag{C.35}$$

where a_n is given by equation 5.7 in chapter 5.

Appendix D

Transformation Matrix for Stability Diagram of Ions in a Digital Ion Trap

The condition of stability of an ion in an ion trap is that the absolute value for the trace of the transformation matrix for a phase difference of π in the wave should be less than 2:[104, 107, 134]

$$|Tr[M_u(\xi|\xi+\pi)]|<2. \tag{D.1}$$

The transformation matrix for changing the position of an ion from position ξ to $\xi+\pi$ is given by $M(\xi|\xi+\pi)$,

$$M(\xi|\xi+\pi) = M(\pi|0) = S(\pi). \tag{D.2}$$

Where, $S(\pi)$ is obtained by a series of matrix multiplication done in the right order,[104, 135]

$$S(\Xi) = \begin{cases} T(a,\Xi), & \text{if } 0<\Xi \leq (\frac{1}{2}-\tau)\pi) \\ T(a+2q,\Xi-[\frac{1}{2}-\tau])S([\frac{1}{2}-\tau]\pi) & \text{if } (\frac{1}{2}-\tau)\pi<\Xi \leq \frac{1}{2}\pi \\ T(a,\Xi-\frac{1}{2}\pi)S(\frac{1}{2}\pi) & \text{if } \frac{1}{2}\pi<\Xi \leq (1-\tau)\pi \\ T(a-2q,\Xi-[1-\tau]\pi)S([1-\tau]\pi) & \text{if } (1-\tau)\pi<\Xi \leq \pi, \end{cases} \tag{D.3}$$

and

$$T(K,l) = \frac{1}{2}\begin{bmatrix} e^{\sqrt{-Kl}} + e^{-\sqrt{-Kl}} & \frac{1}{\sqrt{-K}}(e^{\sqrt{-Kl}} - e^{-\sqrt{-Kl}}) \\ \sqrt{-K}(e^{\sqrt{-Kl}} - e^{-\sqrt{-Kl}}) & e^{\sqrt{-Kl}} + e^{-\sqrt{-Kl}} \end{bmatrix} \text{ if } K \neq 0, \quad \text{(D.4)}$$

$$T(K,l) = \frac{1}{2}\begin{bmatrix} 1 & l \\ 0 & 1 \end{bmatrix} \text{ if } K = 0. \quad \text{(D.5)}$$

The one-period transfer matrix for these pulse-excited systems can be stitched together by the multiplication of four fundamental matrices. The first Matrix is the rightmost one. The absolute value of the trace of the matrix $S(\pi)$ thus obtained dictates the region of stability as given by equation D.1

References

[1] K. S. Twyman. PhD Thesis, University of Oxford. 2013.

[2] R. V. Krems. *Phys. Chem. Chem. Phys.*, 10:4079–4092, 2008.

[3] Martin T. Bell and Timothy P. Softley. *Mol. Phys.*, 107(2):99–132, 2009.

[4] I. W. M. Smith and P. W. Barnes. *Annu. Rep. Prog. Chem., Sect. C: Phys. Chem.*, 109:140–166, 2013.

[5] M. Hawley and M. A. Smith. *J. Chem. Phys.*, 96(2):1121–1127, 1992.

[6] P. W. Atkins. *Molecular Quantum Mechanics*. Oxford, 1970.

[7] M. Brouard. *Nat. Chem.*, 6:274–275, 2014.

[8] D. C. Clary. *Proc. Natl. Acad. Sci.*, 105(35):12649–12653, 2008.

[9] I. W. M. Smith and B. R. Rowe. *Acc. Chem. Res.*, 33(5):261–268, 2000.

[10] D. C. Clary. *A. Rev. Phys. Chem.*, 41:61, 1990.

[11] D. C. Clary and J. P. Henshaw. *Faraday Discuss.*, 84:333, 1987.

[12] J. Troe. *J. Chem. Phys.*, 87:2773, 1987.

[13] C. F. Williams, S. K. Pogrebnya, and D. C. Clary. *J. Chem. Phys.*, 126(15):154321, 2007.

[14] S. Willitsch. *Int. Rev. Phys. Chem.*, 31(2):175–199, 2012.

[15] T. Baba and I. Waki. *Jpn, J. Appl, Phys*, 36:L1134, 1996.

[16] K. Mølhave and M. Drewsen. *Phys. Rev. A*, 62:011401, 2000.

[17] B. Roth, P. Blythe, H. Daerr, L. Patacchini, and S. Schiller. *J. Phys. B: At. Mol. Opt. Phys.*, 39:S1241, 2006.

[18] S. Willitsch, M. T. Bell, A. D. Gingell, S. R. Procter, and T. P. Softley. *Phys. Rev. Lett.*, 100:043203, 2008.

[19] M. A. van Eijkelenborg, M. E. M. Storkey, D. M. Segal, and R. C. Thompson. *Phys. Rev. A*, 60:3903, 1999.

[20] X. Tong, A. H. Winney, and S. Willitsch. *Phys. Rev. Lett.*, 105:143001, 2010.

[21] M. Drewsen, I. Jensen, J. Lindballe, Martinussen R. Nissen, N., A. Mortensen, P. Staanum, and D. Voigt. *Int. J. Mass. Spectrom.*, 229(12):83 – 91, 2003.

[22] Peter F. Staanum, Klaus Højbjerre, Roland Wester, and Michael Drewsen. *Phys. Rev. Lett.*, 100:243003, Jun 2008.

[23] K. Højbjerre, D. Offenberg, C. Z. Bisgaard, H. Stapelfeldt, P. F. Staanum, A. Mortensen, and M. Drewsen. *Phys. Rev. A*, 77:030702, 2008.

[24] B. Roth, P. Blythe, H. Wenz, H. Daerr, and S. Schiller. *Phys. Rev. A*, 73:042712, 2006.

[25] T. Schneider, B. Roth, H. Duncker, I. Ernsting, and S. Schiller. *Nat. Phys.*, 6:275–278, 2010.

[26] A. D. Gingell, M. T. Bell, J. M. Oldham, T. P. Softley, and J. N. Harvey. *J. Chem. Phys.*, 133(19):194302, 2010.

[27] M. T. Bell, A. D. Gingell, J. M. Oldham, T. P. Softley, and S. Willitsch. *Faraday Discuss.*, 142:73–91, 2009.

[28] P. F. Staanum, K. Højbjerre, P. S. Skyt, A. K. Hansen, and M. Drewsen. *Nat. Phys.*, 6:271–274, 2010.

[29] X. Tong, D. Wild, and S. Willitsch. *Phys. Rev. A*, 83:023415, 2011.

[30] X. Tong, A. H. Winney, and S. Willitsch. *Phys. Rev. Lett.*, 105:143001, 2010.

[31] W. W. Smith, O. P. Makarov, and J. Lin. *J. Mod. Opt.*, 52:2253, 2005.

[32] C. Zipkes, S. Palzer, C. Sias, and M. Kohl. *Nature*, 464:388, 2010.

[33] S. Schmid, A. Härter, and Hecker Denschlag J. *Phys. Rev. Lett.*, 105:133202, 2010.

[34] F. H. J. Hall, M. Aymar, N. Bouloufa-Maafa, O. Dulieu, and Willitsch S. *Phys. Rev. Lett.*, 107:243202, 2011.

[35] W. G. Rellergert, S. T. Sullivan, S. Kotochigova, A. Petrov, K. Chen, S. J. Schowalter, and E. R. Hudson. *Phys. Rev. Lett.*, 107:243201, 2011.

[36] K. Ravi, A. Sharma, G. Werth, and S. A. Rangwala. *Appl. Phys. B*, 107:971, 2011.

[37] I. Sivarajah, D. S. Goodman, J. E. Wells, F. A. Narducci, and W. W. Smith. *Phys. Rev. A*, 86:063419, 2012.

[38] S. Haze, S. Hata, M. Fujinaga, and T. Mukaiyama. *Phys. Rev. A*, 87:052715, 2013.

[39] F. H. J. Hall, P. Eberle, G. Hegi, M. Raoult, M. Aymar, O. Dulieu, and S. Willitsch. *Mol. Phys.*, 111(14-15):2020–2032, 2013.

[40] F. H. J. Hall and S. Willitsch. *Phys. Rev. Lett.*, 109:233202, 2012.

[41] D. Rösch, S. Willitsch, Y-P. Chang, and J. Küpper. *J. Chem. Phys.*, 140(12), 2014.

[42] Y-P. Chang, K. Dlugol ecki, J. Küpper, D. Rösch, D. Wild, and S. Willitsch. 342(6154):98–101, 2013.

[43] M. C. Heaven. 342(6154):46–47, 2013.

[44] S. Chefdeville, Y. Kalugina, S. Y. T. van de Meerakker, C. Naulin, F. Lique, and M. Costes. *Science*, 341(6150):1094–1096, 2013.

[45] V. A. Belyaev, B. G. Brezhnev, and E. M. Erastov. *JETP Lett.*, 3:207, 1966.

[46] S. M. Trujillo, R. H. Nenaber, L. Marino, and W. Rothe. Proc. of the ivth int. conf. on the physics of electronic and atomic collisions, new york: Science bookcrafters. page 260, 19665.

[47] A. B. Henson, S. Gersten, Y. Shagam, J. Narevicius, and E. Narevicius. *Science*, 338(6104):234–238, 2012.

[48] E. Lavert-Ofir, Y. Shagam, A. B. Henson, S. Gersten, J. Klos, P. S. Żuchowski, J. Narevicius, and E. Narevicius. *Nat. Chem.*, 6:332–335, 2014.

[49] J. Jankunas, B. Bertsche, and A. Osterwalder. *J. Phys. Chem. A*, 118(22):3875–3879, 2014.

[50] J. Jankunas, B. Bertsche, K. Jachymski, M. Hapka, and A. Osterwalder. *J. Chem. Phys.*, 140(24):–, 2014.

[51] K.-K. Ni, S. Ospelkaus, M. H. G. de Miranda, A. Pe'er, B. Neyenhuis, J. J. Zirbel, S. Kotochigova, P. S. Julienne, D. S. Jin, and J. Ye. *Science*, 322(5899):231–235, 2008.

[52] K.-K. Ni, S. Ospelkaus, D. Wang, G. Quemener, B. Neyenhuis, M. H. G. de Miranda, J. L. Bohn, J. Ye, and D. S. Jin. *Nature*, 464:1324–1328, 2010.

[53] K.-K. Ni, S. Ospelkaus, D. J. Nesbitt, J. Ye, and D. S. Jin. *Phys. Chem. Chem. Phys.*, 11:9626–9639, 2009.

[54] S. Ospelkaus, A. Pe/'er, K.-K. Ni, J. J. Zirbel, B. Neyenhuis, S. Kotochigova, P. S. Julienne, J. Ye, and D. S. Jin. *Nat. Phys.*, 4:622–626, 2008.

[55] H. L. Bethlem, F. M. H. Cropmverts, R. T. Jongma, and G. van der Meerakker, S. Y. T.and Meijer. *Phys. Rev. A.*, 65:053416, 2002.

[56] N. Vanhaecke, U. Meier, M. Andrist, B. H. Meier, and F. Merkt. *Phys. Rev. A.*, 75:031402, 2007.

[57] E. Narevicius, C. G. Parthey, A. Libson, J. Narevicius, I. Chavez, u. Even, and M. G. Raizen. *New J. Phys.*, 9:358, 2007.

[58] S. A. Rangwala, T. Junglen, T. Riegler, and P. W. H. Pinkse. *Phys. Rev. A.*, 67:043406, 2003.

[59] J. K. Messer and F. C. de Lucia. *Phys. Rev. Lett.*, 53:25552558, 1984.

[60] J. M. Doyle, B. Friedrich, J. Kim, and D. Patterson. *Phys. Rev. A*, 52:R2518, 1995.

[61] M. Gupta and D. D. Herschbach. *J. Phys. Chem. A*, 103:1067010673, 1999.

[62] K. E. Strecker and D. W. Chandler. *Phys. Rev. A*, 78:063406, 2008.

[63] J. J. Kay, S. Y. T. van der Meerakker, K. E. Strecker, and D. W. Chandler. *Faraday Discuss.*, 142:143154, 2009.

[64] J. F. Barry, E. S. Shuman, E. B. Norrgard, and D. DeMille. *Phys. Rev. Lett.*, 108:103002, 2012.

[65] I. S. Vogelius, L. B. Madsen, and M. Drewsen. *Phys. Rev. A*, 70:053412, 2004.

[66] N. Deb, B. R. Heazlewood, M. T. Bell, and T. P. Softley. *Phys. Chem. Chem. Phys.*, 15:14270–14281, 2013.

[67] N. Deb, B. R. Heazlewood, C. J. Rennick, and T. P. Softley. *J. Chem. Phys.*, 140(16):–, 2014.

[68] L. D. Harper. PhD Thesis, University of Oxford. 2013.

[69] M. T. Bell. Phd thesis, university of oxford. 2008.

[70] K. Twyman, M. T. Bell, B. R. Heazlewood, and T. P. Softley. *J. Chem. Phys. (accepted)*, 2014.

[71] A. D. Gingell. PhD Thesis, University of Oxford. 2010.

[72] I. S. Vogelius, L. B. Madsen, and M. Drewsen. *Phys. Rev. Lett.*, 89:173003, 2002.

[73] F. H. J. Hall and S. Willitsch. *Phys. Rev. Lett.*, 109:233202, 2012.

[74] M. Schwarz, O. O. Versolato, A. Windberger, F. R. Brunner, T. Ballance, S. N. Eberle, J. Ullrich, P. O. Schmidt, A. K. Hansen, A. D. Gingell, M. Drewsen, and J. R. Crespo Lóppez-Urrutia. *Rev. Sci. Instrum.*, 83(8):083115, 2012.

[75] M. J. Frisch, G. W. Trucks, H. B. Schlegel, G. E. Scuseria, M. A. Robb, J. R. Cheeseman, G. Scalmani, V. Barone, B. Mennucci, G. A. Petersson, H. Nakatsuji, M. Caricato, X. Li, H. P. Hratchian, A. F. Izmaylov, J. Bloino, G. Zheng, J. L. Sonnenberg, M. Hada, M. Ehara, K. Toyota, R. Fukuda, J. Hasegawa, M. Ishida, T. Nakajima, Y. Honda, O. Kitao, H. Nakai, T. Vreven, J. A. Montgomery, Jr., J. E. Peralta, F. Ogliaro, M. Bearpark, J. J. Heyd, E. Brothers, K. N. Kudin, V. N. Staroverov, R. Kobayashi, J. Normand, K. Raghavachari, A. Rendell, J. C. Burant, S. S. Iyengar, J. Tomasi, M. Cossi, N. Rega, J. M. Millam, M. Klene, J. E. Knox, J. B. Cross, V. Bakken, C. Adamo, J. Jaramillo, R. Gomperts, R. E. Stratmann, O. Yazyev, A. J. Austin, R. Cammi, C. Pomelli, J. W. Ochterski, R. L. Martin, K. Morokuma, V. G. Zakrzewski, G. A. Voth, P. Salvador, J. J. Dannenberg, S. Dapprich, A. D. Daniels, . Farkas, J. B. Foresman, J. V. Ortiz, J. Cioslowski, and D. J. Fox. Gaussian09 (Revision D.01). Gaussian Inc. Wallingford CT 2009.

[76] N. Vanhaecke and O. Dulieu. *Mol. Phys.*, 105(11-12):1723–1731, 2007.

[77] W. J. Balfour. *Can. J. Phys.*, 50:1082, 1972.

[78] K. L. Saenger, R. N. Zare, and C. W. Mathews. *J. Mol. Spectrosc.*, 61:216, 1976.

[79] H. J. Werner, P. Rosmus, W. Schätzl, and W. Meyer. *J. Chem. Phys.*, 80:831, 1984.

[80] B. K. Taylor and P. R. Newman. *J. Chem. Phys.*, 118:8770–8780, 2003.

[81] M. Aymar, R. Guérout, M. Sahlaoui, and O. Dulieu. *J. Phys. B: At., Mol. Opt. Phys.*, 42:154025, 2009.

[82] M. Hamdan, N. W. Copp, D. P. Wareing, Jones J. D. C., K. Birkinshaw, and N. D. Twiddy. *Chem. Phys. Lett.*, 89:63–66, 1982.

[83] M. Michel, M. V. Korolkov, and K.-M. Weitzel. *J. Phys. Chem. A*, 108:99249930, 2004.

[84] A. D. Webb, N. H. Nahler, R. N. Dixon, and M. N. Ashfold. *J. Chem. Phys.*, 125:204312, 2006.

[85] X. Tong, A. H. Winney, and S. Willitsch. *Phys. Rev. Lett.*, 105:143001, 2010.

[86] M. Drewsen. *Nature*, in press.

[87] S. Schlemmer, O. Asvany, and T. Giesen. *Phys. Chem. Chem. Phys.*, 7:1592–1600, 2005.

[88] O. Asvany, T. Giesen, B. Redlich, and S. Schlemmer. *Phys. Rev. Lett.*, 94:073001, 2005.

[89] J. T. Hougen. *J. Chem. Phys.*, 36:519–534, January 1962.

[90] G. Herzberg. *Molecular Spectra and Molecular Structure III. Electronic Spectra and Electronic Structure of Polyatomic Molecules*. D. Van Nostrund Company, Inc Princeton, New Jersey New York, 1966.

[91] Istvan Kovacs. *Rotational Structure in the Spectra of Diatomic Molecules*. Adam Hilger LTD London 60 Rochester Place London NW 1, 1969.

[92] Larcher C. Gauyacq, D. and J. Rostas. *Can. J. Phys.*, 57:1634, 1979.

[93] K. Kawaguchi, C. Yamada, and E. Hirota. *J. Chem. Phys.*, 82:1174, 1985.

[94] Facundo Bueso-Sanllehí. *Phys. Rev.*, 60:556–570, Oct 1941.

[95] M. N. R. Ashfold. *Mol. Phys.*, 58(1):1–20, 1986.

[96] Buenker R. J. Perić, M. and S. D. Peyerimhoff. *Mol. Phys.*, 53(5):1177–1193, 1984.

[97] M. N. R. Ashfold, B. Tutcher, B. Yang, Z. K. Jin, and S. L. Anderson. *J. Chem. Phys.*, 87(9):5105–5115, 1987.

[98] Ch. Cha, R. Weinkauf, and U. Boesl. *J. Chem. Phys.*, 103(13):5224–5235, 1995.

[99] S. Earnshaw. *Trans. Camb. Phil. Soc.*, 7:97112, 1842.

[100] R. Blatt, P. Gill, and R.C. Thompson. *J. Mod. Opt.*, 39(2):193–220, 1992.

[101] K. Sheridan and M. Keller. *New J. Phys.*, 13(12):123002, 2011.

[102] E. Fischer. *Z. Phys.*, 156(1):1–26, 1959.

[103] G. Gabrielse. *Int. J. Mass. Spectrom.*, 251:273–280, 2006.

[104] N. Kjærgaard and M. Drewsen. *Phys. Plasmas.*, 8(4):1371–1375, 2001.

[105] N. Kjærgaard, K. Mølhave, and M. Drewsen. *Phys. Rev. E*, 66:015401, 2002.

[106] D. Gerlich. *State-Selected and State-to-State Ion-Molecule Reaction Dynamics. Part 1: Experiment. Advances in Chemical Physics Series, Vol. LXXXII. Chapter- In homogenous RF Fields: A Versatile Tool for the Study of Processes with Slow Ions.* John Wiley and Sons, Inc, USA, 1992.

[107] E. D. Courant and H. S. Snyder. *Ann. Phys. (N.Y.)*, 3:1, 1958.

[108] M. Drewsen and A. Br$\acute{}$oner. *Phys. Rev. A*, 62:045401, 2000.

[109] A. Smith. Part-II Thesis, University of Oxford. 2014.

[110] M. Abramowitz and I. A. Stegun. *Handbook of Mathematical Functions*. Dover, NewYork, USA, 1970.

[111] S. M. Bae G. Ritter and U. Eichmann. *Appl. Phys. B*, 66:609–612, 1998.

[112] J. Jin and D. A. Church. *Phys. Rev. Lett.*, 70:32133216, 1993.

[113] T. Gudjons, B. Hilbert, P. Seibert, and G. Werth. *Phys. Rev. Lett.*, 33:595598, 1996.

[114] J. Emsley. *The Elements*. Oxford University Press, Oxford, UK, 1995.

[115] L. Hornekær, N. Kjærgaard, A. M. Thommesen, and M. Drewsen. *Phys. Rev. Lett.*, 86:1994–1997, Mar 2001.

[116] E. L. Pollock and J. P. Hansen. *Phys. Rev. A*, 8:3110–3122, 1973.

[117] L. Pollum. PhD Thesis, University of Oxford. under preparation.

[118] J. M. Oldham. PhD Thesis, University of Oxford. under preparation.

[119] R. E. March and J. F. Todd. *Quadrupole Ion Trap Mass Spectrometry, 2nd edition.* Hoboken, NJ ; Chichester : Wiley, 2005.

[120] S. Willitsch, M. T. Bell, A. D. Gingell, and T. P. Softley. *Phys. Chem. Chem. Phys.*, 10:7200–7210, 2008.

[121] B. Roth, A. Ostendorf, H. Wenz, and S. Schiller. *J. Phys. B: At., Mol. Opt. Phys.*, 38(20):3673, 2005.

[122] M. Drewsen, A. Mortensen, R. Martinussen, P. Staanum, and J. L. Sorensen. *Phys. Rev. Lett.*, 93:243201, 2004.

[123] W. E. Stephens. *Phys. Rev.*, 69:691, 1946.

[124] W. C. Wiley and I. H MacLaren. *Rev. Sci. Instrum.*, 26:1150, 1955.

[125] C. Schneider, S. J. Schowalter, K. Chen, S. T. Sullivan, and E. R. Hudson. *arXiv:1404.1104v1*, 2014.

[126] Y. Ito, P. Schury, M. Wada, S. Naimi, C. Smorra, T. Sonoda, H. Mita, A. Takamine, K. Okada, A. Ozawa, and H. Wollnik. *Nucl. Instrum Meth. B*, 317, Part B(0):544 – 549, 2013.

[127] A. Ostendorf, C. B. Zhang, M. A. Wilson, Roth B. Offenberg, D., and S. Schiller. *Phys. Rev. Lett.*, 97:243005, 2006.

[128] P. Blythe, B. Roth, U. Frohlich, H. Wenz, and S. Schiller. *Phys. Rev. Lett.*, 95:183002, 2005.

[129] M. Stellpflug, M. Johnsson, I. D. Petrova, and T. Halfmannb. *Eur. Phys. J. D*, 23:35–42, 2003.

[130] J. Qian, H. Fu, and S. L. Anderson. *J. Phys. Chem. A*, 101(36):6504–6512, 1997.

[131] A. D. Webb, N. H. Nahler, R. N. Dixon, and M. N. R. Ashfold. *J. Chem. Phys.*, 125(20), 2006.

[132] R. N. Zare. *Angular Momentum*. John Wiley and Sons, Inc USA, 1988.

[133] G. Herzberg. *Molecular Spectra and Molecular Structure II. Infrared and Raman Spectra of Polyatomic Molecules*. D. Van Nostrund Company, Inc Princeton, New Jersey New York, 1945.

[134] M. G. Raizen, J. M. Gilligan, J. C. Bergquist, W. M. Itano, and D. J. Wineland. *Phys. Rev. A*, 45:6493–6501, 1992.

[135] N. Kjærgaard. private communication.